UNIVERSITÀ
DI PARMA

UNIVERSITA' DEGLI STUDI DI PARMA

DOTTORATO DI RICERCA IN
"SCIENZA E TECNOLOGIA DEI MATERIALI"

CICLO XXX

ALL-CERAMIC ASYMMETRIC MEMBRANES FOR HYDROGEN SEPARATION

Coordinatore:
Chiar.mo Prof. Enrico Dalcanale

Tutore:
Dr.ssa Alessandra Sanson

Dottorando: Daniel Montaleone

Anni 2014/2017

To Annamaria
and Elena

““Intellectual fun” is a great driving force in science.
Trying to keep the right balance between enthusiasm and skepticism
may be a good means to become a happy and successful scientist.”
K. D. Kreuer

“The scientist is not a person who gives the right answers,
he's one who asks the right questions.”
C. Lévi-Strauss

“Non basterebbe una vita.”
N. Sangiorgi

Research Objective and Thesis structure

Considering the limited fossil fuel reserves, the climate changes due to continuous CO_2 emissions, a transition to a cleaner energy economy is vital. The "hydrogen economy" represents a valid solution to move towards a sustainable and cleaner energy-based society. On a short-term period, hydrogen-based technologies using fossil fuel as feedstock could help the transition. In particular, syngas processing intensification and optimization may solve some issues addressed to climate change and green energy carrier. In fact, H_2 is always contained in a gas mixture, therefore H_2 must be selectively and efficiently separated to promote H_2-based technologies.

In this sense, dense ceramic H_2 separation membranes can promote the process intensification of pre-existent implants. One category of dense proton conducting membranes that has received considerable attention in the preceding decade is represented by various type of Mixed Proton-Electron Conductor ceramics (MPECs). A MPEC membrane transports at the same time both protons and electrons and hydrogen separation can be achieved in a non-galvanic mode without using an external power supply. Among these materials, the Y-doped $BaCe_xZr_{1-x}O_{3-\delta}$ system (BCZY) is one of the best candidate for the abovementioned applications thanks to a good compromise between conductivity at medium temperatures (600 - 800°C) and stability under CO_2 and H_2O exposure. However, in these systems, hydrogen permeability is limited by the low electronic conductivity that should be increased to make them useful in pressure driven type devices.

The work reported in this thesis therefore was focused on the materials development and membrane architecture needed to obtain highly performing all-ceramic membranes, in particular on:

1. The production of a two-phase composite membrane (cer-cer), consisting of a primarily proton conducting material (BCZY) and a ceramic electronic conductor.

2. The optimization of the membrane architecture. When permeation across the membrane is controlled by transport through the solid phase and not by boundary layer transport or by the activation of H_2 at membrane surfaces, the permeation rates are inversely proportional to the thickness of the membrane. Therefore, membranes consisting of dense films supported on porous substrates (asymmetric configuration) should lead to much higher permeation rates than the thicker structures currently used.

In summary This thesis reports the activity done on the process optimization need for the manufacturing of a cer-cer asymmetric membrane. In addition, the effect of the engineered architecture on the membrane's performance has been evaluated through H_2 permeation measurements under different condition. Figure 1 schematizes the thesis structure describing the content of each chapter.

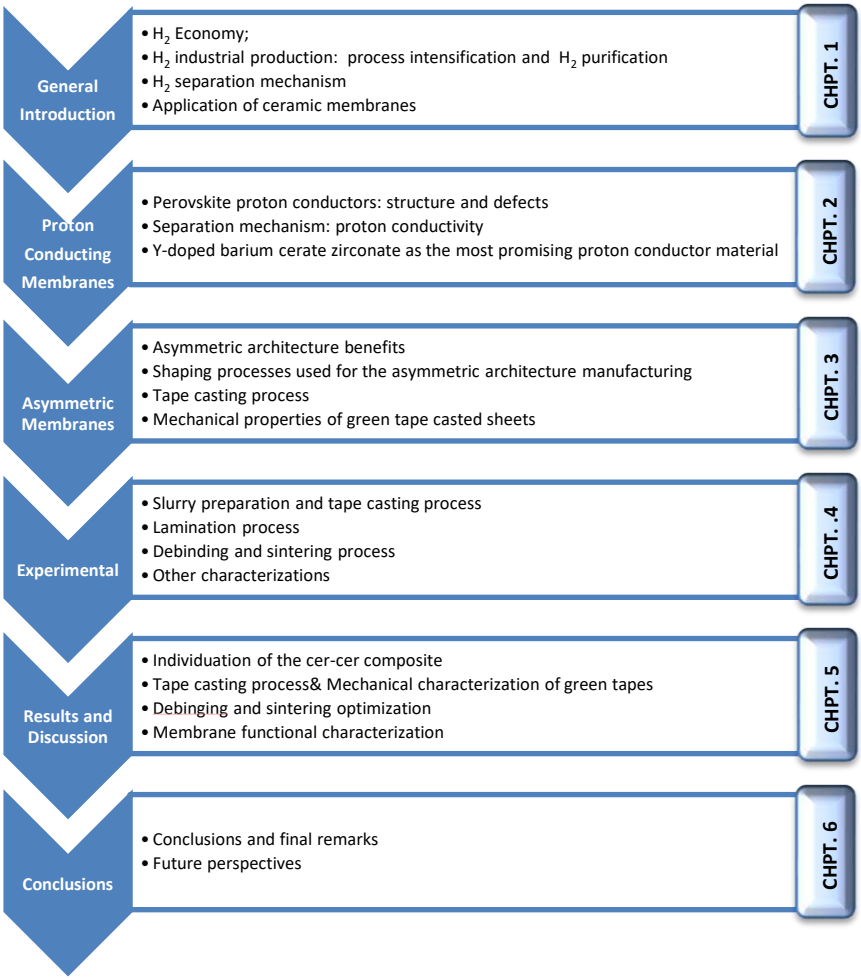

Figure 1 Schematic of the thesis structure.

Contents

Chapter 1
General Introduction

1.1 Introduction

It has been estimated that in 2023 eight billion of people will populate planet Earth with consequent rise in the demand for food, water, energy and infrastructure. Since the industrial revolution in the 18th century, fossil fuels in the form of coal, oil, and natural gas have powered the technology and transportation networks that drive society. However, the carbon-based economy that characterise our century has limitations and drawbacks: it threatens the energy supply owing to limited supply of fossil fuels, generates social tensions because of the concentration of reserves in restricted areas and has a detrimental impact on the environment.

In 2016, the world energy production showed a slight slowdown, mainly because of the Chinese coal production in a move to decarbonisation the economy. The trend of energy production shrinkage in European Union countries has accelerated as well, owing to the depletion of oil and gas resources and to the more and more restrictive climate policy. The main contributors to energy production increase have been the main oil and gas exporting countries (Russia, Saudi Arabia) as well as the fast-developing countries such as India and Turkey (Figure 1.1).

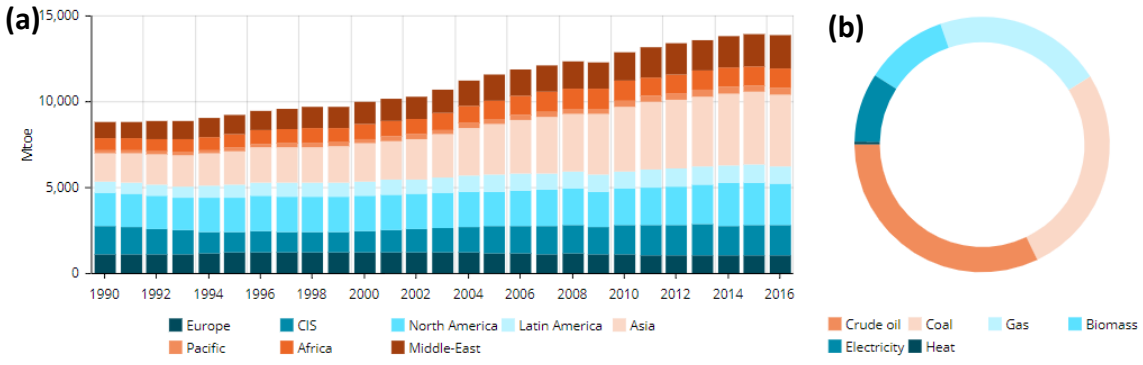

Figure 1.1 (a) World energy consumption trend over 1990-2016 by regions; (b) breakdown by energy (2016). (Source Enerdata).

Electricity represents only the 9% of the energy consumption in 2016, indicating that the CO_2 emissions still represent an environmental issue (Figure 1.2). However, the trend is still away from the climate change targets set at the COP21

(1.5 to 2°C increase by the end of the century) which would require a strong and immediate reduction of CO_2 emission.

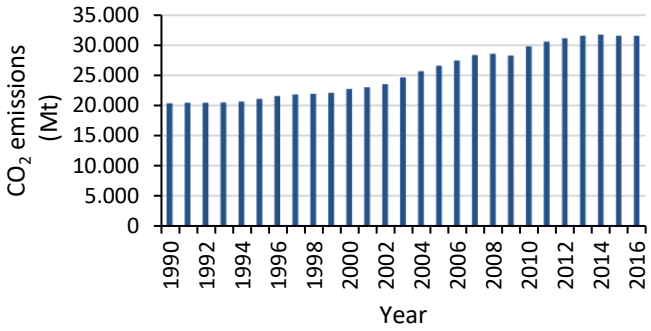

Figure 1.2 CO_2 emissions and refined oil products production trends over 1990-2016. (Source Enerdata).

To tackle these urgent issues, a "sustainable development" must be put in place to face the new world energy demand[1]. The "sustainable development" concept was introduced in 1987 by the World Commission on Environment and Development as the "development that meets the needs of the present without compromising the ability of future generations to meet their own needs. It contains within it two keys concepts: the concept of needs, in particular the essential needs of the world's poor, to which overriding priority should be given; and the idea of limitations imposed by the state of technology and social organization on the environment's ability to meet present and future needs"[2].

The development of clean and durable energy technologies is thus essential to meet the world energy demand and the environmental strains. However, based on present technologies, the independence from fossil fuels is not practical in the immediate future. Therefore, the parallel development of long- and short-term technologies is a more affordable strategy to face these issues. The short-term technologies aim at minimizing gas emissions and increase the efficiency of existent processes based on fossil fuels technologies. To complete the transition to a clean and sustainable energy economy, the development of long-term technologies based on renewable and clean energy sources is vital.

1.2 Hydrogen production and purification needs

On a short-term period, hydrogen-based technologies using fossil fuel as feedstock could help the transition towards a sustainable and cleaner energy-based society. In fact, the worldwide increasing environmental concern is a strong incentive for using hydrogen as a sustainable and clean energy source. "Hydrogen economy" has been around since 1970s, but it started to look practicable only in recent years. Although it is the universe's most abundant element, in our planet ready-to-use hydrogen is not stored in gas cups, but it only exists in chemical compounds, hydrocarbons mainly. Therefore, it must be extracted chemically from hydrogen-rich materials such as natural gas, water, coal, or plant matters. The main product of these processes is the synthesis gas, commonly known as "syngas", a mixture of hydrogen (H_2) and carbon monoxide (CO), which is formed by reforming or gasification of a hydrocarbon feedstock. Syngas is a vitally important chemical feedstock for producing synthetic fuels including H_2 and higher hydrocarbons, chemicals including alcohols, ether, ammonia. Research into the production and processing of syngas has increased dramatically in the last few decades enhancing the impact of anthropogenic climate change. Syngas processing intensification and optimization may solve some issues addressed to climate change and green energy carrier.
Many other technologies are also being studied, including several that produce hydrogen from biomass using solar or other renewable energy. However, these long-term technologies need further efforts to meet the requirements of large-scale, durability and economic feasibility.

1.2.1 Hydrogen from fossil fuels

There are three main reaction pathways commonly used in industry for syngas generation: steam reforming, water-gas shift and partial oxidation.

- S**team reforming:** the main chemical process for the hydrogen production.

This process makes hydrogen from a mixture of water and a hydrocarbon feedstock, usually a fossil fuel. The most common feedstock is natural gas, which consists primarily of methane. When steam and the methane or other hydrocarbons are combined at high pressure and temperature, a chemical reaction converts them into hydrogen and carbon monoxide:

$$C_nH_m + n\ H_2O \leftrightarrow n\ CO + (n + m/2)\ H_2 \quad (1.1)$$

- **Water-gas shift**: reaction coupled with the steam reforming reaction.

The carbon monoxide produced from the steam reforming can further react with steam to produce H_2 and CO_2 by the exothermic reaction:

$$CO + H_2O \leftrightarrow CO_2 + H_2 \quad (1.2)$$

- **Partial oxidation** of methane and other hydrocarbons:

$$CH_4 + 1/2O_2 \leftrightarrow CO + 2\ H_2 \quad (1.3)$$

Less hydrogen is produced per mole of methane by this reaction than the steam reforming reaction. However, for certain applications, the low efficiency may be offset by advantages such as compactness, rapid start-up, responsiveness to load change, and overall cost, especially when O_2 is supplied directly by separation from air using a reactor built with a mixed oxygen ionic and electronic conducting ceramic membrane.

1.2.2 Hydrogen from renewables

Hydrogen's long-term potential value lies primarily in serving as a versatile energy carrier such as a fuel which will be ultimately derived from renewable energy sources and consumed with little or no pollution.

The use of **biomass** instead of fossil fuels has been demonstrated on a small scale and is expected to be the most cost-effective renewable option at large plant sizes. But further technological advances are to be implemented before biomass becomes a major commercial hydrogen source[3].

1.3 Hydrogen Separation Techniques

As described in the previous paragraph, the main product of the fossil fuel processing is a gas mixture called "synthesis gas", with H_2 and CO as predominant components. Regardless of which method is used to produce hydrogen, a cost-effective and efficient hydrogen separation from the other species is required. Since the capital cost of the separation process is very high in these hydrogen generation processes, whether the separation process is efficient and cost-effective or not, will determine the economic margin of the hydrogen generation.

There are two distinct ways in which hydrogen can be used as a fuel. One is to use hydrogen for transportation by mixing it with natural gas in modified internal combustion engines, which would increase engine performance and decrease pollution. The second approach is to use fuel cells. Restructuring of the electric utility industry will present opportunities of using hydrogen for distributed energy generation, where hydrogen-powered fuel cells will provide on-site generation of electricity. However, the fuel cell technology requires highly pure hydrogen (purity ≥ 99.99%), therefore the separation process must show complete selectivity to hydrogen molecules in the gas mixture.

Figure 1.3 schematizes the processing of the carbon-based feedstock for the H_2 production. As showed, the main product of the main processes is the syngas, therefore the separation step is mandatory to obtain pure H_2.

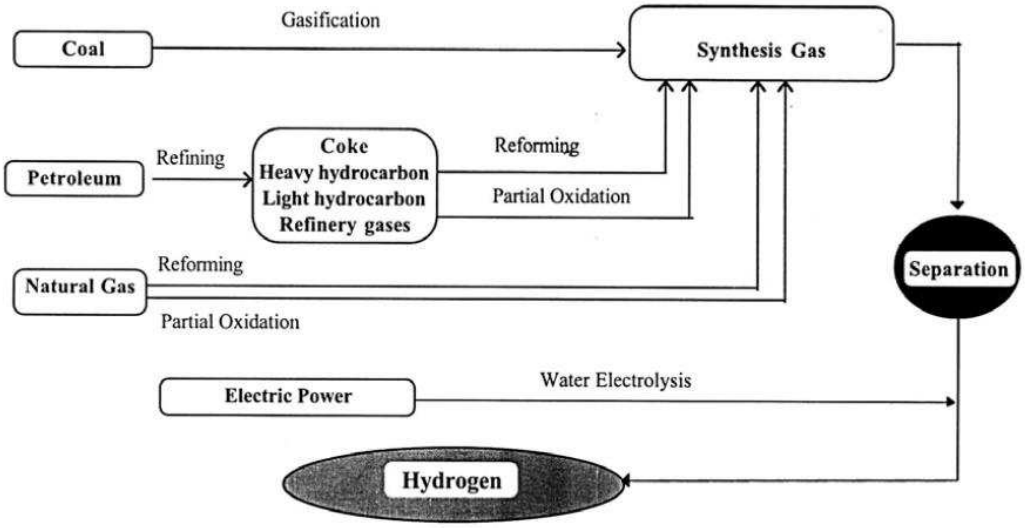

Figure 1.3 Schematic illustration of hydrogen production and separation[7].

Currently, three major approaches are used for industrial hydrogen separation, namely pressure swing adsorption (PSA), cryogenic separation, and membrane separation.

- The *cryogenic separation* exploits the different boiling points of the gas components. It has excellent economies of scale, but it needs a considerable amount of energy to condense the gas mixture[4]. In addition, only moderate purities are achieved (up to a maximum of 95%). Because of these limitations, other technologies are more attractive for hydrogen separation[5].

- In *PSA*, solid particles of adsorbent (e.g. activated carbon, zeolite, silica gel, activated alumina) selectively adsorb carbon-based molecules on their surface. The hydrogen-enriched gas mixture can be stored separately form the feed stream and the adsorbent then must be generated by pressure reduction. To ensure a continuous separation process, multiple columns are required for multiple steps. Recently, there have been significant improvements in PSA implants, and 99.99% product purity is achieved thanks to an extensive experimental and simulation work[6]. Yet some

challenges need to be overcome: plant size reduction, adaptability to fluctuation in feed composition and higher operating temperature. In fact, the feed gas must be cooled, with consequent loss in the overall efficiency[6].

- *Membrane separation* is currently considered to be the most promising among the separation technologies because of the low energy consumption, possibility for continuous operations and process intensification. In fact, the implementation of a membrane in pre-existent syngas implants lead to a continuous hydrogen extraction shifting the thermodynamics towards higher hydrogen yields.

In the next paragraph, different kind of membranes will be described discussing the advantages and disadvantages for each system.

1.4 Membranes for Hydrogen Separation

Figure 1.4 illustrates the nomenclature use for describe the membranes separation processes. The two sides of the membrane are called feed (upstream) side and permeate (downstream) side. Generally speaking, the target molecule (in this thesis, H_2) permeate from the feed to the permeate side. The feed flow resulting after permeation is called retentate.

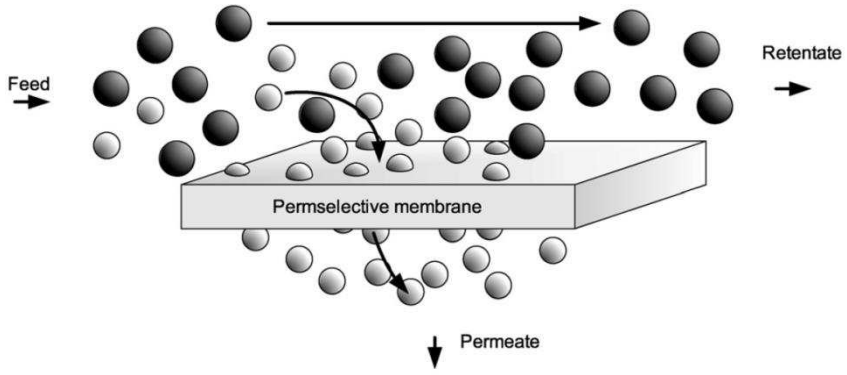

Figure 1.4 Schematic permselective membrane separation concept[8].

The chemical species that permeate through the membrane form the so-called flux. Depending on the separation mechanism of the specific membrane, molecules, electrons, or protons can form the flux. The selectivity towards H_2, as the H_2 flux, is the main indication of the performance and efficiency of the membranes. The selectivity is a measure for the membrane separation effectiveness since it is related to the difference in permeabilities of different components. The selectivity factor $\alpha_{A/B}$ of two components A and B in a mixture is defined as:

$$\alpha_{A/B} = \frac{y_A/y_B}{x_A/x_B} \quad (1.2)$$

Where y_A and y_B are the fractions of components A and B in the permeate and x_A and x_B are the fractions of the components in the feed. Therefore, the higher the selectivity factor, the more selective is the membrane.

The gas separation mechanism depends on the membrane microstructure. Therefore, membranes can be divided in porous and dense, as the permeation takes place through the pores or through the bulk of the material, respectively.

It is worth to point out that hydrogen separation membranes can be made of different materials: polymers, metals, ceramics and carbon. However, for high temperature processes (such as those explained above) only the inorganic membranes can be successfully used thanks to their thermal and chemical stability.

1.4.1 Porous inorganic membranes

Gas transport through porous membranes is controlled by the porous structure of the membrane material. Four main types of diffusion mechanism can be utilized in a porous membrane (Figure 1.5). In some cases, molecules can move through the membrane by more than one mechanism. Knudsen diffusion gives relatively low separation selectivities compared to the other. The separation factor for these mechanisms depends strongly on pore size distribution, temperature, pressure and interaction between gas and membrane surfaces.

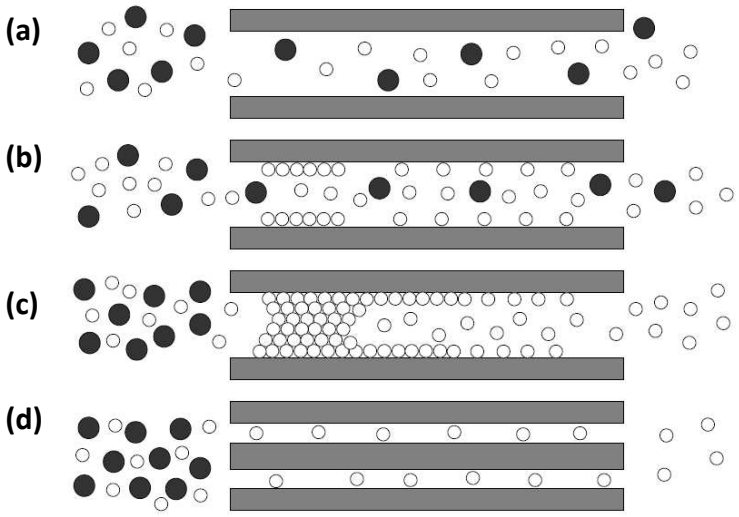

Figure 1.5 Graphical illustration of the H_2 separation mechanism of porous membranes; (a) Knudsen diffusion, (b) surface diffusion, (c) capillary condensation and (d) molecular sieving[7].

In Knudsen (or free-molecule) diffusion the transport is through macro- and mesopores. For Knudsen flow, a permeating molecule is more likely to collide with the pore wall than colliding with another molecule inside the pore; the Knudsen number (Kn) can be described as:

$$Kn = \frac{\lambda}{L} \tag{1.3}$$

Where λ is the mean free path of the gas molecule (average distance between collisions) and L is the pore radius. If Kn value is higher than 10, mainly the lighter molecules permeate through the pores. The larger the pores, the smaller the Kn becomes, as well as the selectivity. For Kn < 1, the dominant transport mechanism is "viscous flow", which is non-selective[7].

Surface diffusion can occur in parallel to Knudsen diffusion. Gas molecules are adsorbed on the pore walls of the membrane and migrate along the surface. Surface diffusion increases the permeability of the components adsorbing more strongly to the membrane pores. At the same time, the effective pore diameter is reduced. Consequently, the transport of non-adsorbed components is reduced and

selectivity is increased. The temperature and the pore diameter highly affect this diffusion mechanism.

Capillary condensation occurs if a condensed phase partially fills the membrane pores. If the pores are completely filled with condensed phase, only the species soluble in the condensed phase can permeate through the membrane. fluxes and selectivities are generally high. The condensation, however, strongly depends on gas composition, pore size and uniformity.

*Molecular sievin*g appears when the pore size is sufficiently small (3.0-5.2 Å) resulting in a separation based on the different kinetic diameter of the gas components. Since H_2 is the smallest among the molecules in syngas-based processes, it can be used to enrich in hydrogen the gas mixture.

Among porous systems, **silica membranes** are one of the candidates for hydrogen separation due to their ease of fabrication, low cost of production, and scalability. Because of their porosity and composition, silica membranes are also less expensive than metals (due to the lack of precious elements) and not susceptible to H_2 embrittlement.
They are inorganic membranes that have a network of connected micropores of approximately 0.5 nm diameter and can accommodate the separations of small molecules such as H_2, He, CO_2, CO, N_2, and O_2.
Contrary to dense metal, alloy, and ceramic membranes, microporous silica membranes are not 100% selective for one component. Their separation of molecular mixtures is based on a competitive process in which individual molecules move by site-hopping diffusion in the connected micropore network.
For transport through macro- and mesopores, molecular diffusion, Knudsen diffusion and viscous flow all contribute to the total transport, while the activated surface flow of the adsorbed phase will affect microporous transport. The pore sizes of silica and silica-derived membranes are in the mesopore and micropore range, therefore Knudsen and activated diffusion or molecular sieving should be considered.

Zeolites form another relevant class of inorganic porous membranes. Zeolite membranes, combine pore size and shape selectivity with the inherent mechanical, thermal, and chemical stability necessary for continuous long-term separation processes. Zeolites are crystalline inorganic framework structures that have uniform, molecular-sized pores, acting as natural molecular sieves. Therefore, the effective pore size distribution of the zeolite membrane, and hence its separation performance, is intrinsically governed by the choice of the zeolitic phase(s). More recently, membranes of continuous polycrystalline zeolite layers have been deposited on porous supports.

However, one of the main challenges in zeolite membrane development is the minimization of inter-crystal pores formed in polycrystalline films. In fact, the existence of inter-crystal pores lowers the molecular separation efficiency, as the non-selective viscous flow can take place through grain boundaries[5].

The drawbacks of silica and zeolite membranes are mainly two: i) the low selectivity because they are permeable, to some extent, to almost all gas species; and ii) their hydrothermal degradation and pore closure in the presence of high stream concentration[8]. To obtain highly pure hydrogen, microporous membranes must be coupled with PSA units, resulting in a low-compact separation system[9].

1.4.1 Dense inorganic membranes

A variety of metallic and ceramic dense membranes have been used for H_2 separation from gas streams through the solution/diffusion mechanism (Figure 1.6). There are five consecutive steps taking place during gas transport. First, the gas molecules diffuse from the bulk gas phase and adsorb on the surface of the membrane. The adsorbed H_2 molecules are then dissociated to form hydrogen atoms. The hydrogen atoms dissolve into the metal/ceramic lattice and diffuse to the opposite side of the membrane. Finally, the hydrogen atoms recombine to reform the H_2 molecule on the surface and desorb from the permeate side.

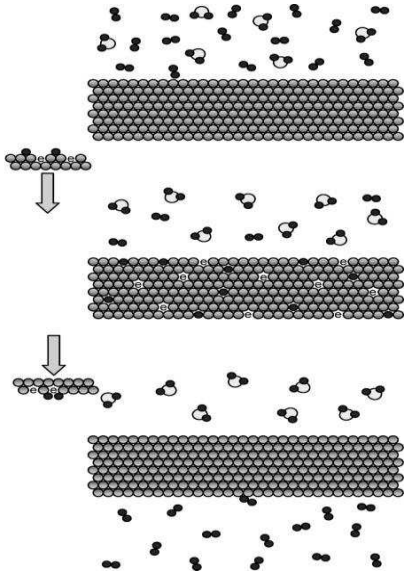

Figure 1.6 Schematic representation for the solution/diffusion mechanism for H_2 separation[5].

Dense metallic membranes

These are primarily Pd-based alloys exhibiting unique perm-selectivity to hydrogen and generally good mechanical stability. The alloying elements (in particular with Ag) enhance the membrane resistance to H_2 embrittlement and increase H_2 flux[8].

The diffusion through a dense metallic membrane of *x* thickness can be described by the Fick's first law:

$$J = -D_H \frac{dC_H}{dx} \quad (1.4)$$

where D_H is the diffusion coefficient of hydrogen and C_H is the hydrogen concentration in the metal solution.

Under high temperature conditions, hydrogen diffusion through the bulk metal is the rate-limiting step for gas transport. In this case, the hydrogen flux can be calculated by:

$$J = \frac{Perm}{\Delta x}\left(P_f^{0.5} - P_p^{0.5}\right) \quad (1.5)$$

Where Perm is the H_2 permeability, which is the product of the H_2 solubility in the metal and the diffusion coefficient, also used in (1.4). Δx is the thickness of the membrane, $P_f^{0.5}$ is the H_2 partial pressure in the feed and $P_p^{0.5}$ the H_2 partial pressure in the permeate.

Even though they are the most used inorganic dense membrane, the separation using precious metals-based membranes is subject to some limitations. Most of them are susceptible to chemical poisoning from gases such as H_2S, CO, and aromatics present in synthesis gas, they show poor thermomechanical stability, and have limited temperature tolerance (300-600°C operating temperature range).

Dense ceramic membranes

The membranes are form by proton conducting materials that selectively transport H^+ ions at high temperatures (typically >800°C) under driving forces such as a pressure differential or an applied voltage. The main families of ceramic proton conductors are perovskites, pyrochlores and acidic phosphates.

One category of dense proton conducting membranes that has received considerable attention in the preceding decade is represented by various type of Mixed Proton-Electron Conductor ceramics (MPECs), such as doped perovskite (rare-earth element doped $BaCeO_3$, $SrCeO_3$, $BaZrO_3$, etc.)[10,11]. MPECs offer an alternative to existing methods of hydrogen recovery and provide a simple, efficient means of separating hydrogen from gas streams at high temperatures. The MPEC membrane transports both protons and electrons at the same time and hydrogen separation can be achieved in a non-galvanic mode without using external power supply.

Among these materials, the Y-doped $BaCe_xZr_{1-x}O_{3-\delta}$ system is one of the best candidate for the abovementioned applications thanks to a good compromise between conductivity at medium temperatures (600 - 800°C) and stability in CO_2 and H_2O rich ambient[12,13]. However, in these systems, hydrogen permeability is

limited by the low electronic conductivity that need to be increased to make them useful in pressure driven type membranes devices[14,15]. The properties, in particular the proton conductivity, of this class of materials will be further described in the next chapter.

The electronic conductivity of these membranes could be increased by the introduction of a metallic phase (usually nickel[16,17], but also other metals such as palladium[18]) in the protonic conducting one producing a percolated and interpenetrated particles network. However, the introduction of this second phase drastically decreases the thermomechanical stability of the device due to the thermal expansion mismatch between the metallic and the ceramic phases. In addition, a strong interaction can occur between metals and ceramics at high temperature particularly due to the ion interdiffusion[19]. For these reasons, the addition of an electronic conductive ceramic phase instead of the metallic one is generally preferred to increase the thermomechanical and chemical stability of the system. The ceramic-ceramic composite material (cer-cer) obtained in this way, shows both proton and electronic conductivity with an increased tolerance to H_2S, CO and carbonaceous species[20].

The two ceramic phases must show mutual chemical and thermomechanical compatibility to obtain a stable and durable all-ceramic membrane for pressure driven separation of hydrogen. So far, only few electronic phases of cer-cer systems have been coupled with barium cerate-based perovskitic phases[12,21]. Fish et al.[22] successfully obtained highly dense (>95%) $BaCe_{0.2}Zr_{0.7}Y_{0.1}O_{3-d}$ - $Sr_{0.95}Ti_{0.9}Nb_{0.1}O_{3-d}$ cer-cer samples by spark plasma sintering. However, the samples showed the formation of a secondary phase present within the bulk as separate grains. Rosensteel et al.[20] fabricated fully dense, $BaCe_{0.8}Y_{0.2}O_{3-\delta}$ – $Ce_{0.8}Y_{0.2}O_{2-\delta}$ membranes with a single synthesis and sintering step, using NiO to facilitate phase formation and sintering. These membranes exhibit relatively high hydrogen permeation rates (0.0744 mL cm^{-2} min^{-1}) but the membrane performance degrades over time due to ceria phase formation near the membrane surface.

Elangovan et al.[21] reported very high fluxes at 900°C for $BaCe_{0.8}Eu_{0.2}O_{3-\delta}$ – $Ce_{0.8}Eu_{0.2}O_{2-\delta}$. The material showed high electronic conductivity but the hydrogen gas transport was rate-limited by the protonic conductivity of the material.

One of the most performing cer-cer system contains Y-doped $BaCe_xZr_{1-x}O_{3-\delta}$ phase (BCZY) for the proton conduction and a Y- or Gd-doped CeO_2 phase for the electron conduction [23]. This system demonstrated a very good chemical stability under CO_2-rich atmosphere typical of the real hydrogen separation processes.

One of the main limiting step for the application of this technology remains the low electronic conduction of the membranes and the identification of an electron conductive phase to be coupled with the barium cerate-based compound. To be highly permeable to hydrogen, both protonic and electronic conductivity should be in fact, sufficiently high. Finally, since the membrane materials will be exposed include hostile chemicals, such as water vapor, CO_2, and H_2S, it must have high chemical stability at high temperatures in gas separation applications under the typical environments for hydrogen separation.

The development of a state-of-the-art hydrogen separation membrane system is essential for the hydrogen economy to overcome the limitations associated with conventional separation technologies. Thanks to their properties, dense ceramic membranes offer the possibility of syngas-based process intensification, which is believed the most straightforward approach for the actualization of the hydrogen economy.

Figure 1.7 and Table 1.2 summarize the properties and the materials for each kind of membrane considered in this chapter.

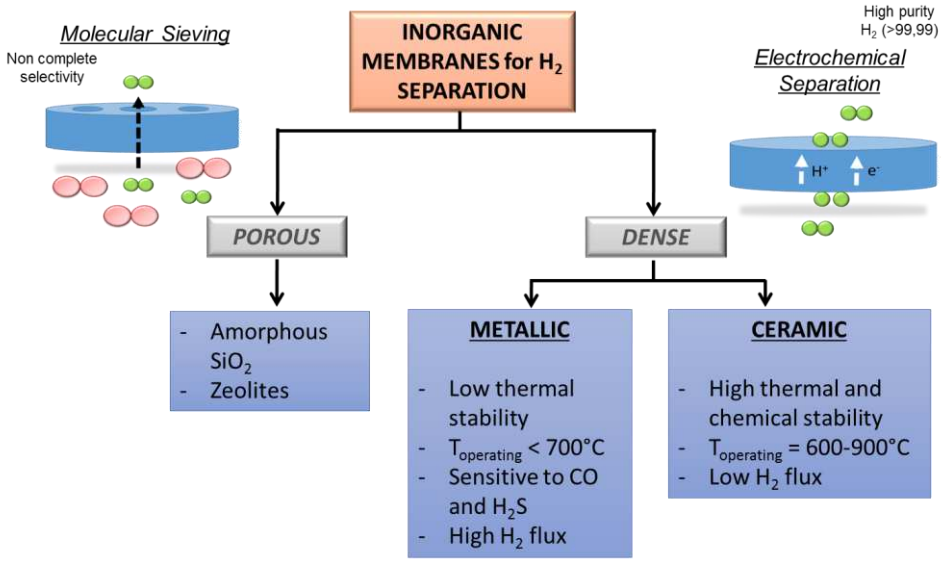

Figure 1.8 Diagram representing the inorganic membrane useful for H_2 separation.

Table 1.2 Properties of different types of hydrogen separation membranes.

Properties	Microporous Ceramic	Dense Metallic	Dense Ceramic
Temperature range	200-600°C	300-600°C	600-900°C
H_2 selectivity	5-139	>1000	>1000
Stability issues	Stability in H_2O	Phase transition	Stability in CO_2
Poisoning issues	HCl	H_2S, HCl, CO	H_2S
Materials	Silica, alumina, zirconia, titania, zeolite	Palladium alloys	Proton conductinig ceramics
Transport mechanism	Molecular sieviing	Solution / diffusion	Proton and electron solution/diffusion
Development status	Prototype membranes available	Commercially avalable	Small samples available for testing

In the next paragraph, the definition of process intensification and the application of dense ceramic membrane reactor will be outlined, stressing the enormous advantages of integrated systems.

1.5 Membrane Applications and Process Intensification

Process intensification (PI) consists of the development of novel apparatuses and techniques that, compared to those commonly used today, are expected to bring dramatic improvements in manufacturing and processing, substantially decreasing

equipment-size/production-capacity ratio, energy consumption, waste production, and ultimately resulting in cheaper, sustainable technologies[24]. In other words, PI leads to a substantially smaller, cleaner, and more energy efficient technology.
Membrane operation represent an interesting answer for the rationalization of chemical productions thanks to their intrinsic characteristics of efficiency and operational simplicity, high selectivity, low energetic requirements, good stability under operating conditions and environmental compatibility, easy control and scale-up[3]. Inorganic membranes can be integrated into syngas processing in two main areas: i) in gas separation to replace sorption-based processes in the purification of H_2; and ii) as a membrane reactor coupling reaction and separation processes in one unit.

1.5.1 H_2 Separation

PI through membrane integration in syngas processing is schematized in Figure 1.9: the membrane works in WGS conditions, purifying H_2 and sequestrating CO_2 at the same time, avoiding the emission of green gasses.

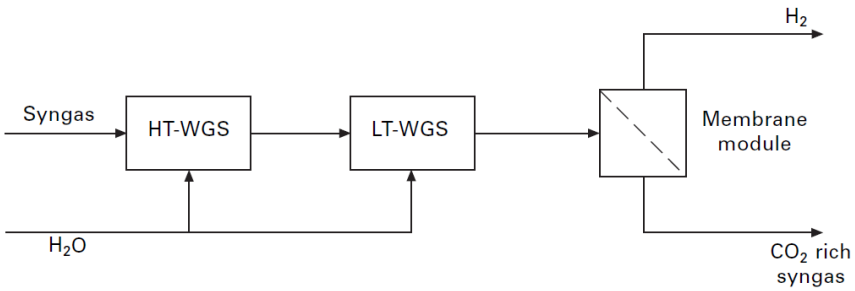

Figure 1.9 Flow diagram for syngas processing incorporating a membrane unit.

Integrated separation membranes can also boost the hydrogen production from renewable feedstock such as biomass. As explained before, biomass gasification, as coal gasification, produces syngas at 700-800°C, from which H_2 can be separated. When biomass (sometimes mixed with coal) gasification and H_2 generation are combined with electricity production via turbine or fuel cell, the

process is known as the integrated gas combined (power generation) cycle (IGCC), represented in Figure 1.10.

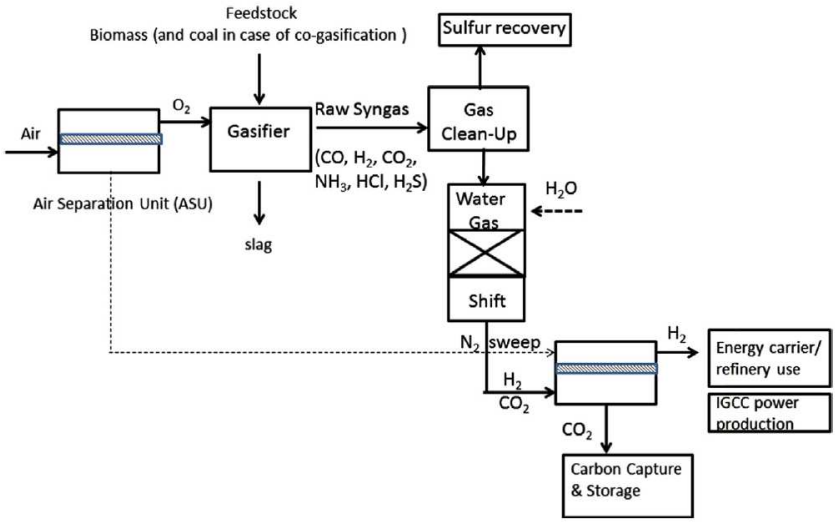

Figure 1.10 Flow diagram for separation of H_2 and CO_2 in IGCC applications[25].

Another important application for dense ceramic membranes is represented by membrane reactor technology.

1.5.2 Membrane Reactors

Membrane reactors couple the hydrogen separation with a hydrogenation\dehydrogenation reaction. Generally, the ceramic membrane is coupled with a catalyst to boost the reaction, to form a "catalytic membrane reactor" technology.

WGS reaction

As explained before, at the moment a two-step process is used on industrial scale: HT-WGS and LT-WGS. A ceramic membrane reactor can continuously remove the H_2 shifting the reaction reducing the thermodynamic limitations and increasing the efficiency in a one-step process at high temperature (Figure 1.11).

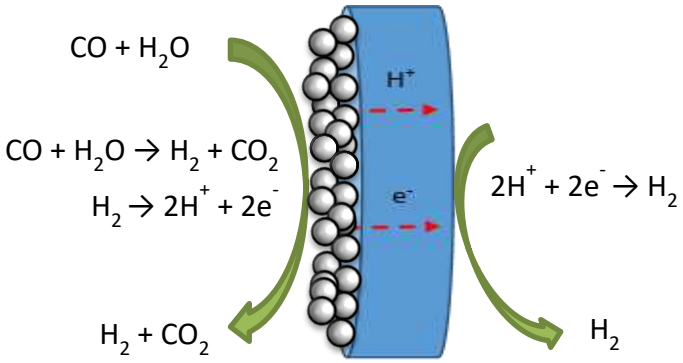

Figure 1.11 Membrane reactor scheme for the WGS reaction.

Li et al. developed a tubular $SrCe_{0.7}Zr_{0.2}Eu_{0.1}O_3$ reactor with CO conversion and H_2 production above the thermodynamic limit at 900°C[26]. Though only few data are available for WGS membrane reactors, is believed that it is one of the most promising applications for proton conducting membranes in the future[27].

Methane Steam Reforming (MSR)

Another possibility of using hydrogen-permeable membranes was shown by Kyriakou et al. where a setup consisting of Ni-$BaZr_{0.7}Ce_{0.2}Y_{0.1}O_{2.9}$ /$BaZr_{0.7}Ce_{0.2}Y_{0.1}O_{2.9}$ / Cu was operated for MSR with a membrane thickness of 30 μm[28]. It is worth to add that due to the dominant proton conductivity of the material, an external circuit was applied to achieve a hydrogen flux. Figure 1.12 schematically represent a membrane reactor for MSR.

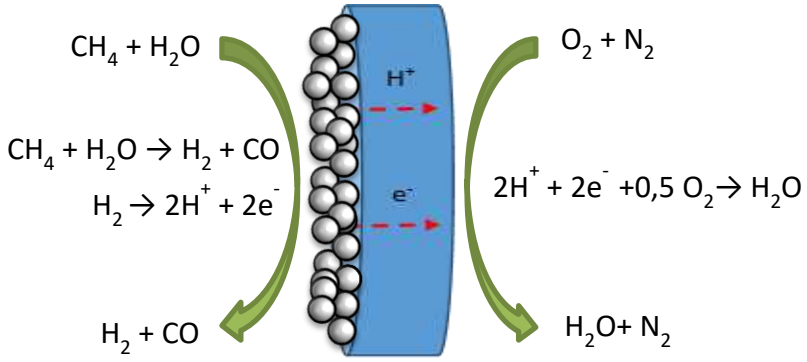

Figure 1.12 Membrane reactor scheme for the MSR reaction.

Methane Non-Oxidative Coupling

The coupling of methane to higher hydrocarbons is a very attractive way to directly transform methane (CH_4) into more valuable chemicals such as ethane (C_2H_6) and ethylene (C_2H_4). In non-oxidative reactions, a hydrogen-permeable membrane continuously removes the protons and electrons formed and the product is formed at the feed side of the membrane (Figure 1.13).

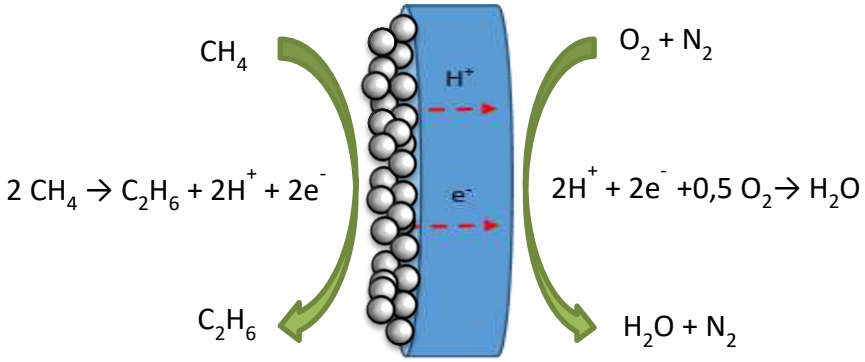

Figure 1.13 Membrane reactor scheme for the methane non-oxidative coupling.

Liu et al. put this principle into operation and used a mixed proton- and electron-conducting $SrCe_{0.95}Yb_{0.05}O_{3-\delta}$ membrane where hydrogen could be removed from the reaction side thus forming water on the permeate side of the membrane[29].

Methane Dehydroaromatisation (MDA)

Methane dehydroaromatisation is a method for directly converting methane into more valuable aromatic compounds such as benzene. An effective method for increasing the conversion of methane is the continuous removal of hydrogen from the reaction zone[30] (Figure 1.14). The mixed proton- and electron-conducting $La_{5.5}W_{0.6}Mo_{0.4}O_{11.25-\delta}$ material was applied in a hollow-fibre membrane reactor by Xue et al. to demonstrate the performance for the production of aromatics[31]. Mo/HZSM-5 was the catalyst for the reaction and a methane conversion of 13% with the aromatics yield of 5% was achieved at an operating temperature of 700 °C.

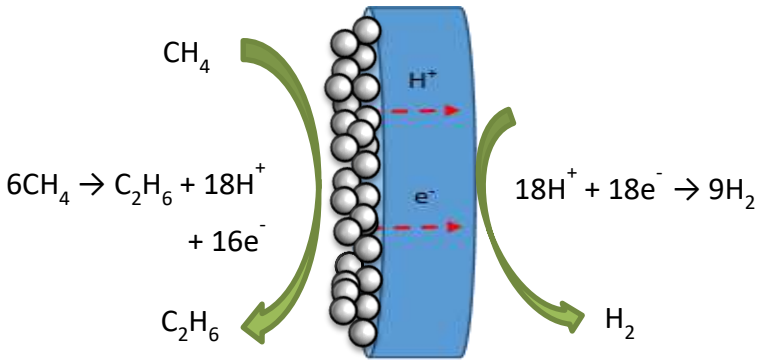

Figure 1.14 Membrane reactor scheme for the MDA reaction.

Morejudo et al. demonstrated the formation of aromatic compounds by using a co-ionic conducting $BaCe_{0.7}Zr_{0.2}Y_{0.1}O_{3-\delta}$ membrane in combination with an externally applied current[32]. The ability of the membrane material to transport both protons and oxygen ions (in opposite directions) at an operating temperature of 710 °C was very beneficial for the performance of the system. Proton transport led to the removal of hydrogen at the reaction side of the membrane while oxygen transport led to steam formation on the reaction side, which suppressed the formation of coke and helped to keep the aromatics yield constant over a longer period of time. The greatest drawback of this technology is the low yield achievable at the moment[33].

In the last decades, a lot of research has been devoted to high performance proton conductors. The next chapter will offer a more detailed dissertation on material selection and perovskite proton conductors.

References

[1] World Population Prospects: the 2017 Revision, https://esa.un.org/unpd/wpp/.../WPP2017_KeyFindings.pdf

[2] Report of the World Commision on Environment and Development: Our common future, www.un-documents.net/wced-ocf.htm.

[3] M. G. Buonomenna, J. Bae, *Membrane processes and renewables energies*, Renew. Sustainable Energy Rev. 43 (2015) 1343-1398

[4] S. Adhikari, S. Fernando, *Hydrogen membrane separation techniques*, Ind. Eng. Chem. Res 45 (2006) 875-881.

[5] N. W. Ockwig, T. M. Nenoff, *Membranes for hydrogen separation*, Chem. Rev. 107 (2007) 4078-4110.

[6] S. D. Sharma, *Gas cleaning: pressure swing adsorption*, Elsevier (2009) 335-349

[7] R. D. Noble, S. A. Stern, *Membrane Separations Technology – Principles and Aplications*, Elsevier Science (1995) Amsterdam.

[8] C. Q. Lu, J. C. Diniz da Costa, M. Duke, S. Giessler, R. Socolow, R. H. Williams, T. Kreutz, *Inorganic membranes for hydrogen production and purification: a critical review and perspective*, J. Colloid Interface Sci. 314 (2007) 589-603.

[9] L. Barelli, G. Bidini, F. Gallorini, S. Servili, *Hydrogen production through sorption-enhanced steam methane reforming and membrane technology: a review*, Energy 33 (2008) 554-570.

[10] I. Guan, *The Effects of Dopants and A:B Site Nonstoichiometry on Properties of Perovskite-Type Proton Conductors*, J. Electrochem. Soc. 145 (1998) 1780–1786.

[11] H. Iwahara, T. Esaka, H. Uchida, N. Maeda, *Proton conduction in sintered oxides and its applications to steam electrolysis for hydrogen production*, Solid State Ionics 34 (1981) 359–363.

[12] K.H. Ryu, S.M. Haile, *Chemical stability and proton conductivity of doped $BaCeO_3$ –$BaZrO_3$ solid solutions*, Solid State Ionics 125 (1999) 355–367.

[13] E. Mercadelli, D. Montaleone, A. Gondolini, P. Pinasco, A. Sanson, *Tape-cast asymmetric membranes for hydrogen separation*, Ceram. Int. (2017) doi:10.1016/j.ceramint.2017.03.099.

[14] Z. Zhong, *Stability and conductivity study of the* $BaCe_{0.9-x}Zr_xY_{0.1}O_{2.95}$ *systems*, Solid State Ionics 178 (2007) 213-220.

[15] D. Medvedev, A. Murashkina, E. Pikalova, A. Demin, A. Podias, P. Tsiakaras, $BaCeO_3$*: Materials development, properties and application*, Prog. Mater. Sci. 60 (2014) 72-129.

[16] C. Zuo, T.H. Lee, S.E. Dorris, U. Balachandran, M. Liu, *Composite Ni-*$Ba(Zr_{0.1}Ce_{0.7}Y_{0.2})O_3$ *membrane for hydrogen separation*, J. Power Sources 159 (2006) 1291-1295.

[17] G. Zhang, S.E. Dorris, U. Balachandran, M. Liu, *Interfacial resistances of Ni-BCY mixed-conducting membranes for hydrogen separation*, Solid State Ionics 159 (2003) 121-134.

[18] U. Balachandran, T.H. Lee, C.Y. Park, J.E. Emerson, J.J. Picciolo, S.E. Dorris, *Dense cermet membranes for hydrogen separation*, Sep. Purif. Technol. 121 (2014) 54-59.

[19] E. Mercadelli, A. Gondolini, P. Pinasco, A. Sanson, *Stainless Steel Porous Substrates Produced by Tape Casting*, Met. Mater. Int. 23 (2017) 184–192.

[20] W.A. Rosensteel, S. Ricote, N.P. Sullivan, *Hydrogen permeation through dense* $BaCe_{0.8}Y_{0.2}O_{3-\delta}$ *-* $Ce_{0.8}Y_{0.2}O_{2-\delta}$ *composite-ceramic hydrogen separation membranes*, Int. J. Hydrogen Energy (2016).

[21] S. Elangovan, B. Nair, T. Small*, Ceramic mixed protonic/electronic conducting membranes for hydrogen separation,* WO 2005/086704 A2.

[22] J.S. Fish, S. Ricote, F. Lenrick, L.R. Wallenberg, T.C. Holgate, R. O'Hayre, N. Bonanos, *Synthesis by spark plasma sintering of a novel protonic/electronic conductor composite:* $BaCe_{0.2}Zr_{0.7}Y_{0.1}O_{3-\delta}/Sr_{0.95}Ti_{0.9}Nb_{0.1}O_{3-\delta,}$ J. Mater. Sci. 48 (2013) 6177-6185.

[23] E. Rebollo, C. Mortalò, S. Escolá, S. Boldrini, S. Barison, J.M. Serra, M. Fabrizio, *Exceptional hydrogen permeation of all-ceramic composite robust membranes based on* $BaCe_{0.65}Zr_{0.20}Y_{0.15}O_{3-d}$ *and Y-or Gd-doped ceria*, Energy Environ. Sci. Energy Environ. Sci. 8 (2015) 3675–3686.

[24] A. Stankiewicz, J. Moulijn, *Process intensification: transforming chemical engineering*, (January) Chem Eng Prog 200: 22-34.

[25] M. G. Buonomenna, J. Bae, *Membrane processes and renewables energies*, Renew. Sustainable Energy Rev. 43 (2015) 1343-1398

[26] J. Li, H. Yoon, T. K. Oh, E. D. Wachsman, *$SrCe_{0.7}Zr_{0.2}Eu_{0.1}O_3$-based hydrogen transport water gas shift reactor*, 37 (2012) 16006-16012.

[27] W. Deibert, M. E. Ivanova, S. Baumann, O. Guillon , W. A. Meulenberg, *Ion-conducting ceramic membrane reactors for high-temperature applications*, J. Membr. Sci. 543 (2017) 79-97.

[28] V. Kyriakou, I. Garagounis, A. Vourros, E. Vasileiou, A. Manerbino, W. G. Coors, et. al., *Methane steam reforming at low temperatures in a $BaZr_{0.7}Ce_{0.2}Y_{0.1}O_{2.9}$ proton conducting membrane reactor*, Appl. Catal., B 186 (2016) 1-9.

[29] Y. Liu, X. Tan, K. Li, *Nonoxidative methane coupling in a $SrCe_{0.95}Yb_{0.05}O_{3-\delta}$ (SCYb) hollow fiber membrane reactor*, Ind. Eng. Chem. Res. 45 (2006) 3782-3790.

[30] E. C. Corredor, P. Chitta, M. Deo, *Membrane reactor system model for gas conversion to benzene*, Fuel 179 (2016) 202-209.

[31] J. Xue, Y. Chen, Y. Y. Wei, A. Feldhoff, H. H. Wang, J. Caro, *Gas to Liquids: Natural Gas Conversion to Aromatic Fuels and Chemicals in a Hydrogen-Permeable Ceramic Hollow Fiber Membrane Reactor*, Acs Catalysis, 6 (2016) 2448-2451.

[32] S. H. Morejudo, R. Zanon, S. Escolastico, I. Yuste-Tirados, H. Malerod-Fjeld, P. K. Vestre, et al., *Direct conversion of methane to aromatics in a catalytic co-ionic membrane reactor*, Science 353 (2016) 563-566.

[33] R. J. Kee, C. Karkaya, H. Zhu, *Process intensification in the catalytic conversion of natural gas to fuels and chemicals*, Proc. Combust. Inst. 36 (2017) 51-76.

Chapter 2
Ceramic Proton Conductive Membrane

2.1 Introduction

The previous paragraph described the benefits of coupling an inorganic separation membrane in syngas processes in terms of process intensification aiming at a sustainable carbon constrained economy. In this paragraph, a more detailed description of ceramic proton conducting materials and of the proton conductivity is given. At the end, the most promising membrane architectures and geometries will be outlined.

2.2 Perovskite Proton Conductors

As previously mentioned, numerous perovskite cerate and zirconate ($BaCeO_3$, $SrCeO_3$, $SrZrO_3$) have been reported to have reasonable proton conductivity in hydrogen-rich and humid atmospheres, particularly at high temperatures when doped with a rare earth ion[1,2]. The proton conductivity of the perovskite systems strongly depends on the defect structure of the lattice. In this chapter, the Kröger-Vink notation will be used[3] to denote species and defects in crystalline lattices. This notation can describe any entity in a crystalline structure and it is represented by tree symbols:

$$A_S^C$$

Where A represent the chemical nature of the entity (chemical symbol to represent an atom, or "V" for a vacancy). The subscript S indicates which site the entity A is occupying (chemical symbol of "i" for a normally empty interstitial position). The superscript C represents the real (+ or -) effective charge. The effective charge is defined as the real charge minus the real charge that the perfect crystal would have had in that location. Positive effective charge is denoted by dots (•), negatives by slashes (/), and optionally, neutral charges by an "x".

2.2.1 *Perovskite Structure and Defects*

Perovskites are the most abundant mineral on the earth. Ideal perovskites have the general formula ABO_3, where the A-site are typically larger cations than the B-site and analogous in size to the O-site anions. ABO_3 structure (Figure 2.1) can be considered as a face centered cubic (fcc) lattice with the A atoms at the corners and the O atoms on the faces. The B atom is located at the center of the lattice. The structure of perovskite if formed by a three dimensionally connected system of BO_6 octahedra and a AO_{12} cube-octahedra at the edges of the B-centered cubic lattice.

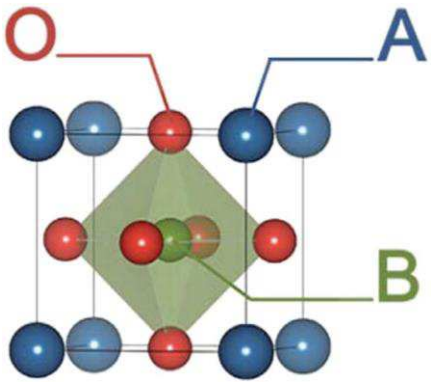

Figure 2.1 ABO_3 perovskite structure.

Figure 2.1 represents the ideal cubic structure, however, ABO_3 perovskites can display also others crystallographic systems, depending on the cation relative sizes.

For this reason, in real structures, the Goldsmidt "tolerance factor" (t) might predict the stability and the crystal system of perovskites. The tolerance factor may be derived from:

$$t = \frac{R_A+R_O}{\sqrt{2}(R_B+R_O)} \qquad (2.1)$$

Where R_A, R_B and R_O are the radii of A cation, B cation and oxygen anion, respectively. A cubic phase is likely to be stable if $0.9 \leq t \leq 1.0$, while a hexagonal

or tetragonal phase are stable for t > 1.0 and orthorhombic or rhombohedral phase may form if t < 0.9. However, the tolerance factor is only a guideline: the equation does not consider the interaction between metal and metal, the degree of covalence, the John-Teller and lone pair effects which define the structure adopted. The distortion on perovskites can have four mechanisms as described by Knight[4]:

- Distortions of the BO_6 octahedra;
- Twisting or tilting of the BO_6 octahedra;
- Substitution or displacement of the A-site cation;
- Substitution or displacement of the B-site cation.

The proton conductivity of these systems relies on the defect formation and their distribution in the perovskite lattice. Both the nature of defects and their interaction depend on internal conditions, as well as external conditions, including factor as temperature, partial pressure of the gas components and moisture presence. Modification of the oxide lattice can be performed (i) as a change in stoichiometry (A- or B-site non-stoichiometry) or (ii) by doping with acceptor impurities.

In fact, shift in stoichiometry and electronic defect can occur under reducing atmospheres. For example, oxygen exit from the lattice creates oxygen vacancies and electronic defects that modify the material properties[5]:

$$O_O^x = V_{\ddot{O}} + \frac{1}{2} O_2 + 2e' \qquad (2.2)$$

ABO_3-based proton conductors may be also doped with trivalent cations in the B-site to create oxygen vacancies and other charged defects, entities that play an important role in the proton defect formation and its conductivity.

For example, when $BaCeO_3$ is doped with trivalent elements, the following defect reaction takes place:

$$2Ce_{Ce}^x + R_2O_3 = 2R'_{Ce} + V_{\ddot{O}} + 3O_O^x \qquad (2.3)$$

This leads to the appearance of oxygen vacancies in the anion sublattice ($V_O^{\cdot\cdot}$), which can be hydrated, dissolving protons in the oxide lattice[6]:

$$H_2O_{(v)} + V_O^{\cdot\cdot} + O_O^x = 2OH_O^{\cdot} \quad (2.4)$$

Where two hydroxide ions substitute for oxide ions, forming two positively charged protonic defects ($OH_O^{\cdot}$)[7].

The equilibrium constant for reaction (2.4) can be expressed as:

$$K_w = \frac{[OH_O^{\cdot}]^2}{[V_O^{\cdot\cdot}]\, pH_2O} \quad (2.5)$$

The concentration of proton defects changes with temperature and partial pressure thus giving information about the thermodynamic stability of proton defects. Equation 2.5 shows that, since the reaction is exothermic, the equilibrium shifts to the left with increasing the temperature. This means that the more negative the hydration enthalpy, the higher the proton content and the dehydration temperature. Atomistic simulations[8,9] and experimental results[10] showed negative dissolution enthalpy for $BaCeO_3$, $SrZrO_3$ and $CaZrO_3$, leading to a main proton conductivity at low temperature, depending on the dopant type and doping level (Figure 2.2).

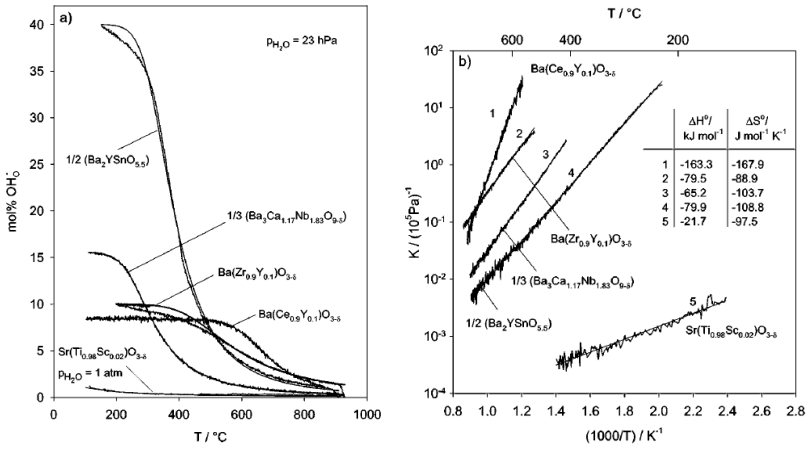

Figure 2.2 (a) Hydration isobars and (b) corresponding data of the K_w of different perovskite systems from[6].

The formation of protons may also occur in hydrogen-containing atmosphere according to:

$$H_2+2O_O^x = 2OH_O^{\cdot}+2e^{'} \quad (2.4)$$

Several factors strongly affect the stability and the mobility of proton defects: crystal symmetry, acidity or basicity of the sites, the repulsive forces between the hydroxide ions and their surroundings[11,12].

2.2.2 *Proton Mobility*

In the literature, two mechanisms for the proton diffusion are mainly reported: (i) the "vehicle" mechanism and (ii) the Grotthuss mechanism.

In the "vehicle" mechanism, proton transport is due to the migration of hydroxide ions, where the oxygen acts as the vehicle. This simple mechanism model is supported by the facts that the conductivity is dependent on the dopant concentration, which influences the $[V_{\ddot{O}}]$. This mechanism is mainly applied in compounds with loose bonded small molecules, especially acidic hydrates, such as Nafion[13], HCl and $Sb_2O_3 \bullet nH_2O$[14].

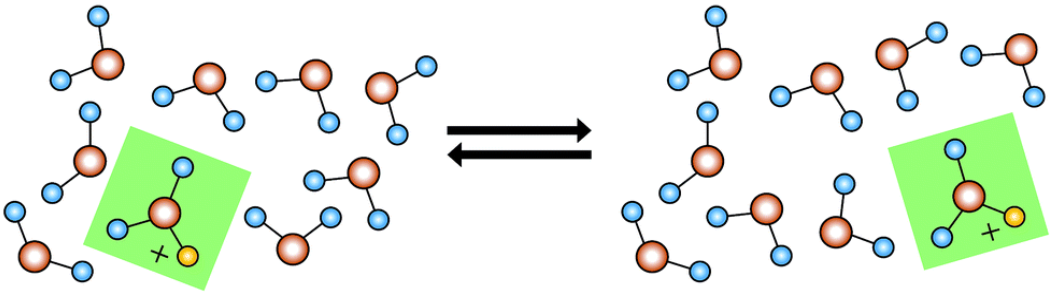

Figure 2.3 Schematic representation of the "vehicle mechanism" proton diffusion. Red circles represent the oxide ion and the yellow circle the proton dissolved in the material. The molecule in the green rectangle stands for the H_3O^+ specie that diffuses through the material.

With the Grotthuss mechanism, the oxygen ions in hydroxyl ions show pronounced dynamics on their own site and the proton diffuses through molecular orientation and proton displacement (also known as proton "hopping"). According to the Grotthuss mechanism, the principal features of the transport mechanism are

the rotational diffusion of the protonic defect and proton transfer toward a neighboring oxide ion. Thus, on the contrary of the "vehicle" mechanism, only the proton shows long-range diffusion, while the oxygens stay in their crystallographic positions (Figure 2.4). This mechanism is observed in proton conducting perovskites.

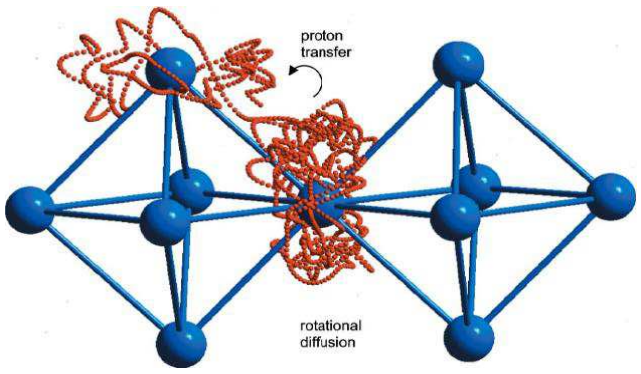

Figure 2.4 Schematic representation of Grotthuss mechanism for proton transfer through two connected BO_6 octahedra in a perovskite lattice[6].

The protons exhibit thermal rotational and stretching vibrations. They may be located in a variety of local energy minima, depending on the geometry of the neighboring oxide sublattice. Depending on the O-O distance, OH-O hydrogen bonds may occur, decreasing the O-O distance and so, affecting the structure. Since the rotation of the proton around the oxygen is very fast, the proton transfer between the neighboring oxygen is the rate-limiting step for the proton conduction. The diffusivity of protons can therefore be expressed[15] by:

$$D_{H^+}=\left(1-x_{H^+}\right)a\ Z\ s^2_{OH\text{-}O}\ \nu_{H^+}\ \exp\frac{\Delta S}{k}\exp\frac{-\Delta H}{kT} \qquad (2.5)$$

Where x_{H^+} is the fraction of protons over oxide ion sites, a is a factor arising from geometry, Z is the number of neighbors, $s^2_{OH\text{-}O}$ the square of the jump distance, ν_{H^+} is the effective attempt vibrational frequency and ΔS and ΔH are the entropy and enthalpy of activation migration, respectively.

Quantum MD simulations revealed that the activation energy for a proton jump is dependent on the O-O distance (Equation 2.5) because the electron density

decreases and the potential increases in between. The activation energy is thus high in un-polarizable, stiff lattices, and it decreases temporally during O-O vibrations in softer lattices. These vibrations lower the O-O distance but also promote the linearization of the OH-O hydrogen bond helping the proton transfer[16].

Two states then describe the transfer process: the average configuration (or ground state) in which the proton is bonded to a specific oxygen ion (Figure 2.4 (b)); and the instant configuration (or barrier state) in which the proton is equidistant between two adjacent oxygen ions (Figure 2.4 (a)).

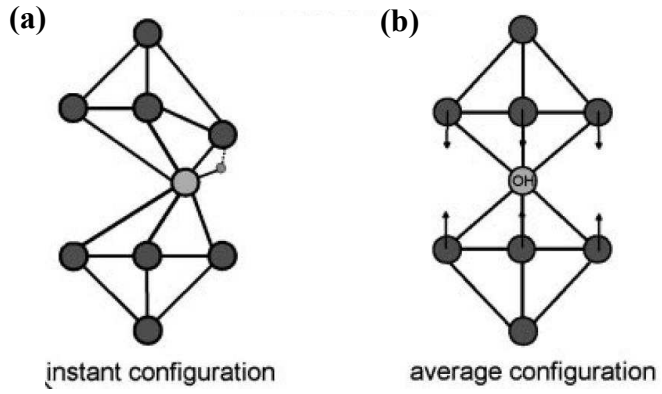

Figure 2.4 Schematic of dynamical hydrogen bonding in a perovskite lattice, (a) instant distorted configuration, and (b) average configuration[6].

Based on this theory, any reduction of the symmetry, coordination number, and oxygen separation tends to reduce proton diffusivity. This difference is rationalized by the oxide ion sites being equivalent, so that there are no sites that acts as a trap and the probability pathway is maximized.

2.3 Y-doped $BaCe_{1-x}Zr_xO_{3-\delta}$ system

As already introduced in the previous chapter, $BaCeO_3$ and $BaZrO_3$ solid solutions may combine the high proton conductivity of barium cerate with the good chemical stability of barium zirconate in CO_2-containing atmospheres.

Thanks to their interesting properties, Y-doped $BaCe_{1-x}Zr_xO_{3-\delta}$ system has been one of the most extensively examined.

2.3.1 Conductivity

Even if thermodynamic calculations revealed that the proton conductivity of $BaZrO_3$ is the highest among this class of material[6], experimental data show that the conductivity of zirconate sintered pellets is in general one order of magnitude lower than the cerate samples measured under the same conditions[17] (Figure 2.5).

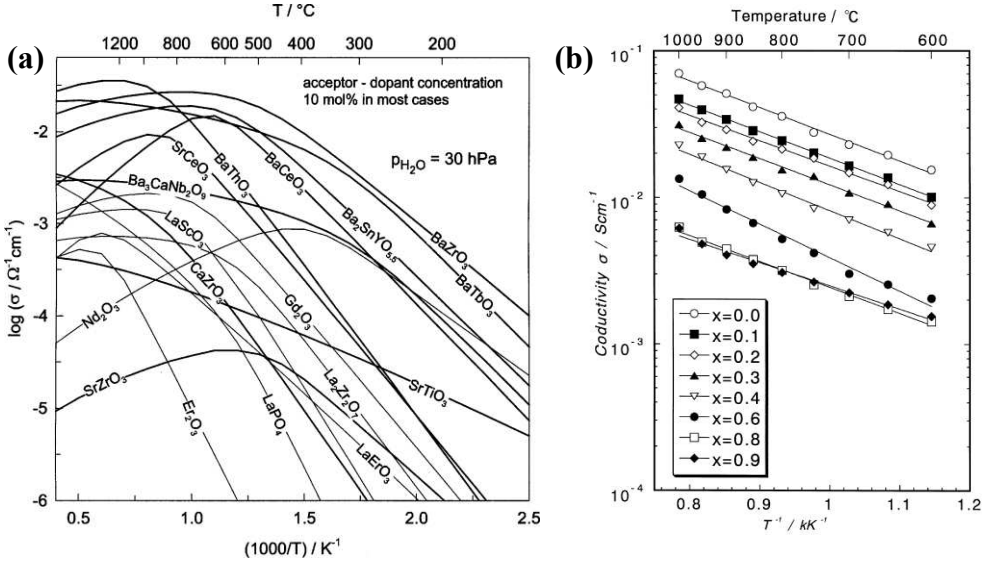

Figure 2.5 (a) Conductivities of different classes of proton conducting perovskites[6] and (b)shows the Arrhenius plots of conductivities as a function of the Zr-content for the $BaCe_{0.9-x}Zr_xY_{0.1}O_{3-\delta}$ system ($0.0 \leq x \leq 0.9$)[17].

This effect is caused by the grain boundary impedance, which is usually lower in $BaCeO_3$ compared with $BaZrO_3$-based ceramics. In addition, zirconate systems display a lower sinterability than the cerate ones, leading to the formation of a higher grain boundary volume content. Figure 2.6 discriminates the contribution of the bulk conductivity from the total conductivity for zirconate-cerate solid solutions with different composition.

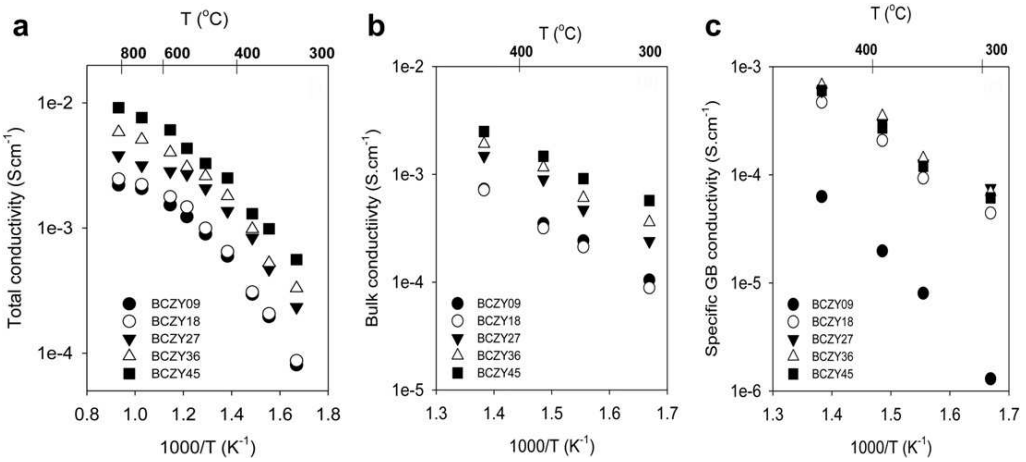

Figure 2.6 Conductivity dependence curves for $BaCe_{0.9-x}Zr_xY_{0.1}O_{3-\delta}$ systems as a function of temperature: (a) total, (b) bulk and (c) grain boundary specific contribution[18].

Studies showed that the total conductivity increased with the content of Ce[19]:in fact, Zr-containing systems display a lower grain boundary specific conductivity[18]. The very high grain boundary resistances observed for these systems have been attributed to the space charge layer effect[20]. Even though several experiments show the same detrimental effect of the grain boundaries on the total conductivity, discrepancies emerge in the literature on the total and bulk conductivities, as pointed out by Fabbri et al.[21]. In fact, sintering temperature and time have distinct but poor reproducible effects on the total conductivity and the appearance of second phases, especially on the outermost layer of the pellets[22]. Second phases are typically caused by the BaO evaporation at high temperatures for prolonged time leading to the precipitation of Y_2O_3 or CeO_2, resulting in a detrimental effect on conductivity[23]. Issues related to the processing of highly refractory materials will be discussed in the next paragraph in more detail.

2.3.2 Sinterability

As previously mentioned, zirconate-based materials typically show high sintering temperatures which may cause a change in stoichiometry due to partial Ba loss during the thermal treatment. This issue was efficiently faced using an extra quantity of Ba in the powder precursors during the synthesis of the material[24, 25].

In order to decrease the sintering temperature of these systems moreover, a small amount of sintering additives can be used for the preparation of high-dense materials based on zirconium oxide. ZnO is the most common used for $BaCeO_3$-$BaZrO_3$ based materials. Babilo et al.[26] prepared 93% dense $BaZr_{0.85}Y_{0.15}O_{3-\delta}$ at a sintering temperature of 1300 °C, by adding 4 mol% of ZnO to the pre-synthesized powder. Tao and Irvine, produced 96% dense samples of $BaZr_{0.8}Y_{0.2}O_{3-\delta}$ by adding ZnO as a sintering add at 1325 °C[27].
Zhang et al. [28] and Wang et al.[29] assumed that the densification of oxide ceramics with ZnO addition took place due to the formation of BaO•ZnO eutectic:

$$BaCe_{1-x}Zr_xO_{3-\delta}+ZnO = Ba_{1-y}Ce_{1-x}Zr_xO_{3-\delta}+yBaO•ZnO \quad (2.6)$$

The sintering aid amount should be as lower as possible because the low deficiency of barium in a perovskite system (due to the formation of eutectic BaO•ZnO) could lead to structural instability and, as a rule, degradation of the mechanical and electrical properties[29].
Ricote et al. evaluated the effect of the composition on the microstructure of $BaCe_xZr_{(0.9-x)}Y_{0.1}O_{(3-\delta)}$ samples ($0 \leq x \leq 0.4$) sintered at 1550°C with NiO as sintering aid. Results revealed that the grain size and the relative density increased with the Ce content. Moreover, samples without the sintering aid revealed a certain residual porosity even if sintered at higher temperatures (1700°C for 6 hours)[18]. At the same time, it should be noted that the solubility limit of nickel in the B-sublattice of barium cerate, zirconate or cerate-zirconate is very low (1–2 mol.%).

2.3.3 Chemical Stability

According to thermodynamic calculations, barium cerate is the most unstable material in a CO_2 atmosphere among the other perovskites. Each line in Figure 2.7 stands for a boundary of stable region[30]: below the line the ABO_3 is thermodynamically stable, while above the line, ABO_3 is decomposed into ACO_3 and BO_2.

The carbonation reaction of a generic perovskite can be described as:

$$ABO_3 + CO_2 = ACO_3 + BO_2 \quad (2.6)$$

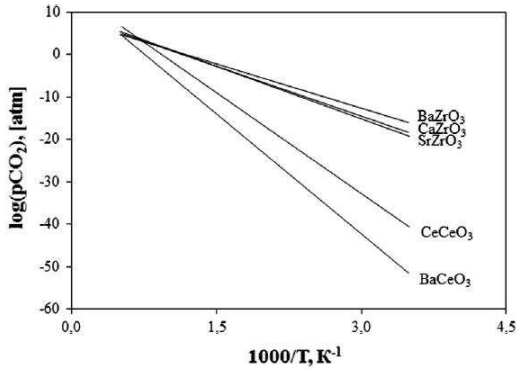

Figure 2.7 Stable region plot as a function of temperature of the critical CO_2 partial pressure from the decomposition of some perovskite-type oxide materials.

Based on these data, $BaCeO_3$ stability can be increased through partial substitution of cerium with zirconium. Ruy and Haile were the first to obtain barium cerate-zirconate solid solution and investigate their chemical stability and proton conductivity[31] (Figure 2.8).

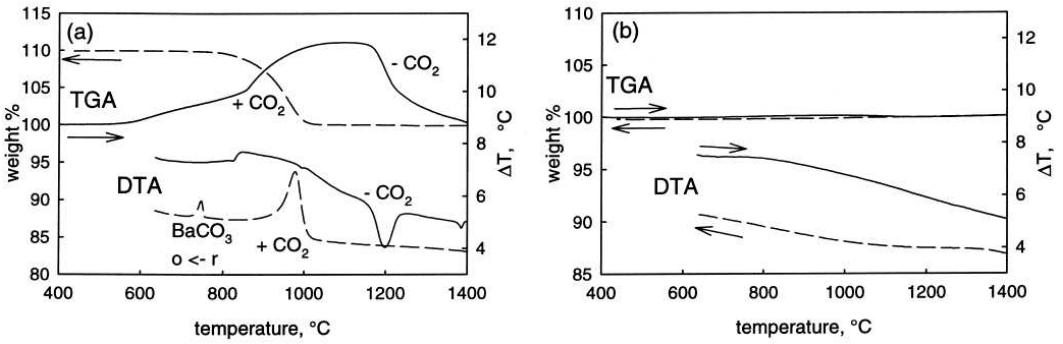

Figure 2.8 TGA and DTA of (a) $BaCe_{0.9}Gd_{0.1}O_{3-\delta}$ and (b) $BaCe_{0.5}Zr_{0.4}Gd_{0.1}O_{3-\delta}$ in flowing CO_2.

Thermogravimetric analysis (TGA) and differential temperature analysis (DTA) were used to assess the stability against CO_2: with the introduction of Zr in the B-site, the carbonization/decarbonation peaks disappeared indicating a good chemical stability was achieved with a 40% Zr-subtitution. Figure 2.9 indicates that the 20% substitution of Zr in the B-site highly enhances the chemical stability.

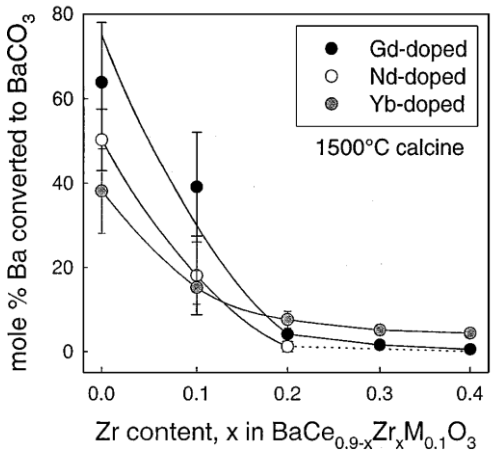

Figure 2.9 Stability against CO_2 as a function of the Zr content in the B-site for Gd-, Nd-, Yb-doped barium cerate zirconate systems.

According to the consideration made, the $BaCe_{0.65}Zr_{0.20}Y_{0.15}O_{3-\delta}$ is one of the most promising proton conductor thanks to the good compromise between chemical stability, sinterability and conductivity. Therefore, this system was selected as the proton conductor phase for the realization of the cer-cer membrane.

References

[1] H. Iwahara, *Hydrogen pumps using proton-conducting ceramics and their applications*, Solid State Ionics 125 (1999) 271-278.

[2] H. Iwahara, *Proton conducting ceramics and their applications*, Solid State Ionics 86-88 (1996) 9-15.

[3] T. Norby, *A Kröger-Vink compatible notation for defects in inherently defective sublattices*, J. Korean Ceram. Soc. 47 (2010) 19-25.

[4] K. S. Knight, *Structural phase transitions, oxygen vacancy ordering and protonation in doped $BaCeO_3$: results from time-to-flight neutron powder diffraction investigations*, Solid State Ionics 145 (2001) 275-294.

[5] R. Glöcker, M. S. Islam, T. Norby, *Protons and other defects in $BaCeO_3$: a computational study*, Solid State Ionics 122 (1999) 145-156.

[6] K. D. Kreuer, *Proton-conducting oxides*, Annu. Rev. Mater. Res. 33 (2003) 333-359.

[7] T. Norby*, Solid-state protonic conductors: principles, properties. Progress and prospects*, Solid State Ionics 125 (1999) 1-11.

[8] M. S. Islam, *Ionic transport in ABO_3 perovskite oxides: a computer modelling tour*, J. Mater. Chem. 10 (2000) 1027-1038.

[9] J. Wu, R. A. Davies, M. S. Islam, S. M. Haile*, Atomistic study of doped $BaCeO_3$: dopant site-selectivity and cation non-stoichiometry*, Chem. Mater. 17 (2005) 846-851.

[10] Y. Yamazaki, P. Babilo, S. M. Haile, *Defect chemistry of yttrium-doped barium zirconate: a thermodynamic analysis of water uptake*, Chem. Mater. 20 (2008) 6352-6357.

[11] K. D. Kreuer, *On the development of proton conducting materials for technological applications*, Solid State Ionics 97 (1978) 1-15.

[12] K. D. Kreuer, *On the complexity of proton conduction phenomena*, Solid State Ionics 136-137 (2000) 149-160.

[13] K. D. Kreuer, *On the development of proton conducting polymer membranes for hydrogen and methanol fuel cells*, J. Membr. Sci. 185 (2001) 29-39.

[14] T. Dippel, K. D. Kreuer, *Proton transport mechanism in concentrated aqueous solutions and solid hydrates of acids*, Solid State Ionics 46 (1991) 3-9.

[15] T. Norby, *Perovskite oxide for solid oxide fuel cells*, Springer (2009) 217-241.

[16] W. Munch, K. D. Kreuer, G. Seifert, J. Maier, *A quantum molecular dynamics study of proton diffusion in $SrTiO_3$ and $CaTiO_3$*, Solid State Ionics 125 (1999) 39-45.

[17] K. Katahira, Y. Kohochi, T. Shimura, H. Iwahara, *Protonic conduction in Zr-substitutes $BaCeO_3$*, Solid State Ionics 138 (2000) 91-98.

[18] S. Ricote, N. Bonanos, A. Manerbino, W. G. Coors, *Conductivity study of dense $BaCe_xZr_{(0.9-x)}Y_{0.1}O_{(3-\delta)}$ prepared by solid reactive sintering at 1500°C*, Int. J. Hydr. En. 37 (2012) 7954-7961.

[19] E. Fabbri, A. D'Epifanio, E. Di Bartolomeo, S. Licoccia, E. Traversa, *Tailoring the chemical stability of $Ba(Ce_{0.8-x}Zr_x)Y_{0.2}O_{3-\delta}$ protonic conductors for intermediate temperature solid oxide fuel cells (IT-SOFCs)*, Solid State Ionics 179 (2008) 558-564.

[20] C. Kjolseth, H. Fjeld, Ø. Prytz, P. I. Dahl, C. Estourenès, R. Haugsrud, T. Norby*, Space-charge theory applied to the grain boundary impedance of proton conducting $BaZr_{0.9}Y_{0.1}O_{3-\delta}$*, Solid State Ionics 181 (2010) 268-275.

[21] E. Fabbri. D. Pergolesi, E. Traversa, *Materials toward proton-conducting oxide fuel cells: a critical review*, Chem. Soc. Rev. 39 (2010) 4355-4369.

[22] X. Chi, Z. Wen, J. Zhang, Y. Liu, *A novel facile way to synthesize proton-conducting $Ba(Ce,Zr,Y)O_3$ solid solution with improved sinterability and electrical performances*, J. Eur. Cer. Soc. 35 (2015) 2109-2117.

[23] F. Iguchi, T. Yamada, N. Sata, T. Tsurui, H. Yugami, *The influence of grain structures on the electrical conductivity of a $BaZr_{0.95}Y_{0.05}O_3$ proton conductor*, Solid State Ionics 177 (2006) 2381-2384.

[24] J. H. Lee, Z. Gan, O. H. Han*, Effect of Ba Nonstoichiometry in $Ba_x(Zr_{0.8}Y_{0.2})O_{3-d}$ on Population of 5-Coordinated Y*, J. Am. Ceram. Soc., (2014) 1-6.

[25] F. M. M. Snijkers, A. Buekenhoudt, J. Cooymans, J. J. Luyten, *Proton conductivity and phase composition in $BaZr_{0.9}Y_{0.1}O_{3-d}$*, Scripta Materialia 50 (2004) 655–659.

[26] P. Babilo, S. M. Haile, *Enhanced sintering of yttrium-doped Barium zirconate by addition of ZnO*, J. Am. Cer. Soc. 88 (2005) 2362-2368.

[27] S. Tao, J. T. S. Irvine, *Conductivity studies of dense yttrium-doped $BaZrO_3$ sintered at 1325 °C*, J. Solid State Chem. 180 (2007) 3493-3503.

[28] C. Zhang, H. Zhao, N. Xu, X. Li, N. Chen, *Influence of ZnO addition on the properties of high temperature proton conductor $Ba_{1.03}Ce_{0.5}Zr_{0.4}Y_{0.1}O_{3-d}$ synthesized via citrate–nitrate metho*d, Int. J. Hydrogen Energy 36 (2009) 2739–2746.

[29] Wang H, Peng R, Wu X, Hu J, Xia C. *Sintering behavior and conductivity study of yttrium-doped $BaCeO_3$–$BaZrO_3$ solid solutions using ZnO additives*, J. Am. Ceram. Soc. 92 (2009) 2623–2629.

[30] J. Lu, I. Wang, I. Fang, Y. Li, I. Dai, H. Guo, *Chemical stability of doped $BaCeO_3$-$BaZrO_3$ solid solutions in different atmospheres*, J. Rare Earth 26 (2008) 505-510.

[31] K. H. Ryu, S. M. Haile, *Chemical stability and proton conductivity of doped $BaCeO_3$-$BaZrO_3$ solid solutions*, Solid State Ionics 125 (1999) 356-367.

Chapter 3
Asymmetric Ceramic Membranes

3. 1 Introduction

The performance of the membrane in terms of hydrogen flux is commonly described by the Wagner equation:

$$J_{H_2} = \frac{RT}{4F^2L} \frac{\sigma_{H^+} \sigma_{el}}{\sigma_{H^+} + \sigma_{el}} \ln\left(\frac{P'_{H_2}}{P''_{H_2}}\right) \quad (3.1)$$

Where:

- R is the gas constant; F the Faraday's constant;
- T is the temperature;
- σ_{H^+} in the proton conductivity; σ_{el} the electron conductivity;
- L is the thickness of the membrane;
- P'_{H_2} is the hydrogen concentration in the feed side; P''_{H_2} the hydrogen concentration in the sweep site.

As postulated in (3.1), the performance of the membrane in terms of hydrogen flux not only depends on the ambipolar conductivity of the material, but it is also related to the thickness of the membrane. For this reason, Asymmetric membranes are a promising set-up for combining mechanical stability with reduced membrane thickness therefore achieving increased hydrogen permeability. However, fabrication issues emerge when processing the more complex asymmetric architecture rather than the symmetric bulk membrane[1,2]. In fact, it is well known that material's shrinkage during thermal treatment depends, among the others, on its green composition, on the particles packing and on the material's physical and chemical properties. Thus, combining a gas-tight and thin membrane layer with a porous thick support may led to a defected sintered membrane. Cambering could occur if the layers show light mismatches, while delamination and cracks could appear if the two layers are thermomechanically incompatible.

Asymmetric membranes are a promising set-up for combining mechanical stability with reduced membrane thickness therefore achieving increased hydrogen permeability.

This approach was successfully demonstrated by Hamakawa et al.[3] that produced a 2 µm thick $SrCe_{0.95}Yb_{0.05}O_{3-\delta}$ (SCYb) film onto porous substrate of the same

material by spin coating. The H_2 permeation rate reached up to 13.44 mL cm^{-2} min^{-1} at 677°C, which is 500 times higher than the conventional 1 mm thick membrane of the same material.

Asymmetric architectures can be produced through different ceramic processes: dry pressing, extrusion, tape casting, phase inversion, etc. In some cases, two or more techniques must be coupled to obtain either support and membrane layers in multiple processing steps. Among the others, the coupling of tape casting (to produce porous layers) and screen-printing (for the application of dense layers) is commonly used for engineered planar devices such as solid oxide fuel cells (SOFCs) or O_2-asymmetric membranes. Often pre-sintering thermal steps are required to obtain multi-layered complex structures.

Even though the production of asymmetric O_2-separting membranes is widely reported in the literature, very little has been done up to now for the H_2-separating ones. This thesis aims at fulfilling this technological gap obtaining a cer-cer membrane exclusively through tape casting and lamination process.

3.2 Shaping processes for H_2 separation membranes

Although the very promising results obtained from the asymmetrical configuration, only few attempts could be found in literature either for single phase perovskite[4,5,6,7]or metal-perovskite composite[8].

Table 3.1 summarizes the asymmetric proton conducting membranes present in the literature.

Dry pressing is the most exploited process, even though the technique must face several technological issues to be easily scale up. In addition, the control on the dense layer thickness is tricky, particularly for layer as thin as 20 μm.

Table 3.1 Asymmetric ceramic membranes examples.

	Material	Geometry	Proces(ses)	Ref.
Support	$BaCe_{0.8}Y_{0.2}O_{3-\delta}$	hollow fiber	phase inversion	[4]
Membrane	$BaCe_{0.8}Y_{0.2}O_{3-\delta}$			
Support	Ni- $Ba(Zr_{0.1}Ce_{0.7}Y_{0.2})O_{3-d}$	planar	dry pressing	[6]
Membrane	$Ba(Zr_{0.1}Ce_{0.7}Y_{0.2})O_{3-d}$			
Support	Ni- $BaZr_{0.1}Ce_{0.7}Y_{0.1}Yb_{0.1}O_{3-\delta}$	planar	dry pressing and	[9]
Membrane	Ni-$BaZr_{0.1}Ce_{0.7}Y_{0.1}Yb_{0.1}O_{3-\delta}$		particle suspension coating	
Support	NiO-$SrCe_{0.95}Y_{0.05}O_{3-\delta}$	planar	dry pressing	[8]
Membrane	$SrCe_{0.95}Y_{0.05}O_{3-\delta}$			
Support	$SrCe_{0.95}Tm_{0.05}O_{3-\delta}$	planar	dry pressing	[7]
Membrane	$SrCe_{0.95}Tm_{0.05}O_{3-\delta}$			
Support	Ni-$La_{0.5}Ce_{0.5}O_{2-\delta}$	planar	dry pressing	[10]
Membrane	$La_{0.5}Ce_{0.5}O_{2-\delta}$			
Support	Ni-$SrCeO_3$	tubolar	tape casting and rolling and	[11]
Membrane	$SrCe_{0.9}Eu_{0.1}O_{3-\delta}$		slurry coating	
Support	Ni-$Ba(Zr_{0.1}Ce_{0.7}Y_{0.2})O_{3-\delta}$	planar	dry pressing	[12]
Membrane	Ni-$Ba(Zr_{0.1}Ce_{0.7}Y_{0.2})O_{3-\delta}$			
Support	$BaCe_{0.85}Tb_{0.05}Zr_{0.1}O_{3-\delta}$	planar	dry pressing	[13]
Membrane	$BaCe_{0.85}Tb_{0.05}Zr_{0.1}O_{3-\delta}$			
Support	$Ce_{0.7}Zr_{0.2}Eu_{0.1}O_{3-\delta}$	tubular	tape casting and rolling and	[14]
Membrane	$Ce_{0.7}Zr_{0.2}Eu_{0.1}O_{3-\delta}$		slurry coating	
Support	$La_{6-x}WO_{12-\delta}$	planar	tape casting and lamination	[15]
Membrane	$La_{6-x}WO_{12-\delta}$			

Dry pressing is the most exploited process, even though the technique must face several technological issues to be easily scale up, therefore is not appropriate for mass production. Due to the problematic in controlling the uniform distribution of the powder for layers as thin as 20 μm, it is very difficult to prepare supported thin and dense membrane layers[16]. Another disadvantage of this technique is the inhomogeneous density of green compacts, that results in warpage and crack during sintering[17].

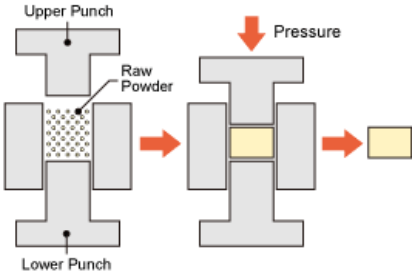

Figure 3.1 Schematic of the dry pressing process.

Some authors consider membranes in form of hollow fibers produced through a combination of phase inversion and sintering techniques, achieving 130-150 µm thick dense barium cerate based membrane[4,18]. This method starts with the preparation of a dope mixture, where perovskite powders are mixed in a solution containing a polymeric binder and solvent. These are then mixed thoroughly under constant stirring. Then, the obtained dope solution is spun into hollow fibers as displayed in Figure 3.2.

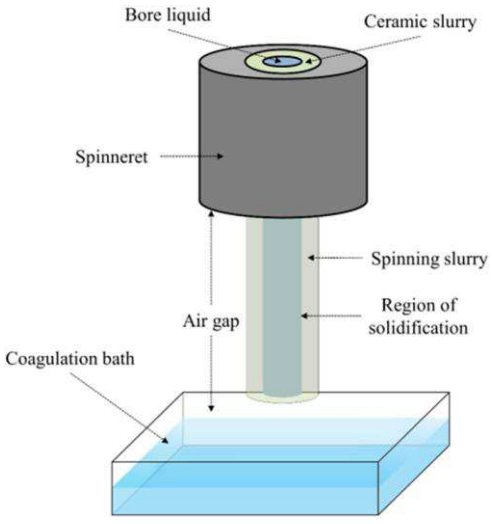

Figure 3.2 Schematic of a hollow fiber spinneret[19].

The dope solution is injected through a spinneret under pressure where the inner shell contains a liquid also injected under pressure, also known as the bore-liquid. This process creates a hollow fiber geometry, which is completed upon contact in a coagulation bath. Binders that delivered best spinning properties were those

based on sulphur containing polymers such as polyethersulfone (PESF) or polysulfone (PSF)[20].

The tape casting technique has been used in the production of thin film and both flat and dense membranes, as it is the best way to form large-area, flat ceramics with different thickness. This method consists on the preparation of a slurry in which an inorganic powder is dispersed in solution of a solvent, water or organic liquids. The slurry viscosity plays an important role on the thickness of the obtained tape and is controlled by the addition of dispersing agent, binders, and plasticizers. The slurry is then placed on the top of a flat support to form a tape as schematically shown in Figure 3.3.

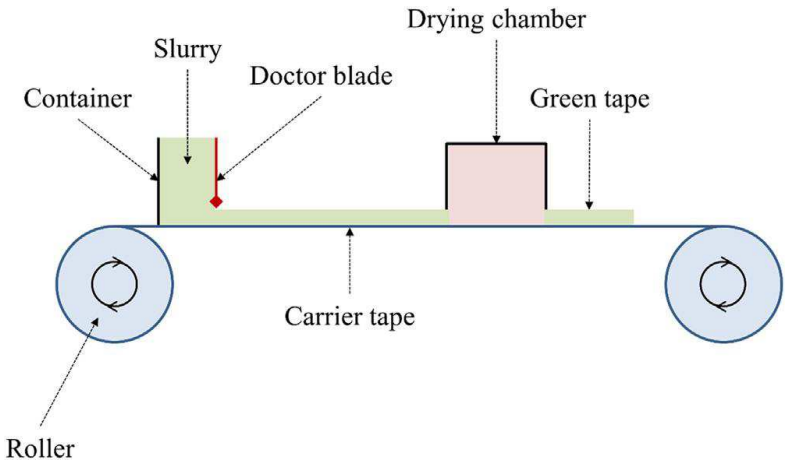

Figure 3.3 Schematic of a tape casting process[19].

The thickness of the tape is controlled by blades which can be regulated to the required thickness value: both thin membrane and support can therefore obtained.

Some authors suggested the tape casting and rolling technique as a possible version to obtain tubular architectures from green planar tapes: dried tapes are rolled on a steel core polytetrafluoroethylene rod and capped with a circular piece of the same tape as shown in Figure 3.4.

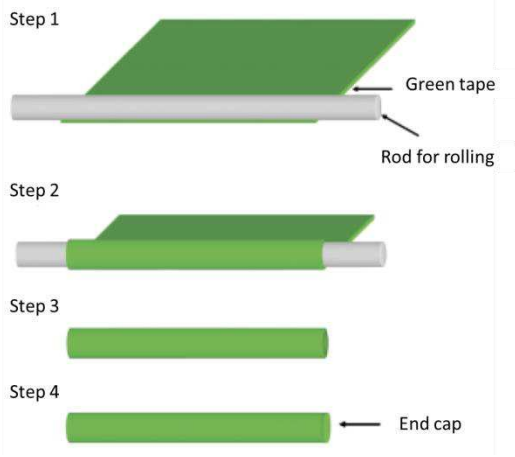

Figure 3.4 Schematic of a tape casting and rolling process[11].

3.3 Tape Casting

Tape casting is one of the most utilized process for the formation of ceramic layers with different thickness. The production of ceramic tapes by this process needs the use of significant amounts of organic compounds: besides the powder others ingredients are needed, such as binder, solvent, plasticizer and dispersing agents.

3.3.1 Slip ingredients

The slip for tape casting is a very complex system were different ingredients must interact to form a planar ceramic-containing tape with suitable properties: integrity, homogeneity, good mechanical and thermo-mechanical (if multilayers are required) properties. Since the pioneer work of G. Howatt et al.[21] seventy years ago, a lot of experimental activity has been carried out on tape casting of different materials, giving an enormous impact on the material processing industry.

Powder

In any materials fabrication process, the most important ingredient is the powder, as it is the only portion that defines the material's properties after binder removal

and sample consolidation. To obtain a porous support after sintering, pore formers (organic or inorganic) are added during the slip preparation.
The important powder parameters that influence the whole process are the particle size distribution, the shape, density, and surface area.

Solvent

The solvent is an important ingredient, as tape casting may be defined as a "fluid forming process". The liquid, besides allowing to shape the ceramic material, distributes the ingredients homogeneously throughout the slip to create a uniform mixture. The solvent is generally organic (ethanol, toluene, methyl ethyl ketone, etc.) and it might be formed by binary solvent systems. The main advantage in using multiple solvent is the increased ability to dissolve. Azeotropes have also been used thanks to the possibility of tuning the dissolving capability and thanks to the greater control over drying speed, parameter that highly affects the morphology or even integrity of the dried tape. In fact, the solvent must be volatile, but the drying rate should not create tensions that may led to defects.
However, due to health, safety and environmental issues, water-based slips are gaining increasingly attention.

Deflocculants/Dispersants

They are the key to dispersion, wetting, and slip stability. Even though deflocculation and dispersion are two distinctly different need, they are usually accomplished by a single additive.
The deflocculant essentially keep particles apart: when primarily powder particles are added in a liquid medium, they have the tendency to flocculate forming loosely bonded aggregates called flocs. This tendency of the system to rearrange has as a thermodynamic nature: the driving force is the reach a status of lower energy. When a slip is deflocculated, the liquid medium is a continuous phase that fully surrounds primarily particles. On the other hand, the dispersant purpose is to disperse primary particles and to hold them in a homogenous suspension through steric hindrance and/or ionic repulsion.

Ionic repulsion is generated through the introduction of soluble polyelectrolytes which coat the particle surface changing or providing the surface charge.
Steric hindrance is accomplished by physically separating the particles: the dispersant is adsorbed on the particle surface and its polymeric chains avoid particles interaction.

Binder

The binder supplies the network that holds the entire system together for further processing. Essentially, the green ceramic tape can be thought as a ceramic-filled polymer tape, since its mechanical properties strongly depend of the polymer matrix that surrounds the powder fraction. The binder system is the main responsible of tape proprieties as; strength, flexibility, plasticity, laminability, toughness and smoothness.
Factors taken into account when choosing a tape casting binder include solubility, viscosity, cost, glass temperature transition (T_g) and ability to modify the T_g. In order to meet specific needs, the binder can be a copolymer (generally statistic) with different functional groups (polar, non-polar, and with different steric hindrance).

Plasticizer

The role of the plasticizer is to modify the properties of the binder system, giving the capability to the tape to be bent without cracking. It has been defined as “a substance or material used to increase the binder’s flexibility, workability, or distensibility[22].
Two different mechanism can be used to plasticize a green tape. The first type of plasticizer (Type I) is a chemical that softens the polymer chains between particles, allowing them to stretch more easily. A second type of plasticizer (Type II) works as a lubricant in the tape matrix, imparting plasticity (ability to deform permanently) to the green tape. The influence of Tape I and II plasticizers on the mechanical properties of the green tape can be assessed with tensile stress-strain experiments, as displayed in Figure 3.5.

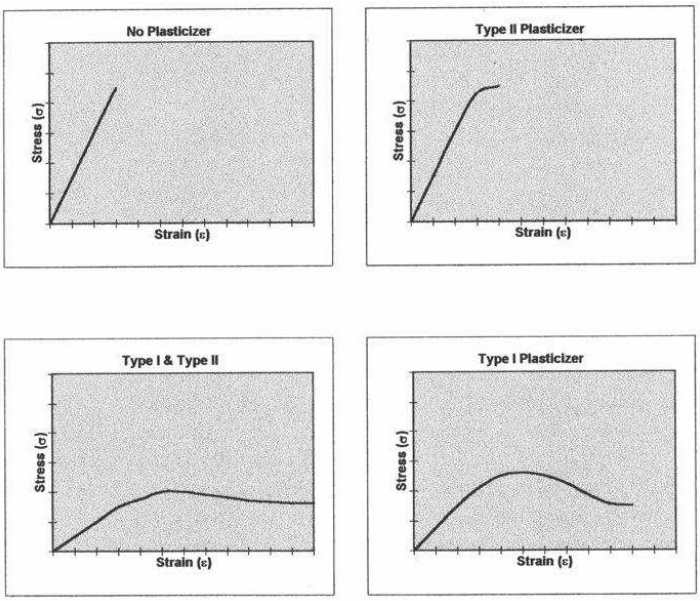

Figure 3.5 Effect of the plasticizer type on the stress-strain properties[22].

Without plasticizer(s) the tape is brittle and stiff. Type I, as explained, softens the polymer chains, therefore the modulus is lowered, and the polymeric network can be stretched more. With Type II the tape displays increased motion of the matrix and then yield before failure.

3.3.2 Slip preparation, Casting, and Lamination

In order to obtain multilayered manufactures such as asymmetric membranes through tape casting, the whole process can be divided in the following steps:

- Slurry preparation and homogenization;
- Casting and drying;
- Punching and lamination;
- Thermal treatments.

<u>Slurry preparation</u>

Ball-milling is an effective and low-cost method to produce homogeneous suspensions. Slurries are typically prepared by subsequent addition of the

ingredients, and several homogenization steps are required. Ball-milling is an effective and low-cost method to produce homogeneous suspensions.
The ball-milled suspension is then deaerated under vacuum, carefully poured in the doctor blade reservoir, and casted (Figure 3.6).

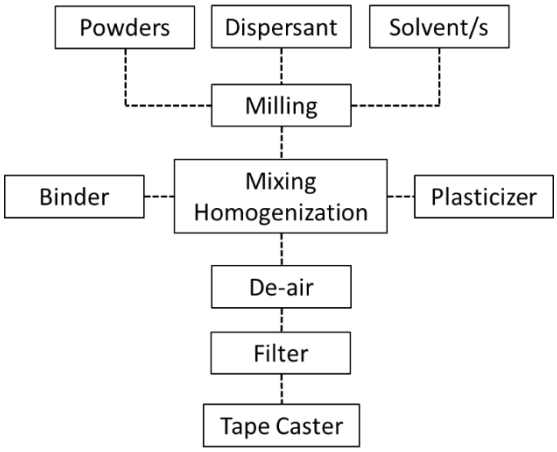

Figure 3.6 Schematic of a tape casting and rolling process.

Slurry casting

In the tape-casting process the slip flows from a reservoir into an antechamber from which it spreads on the carrier tape. An external transportation mechanism transports this. The cast slip is drawn with the support tape under a wiper called a doctor blade. This doctor blade, the slip viscosity and the transportation speed govern the thickness and the width of the resulting tape.

Drying

After moving under the doctor-blade the tape is dried in a drying chamber under controlled conditions, for example, temperature, humidity, and air flow. If the drying speed is too high the tape may crack due to the fact that the evaporation on the top side of the tape is faster than the transportation time for humidity from inside the tape to reach the surface.
Defects arising in the process are: non-uniform shrinkage in the *x*–*y*-direction due to textures caused by casting in one direction; cracking due to drying too quickly; adhesion to the carrier tape.

Lamination

After drying the tapes can be either unrolled, cut into stripes and unrolled, or punched into single plates. If holes are necessary, they can even be made in the green state of the tape. The actual manufacturing process depends very much on the application of the tapes. They can be sintered to final density, coated in the green state, pre-sintered, laminated, or calendered.

Regarding the process used for the manufacturing of green asymmetric membranes, the next Chapter will systematically describe each and every step, from the slip preparation to the lamination.

3.3.3 Green tapes mechanical properties

Since the mechanical properties of tapes are strongly influenced by the organic phase concentration, slip formulation needs to be optimized[23].

In fact, the mechanical and physical characteristic of the green tapes are very important for further processing and the final properties of the material. Indeed, ceramic green tape needs to endure drying, punching, and lamination steps to obtain multilayer structures. Thus, the green tapes must possess the flexibility and strength required for tape handling, which depend on the tape-casting slip formulation.

Tensile testing is a valid way to characterize the mechanical properties of the cast films. For this mechanical test, the dried tape is cut into a dog bone shape using a proper punch. The sample is held between two clamps and then is applied a load maintaining the same strain rate for the entire study, since tensile strength depend on the rate of loading[24].

An idealized stress-strain curve for polymer tape tensile testing is shown in Figure 3.7.

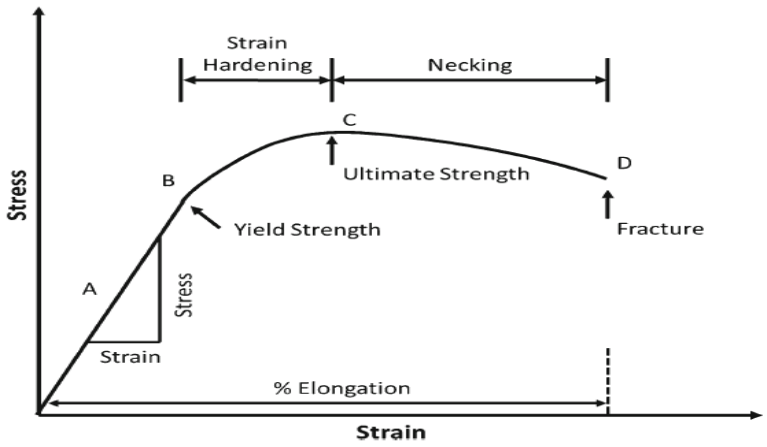

Figure 3.7 Typical stress-strain curve for a polymer film undergoing to tensile strain.

In terms of mechanical properties, an ideal green sheet of tape casting should have a high tensile strength, a large elongation to break and a high elastic modulus. Such green sheets will be tough without being brittle.

Tough tapes are also characterized by high work of failure. The ratio of tensile strength to elastic modulus is a valuable tool with high values preferable for film formulations as these are indicative of fewer process related problems.

Below is described the relationship between the different components of the tape and its mechanical behavior.

Powder

As a general trend, the maximum stress increases, and the maximum strain decreases with increasing solid loading. The porosity gradually decreased with increasing solid loading. This reduction of the porosity produced the increase in the green density of the tapes, which leads to a decrease shrinkage during sintering of powders. In this way, less stresses are induced by the densification of the material and the risk of defects is decreased[25].

In addition, according to the model proposed by Onoda[26], strength of ceramic green bodies is correlated not only to the cohesive strength and quantities of binder but also to the packing density of the particulates.

Pore volume is an important factor also in green tapes. In fact, Descamps et al. showed that for slurry compositions in which the organic volume was lower than

the pore volume of the tape, increasing the binder content resulted in an increase in the tape mechanical strength. However, when the organic volume (binder plus plasticizer) was higher than the pore volume a large decrease of strength was observed[27]. Thus, physical properties of powder decide the optimal quantity of binder, which requires the addition of plasticizer in order to obtain the best mechanical behavior.

Binder

The binder provides strength to green tapes after evaporation of the solvent through organic bridges between the ceramic particles.

When there is not enough binder, the resulting green tape tends to develop cracks during the drying stage. On the other hand, when the amount of binder is too high, on the other hand, the tapes will contain many voids.

Tape strength increases, and green tape density decreases with increasing binder content, showing that a compromise must always be found[28]. As a general trend, the maximum stress decreases, and the maximum strain increases with increasing binder content. In addition to the quantity of the binder in the slip formulation, mechanical properties depend also to chemical-physical properties of the binder, as the glass temperature transition (T_g), the functional groups of the polymeric chain and the molecular weight[29].

This trend is well described by Doreau et al. and reported in Figure 3.8, where binders with two Tg values are tested in different amounts for a aqueous tape casting of alumina[30].

In both cases, the 5% of binder is not enough to keep the mechanical integrity of the alumina green sheets. For higher amounts of binder, the stress/strain curves show an elastic domain and a plastic domain.

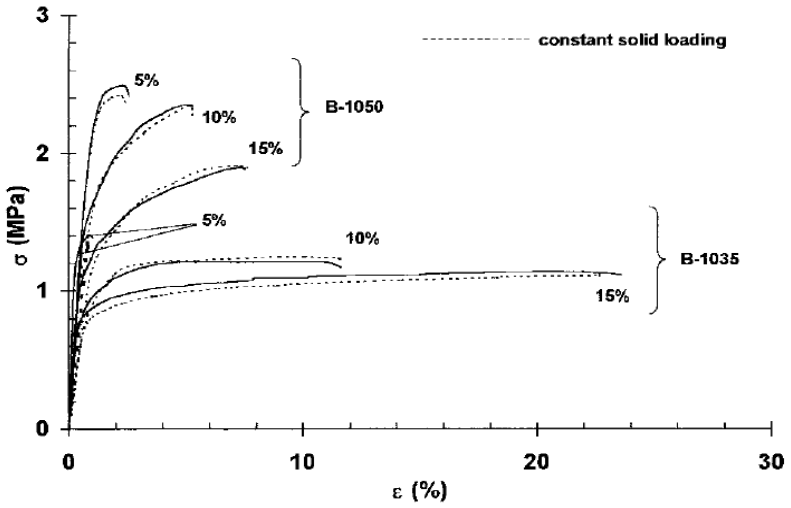

Figure 3.8 Stress-strain curves of samples with different kind and amount of binder.

Whatever the binder composition tested, the maximum stress linearly decreases with increasing binder contents, whereas the maximum strain exhibits an opposite trend.

Other times, the increase of binder content leads to an increase in tensile strength: it depends on the chemical nature of the binder, as reported by Albano et al[31].

In fact, as showed in Figure 3.9 (a), increasing the amount of binder causes an increase in tensile strength, while the strain to failure is independent from the amount of binder (Figure 3.9 (b)).

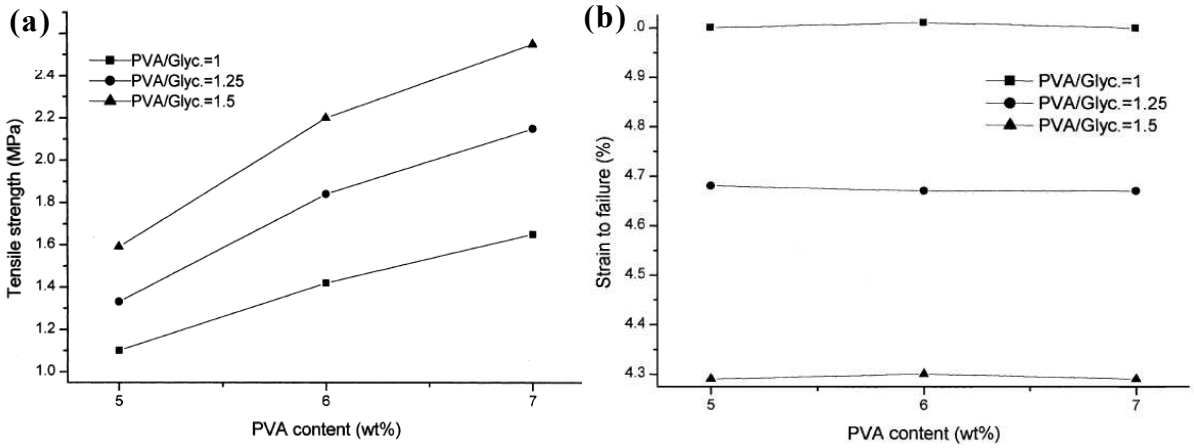

Figure 3.9 (a) tensile strength of green tapes as a function of the binder content for different binder/plasticizer ratios. (b) Strain to failure of green tapes as function of the binder content for different binder/plasticizer ratios[31].

Different behaviors related to different amounts of binder are also caused by the reciprocal position occupied by the binder and the ceramic particles. In fact, the strength depends on how much binder is concentrated at the neck (Figure 3.10). Therefore, distribution of the binder throughout the green body is of primary importance.

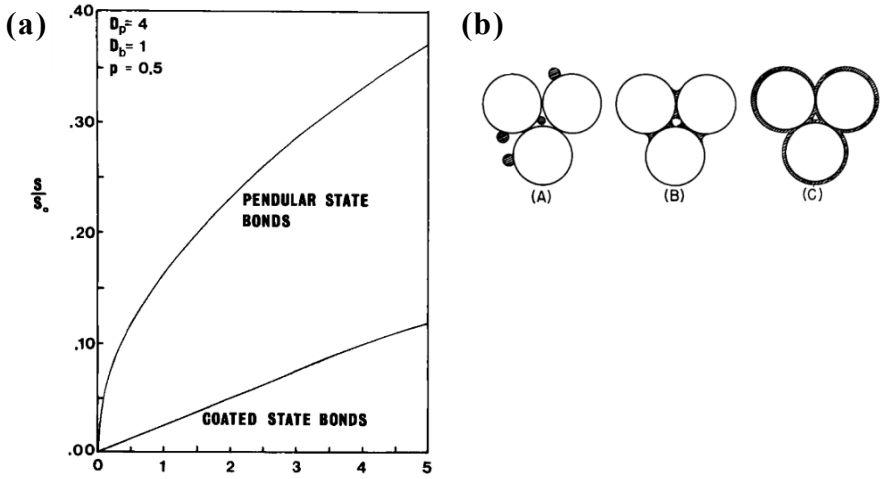

Figure 3.10 (a) Strength VS wt% binder for pendular and coated states. (b) Location of binder around particles of (A) non-wetting, (B) pendular state and (C) coated state[31].

Beyond the nature and amount of binder, the maximum values reached for stress and for strain also could depend on the orientation of the sample with respect to the casting direction, (i.e. parallel or perpendicular to the casting direction). Specimens aligned in the casting direction can sometimes exhibit higher values of tensile strength and elongation that those orientated perpendicularly. This anisotropy might probably be due to some preferential orientation of the polymer chains, originated by the shear stress imposed under the blade during casting (Figure 3.11).

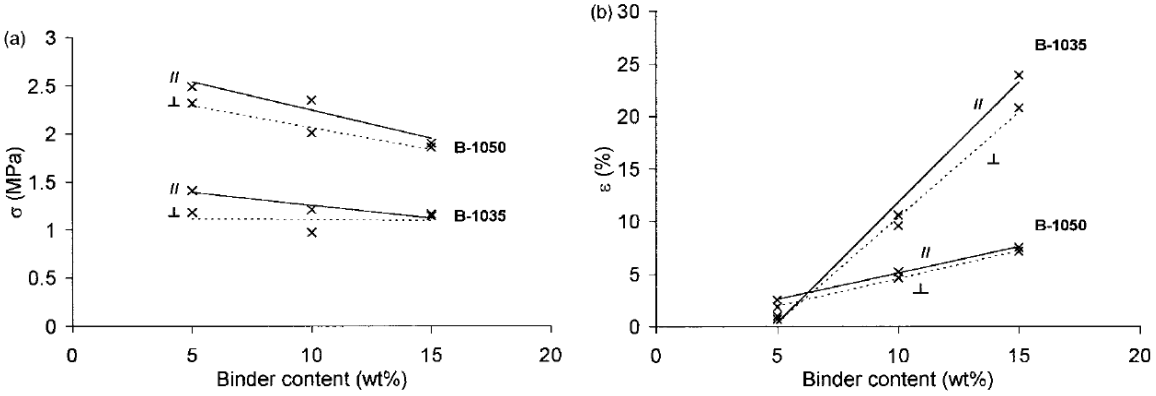

Figure 3.11 Influence of the cutting direction, with respect to the casting direction, on (a) the maximum stress and (b) the maximum strain prepared with different amounts of pure binders[30].

Plasticizer

Plasticizers are generally nonvolatile, low molecular weight compounds added to a polymer to improve its processability, flexibility, and stretchability by modifying the mechanical properties making the tapes more ductile[32]. In fact, when incorporated into the polymer system, plasticizers can increase the free volume between the polymer chains, which allows the chain segments to move and rotate more freely. That leads to a lower Tg of the tape without altering the fundamental chemical character of the binder compound.

To characterize the efficiency of the plasticizer, the mechanical properties of the binder system additivated with different kind of plasticizers are evaluated and directly compared.

In fact, as seen in Figure 3.12, different types of plasticizer modify differently the mechanical properties, like toughness of binder system.

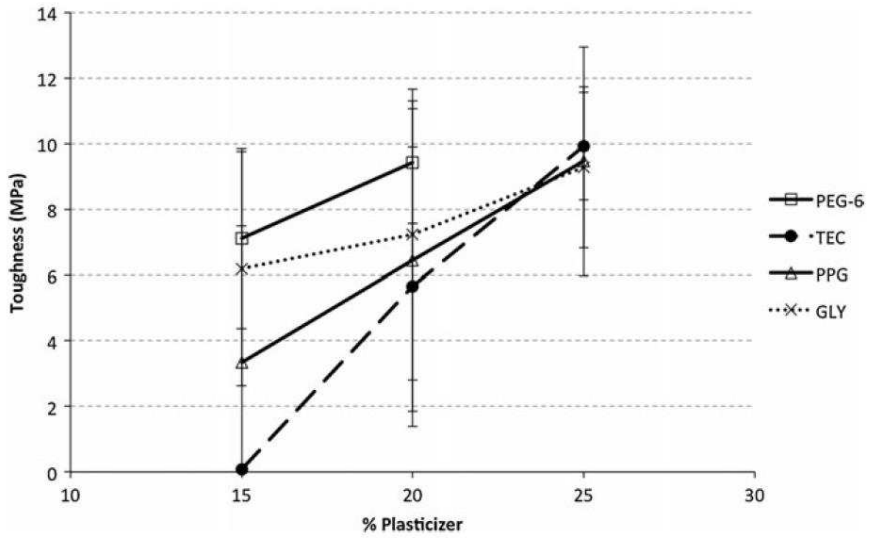

Figure 3.12 Toughness of binder tape with different plasticizers[30].

The mechanical properties of the polymer that may be improved by the addition of plasticizers include decreased the tensile strength and Young's modulus and increased in percent elongation, toughness and resistance to cracking, all fundamental properties for a green tape[33].

The maximum tensile strength of a tape is the maximum stress that a film can withstand being stretched before necking or failing. Therefore, a plasticized polymer would be less resilient and would deform at a lower force than without the plasticizer. Hence, lower tensile strength is expected with the addition of plasticizer, while the elongation is expected to be higher.

As mentioned earlier, the ratio of tensile strength to elastic modulus (T/E) is a valuable parameter that predicts process related problems[32, 34].

In particular, highest values of T/E indicate a better crack resistance of a film (Figure 3.13).

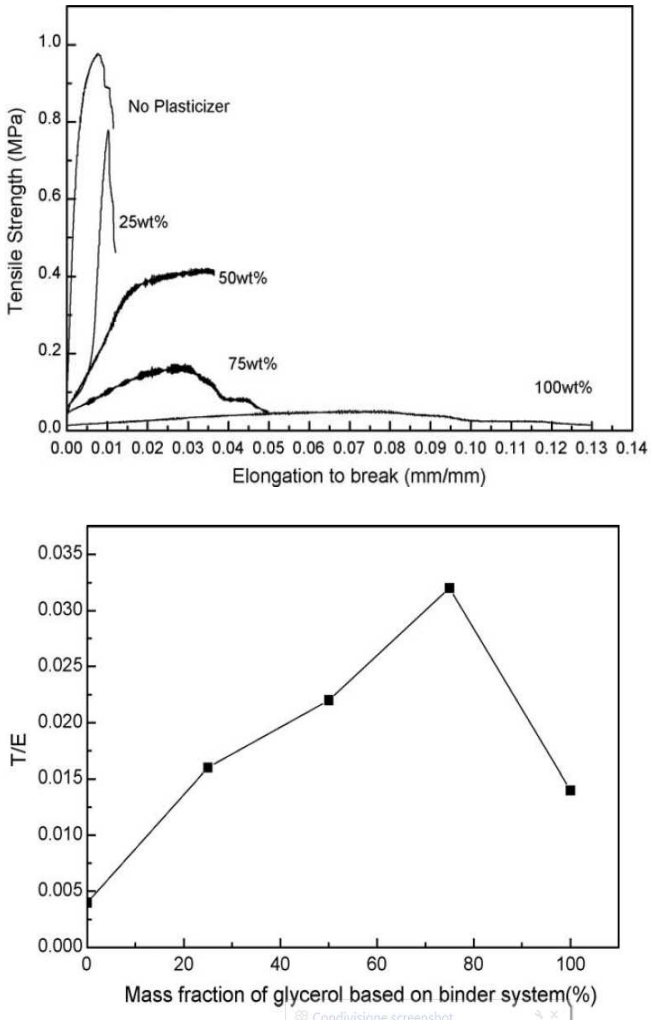

Figure 3.13 Elongation-tensile strength curves and T/E values of green sheets with different amounts of plasticizer[33].

In conclusion, tensile strength is a valid test for the characterization of the green tape mechanical properties.

Thanks to the mechanical analysis is possible to tune the slip formulation in terms of type and relative quantities of organic compounds necessary to the obtain a green tape with the best mechanical properties.

References

[1] W. Deibert, M. E. Ivanova, W. A. Meulenberg, R. Vaßen, O. Guillon, *Preparation and sintering behavior of $La_{5.4}WO_{12-\delta}$ asymmetric membranes with optimized microstructure for hydrogen separation*, J. Membr. Sci. 492 (2015) 439-451.

[2] W. Debeirt, F. Schulze-Kuppers, E. Forster, M. E. Ivanova, M. Muller, W. A. Meulenberg, *Stability and sintering o MgO as substrate material for Lanthanum Tungstate membranes*, J. Eur. Ceram. Soc. 37 (2017) 671-677.

[3] S. Hamakawa, L. Li, A. Li, E. Iglesia, *Synthesis and hydrogen permeation properties of membranes based on dense $SrCe_{0.95}Yb_{0.05}O_{3-\alpha}$ thin films*, Solid State Ionics 148 (2002) 71–81.

[4] X. Tan, X. Tan, N. Yang, B. Meng, K. Zhang, S. Liu, *High performance $BaCe_{0.8}Y_{0.2}O_{3-\alpha}$ (BCY) hollow fiber membranes for hydrogen permeation*, Ceram. Int. 40 (2014) 3131–3138.

[5] J. Song, J. Kang, X. Tan, B. Meng, S. Liu, *Proton conducting perovskite hollow fibre membranes with surface catalytic modification for enhanced hydrogen separation*, J. Eur. Ceram. Soc. 36 (2016) 1669–1677.

[6] Z. Zhu, J. Hou, W. He, W. Liu, *High-performance $Ba(Zr_{0.1}Ce_{0.7}Y_{0.2})O_{3-\delta}$ asymmetrical ceramic membrane with external short circuit for hydrogen separation*, J. Alloy. Compd. 660 (2016) 231-234.

[7] S. Cheng, V.K. Gupta, J.Y.S. Lin, *Synthesis and hydrogen permeation properties of asymmetric proton-conducting ceramic membranes*, Solid State Ionics 176 (2005) 2653–2662.

[8] S. Zhan, X. Zhu, B. Ji, W. Wang, X. Zhang, J. Wang, W. Yang, L. Lin, *Preparation and hydrogen permeation of $SrCe_{0.95}Y_{0.05}O_{3-\delta}$ asymmetrical membranes*, J. Membr. Sci. 340 (2009) 241–248.

[9] M. Liu, W. Sun, X. Li, S. Feng, D. Ding, D. Chen , M. Liu,H. C. Park, *High-performance Ni-$BaZr_{0.1}Ce_{0.7}Y_{0.1}Yb_{0.1}O_{3-d}$ (BZCYYb) membranes for hydrogen separation*, Int. J. Hydrog. Energy 38 (2013) 14743-14749.

[10] Z. Zhu, L. Yan, H. Liu, W. Sun, Q. Zhang ,W. Liu, *A mixed electronic and protonic conducting hydrogen separation membrane with asymmetric structure*, Int. J. Hydrog. Energy 37 (2012) 12708-12713.

[11] H. Yoon, T. Oh, J. Li, K.L. Duncan, E. D. Wachsman, *Permeation through $SrCe_{0.9}Eu_{0.1}O_{3-\delta}$/Ni-$SrCeO_3$ tubular hydrogen separation membrane*, J. Electrochem. Soc. 156 (2009) B791-B794.

[12] Z. Zhu, W. Sun, L. Yan, W. Liu, W. Liu, *Synthesis and hydrogen permeation of Ni-Ba(Zr0.1Ce0.7Y0.2)O3Ld metal ceramic asymmetric membranes*, Int. J. Hydrog. Energy 36 (2011) 6337-6342.

[13] Y. Wei, J. Xue, H. Wang, J. Caro, *Hydrogen permeability and stability of $BaCe_{0.85}Tb_{0.05}Zr_{0.1}O_{3-\delta}$ asymmetric membranes*, J. Membr. Sci. 488 (2015) 173-181.

[14] J. Li, H. Yoon, E. D. Wachsman, *Hydrogen permeation through thin supported $SrCe_{0.7}Zr_{0.2}Eu_{0.1}O_{3-d}$ membranes; dependence of flux on defect equilibria and operating conditions*, J. Membr. Sci. 381 (2011) 126-131.

[15] M. Weirich, J. Gurauskis, V. Gil, K. Wiik, M. A. Einarsrud, *Preparation of lanthanum tungstate membranes by tape casting technique*, Int. J. Hydrog. Energy 37 (2012) 8056-8061.

[16] H. Choi,G. Y. Cho,S. W. Cha, *Fabrication and characterization of anode supported YSZ/GDC bilayer electrolyte SOFC using dry press process*, International J. Precision Eng. Manuf.- Green Technol. 1 (2014) 95-99.

[17] P. Chen,G. Y. Kim, J. Ni, *Investigations in the compaction and sintering of large ceramic parts*, J. Mater. Process Technol. 190 (2007) 243-250.

[18] J. Song, J. Kang, X. Tan, B. Meng, S. Liu, *Proton conducting perovskite hollow fibre membranes with surface catalytic modification for enhanced hydrogen separation*, J. Eur. Ceram. Soc. 36 (2016) 1669–1677.

[19] D. D. Athayde, D. F.Souza, A. M. A. Silva, D. Vasconcelos, E. H. M. Nunes, J. C. D. da Costa, W. L. Vasconcelos, *Review of perovskite ceramic synthesis and membrane preparation methods*, Ceramics International 42 (2016) 6555-6571.

[20] X. Meng, W. Yan, N. Yang, X. Tan, S. Liu, *Highly stable microtubular solid oxide fuel cells based on integrated electrolyte/anode hollow fibers*, J. Power Sources 275 (2015) 362-369.

[21] G. N. Howatt, R. G. Breckenridge, J. M. Browlow, *Fabrication of thin ceramic sheets for capacitors*, J. Am. Ceram. Soc. 30 (1947) 237-242.

[22] R. E. Mistler, E. R. Twiname, *Tape casting: theory and practise*, (2000) The American Ceramic Society .

[23]Z. Liu, Y. Wang, Y. Li, *Combinatorial Study of Ceramic Tape-Casting Slurries*, ACS Comb. Sci. 14 (2012) 205−210.

[24] S. Forte, J. R. Morris, W. R. Cannon, *Strength of tape casting tapes*, Am. Ceram. Soc. Bull. 64 (1985) 724-5.

[25] S. Li, Q. Zhang, H. Yang, D. Zou, *Fabrication and characterization of* $Li_{1+x-y}Nb_{1-x-3y}Ti_{x+4y}O_3$ *substrates using aqueous tape casting process*, Ceram. Int. 35 (2009) 421–426.

[26] G. Y. Onoda, *Theoretical strength of dried green bodies with organic binders*, J. Am. Ceram. Soc. 59 (1976) 236-9.

[27] M. Descamps, G. Ringuet, D. Leger, B. Thierry, *Tape-casting: Relationship Between Organic Constituents and the Physical and Mechanical Properties of Tapes*, J. Eur. Ceram. Soc. 15 (1995) 351-362.

[28] D. Hotza, P. Greil, *Review: aqueous tape casting of ceramic powders*, Mat. Sci. Eng. A202 (1995) 206-217.

[29] D. Yoon, B. I. Lee, *Processing of barium titanate tapes with different binders for MLCC applications—Part I: Optimization using design of experiments*, J. Eur. Ceram. Soc. 24 (2004) 739–752.

[30] F. Doreau, G. Taroa, M. Guedes, T. Chartier, C. Pagnouxc, J. M. F. Ferreira, *Mechanical and Lamination Properties of Alumina Green Tapes Obtained by Aqueous Tape-casting,* J. Eur. Ceram. Soc. 19 (1999) 2867-2873.

[31] M. P. Albano, L. B. Garrido, *Influence of the slip composition on the properties of tape-cast alumina substrates*, Ceram. Int. 31 (2005) 57–66.

[32] H. Lim, S. W. Hoang, *Plasticizer effects on physical-mechanical properties of solvent cast Soluplus films*, Pharm. Sci. Tech. 14 (2013) 903-910.

[33] Paul W.S. Heng, L.W. Chan, K.T. Ong, *Influence of storage conditions and type of plasticizers on ethylcellulose and acrylate films formed from aqueous dispersions*, J. Pharm. Pharmaceut. Sci. 6 (2003) 334-344.

[34] T. Xie, S. Jiang*, Improvement on the mechanical properties of zinc oxide green sheets by aqueous acrylamide gel tape casting*, Cer. Int. 35 (2009) 2645-2649.

Chapter 4
Experimental

4.1 Introduction

The first part of this chapter describes the procedures developed for the membrane fabrication, schematized in Figure 4.1.

- The realization of green ceramic sheets through the tape casting process described in the previous chapter;
- The lamination of one thin (≈ 20μm) with two support layer(s) (≈ 450μm) to obtain circular asymmetric green samples;
- The thermal treatments of debinding and sintering to obtain the final asymmetric membrane.

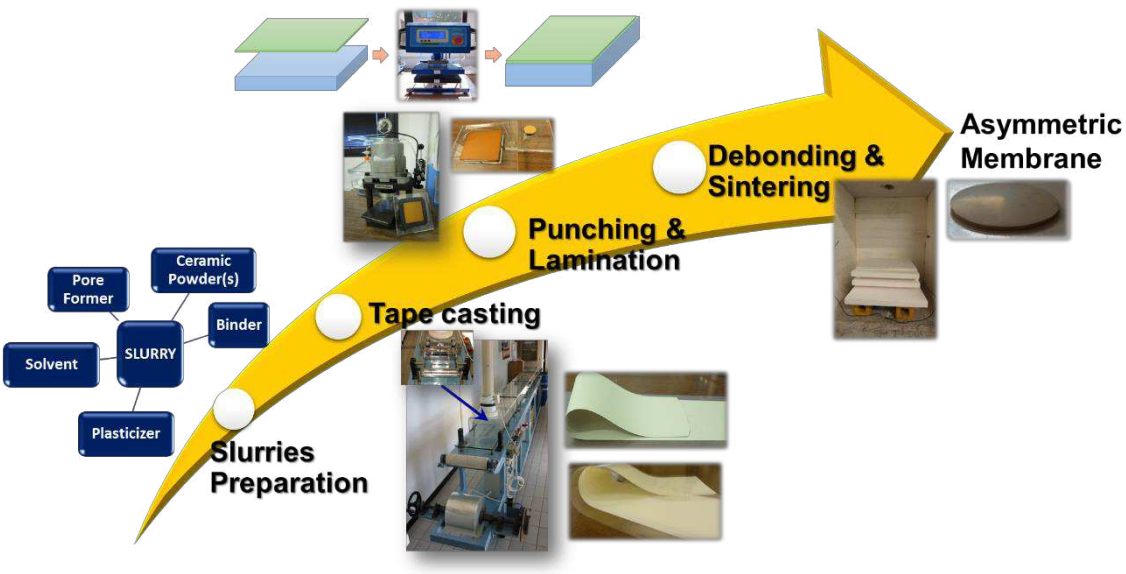

Figure 4.1 Schematic representation of the production of the slurry for the membrane layer.

The central part of the chapter is focused on the experimental procedures for the microstructural, chemical, and compositional characterizations.
The last part is dedicated to the membrane functional characterization by means of the hydrogen separation measurements.

4.2 Asymmetric Membrane Production

4.2.1 *Slurries Preparation*

BCZY-GDC Membrane layer

Figure 4.2 shows the steps followed for the preparation of the slurry to obtain the membrane layer.

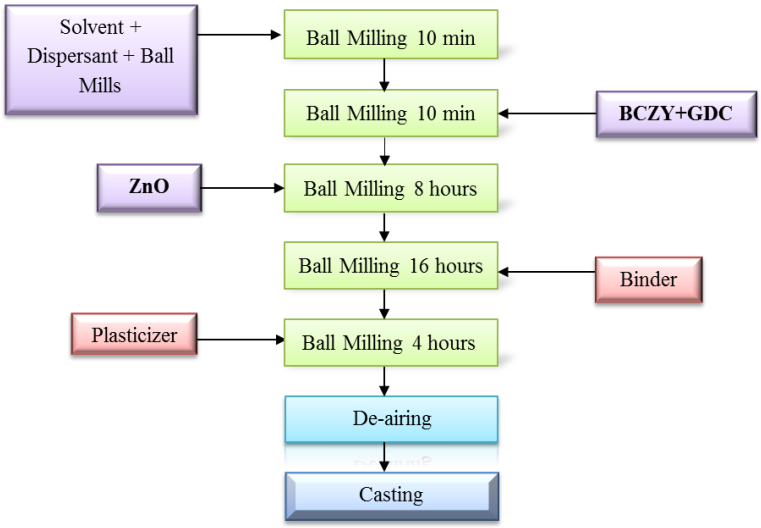

Figure 4.2 Schematic representation of the production of the slurry for the membrane layer.

In order to minimize undesired competitive adsorptions, the slurry is prepared through subsequent addition steps, starting from the introduction of dispersant and powders then moving to the addition of binder and plasticizer. In the last ball milling step the slurry is homogenized at very low speed to remove trapped air.
The ball milling is a very common procedure for the tape casting slurries preparation, as it can effectively de-agglomerate the powder and homogenize the suspension. Figure 4.3 represents the milling step performed in a HDPE jar using ZrO_2 balls (ø = 20 mm) as milling media.

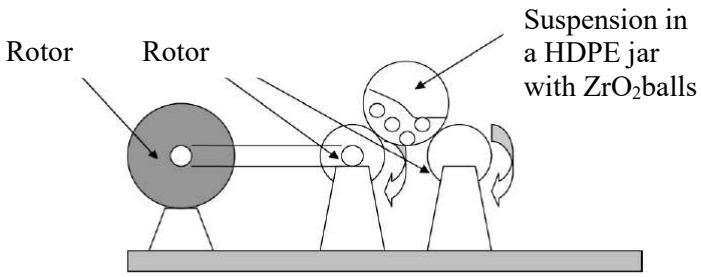

Figure 4.3 Schematic representation of the milling process.

After the last addition step, the suspension is filtered to remove unwanted agglomerates and the milling media with a nylon mesh (mesh ≈ 100μm).

During the milling and filtration steps air bubbles can be easily entrapped in the slurry's body, a de-airing step is mandatory to avoid the formation of defects in the green tapes. The technique used is a vacuum de-airing with gentle agitation. When the evolvement of air bubbles stopped, the vacuum was removed in order to avoid large solvent evaporation.

BCZY Support Layer

Like the membrane layer, the support was obtained through tape casting as well. Figure 4.4 shows the steps followed for the preparation of the slurry to obtain the support layer.

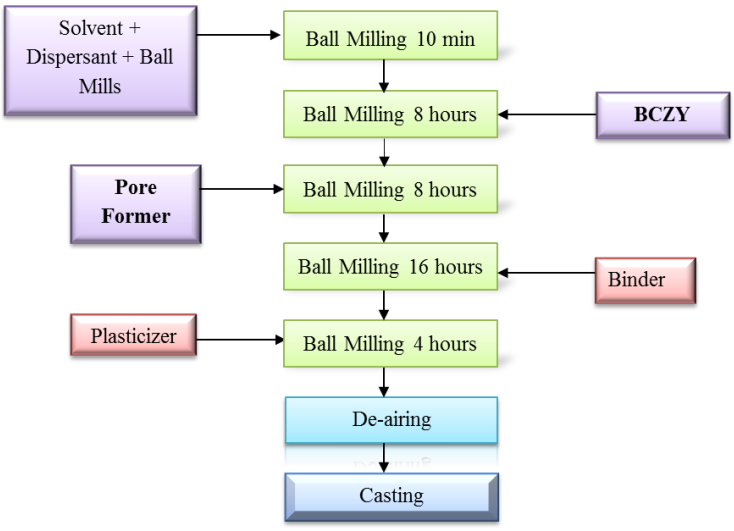

Figure 4.4 Schematic representation of the production of the slurry for the support layer.

Note that in the previous formulation ZnO is not introduced, as the support densification is not desired. On the other hand, rice starch is used to obtain a sufficient degree of porosity after the burnt out of the organic fraction.
Table 4.1 summarizes the components added to the ceramic powders used for the slurries preparation.

Table 4.1 Chemicals used as raw materials for the realization of the slurries.

Material	Function	Supplier	Chemical structure
Azeotropic Methyl ethyl Ketone-Ethanol mixture (MEK-EtOH)	Solvent	Sigma Aldrich	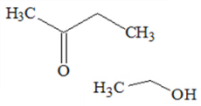
Glyceryl Trioleate (GTO)	Dispearsant	Sigma Aldrich	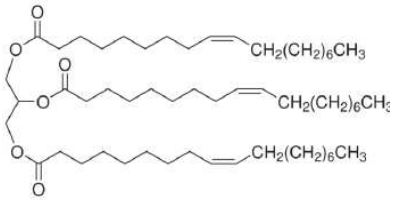
B98	Binder	Monsanto Co., St Louis, MO, USA	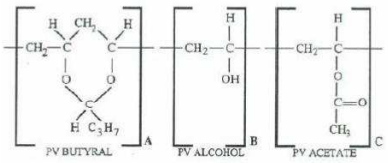
Benzyl butyl phtalate (S261)	Plasticizer	Monsanto Co., St Louis, MO, USA	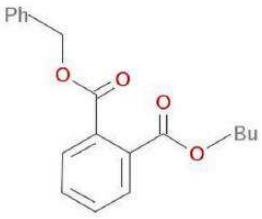
Rice Starch	Pore former (for the support layer only)	Fluka	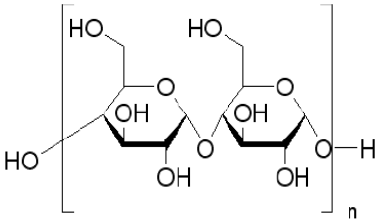

4.2.2 Tape Casting

The homogeneous suspension was then carefully poured in the doctor blade reservoir (Figure 4.5) and casted (Figure 4.6). The speed of the moving Mylar film was 40 cm/min. The gap between the mylar and the blades was set at 1.5 cm for the casting of the support layer, and 200 µm in the case of the membrane layer.

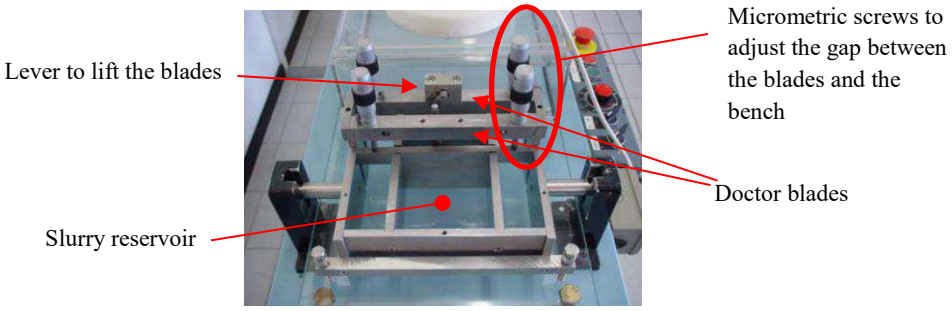

Figure 4.5 Picture of the Doctor Blade system.

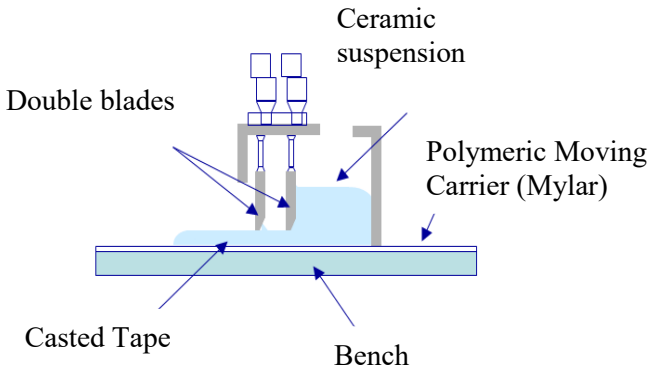

Figure 4.6 Schematic of the casting set-up.

Figure 4.7 shows the casting set-up used in this activity. The drying step was performed in a solvent-enriched chamber to slow down the drying rate, to limit the formation of stresses during this delicate step.

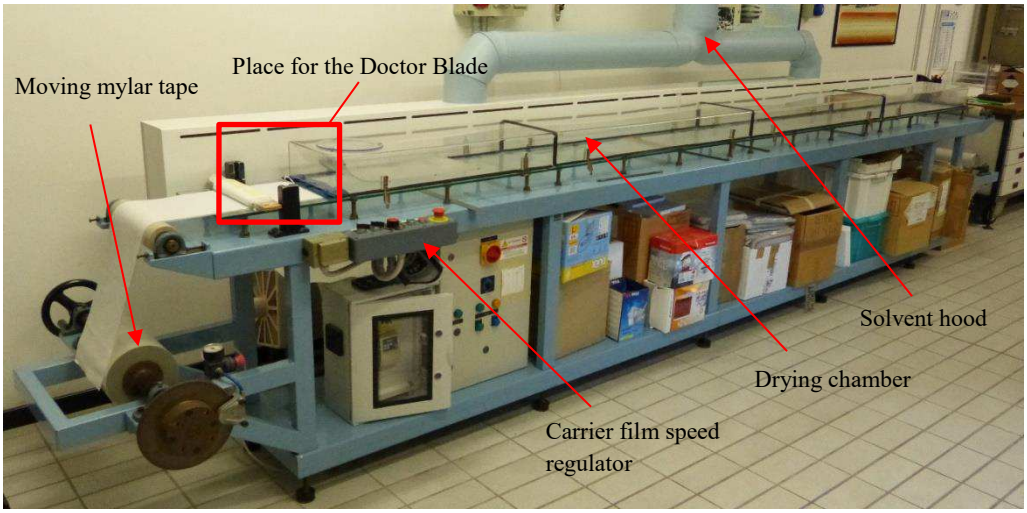

Figure 4.7 Picture of the casting bench.

4.2.3 Punching and Lamination

The dried green tape was then removed from the carrier and punched with the desired geometry.

Then, two support layers and one membrane layer were stacked and laminated to form the asymmetric green membrane. The lamination was performed with a pneumatic heat-press (Memopresse).

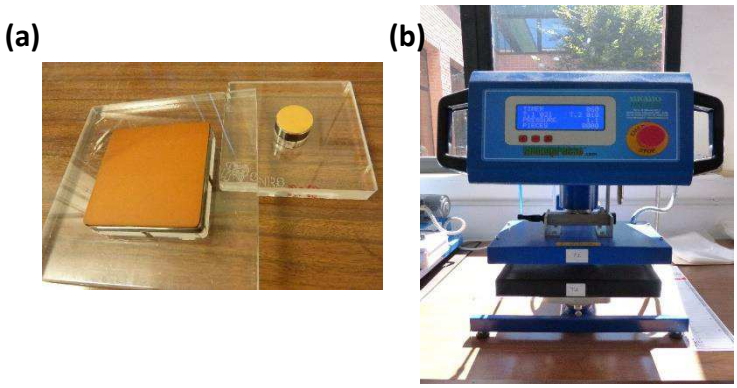

Figure 4.8 Picture of the (a) punchers and (b) of the memopresse.

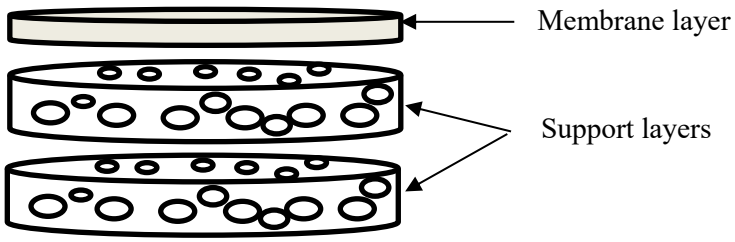

Figure 4.9 Schematic representation of the stacked layers to obtain the asymmetric architecture.

Generally, the lamination conditions for the bilayers (ϕ=24mm) made of the tapes with the composition used in this activity are a temperature between 40-65°C with a pressure of one bar for five to ten minutes.

4.2.4 *Debinding and Sintering*

Green asymmetric samples were then placed on a ZrO_2 plate and covered with a second plate using ≈ 1.5 cm spacers (Figure 4.10).

Figure 4.10 Standard set-up for the debinding and sintering thermal treatments.

The debinding heating program had two steps characterized by different heating rates:

1. 50ºC/h up to 150ºC;
2. 4ºC/h up to 600ºC.

Then, samples were sintered at 1400°C for four hours.

4.3 Characterizations

4.3.1 Dilatometry

The sintering behavior of the materials was analyzed in an horizontal dilatometer (DIL402/E, Netzsch, Germany) on green bars uniaxially pressed at 750 MPa and heated up to 1500°C at 5°C/min in static air.

The thermal compatibility of the selected electron conductive phases with the proton-conductive one was assed calculating the Thermal Expansion Coefficient in the operating temperature range between 100 – 1000°C, from the dilatometric curves. Linear thermal expansion coefficients α of the materials were calculated using Eq. (4.1), where L_0 and dL are respectively the initial length and the length change of the sample, while T_0 and T are the starting and the final temperature, respectively:

$$\alpha = dL / L_0 (T - T_0) \quad (4.1)$$

For the dilatometric analyses, the powders were uniaxially pressed (750kg/cm^2) in 5 x 30 mm^2 rectangular bars and sintered at 1400°C for 4 hours in air with a heating rate of 100°C/h. The measurements were performed between 20 and 1000°C, in static air, at a heating rate of 5°C/min. To subtract the expansion contribution of the sample holder and pushrod, a calibration analysis was carried out in the same conditions using a standard Al_2O_3 material prior to measurement.

4.3.2 Thermogravimetric analysis – Differential Scanning Calorimeter (TGA-DSC)

Scanning calorimeter (DSC) and thermogravimetric analysis (TGA) on a NETZSCH STA 409 CD thermal analyzer was utilized to check the thermal evolution of the materials[1]. Thermal analysis was performed for the characterization of decomposition behavior of the organic fraction in the green tapes. The temperature range investigated was 25-600°C with a heating rate of 5°C/min in air flux.

TGA was also used to assess the thermal stability of the different ceramic powders. These analyses were performed in air flux, from room temperature to 1550°C, with a heating rate of 5°C/min.

4.3.3 X-ray Diffraction (XRD)

XRD analyses were performed on the dense surface at room temperature using a Bruker D8 Advance diffractometer (Bruker AXS GmbH, Karlsruhe, Germany) with a Bragg-Brentano geometry and an X-ray tube operating at 40 kV and 40 mA. Data were collected through a one-dimensional LynkEye detector based on silicon strip technology, set to discriminate Cu $K\alpha_{1,2}$ radiation, in the 10-80° 2θ measuring range, with an equivalent counting time of 10s per 0.02° 2θ step anode X-ray. Phase analysis of XRD collected data were performed by means of HighScore Plus v.3.0 (PANalytical B. V., Almelo, The Netherlands). EXPGUI v.1208 interface[2] for the GSAS[3] was used to achieved quantitative phases analysis and unit-cell parameters perovskite main phase from X-ray diffraction data. The data were collected, in the 2θ region from 20° to 80° in 2Θ with 0.02° for 2θ-step and 5 s/step. All the powders were sieved using a 100 μm mesh prior the XRD analysis.

4.3.4 Dynamic mechanical analysis (DMA)

A dynamic mechanical analyzer (DMA Q800, TA Instruments, USA) was used to assess the thermo-mechanical properties of green tapes of BCZY with different solid content and with or without rice starch. The effect of different amount of rice starch on the thermomechanical properties was evaluated as well.
DMA is a technique to investigate the viscoelastic properties of a polymer[4]. The mechanical analyzer used allowed to apply both oscillating and static stresses, measuring the resulting strain or vice versa. Therefore, two types of analyses were performed: static and dynamic.

Dynamic Analyses

This kind of measurements were performed by applying an oscillating sinusoidal stress and measuring the resulting oscillating sinusoidal strain or applying an oscillating sinusoidal strain and measuring the resulting oscillating sinusoidal stress. The oscillating sinusoidal stress and strain can be exhibited the phase angle (δ) difference between 0° and 90° as shown in Figure 4.11.

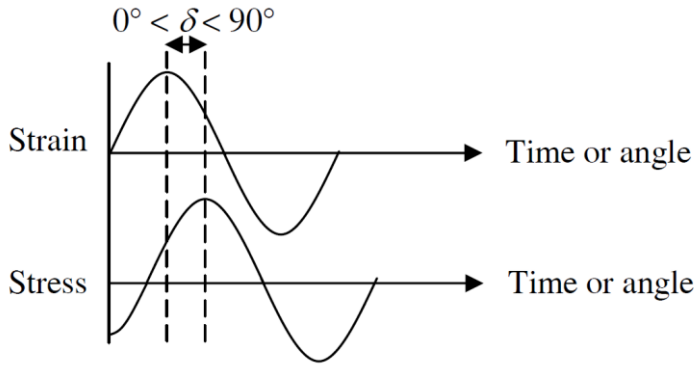

Figure 4.11 Sine wave of stress and strain in DMA.

A material that deforms in-phase with the application of the stress is purely elastic, whereas, a material that deforms 90° out-of-phase with the application of the stress is purely viscous. The modulus from the δ difference between stress and strain is represented in terms of complex modulus (E^*), corresponding to the storage modulus (E') and loss modulus (E''). The parameter E' relates to the elastic part of the polymer while E'' relates to the viscous part of the polymer. These values can be given as:

$$E^* = \frac{\text{stress}}{\text{strain}} \tag{4.2}$$

$$E' = E^* \cos\delta \tag{4.3}$$

$$E'' = E^* \sin\delta \tag{4.4}$$

The tanδ can be determined by:

$$\tan\delta = \frac{E''}{E'} \tag{4.5}$$

The complex vector is illustrated in Figure 4.12.

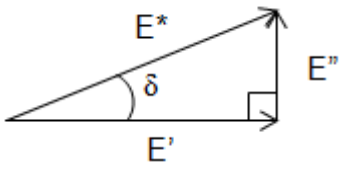

Figure 4.12 Complex modulus vector.

The clamp used for this kind on analyses was the tension film/fiber (Figure 4.13): a rectangular shaped sample is obtained by cutting the dried tape and mounted in the clamp, were a moving part applies the stress and a fixed part fixes the sample.

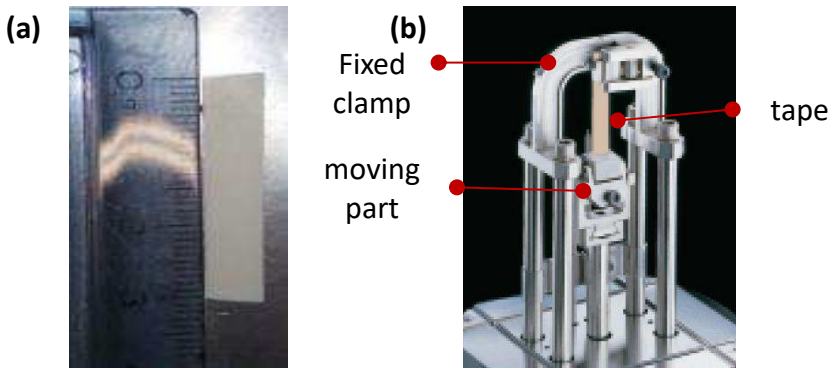

Figure 4.13 (a) Picture of the sample cut from the tape and (b) representation of the tensile film/fiber clamp supplied with the Q800 analyzer.

DMA allows to follow the variation of the moduli as a function of the temperature, therefore can give information about the thermo-mechanical behavior of the tape, therefore on the laminability of the tape.

In principle, temperature-programmed DMA is a useful tool to determine the glass transition temperature (T_g) of a polymer, which is the temperature that determines the reversible transition from a hard and relatively brittle "glassy" state into a viscous or rubbery one as the temperature is increased.

DMA was carried out at a frequency of 1 Hz and amplitude (strain) of 0.2% within the temperature from room temperature to 100 °C at a heating rate of 3

°C/min. The measurement was performed in triplicate. The storage and loss moduli at different temperatures were reported.

Static Analyses

The Q800 analyzer can also work in the dynamometric mode, applying a force or strain ramp and checking the material's response in terms of stress / strain. In this mode, creep tests (at different and constant temperatures) and the classical stress-strain tests were carried out.

1. **Creep tests**

Creep tests consist in experiments performed at various isothermal temperatures applying a certain stress and observing the sample's deformation over time. In this activity, creep tests were performed with the film/fiber tension (Figure 4.13) to obtain information about the development of the tape viscosity as a function of the temperature.

In addition, particular creeps tests were carried out aiming at miming and reproduce the thermocompression process occurs during lamination. For that purpose, two rectangular samples cut from green tapes (5.0 mm x 0.4 mm; Figure 4.14 (a)) are staked and insert in the compression clamp (Figure 4.14 (b)).

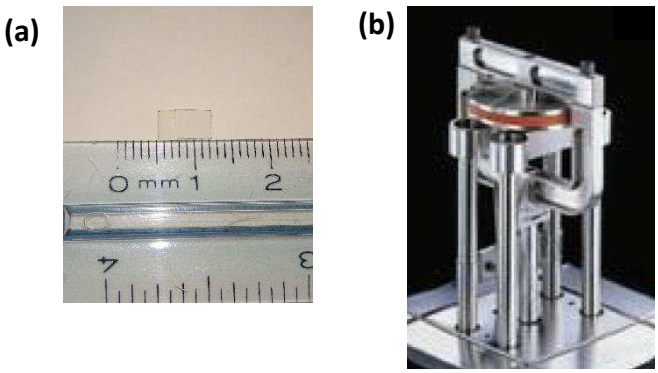

Figure 4.14 (a) Picture of the sample cut from the tape and (b) representation of the compression clamp supplied with the Q800 analyzer.

The creep curve reported in Figure 4.15 shows that dynamic viscosity values can be calculated from the strain curve. The viscosity is the reciprocal of the slope of the final curve portion. Viscosity values were obtained applying 0.4 MPa for 5 minutes at constant temperature (45, 50, 55, 60, 65, 70, 75°C). After each test, samples were cut and the cross section observed with an optical microscope to evaluate the lamination degree and to individuate the lamination temperature.

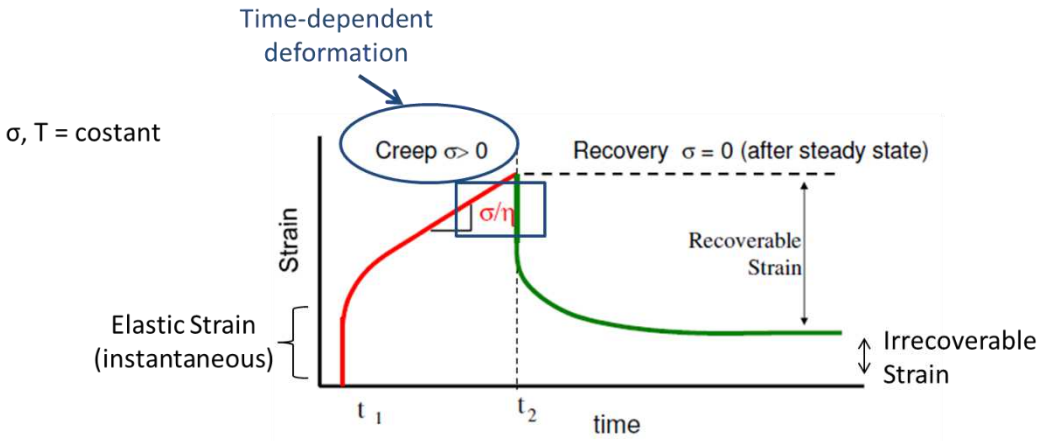

Figure 4.15 Schematic of a creep curve. The red segment is the material deformation because of the applied stress. The dynamic viscosity can be obtained by the reciprocal of the slope of the final part of the segment. The green curve represents the recovery of the material as the stress is removed.

Analytically, the viscosity was obtained by the time derivative of the creep compliance (J), defined as:

$$J = \frac{\text{strain of the sample}}{\text{Stress applied}} \tag{4.6}$$

Then the viscosity was obtained directly from the creep compliance curve, as reported in Figure 4.16.

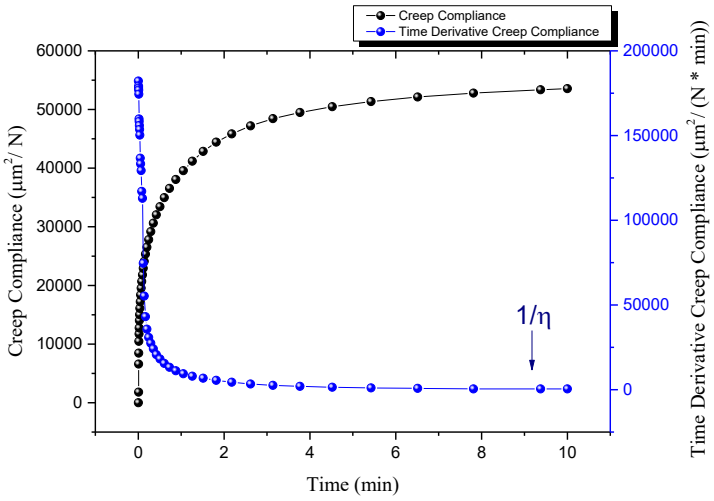

Figure 4.14 Creep compliance curve and graphical determination of the viscosity.

2. Stress strain

As described in Chapter 3, tensile testing is the main test used for the mechanical characterization of the green tapes. Tensile testing was used to determine the mechanical properties at room temperature. The specimen was prepared in dog-bone shape as shown in Figure 4.16.

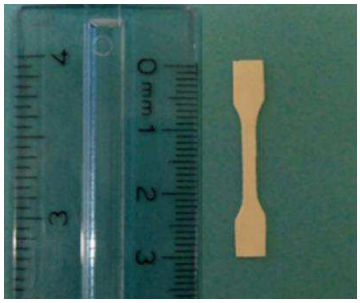

Figure 4.16 Dog-bone specimen (for tensile tests).

The dog-bone specimen was punched from the green tape with gauge length 12 mm, width of narrow section of 4 mm, and overall length of 30 mm.

A stress-strain curve was obtained and the tensile strength, elongation at break and modulus of elasticity were determined. At least three specimens were tested and reported as the average values. The different values were calculated from the following equations:

$$\text{Stress} = \frac{\text{load}}{\text{cross section area}} \tag{4.6}$$

$$\text{Strain} = \frac{\Delta L}{L_{initial}} \tag{4.7}$$

$$\text{Elastic Modulus} = \frac{\Delta stress}{\Delta strain} \tag{4.8}$$

(Linear portion of stress-strain curve)

Ideally, the modulus of elasticity or Young's modulus is the slope of the stress-strain curve at the linear part. In this work, the modulus measurements were performed selecting the pseudo-linear part up to 3.5% strain from stress-strain curve of the sample. Table 4.2 summarizes the mechanical tests performed.

Table 4.2 Schematic of the experiments carried out with the DMA.

Clamp	**Mode**	**Sample shape**	**Operative Parameters**	**Properties evaluated**	
Tension film - fiber	Strain rate	Dog-bone	Strain = 5000-25000 µm; $F_{statica}$ = 0.01 N	C_{max} [MPa] ε_{max} [%]	Stress, strain, yield to fracture, elastic modulus, toughness
	Multi frequency - strain	rectangular	ε= 0,2%; frequency= 2 Hz; $\Delta T = T_{amb} - 100°C$	E' [MPa] E'' [MPa] tan δ	Determination of the moduli as functions of temperature
Compression film - fiber	DMA creep	Squared bilayers	σ = 0,4 MPa; t = 5 min; T = 45 - 75°C	η [Pa · s] $\Delta l/l_0$ (z) [%]	Viscosity and deformation values as functions of the temperature

4.3.5 Profilometry

Profilometry analyses were conducted to assess membrane deformations after sintering, using a non-contact system (Contour GT-K 3D non-contact profilometer, Bruker, Germany). This system is based on white light

interferometry, exploiting the wave superimposition principle to combine waves in order to extract information from the results of their combination. The waves form a pattern depending on the phase difference between them, which will generate a constructive or destructive interference. The returning beams are then collected by the CCD (Charge-Coupled Device) sensor that converts the resulting interference pattern into the surface topography.

4.3.6 Polishing of the membrane cross sections

Polished membrane's cross sections were obtained embedding the cross sections under vacuum in epoxy resin (EpoFix, Struers, Figure 4.17 (a)) and then polishing them down to 0.25 μm finish with the automatic polishing machine (Tegramin-25, Struers, Figure 4.17 (b)).

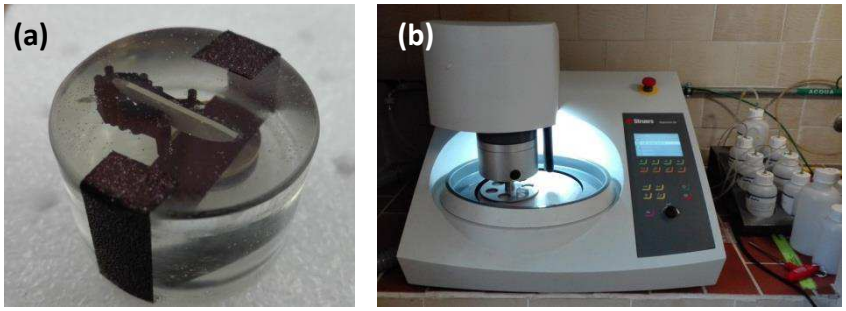

Figure 4.17 Pictures of (a) polished sample for SEM analyses and (b) Tegramin-25 polishing machine.

4.3.7 Scanning electron microscopy (SEM)

Scanning electron microscopy was used to observe the microstructure of the asymmetric membranes. This technique exploits an accelerated electron beam to scan the surface of the sample and register an image. This process generates different signals, the most used are the ones produced by secondary and back-scattered electrons. The first are electrons with energy up to 50 eV, deriving mainly from the interaction between the beam and the nuclei of the sample atoms[5]. In this case a field emission gun-scanning electron microscope (SEM-

FEG, Carl Zeiss Sigma NTS GmbH, Oberkochen, Germany) with EDS probe (EDS, X-Act, INCA Energy 300, Oxford Instruments, Abingdon, UK) was used.

4.4 H_2 permeation measurements

The membrane gas-tightness was assessed evaluating the He leakage at room temperature using the apparatus reported in Figure 4.18: the membrane is placed in correspondence of the hole and fixed with the nut. The chamber is pressurized and gas leakage is verified dropping some water and checking if bubbles appeared.

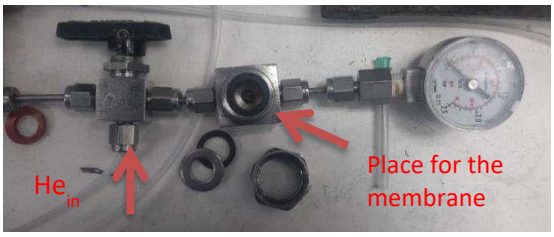

Figure 4.18 Apparatus for the gas-tightness test.

Permeation measurements were performed on a cylindrical two chambers quartz reactor schematized in Figure 4.19. The inner chamber is 16 mm diameter with a flat holed bottom that supports the membrane. Sealing was done using Ag-alloys rings heated at temperature > 750ºC. Permeation measurements were performed on 15 mm diameter membranes.

Figure 4.19 schematically describes the measurement set up used for the H_2 permeation evaluation, where the feed gas is put in contact with the dense layer. Because of the membrane's asymmetric architecture, the influence of the set up used for the measurements was assessed switching the feed membrane's side from the dense layer to the porous support.

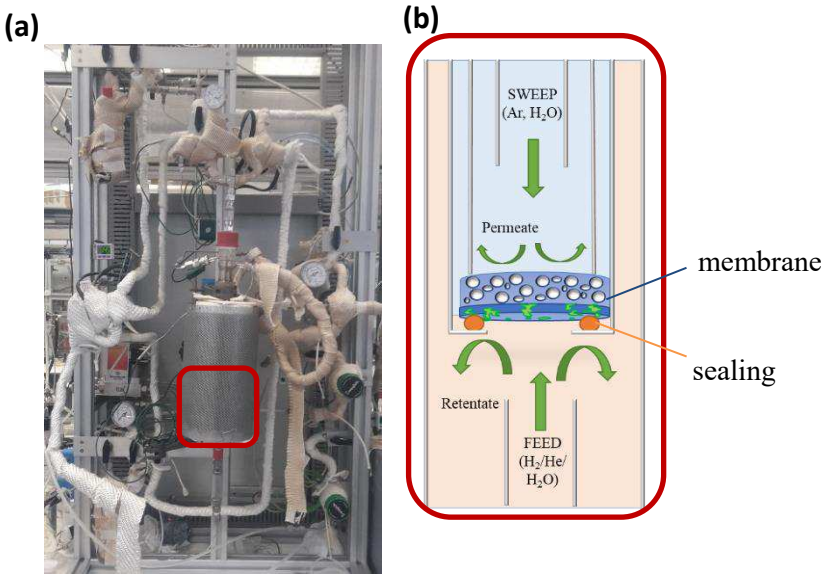

Figure 4.19 (a) Picture of the membrane reactor; (b) schematic representation of the permeation set-up.

The flow rate of all gas feed streams was controlled using mass flow controllers (MFCs). The standard flow rates used were 100 mL min^{-1} for feed and 150 mL min^{-1} for sweep, although they were modified in the different experiments in order to determine their influences on the H_2 separation.

Ar was used as sweep gas to obtain a clearer signal since it is also the gas carrier of the GC. An acceptable sealing was achieved when the He concentration was lower than 5% of the permeated H_2.

Permeation measurements were carried out evaluating the influence of three different parameters on the hydrogen separation:

- different partial pressures of H_2 on the feed side (80%, 50%, 20% of H_2 balanced with He)
- temperature range (600-750°C);
- humidification degree (both sides humified, sweep side humidified only, and feed side humidified only);
- feed side: the membrane at first was fed from the dense layer, then the feed side was switched from the dense layer to the porous support one.

Humidification of the sweep and feed streams was accomplished by saturation at room temperature using Milli-Q water. The H_2 content in the permeate side was analysed using a micro-GC Varia CP-4900.

Data reported are achieved at steady state after flux stabilization and each test was repeated three times to minimize analysis relative error. Hydrogen concentration wss calculated from the H_2 signal area and its response factor, previously calibrated. Permeation flux (mL min^{-1} cm^{-2}) wass extracted from the hydrogen flux and the effective area of the membrane. The hydrogen flux was corrected by the hydrogen leakage from the He concentration of the permeate side:

$$J_{H2,leakage} = \frac{F}{A} C_{s,He} \frac{C_{f,H2}}{C_{f,He}} \quad (4.9)$$

Where F is the total gas flow rate on the sweep gas side; A is the effective area of the membrane for H_2 permeation; $C_{f,He}$ and $C_{f,H2}$ are He and H_2 concentration in the feed gas, respectively; $C_{s,He}$ is the He concentration in the sweep side. Then the corrected hydrogen flux was calculated as:

$$J_{H2,corr} = J_{H2,perm} - J_{H2,leakage} \quad (4.10)$$

The effect of Pt-catalytic activation of the surfaces was also evaluated.

Dense layer activation was performed screen printing a Pt ink (Matek, Germany) onto the dense layer. The porous support layer was activated by dropping into the porous support a 0.065 M solution of the $Pt(NH_3)Cl_2 \cdot H_2O$ salt precursor (Sigma-Aldrich) in H_2O-EtOH (75-25 vol %). The infiltration process was repeated 5 times, with a drying step of 30 minutes at 50°C after each infiltration. Then, membranes underwent calcination (Figure 4.20) at 950°C for 2 hours (heating rate of 2°C/min).

References

[1] G. Della Gatta, A. Lucci "Principi ed Applicazioni di Calorimetria e Analisi Termica" Ed. Piccin (1983) 1-15.

[2] B. H. Toby, EXPGUI, a Graphical User Interface for GSAS. J. Appl. Crystallogr. 34 (2001) 210-213.

[3] A. C. Larson.; R. B. Von Dreele. General structure analysis system (GSAS); Los Alamos National Laboratory Report LAUR 86-748 (2004).

[4] K. P. Menard, "Dynamic Mechanical Analysis: a Practical Introduction" CRC Press, (1999).

[5] J. Goldstein, D.E. Newbury, P. Echlin, C.E. Lyman, D.C. Joy, E. Lifshin, L. Sawyer, J.R. Michael "Scanning Electron Microscopy and X-ray Microanalysis" Ed. Springer (2003) 21-60.

Chapter 5
Results and Discussion

5.1 Introduction

This chapter reports the results on the development of an asymmetric cer-cer membrane for hydrogen separation. The experimental activity be schematized in the following points:

- Individuation of a cer-cer composite suitable for the application with improved sinterability;

- Study and optimization of the tape casting process for the thin membrane layer and of the thick support with particular attention to the effects of the slurries composition on the mechanical and thermomechanical properties of the respective green sheets;

- Optimization of the debinding and sintering processes, in particular tuning the sintering atmosphere to face the barium loss from the protonic conducting phase of the cer-cer;

- Optimization of the ceramic process to obtain planar and crack free asymmetric membranes;

- Hydrogen permeation measurements of the engineered structures and evaluation of the influence of the ceramic process on the membrane's performances.

5.2 Cer-cer composite individuation

As explained in Chapter 2, dense ceramic membranes for hydrogen separation are very promising for a wide range of separation processes. Among the different type of dense ceramic membranes, the ceramic-ceramic composite ones have recently gained lot of the interest from the scientific community thanks to their enhanced performances. In them, it is possible to tune the ambipolar conductivity properties modifying the composition of the composite to match a high proton conducting phase with a high electron conductive one, reaching high separation performances. In order to do so, however, it is necessary to match the chemical and thermomechanical properties of the two ceramic phases to form a crack-free and robust membrane. The most performing protonic systems are based on Y-doped $BaCe_xZr_{1-x}O_{3-\delta}$. These compounds are then coupled with Y- or Gd-doped CeO_2 for the electron conduction to produce the cer-cer composite[1]. $BaCe_{0.65}Zr_{0.2}Y_{0.15}O_{3-\delta}$ system (BCZY) demonstrated high separation capability and very good chemical stability under CO_2-rich atmosphere typical of the real hydrogen separation processes.

Despite the remarkable number of recent studies dedicated to the BCZY system[2,3] to the best of our knowledge, no systematic work has been dedicated to the choice of the electronic conductive ceramic phase to be coupled with the BCZY for hydrogen separation applications. The selected electronic conductive phase, in addition to a high conductivity, must show good chemical and thermomechanical compatibility with the barium cerate-based system up to the high temperature needed to produce these devices (around 1400°C) and in oxygen poor and oxygen rich atmospheres.

This first part of the activity was devoted to a compatibility study between the most promising $BaCe_{0.65}Zr_{0.2}Y_{0.15}O_{3-\delta}$ proton conductive system and five different possible electronic conducting compounds belonging to four families:

- Ceria-based systems: they are known to exhibit remarkable n-type electronic conductivity in a reducing atmosphere at high temperature (600°C) due to the co-existence of the Ce^{4+}/Ce^{3+} pair[4,5]. CeO_2 and

$Ce_{0.8}Gd_{0.2}O_{1.9}$ compositions were studied to verify any differences induced by the presence of the aliovalent cation;

- Lanthanum nickelate cobaltite systems: they are well known for their high electronic conductivity, in particular the selected $La_{0.95}Ni_{0.6}Co_{0.4}O_{3-\delta}$ is a typical highly conductive perovskite used as contact coating[6,7] or as cathode in SOFCs[8,9];

- Strontium titanate-based perovskites: they have been reported to show high electron conductivity in reducing atmosphere at high temperature (T > 700°C) due to the formation of the Ti^{4+}/Ti^{3+} pair. The selected $Sr_{0.9}La_{0.1}TiO_{3-\delta}$ composition has been successfully exploited as pure ceramic anode (Ni-free) in solid oxide fuel cells (SOFCs) devices[10,11,12].

- α-SiC: chosen as a possible non-oxide electro-conductive phase since it has been reported as a possible electron-conductive phase to be used in cer-cer systems[13].

All the powders considered in this study were commercially available. The suppliers are indicated in Table 1.1.

Table 1.1 Systems evaluated to produce the cer-cer composite.

	Stoichiometry	**Supplier**
Proton conductor		
BCZY	$BaCe_{0.65}Zr_{0.2}Y_{0.15}O_{3-\delta}$	Marion Technology
Electron conductors		
Ceria	CeO_2	Pi-Kem
GDC	$Ce_{0.8}Gd_{0.2}O_{1.9}$	FuelCellMaterials
LNC	$La_{0.95}Ni_{0.6}Co_{0.4}O_{3-\delta}$	Nex Tech Materials
LST	$Sr_{0.9}La_{0.1}TiO_{3-\delta}$	Nex Tech Materials
α-SiC	SiC	H.C. Starck

The phase stability as a function of the thermal treatment temperature and atmosphere for each system reported in Table 1 was firstly assessed. For this purpose, the five oxide powders were treated at 1400°C for 4h either in air and in reducing atmosphere (H_2/Ar 4%), while SiC powder was treated at the same temperature but only in H_2/Ar 4% atmosphere. The conditions were the ones commonly used to sinter dense ceramic membranes.

5.2.1 Stability of single phases

A preliminary study was done on the effect of the thermal treatment on each single component.

The XRD pattern of the as-received BCZY revealed the coexistence of the BCZY phase with a Ba-deficient and a $BaCO_3$ phases (Figure 1.1).

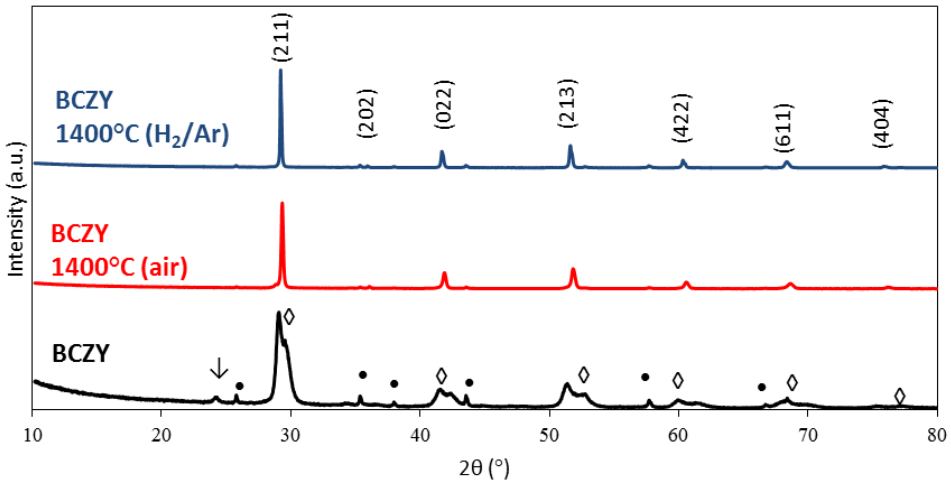

Figure 1.1 XRD patterns of the as received BCZY powder and after sintering at 1400°C for 4 hours in different atmospheres. Peaks refer to an orthorhombic phase. ◊ Ba-deficient phase; • Al_2O_3 (int.ref.); ↓$BaCO_3$.

The biphasic nature of this raw material, is due to the reversible carbonisation reaction of barium-based materials with the atmospheric CO_2 according to the Equation:

$$BaCe_{0.65}Zr_{0.2}Y_{0.15}O_{3-\delta} + CO_2 \leftrightarrow xBaCO_3 + Ba_{1-x}Ce_{0.65}Zr_{0.2}Y_{0.15}O_{3-\delta-x} \quad (5.1)$$

After the thermal treatment in air at 1400°C, in fact the powder showed a single phase with orthorhombic structure as previously reported[14]. This behaviour has been already observed in literature[15] and it is attributed to the mobility of the cation Ba^{2+} produced by the decomposition of $BaCO_3$ at temperatures higher than 800°C: during the heat treatment, Ba^{2+} migrates and enriches the Ba-deficient perovskite lattice leading to the desired BCZY orthorhombic crystallographic system, whereas the carbonate decomposes in CO_2 leaving the system.

Figure 1.2 (a) and (b) reports the XRD spectra of the ceria-based electronic conductive phases collected before and after the thermal treatments in air and H_2/Ar.

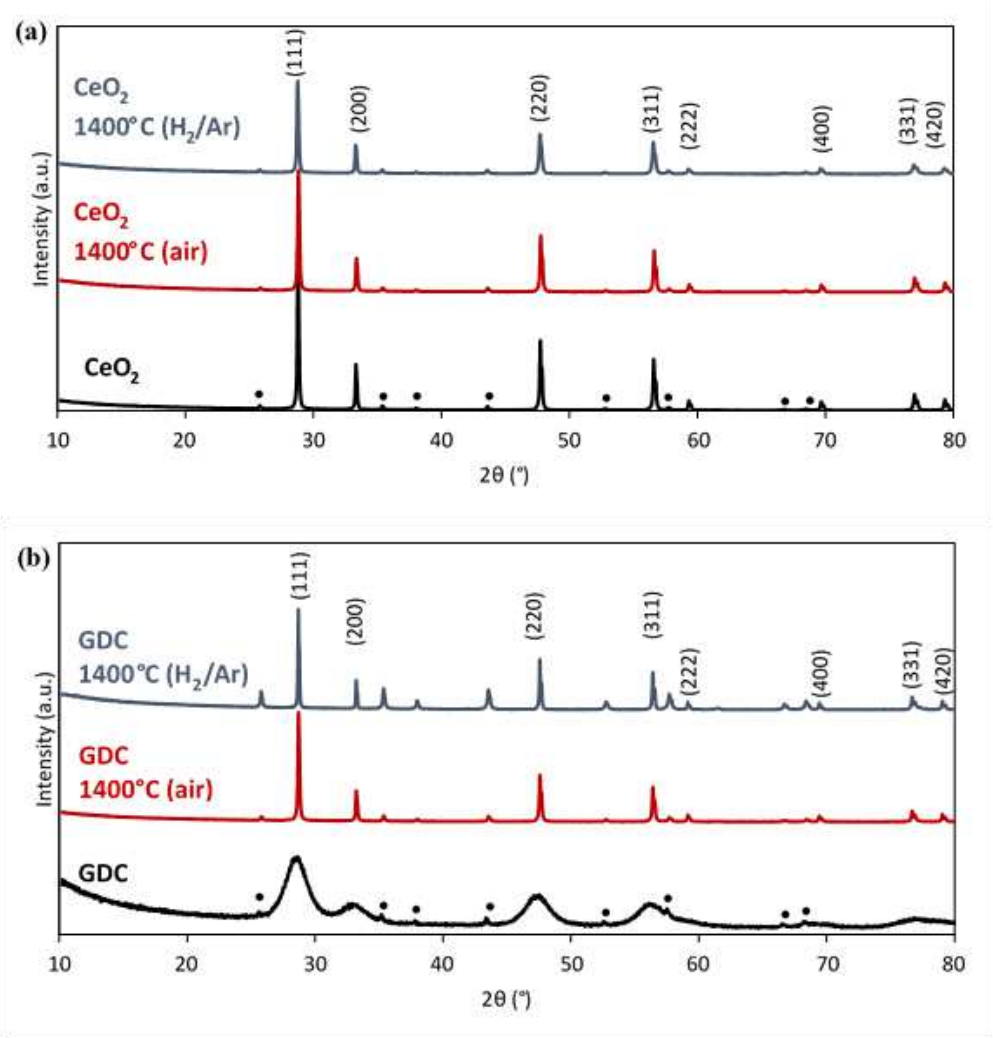

Figure 1.2 XRD patterns of (a) CeO_2 (JCPDS 34-394, cubic) and (b) GDC (JCPDS 50-20, cubic) before (black line) and after 4 hours of permanence at 1400°C in air (red line) and in H_2/Ar mixture (4%, blu line). • Al_2O_3 is added as internal reference.

Both CeO_2 and GDC were stable after the treatments. The very broad peaks that characterized the raw GDC reported in Figure 3 (b), is due to the small particles size of this powder, as confirmed by its large specific surface area (220 m^2/g). After the thermal treatments, the GDC peaks become narrower as expected consequence of the grain growth[16].

LST phase (Figure 1.3), as well as the ceria-based ones, exhibited no differences in the diffractometric pattern before and after the thermal treatment neither in oxidant nor in reducing atmospheres.

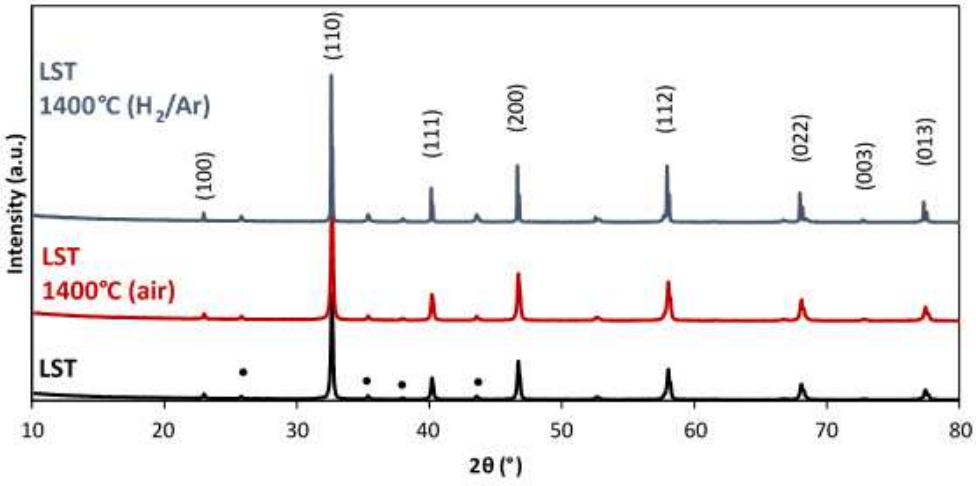

Figure 1.3 XRD patterns of LST (JCPDS 55-926, cubic) before (black line) and after 4 hours of permanence at 1400°C in air (red line) and in H_2/Ar mixture (4%, blu line). • Al_2O_3 is added as internal reference.

On the other hand, LNC is not stable neither in air nor in reducing atmosphere as shown by the XRD analysis reported in Figure 1.4.

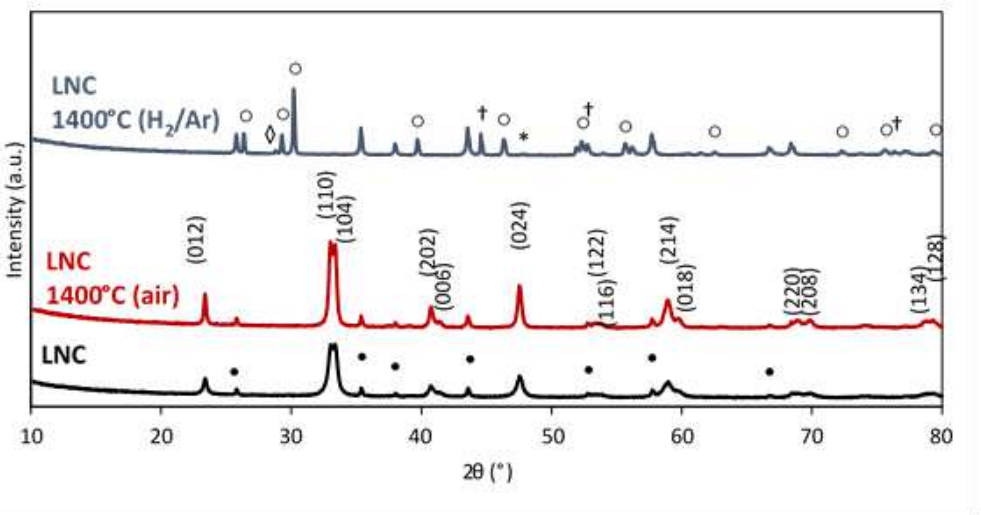

Figure 1.4 XRD patterns of LNC (JCPDS 32-296, rhombohedric) before (black line) and after 4 hours of permanence at 1400°C in air and (red line) in H_2/Ar mixture (4%, blue line). • Al_2O_3 is added as internal reference; ◊ $LaNi_{0,9}Co_{0,1}O_{2,54}$; ○ La_2O_3; † Ni; * Co.

LNC, was stable at high temperature in oxidizing atmosphere (red line, Figure 1.4), while the phase decomposed when thermally treated in reducing atmosphere (blue line). Under these conditions, the LNC phase was replaced by other products, such as La_2O_3 (JCPDS 03-065-2923, with the most intense peak at 30°), Ni (JCPDS 03-065-2923, with the most intense peak at 44°), Co (JCPDS 03-065-2923, with the most intense peak at 47°) and $LaNi_{0.9}Co_{0.1}O_{2.54}$ (JCPDS 03-065-2923, with the most intense peak at 29°). The exolution of metals from similar structures, is a well-known phenomenon that can take place in reducing atmosphere: the exit of Ni and Co from the LNC lattice leave as main phase La_2O_3, with small amount of $LaNi_{0.9}Co_{0.1}O_{2.54}$(LNC) and Co. SEM-EDS analysis performed onto LNC reduced powder confirmed the Ni and Co exolution from the perovskitic lattice (Figure 1.5). The EDS elements mapping showed in fact the presence of Ni- and Co-enriched areas in correspondence to O- and La-impoverished regions (red circles).

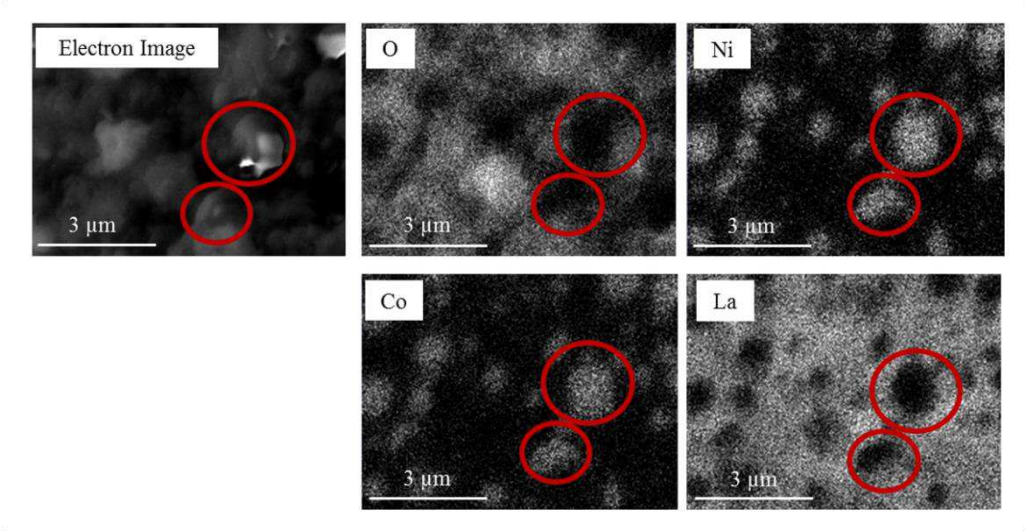

Figure 1.5 SEM image and O, Co, La, Ni EDS mapping of LNC powder after thermal treatment (1400°C for 4 hours) in reducing atmosphere. Red circles evidence Ni-Co enriched particles.

Finally, Figure 1.6 shows the XRD spectra registered for α-SiC before and after 4 hours of dwelling time at 1400°C in reducing atmosphere. As expected, the silicon carbide was stable in these conditions.

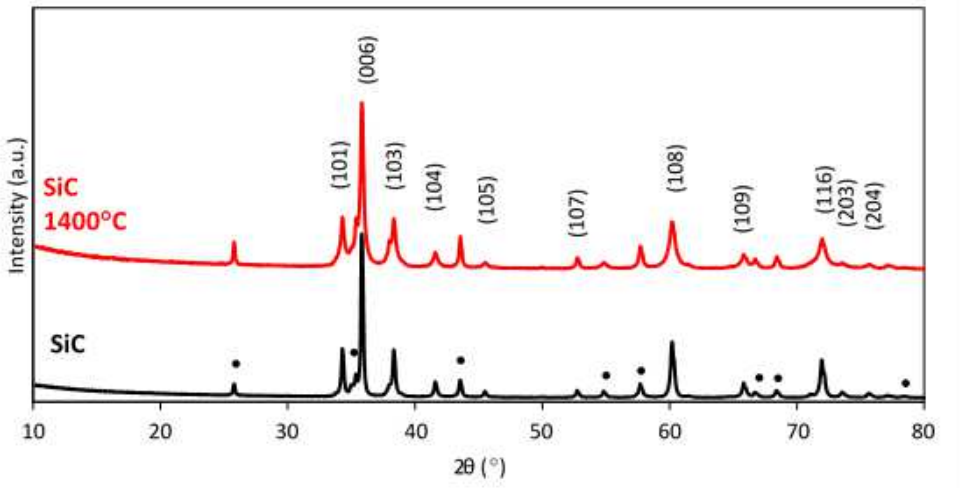

Figure 1.6 XRD patterns of α-SiC (JCPDS 73-1663, hexagonal) before and after 4 hours of permanence at 1400°C in reducing atmosphere (mixture 4% H_2 in Ar). • Al_2O_3 added as internal reference.

These results suggested that all the studied systems, except LNC and α-SiC, could be considered stable in the condition commonly used for the production and/or operation of BCZY-based membranes.

5.2.2 Biphasic systems

After having analysed each single system, mixtures BCZY + electronic phase, 50:50 vol. % were treated in the same conditions (1400°C for 4 hours) to evaluate possible detrimental interactions.

BCZY-LNC

Figure 1.7 reports the XRD patterns of the system after the thermal treatments compared with the ones of each parent compounds.

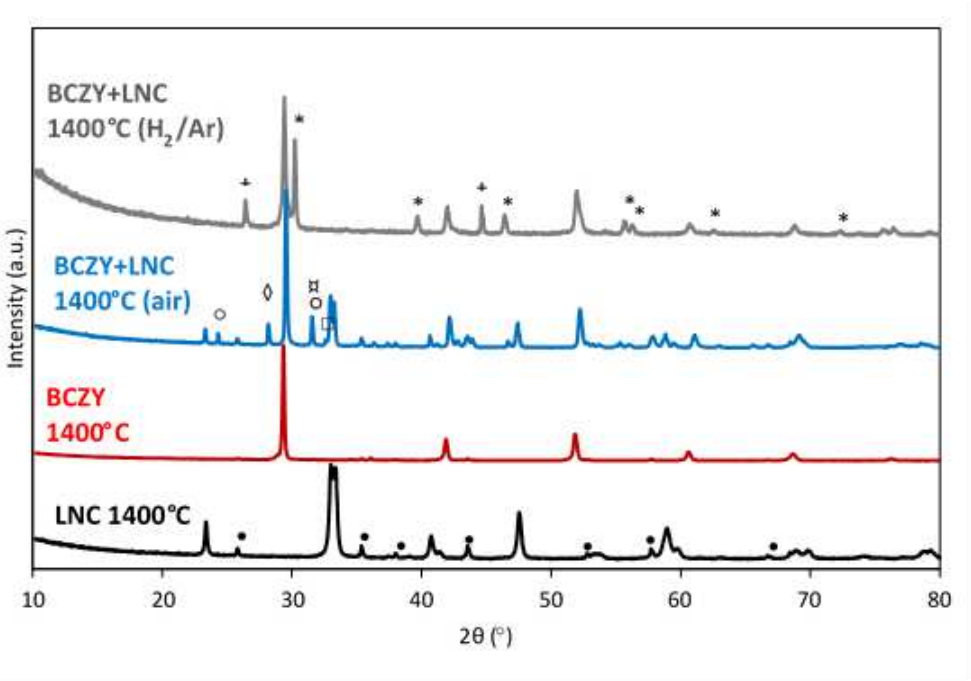

Figure 1.7 XRD patterns of BCZY/LNC mixture after 4 hours dwelling at 1400°C in air and in reducing atmosphere (mixture 4% H_2 in Ar). ◊ BaO; ○ La_2NiO_4; □ $La_4Ni_3O_{10}$; ¤ $Ba_{10}Co_9O_{27}$; † Ni; ‡ $Ba_6Co_4O_{12}$; * La_2O_3; • Al_2O_3 (int. ref.). XRD patterns of BCZY and LNC thermally treated are added for comparison.

In air, LNC was still detected, but secondary phases could also be clearly identified: La_2NiO_4 (JCPDS 76-0055 with the most intense peak at 31°) and $La_4Ni_3O_{10}$ (JCPDS 01-083-1164, with the most intense peak at 32°) whereas diffraction peaks ascribable to BaO (JCPDS 03-065-2923, with the most intense peak at 28°) and to $Ba_{10}Co_9O_{27}$ (JCPDS 54-0612, with the most intense peak at 31°) confirmed reaction

between the two phases at high temperature. These data suggested that, in these conditions, some Co could migrate from LNC and react with the BaO derived from the BCZY producing the $Ba_{10}Co_9O_{27}$ perovskitic structure and the lanthanum nickelate phase poor in Co. The segregation of BaO from the perovskite lattice shifts the BCZY peaks to higher 2θ values as a consequence of a lattice contraction[17].

As detected for the single phase, LNC decomposes in reducing atmosphere even in presence of BCZY: La_2O_3 (JCPDS 01-074-1144), $Ba_6Co_4O_{12}$ (JCPDS 48-1773) and Ni (JCPDS 001-1260) exolved from the structure were found to be the products of the LNC decomposition (Figure 1.5). Also in this case, the presence of the Ni phase was confirmed by the EDS element mapping of the reduced powder mixture (Figure 1.8).

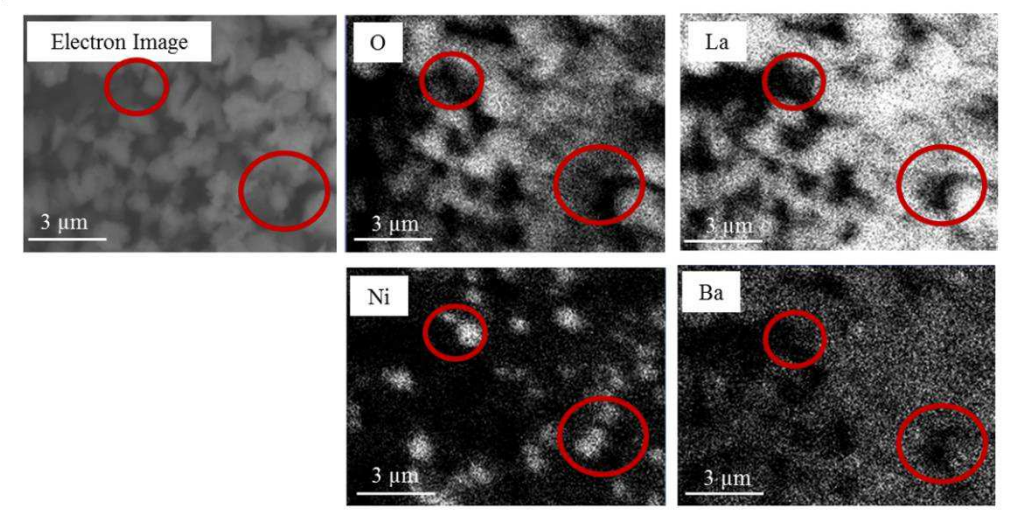

Figure 1.8 SEM image and O, La, Ni, Ba EDS mapping of the BCZY/LNC powder after thermal treatment (1400°C for 4 hours) in reducing atmosphere. Red circles show the Ni exoluted particles.

These results suggested that despite the stability of the single LNC, this phase reacts BCZY also in oxidant environment and cannot therefore be considered for the production of the cer-cer separation membrane.

BCZY-LST

In the case of the BCZY/LST mixture (Figure 1.9), the thermal treatment in air caused the segregation of CeO_2 (JCPDS 04-0593) from the BCZY lattice and therefore a shift of the protonic conductive phase peaks to higher values of 2θ as a consequence of the lattice contraction[18].

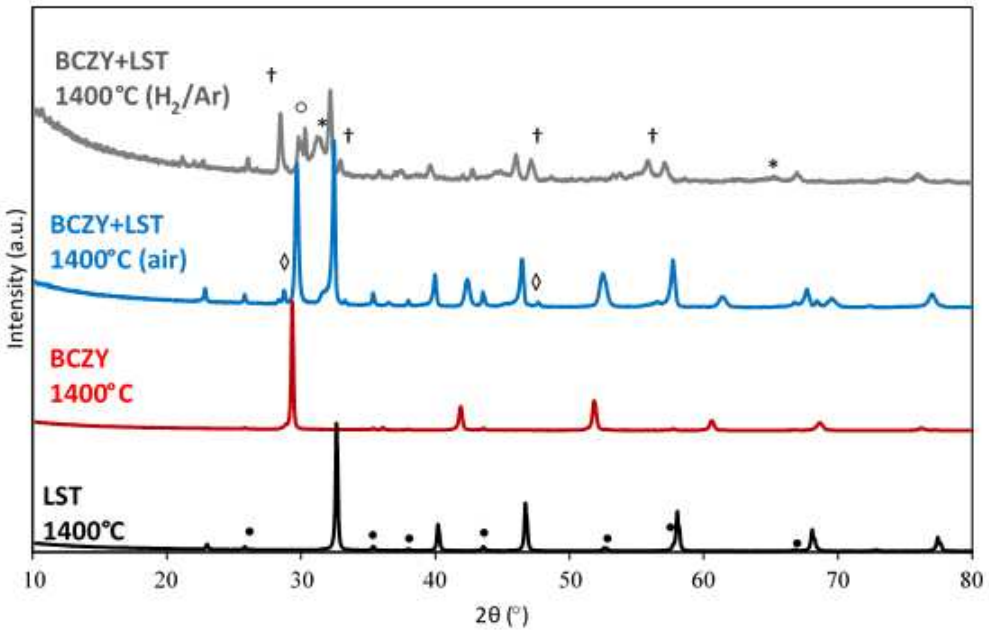

Figure 1.9 XRD patterns of BCZY/LST mixture after 4 hours of permanence at 1400°C in air and in reducing atmosphere (mixture 4% H_2 in Ar). ◊ CeO_2; ○ $Sr_{(1-x)}La_xTiO_3$; † $La_{0,5}Zr_{0,5}O_{1,75}$; * $Sr_3La_2Ti_2O_{10}$; • Al_2O_3 (int. ref.). XRD patter of BCZY and LST thermally treated are added for comparison.

The dual system was poorly chemically stable also in reducing atmosphere (Figure 1.9). In fact, even if LST alone was found to be stable (Figure 1.2 d)), a large number of secondary phases appeared in the XRD pattern when it was coupled with BCZY. Only few of these secondary phases could be detected: $Sr_3La_2Ti_2O_{10}$ (JCPDS 50-0522), $La_{0,5}Zr_{0,5}O_{1,75}$ (JCPDS 01-75-0346) with the most intense peak at 29° and compounds of the family $Sr_{(1-x)}La_xTiO_3$ which have characteristic peaks with 2θ values at 31.0 ± 0.5°.

BCZY/SiC

The XRD spectrum of BCZY/αSiC mixture treated at 1400°C in reducing atmosphere is reported in Figure 1.10.

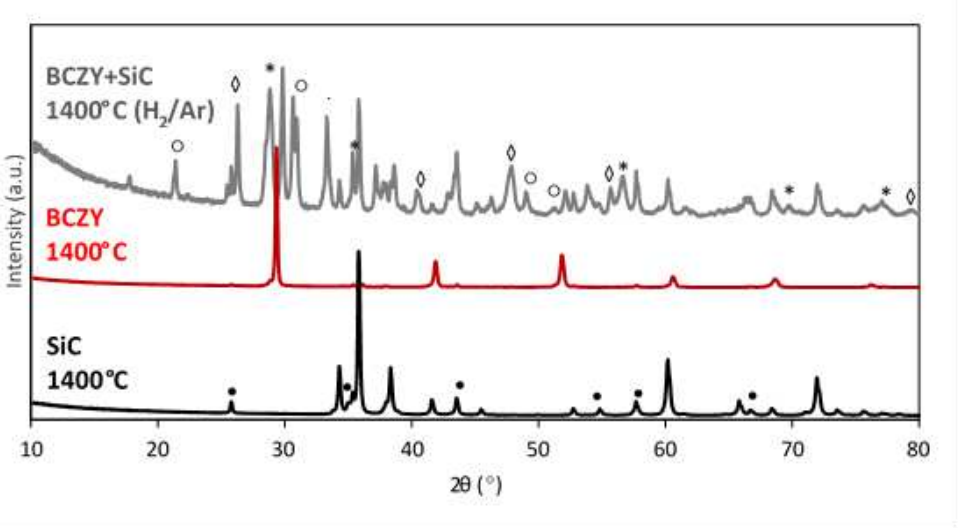

Figure 1.10 XRD patterns of BCZY/αSiC mixture after 4 hours of permanence at 1400°C in reducing atmosphere (mixture of 4% H_2 in Ar). ◊ BaO; * CeO_2; ○ $BaCO_3$; • Al_2O_3 (int. ref.). XRD patter of BCZY and α-SiC thermally treated are added for comparison.

The analyses showed that BCZY was not chemically compatible with α-SiC in such conditions since a lot of secondary phases were detected (including BaO JCPDS 01-0746, with the most intense peak at 26°, CeO_2 JCPDS 04-0593, with the most intense peak at 28°).

Also in this case, as for the BCZY/LNC system, the formation of BaO lead to a shift of the BCZY peaks due to the presence of a Ba-deficient lattice. The peak shifting effect was also caused by the formation of CeO_2, as previously described for BCZY/LST mixture. The presence of $BaCO_3$ (JCPDS 03-06559, with the most intense peak at 31°) was due to the carbonatation of BaO by the atmospheric CO_2 after thermal treatment.

BCZY/Ceria-based Systems

The XRD spectra of the as-treated BCZY/CeO_2 and BCZY/GDC mixtures are reported in Figure 1.11 (a) and (b), respectively.

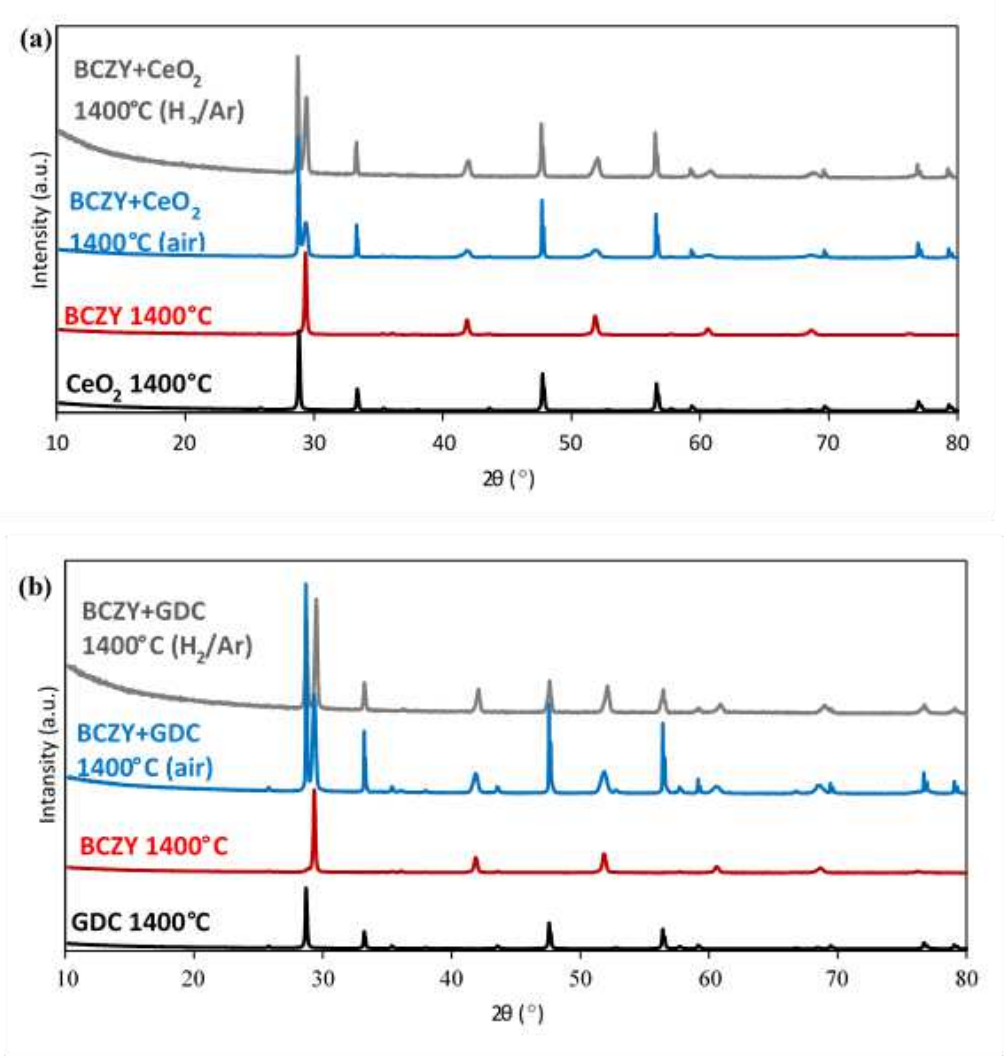

Figure 1.11 XRD patterns of (a) BCZY/CeO_2 and (b) BCZY/ GDC mixture after 4 hours of permanence at 1400°C in air and in reducing atmosphere (mixture 4% H_2 in Ar). Al_2O_3 is added as internal reference and XRD patter of BCZY, GDC and CeO_2 thermal treated for comparison.

After the thermal treatment in air and in reducing atmosphere at high temperature (1400°C), the two mixtures exhibited no additional peaks in comparison to the raw powders, confirming that the un-doped ceria is compatible with BCZY under such conditions as has been already proved for GDC.

Therefore, based on the chemical compatibility, only ceria-based systems can be coupled with BCZY to produce a cer-cer membrane, as the other systems reacted at high temperature with the proton conductive phase under both oxidant and reducing atmosphere.

However, chemical compatibility is not the only condition that has to be satisfied for the reliability of a cer-cer composite. The electron conductive phase must, in

fact, be thermo-mechanically compatible with the proton conductive phase during the operation temperature range. The volumetric expansion of the two different phases must be considered to avoid residual internal stresses that may induce cracks.

The TEC values of both single phases and the BCZY/Ceria-based mixtures (Table 1.2) were calculated in the 100-1000°C operating temperature range from the dilatometric curves reported in Figure 1.12.

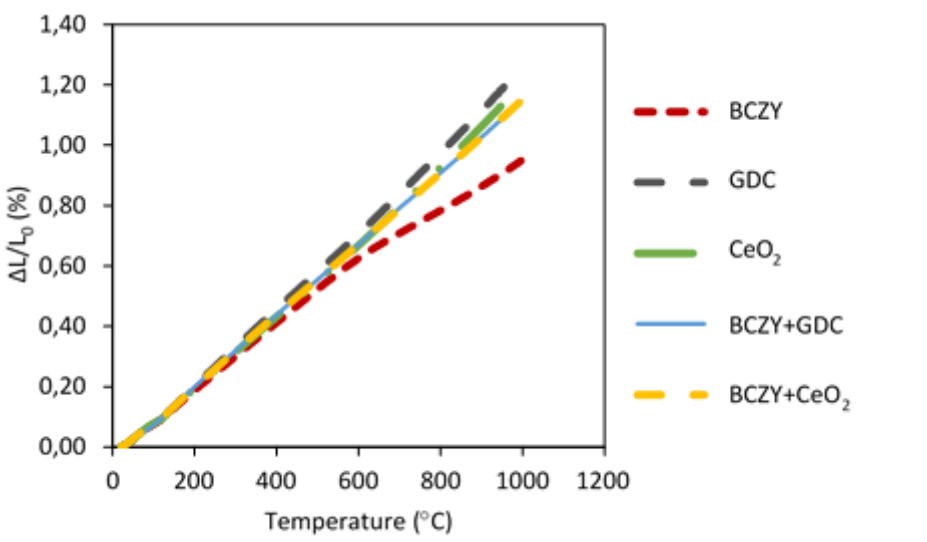

Figure 1.12 Dilatometric curves for BCZY, GDC, CeO_2 and the BCZY/GDC and BCZY/CeO_2 mixtures in static air with a heating rate of 5°C/min. Note that the two curves related to the two mixtures are overlapped.

Table 1.2 Thermal Expansion Coefficients (α) of single CeO_2 and GDC phases and BCZY-based mixtures.

	α (x10^{-6} K^{-1})
BCZY	9.8
CeO_2	12.5
GDC	13.2
BCZY+CeO_2	11.9
BCZY+GDC	12.0

As shown in Figure 1.12, the profile of the BCZY thermal expansion exhibited a deviation from the linearity in the temperature range between 500-600°C, caused

by hydration/dehydration phenomena and consequent changes in lattice constants, typical of barium cerate-zirconate materials[19].
Even if Gd-doped Ceria exhibited a higher TEC value (13.2 x 10^{-6} K^{-1}) than the un-doped Ceria (12.5 x 10^{-6} K^{-1}), both values are comparable with the BCZY one. Despite the TEC of GDC is quite higher than the one of CeO_2, BCZY/GDC and BCZY/CeO_2 mixtures displayed a comparable TEC value, 12.0x10^{-6} K^{-1} and 11.9x10^{-6} K^{-1} respectively.

Being both ceria-based materials chemically and thermo-mechanically stable with BCZY, GDC was preferred as the electron conductive phase of the cer-cer composite. In fact, for the same chemical and thermomechanical compatibility, the 20 % Gd-doping enhances the electron conductivity and lowers the temperature formation of the Ce^{4+}/Ce^{3+} pair of the fluorite in reducing atmospheres[4,20,21] increasing in this way the separation performances of the final membrane. Thus, BCZY-GDC mixture were further investigated as the most promising system for the production of asymmetric cer-cer membranes.

5.2.3 Sinterability of the BCZY-GDC composite

Having selected the cer-cer formulation, it was necessary to assess the physical properties of the powder to be used. Similar sintering behavior of the phases are in fact mandatory to avoid the formation of stresses and to obtain a crack free asymmetrical membrane.
In order to match the sintering behavior of the BCZY powder with the one associated to the GDC phase, three different GDC powders with different SSA (specific surface area) values were investigated.
Powders with high SSA are then preferred as densification occurs at lower temperatures, facilitating the process. In addition, BCZY powder with SSA higher than the one used is difficult to obtain industrially because of issues related to the stoichiometry control. Figure Table 1.3 and Figure 1.13 show that both the shrinkage and the T_{onset} of GDC powders with the highest SSA values were not

compatible with the ones registered for the BCZY systems in the temperatures range considered.

Table 1.3 SSA values provided by the powders suppliers and T_{onset} calculated from the shrinkage curves, for each starting material and for the BCZY-GDC composite.

	SSA (m^2/g)	**T_{onset} (°C)**
BCZY	12.2	1280
GDC 20	6.8	1120
GDC 20M	37	650
GDC 20N	220	210
BCZY + GDC TC	/	1390

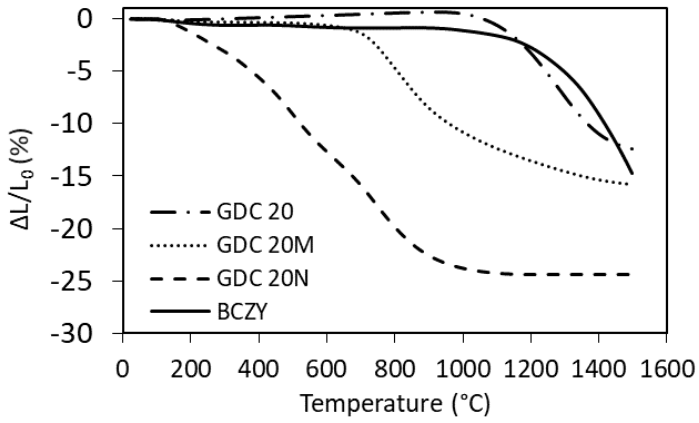

Figure 1.13 Sintering behavior of the starting materials and of the BCZY-GDC composite.

On the other hand, only the GDC with the lowest SSA value shows a sintering behavior comparable to the one of BCZY. Its sintering curve and the T_{onset} value of the composite material resulted in fact very similar to the one of BCZY. For this reason, GDC 20 was selected to be coupled with fine BCZY to produce the dense composite membrane layer.

The thermomechanical results however suggested also that a complete densification of the cer-cer membrane would be very difficult at $T \leq 1500$°C, due to the well-known refractory behavior of the BCZY system.

Aiming at lowering the sintering temperature, a detailed study on its sinterability was performed. High sintering temperatures are not only detrimental as a consequence of the high cost of the process but can also lead to increased barium oxide evaporation and abnormal and discontinuous grain growth that are negative for both electrical and mechanical properties[1].

A common method to improve the sintering behavior of a ceramic material is the introduction of a sintering aid. As anticipated in Chapter 2, ZnO is the most common used for $BaCeO_3$-$BaZrO_3$ based materials[1,22,23] and it was demonstrated to be effective also for the sintering of GDC systems[24].

Commercial ZnO nanopowder (Sigma Aldrich) was therefore added to the BCZY-GDC suspension following the standard procedure reported in Figure 1.14.

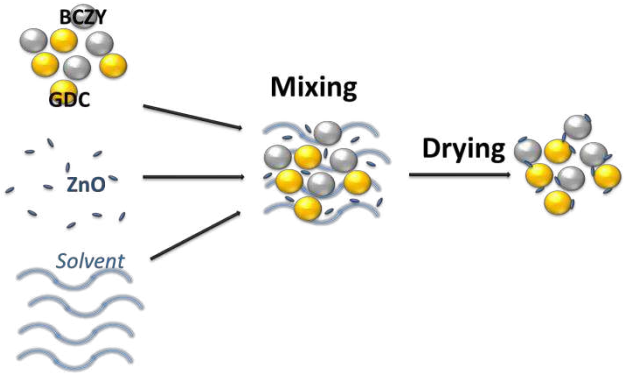

Figure 1.14 Scheme of the approach followed for the incorporation of the sintering aid to the BCZY-GDC system.

This conventional route was used to obtain a well-controlled ZnO dispersion step in order to avoid aggregates and/or non-homogeneities into the final sintered samples.

Based on the literature reported in Table 1.4, the 0.8 wt.% of ZnO was selected as the optimal amount of sintering aid for the BCZY-GDC.

Table 1.4 Sinterability studies reported in the literature for zirconate-based and GDC systems.

Material	ZnO amount	$T_{sintering}$ with ZnO (°C)	$T_{sintering}$ without ZnO (°C)	Relative density with ZnO (%)	Relative density without ZnO (%)	Ref.
$BaZr_{0.8}Y_{0.2}O_3$	4 mol. %	1300	1325	96	68	[25]
$BaZr_{0.85}Y_{0.15}O_3$	4 mol. %	1300	1300	95	60	[26]
$SrZr_{0.9}Y_{0.1}O_{2.95}$	2 mol. %	1350	1350	95	85	[27]
	3 mol. %			96		
	4 mol. %			97		
	5 mol. %			95		
$BaCe_{0.5}Zr_{0.3}Y_{0.2}O_{3-\delta}$	2 mol. %	1300	1300	97	66	[28]
	4 mol. %	1320	1320	95	57	[22]
$Ba_{1.03}Ce_{0.5}Zr_{0.4}Y_{0.1}O_{3-\delta}$	0.5 wt. %	1250	1250	96	50	[29]
	1% wt. %	1150	1250		50	
$Ce_{0.8}Gd_{0.2}O_{1.9}$	1 mol. %	1200	1300		95	[24]

Figure 1.15 reports the results of the thermomechanical analyses performed onto both the single phases (BCZY or GDC) and the composite BCZY-GDC additivated with 0.8 wt% of ZnO.

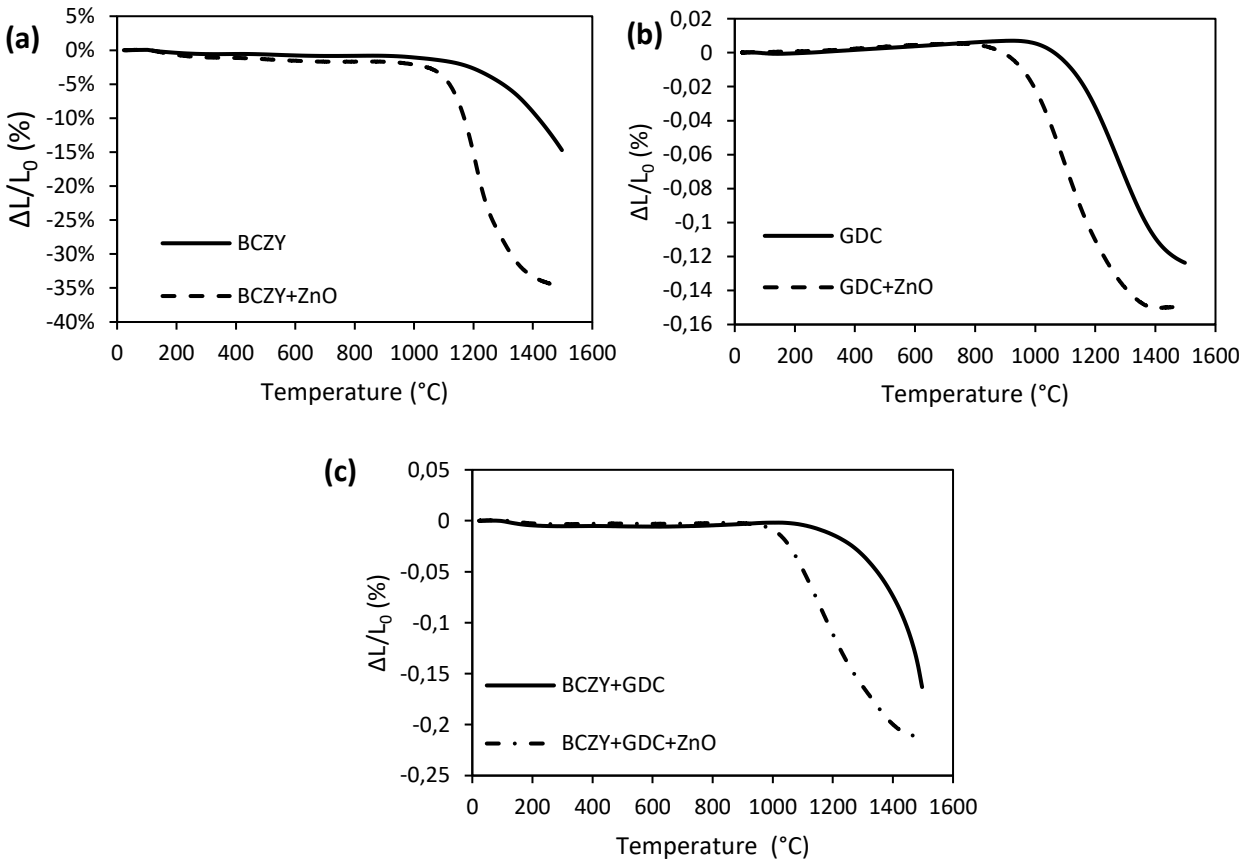

Figure 1.15 Sintering behavior of (a) the single BCZY, (b) GDC and (c) of the BCZY-GDC mixture additivated with ZnO.

Table 1.4 Influence of the sintering aid to the T_{onset} and total shrinkage of the different systems calculated from the shrinkage curves reported in Figure 1.15.

	T_{onset} (°C)	**Shrinkage (%)**
GDC	1120	12.37
GDC+ZnO	950	15.12
BCZY	1380	14.71
BCZY+ZnO	1130	34.81
BCZY+GDC	1390	16.31
BCZY+GDC+ZnO	1030	21.16

For the BCZY system (Figure 1.15 (a)), the direct incorporation of 4 mol% of nanometric ZnO decreased its T_{onset} by 250°C (Table 5). On the other hand, the addition of 1 mol% of sintering aid to the GDC system leads to decrease the T_{onset}

of 170°C and to increase the shrinkage level (Table 1.4). The sintering behavior of the BCZY-GDC composite is more similar to the GDC one. The method considered allowed to decrease the T_{onset} of more than 350°C with an increase of the shrinkage value.

The effect of ZnO on the density and microstructure of BCZY-GDC was considered on pressed pellets sintered at 1400°C for 4h. Archimedes' density values above 96.8 ± 0.6% were obtained while the micrograph of fresh and polished surface shown the presence of a low level of porosity with the good distribution of BCZY (finer) and GDC (coarser) grains, therefore with characteristic suitable for application in gas separation.

Figure 1.16 Picture of the BCZY-GDC pellet sintered with ZnO as sintering aid at 1400°C for four hours.

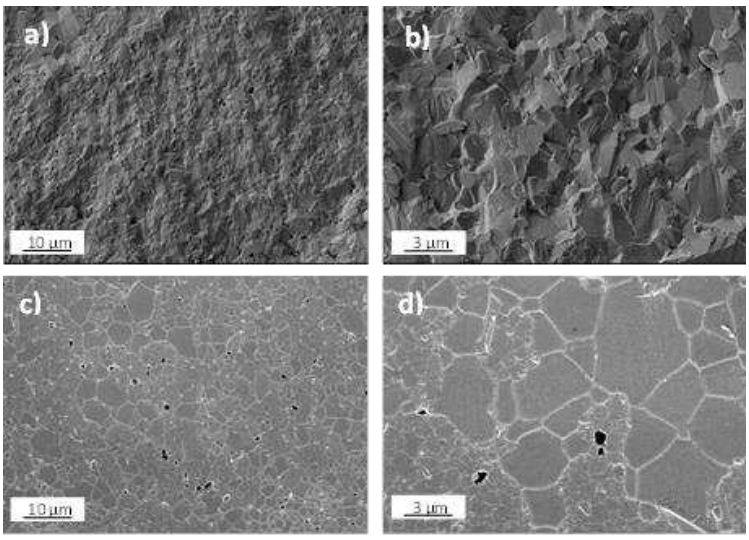

Figure 1.17 SEM micrographs of a-b) the fresh fracture surfaces and c-d) polished surfaces of the BCZY-GDC pellets additivated with ZnO. The polished surfaces thermally etched at 1250°C x 15 min to underline the grain boundaries.

5.3 Tape-casting and Lamination

Having assessed the compatibility between the BCZY and the GDC materials, green ceramic sheets were obtained through tape casting technique. As previously explained, the tape-casting is a well-established technique to obtain large and planar ceramic sheets with thickness from 20 μm to 1.5 mm where the formulation of the slurry plays a key role in obtaining planar and defect free samples. On the other hand, engineered architectures such as asymmetric ones and multilaminates can be easily obtained with this technique by laminating green tapes of different thickness and composition. The lamination process plays a key role on the properties of these final products, since defects induced in this step affect the final shape and microstructure of the membrane after the thermal treatments. If the layers hardly laminate together, delamination may occur while, if the tapes are too soft, the sample may deform during lamination and residual stresses may tension the system causing warping or even cracking during the organics burnout. The lamination parameters (time, pressure, and temperature) must therefore be tuned in order to obtain a fully laminated multilayer without mass flow.

This chapter reports activity devoted to the production by tape casting of the layers for the formation of the asymmetric membrane. It is divided in two parts: one relative to the production of the two different green tapes (membrane and support) and the other on the study and optimization of the lamination process of the green tapes previously produced to obtain an asymmetric structure.

Two slurry formulations were obtained, one for the thin membrane and the other for the porous support. The first contained BCZY, GDC and ZnO as a result of the study reported in the previous paragraph; the one of the support layer was previously optimized in the ISTEC laboratories. The processes and materials used for the tape casting are reported in Chapter 4.

The work on the lamination is dominated by the activity done of the identification of the right process parameter using the Dynamic Mechanical Analysis (DMA). This analysis can be used to measure the thermomechanical properties of the green tapes and was used to understand how these properties are related to the mutual interaction between ceramic particles, starch powder, binder chains and plasticizer

and analyse in the systems. The green tape plasticity, elasticity, stiffness and toughness are in fact strongly affected by its components. On the other hand, such properties are very important for the further processing of the casted tapes since they have to show sufficient mechanical properties to be handled, punched, stacked and laminated to obtain the green multilayer structure. As already explained in Chapter 3, tensile testing usually measures these properties, here performed with a DMA equipment. DMA was chosen thanks to the possibility of studying the tape's mechanical properties as a function of the temperature applying static or dynamic loadings. In addition, different clamps could be used to study the properties of samples with different geometries. In this sense, particular attention was paid to the moduli behavior as a function of temperature obtaining useful information for the lamination process.

5.3.1 *Tapes production*

BCZY-GDC Membrane Layer

The slurry preparation for the thin membrane layer followed the procedure described in Chapter 4. Table 2.1 reports the slurry formulation used to obtain a 20 μm-thick defect-free tape (Figure 2.1).

Table 2.1 Slurry composition for the membrane layer.

Ingredients	BCZY	GDC	ZnO	Solvent	Dispersant	Binder	Plasticizer
(vol.%)	*5.67*	*5.67*	*0.11*	*70.24*	*1.22*	*8.62*	*8.47*

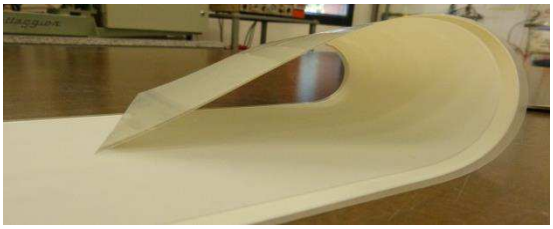

Figure 2.1 Picture of the dried BCZY-GDC membrane tape.

The tape contained as ceramic fraction the BCZY, GDC and ZnO (0.8 w. %) to obtain the dense cer-cer layer after thermal treatment.

BCZY Support Layer

The green support layer has to display different properties: it must be flexible, but also sufficiently strong to bear further processing, such as handling, punching and lamination. In addition, to be useful as support layer in a gas separation membrane it has to ensure a sufficient degree of porosity after thermal treatment.

The support green tape was obtained following the process optimized in previous activities[30].

Table 2.2 Slurry composition for the BCZY support layer.

Ingredients	**BCZY**	**Rice Starch**	**Solvent**	**Dispersant**	**Binder**	**Plasticizer**
(vol.%)	*16.13*	*6.43*	*61.83*	*0.52*	*10.29*	*11.29*

The resulted green tape was defect-free, and it exhibited good flexibility.

5.3.2 Lamination Process

Having obtained both support and memrbaen green tapes, circular samples were obtained, staked and laminated together as described in Chapter 4. However, difficulties in the lamination step optimization appeared, as the optimal parameters were difficult to establish. Therefore, the analysis of the mechanical behavior of green tapes as a function of temperature have been performed aiming at a better understanding of the link between the tape formulation and its thermomechanical properties. Then, experiments devoted to mimic the lamination process were done to individuate the parameters to obtain well-laminated multilayers.

Thermomechanical Characterization

Despite the growing interest on advanced ceramics shaping, only few studies have been performed on the influence of the green tape formulation and its mechanical properties, evaluating also the contribution of the organic pore former.
The mechanical properties of BCZY tapes were evaluated studying the effect of the **ceramic and pore former (rice starch) load** and **starch rice addition**, since they modify the green density of green tapes and consequently their mechanical properties. These variables are also the main one used to govern the final porosity of the ceramic layers, fundamental property for the membranes performances
To verify the blocking effect of the ceramic particles on the binder's macromolecules, tapes with different BCZY content were tested. The data collected were then compared with the results obtained with the tape with the rice starch as organic pore former (40 vol. % respect to the ceramic phase). Finally, also the influence of the amount of rice starch on the thermomechanical properties of the tape was assessed.

Four formulations with different ceramic content and one with the presence of starch were taken into account (Table 2.3):

1. BCZY_15: ceramic content 0.15 vol. %;
2. BCZY_25: ceramic content 0.25 vol. %;
3. BCZY_35: ceramic content 0.35 vol. %;
4. BCZY_45: ceramic content 0.45 vol. %;
5. BCZY_25RS: ceramic content 0.25 vol. % with rice starch (40 vol. % related to the powder).

The ceramic content was increased lowering the amount of the organics (binder + plasticizer) but keeping constant the binder/plasticizer ratio and the amount of dispersant. The rice starch-containing tape was obtained substituting the amount of the organics (binder + plasticizer) with rice starch

Table 2.3 Volume composition of the green tapes studied for the evaluation of the effect of the ceramic load and rice starch on the tape's properties.

Tape	% V_{powder}	% $V_{dispersant}$	% V_{binder}	% $V_{plasticizer}$	% $V_{rice\ starch}$
BCZY_15	15,00	0,81	40,15	44,05	-
BCZY_25	25,27	1,36	34,98	38,38	-
BCZY_25RS	25,27	1,36	26,95	29,57	16,84
BCZY_35	35,00	1,89	30,09	33,02	-
BCZY_45	45,00	2,43	25,07	27,50	-

As expected the formulation highly affected the physical and morphological aspect of the tapes. Tape BCZY_15 after drying showed an organic phase segregation at the surface (Figure 2.2).

Figure 2.2 Picture of the BCZY_15 tape after drying.

This may be provoked by an excess of binder and/or plasticizer respect to the ceramic particle which led to the formation of areas with the only organic phase. The segregation of organics phases can lead to defects formation (such as delamination) after sintering as a consequence of non-homogeneous distribution of the ceramic particles in the sample's body after the organics burnout.

On the other hand, the tape with the minor amount of binder and plasticizer BCZY_45 was completely fractured after drying (Figure 2.3), due to an insufficient cohesion between ceramic particles given by the low binder content.

Figure 2.3 Picture of the BCZY_45 tape after drying.

Only the formulations BCZY_25, BCZY_25AR and BCZY_35 were crack free and they did not show phase separation (Figure 2.4).

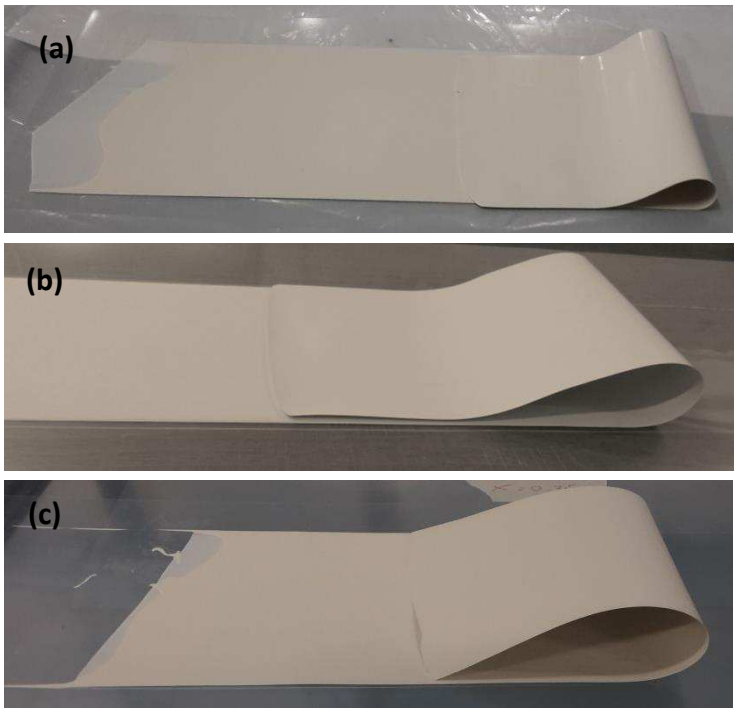

Figure 2.4 Pictures of BCZY_25 (a), BCZY_25RS (b) and BCZY_35 (c) tapes after drying.

All the tapes, except BCZY_45, were then tested. To avoid any aging effect, all the tapes were stocked in the same conditions for the same period of time before tests: away from light sources after three weeks of being casted. Dog-bone samples were then obtained by punching the different tapes and stress-strain curves were collected using the film-tension clamp. The results showed that the tape formulation highly

affected various aspects of the mechanical properties: the elastic modulus, the elongation and stress to break (Figure 2.5 and Table 2.4).

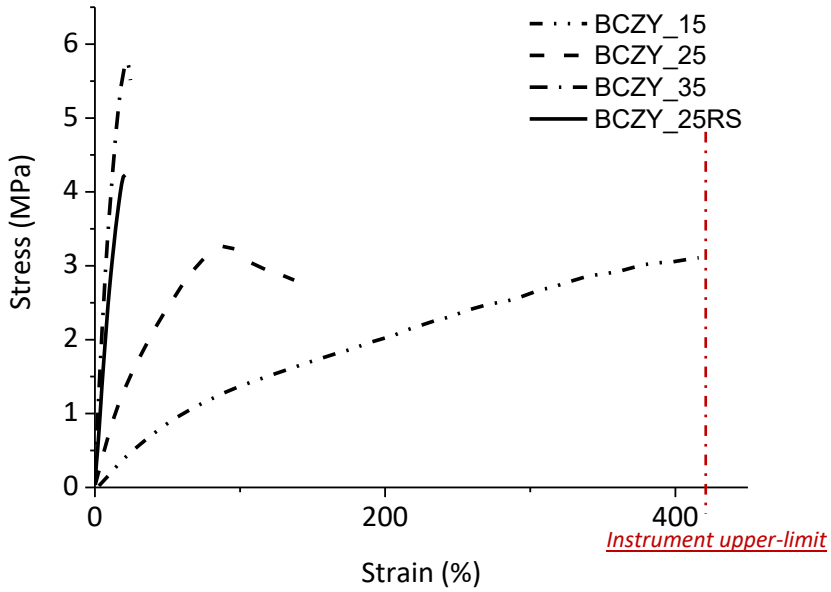

Figure 2.5 Stress-strain curves of the BCZY tapes with different ceramic load and with the rice starch as pore former.

Table 2.4 Stress to break **(σ max,** MPa) and elongation to break (%) for the BCZY tapes with different ceramic load and with the rice starch as pore former obtained by the stress-strain curves.

BCZY (%)	**R.S. (%)**	**σ_{max} (MPa)**	**Elongation to break (%)**	**Elastic Modulus (MPa)**
15	-	n.a.	> 400	0,9 ± 0,2
25	-	3,4 ± 0,2	133,9 ± 3,1	6,7 ± 0,6
35	-	4,1 ± 0,3	22,1 ± 1,2	24,3 ± 2,5
25	40	5,7 ± 0,1	23,6 ± 1,2	42,5 ± 2,0

The ceramic load highly affected the mechanical properties through two synergic effects:

- The ceramic particles block the free elongation of the polymeric net, thus the higher the ceramic content, the higher the elastic modulus;

- The binder content is strictly related to the ceramic fraction amount: the higher the ceramic fraction, the lower the binder content. This affected the elongation to break, which decreased as the binder content decreased. The binder provides strength to the green tapes after evaporation of the solvent through organic bridges between the ceramic particles. When there is not enough binder, the resulting green tape developed only the elastic portion of the stress-strain curve.

The tape BCZY_15 reached the upper limit of the instrument (vertical red line in Figure 5) without reaching the stress at break. This indicates that the solid content in the tape was not as high to block the macromolecular stretching of the binder.
The results showed that, keeping constant the solid content, the introduction of an organic pore former in the tape increased its elastic modulus. This may be due to two reasons: i) the blocking effect of the rice starch on the mobility of the B98 polymeric chains and ii) the reduced content of the binder which results in a more rigid net. This was confirmed by the results showed in Figure 2.6, where the elastic modulus is plotted as a function of the B98 content.

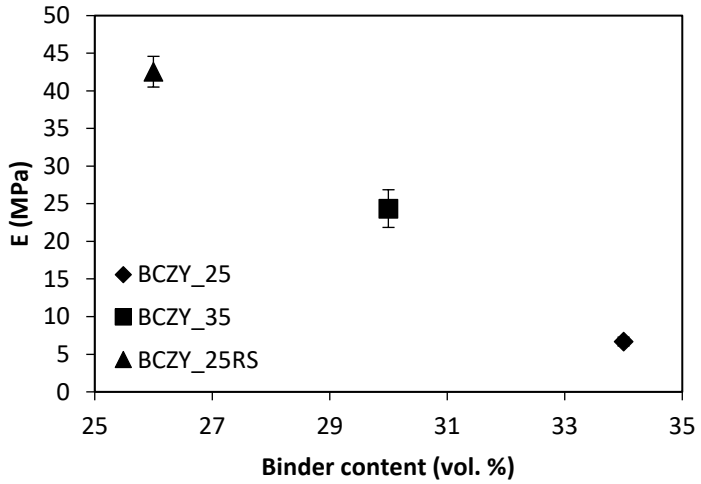

Figure 2.6 Elastic modulus(E) values as a function of the binder content. Standard deviations are also reported.

The elastic modulus linearly decreased with the binder content, confirming the ceramic particle-like blocking effect of the rice starch that at room temperature

interacts with the binder chains like the ceramic particles. Considering the assumption, the volume of interacting particles in BCZY_25RS is equal to:

$$V_{R.S.} + V_{BCZY\_25} = 16.84 + 25.27 = 41.41 \text{ (vol. \%)}$$

Were, $V_{R.S.}$ is the volume of the rice starch and V_{BCZY_25} is the volume of the ceramic powder. The total volume of interacting particles is higher than the one of the BCZY_35 tape, in agreement with the trend showed in Figure 2.6.

In literature, one of the parameter used for estimating the tape toughness is the tensile strength/elastic modulus ratio (σ_{max}/E): a value is an indication of tapes with good crack resistance.

Figure 2.7 graphs the σ_{max}/E values as a function of the binder content for the systems studied (with the exception the BCZY_15 for which, as abovementioned, was not possible to detect the σ_{max}). The results show that increasing the binder content, the σ_{max}/E increased. The tape with rice starch had a ratio close to the tape without the pore former with higher ceramic load. This means that, even if the binder content of the BCZY_25RS tape is lower than the BCZY_35 one, the fracture toughness is mainly the same.

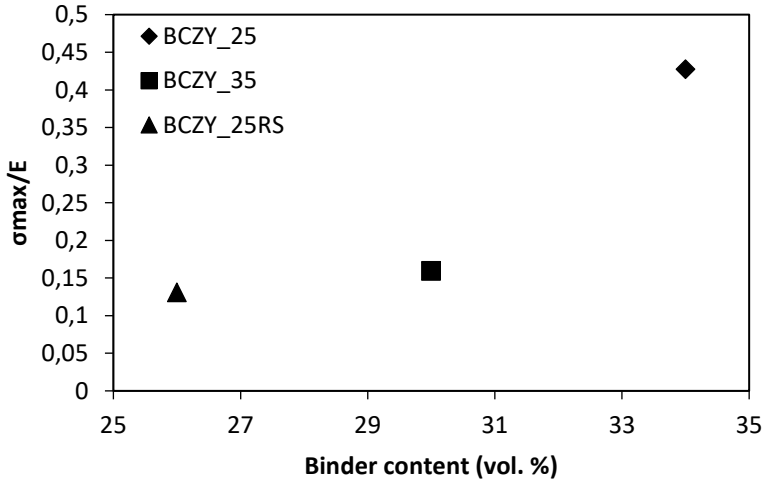

Figure 2.7 Tensile stress/E ratio (σ_{max}/E) values as a function of the binder content. The standard deviation indicators are smaller than the symbols.

All the previous tests confirmed how at room temperature the organic pore former increased the elastic modulus of the tape acting like a ceramic fraction.

In principle, the rice starch is an organic polymer, therefore its thermomechanical properties should vary with the temperature, i.e. during the lamination process. To study the effect of the temperature on the behavior of the tape with pore former, rectangular samples were cut from the different tapes and a sinusoidal stress was applied increasing the temperature.

The dynamic mechanical properties of the tapes are shown in Figure 2. 8 in terms of storage modulus (black lines, E'), loss modulus (red lines, E'') and the tanδ value (blue line, E''/E') between room temperature and 100°C.

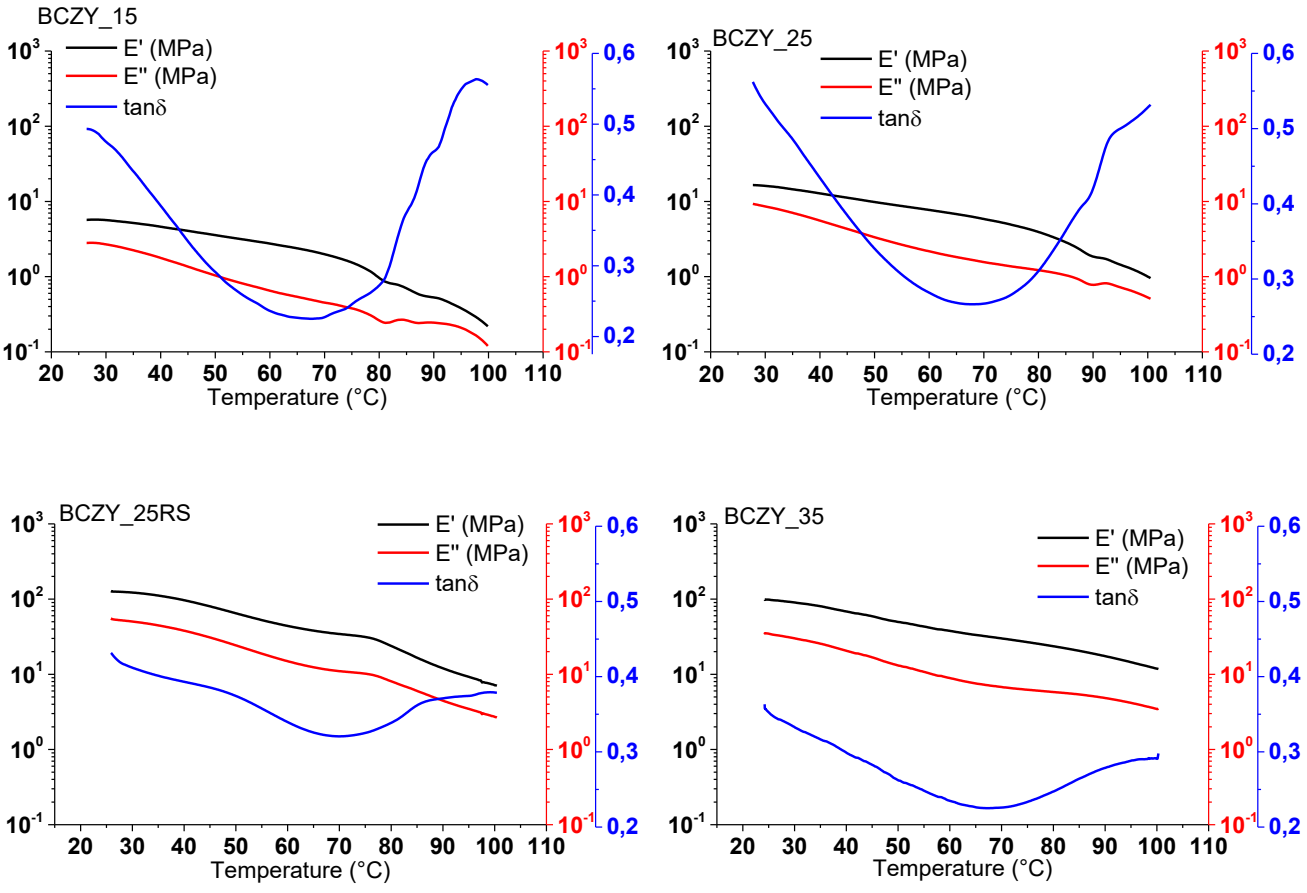

Figure 2.8 Mechanical properties as a function of temperature of the four tapes BCZY_15, BCZY_25; BCZY_25RS and BCZY_35.

E' values decreased in the whole temperature range for all the tapes. No tanδ peaks, corresponding to the B98 glass transition (T_g) were found in the range of temperature considered. T_g is the temperature that determines the reversible transition from a hard and relatively brittle "glassy" state into a viscous or rubbery one as the temperature is increased. This means that the T_g of all tapes is above room temperature, as a consequence of the high amount of plasticizer used. In fact, the tape could be easily bended and handled at room temperature, but also easily laminated with a little increase of temperature.

Figure 2.9 compares the different E' values: increasing the ceramic loading, E' increases, due to the blocking effect of the ceramic particle on the chain mobility of the B98.

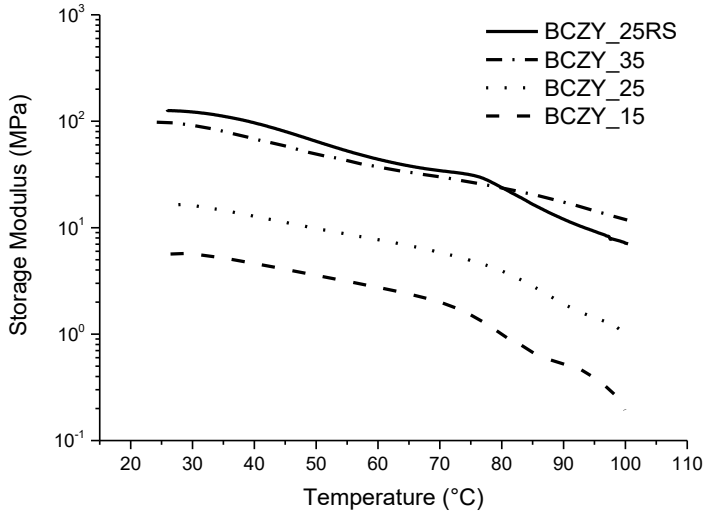

Figure 2.9 Storage modulus (E') development with the temperature of the four tapes BCZY_15, BCZY_25; BCZY_25RS and BCZY_35.

The higher E' value of the tape BCZY_25RS than BCZY_25 can be explained by the blocking effect of the starch similar to the ceramic particles. The tape BCZY_25RS has also an E' higher than BCZY_35 at low temperatures, but at 60°C the E' of BCZY_35 becomes higher than the E' of BCZY_25RS. Rice starch then has a ceramic particle-like blocking effect on the chain mobility at low temperature,

but this effect disappears increasing the temperature because of the polymeric nature of the pore former.

Creep tests also assessed the temperature-dependence of the rice starch blocking effect, mounting rectangular samples on the clamp for films and then measuring the strain while a static load was applied at a certain temperature. As explained in Chapter 4 through the creep curve is possible to obtain the values of viscosity of the sample as a function of the temperature (Figure 2.10).

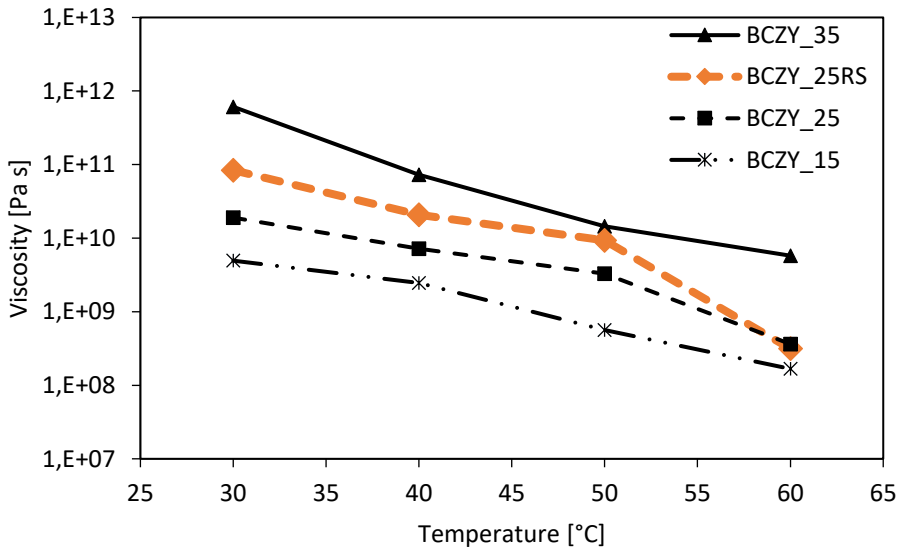

Figure 2.10 Temperature dependence of the viscosity for the four tapes BCZY_15, BCZY_25; BCZY_25RS and BCZY_35.

As it can be seen, the curve of BCZY_25RS is characterized by an abrupt decrease in viscosity between 50°C and 60°C, reaching the same value of the tape with the same ceramic load, but without rice starch.

This shows that above 50°C the network is free to rearrange itself under an applied load because of the inhibition of the blocking effect of the starch.

The temperature-dependence of the organic pore filler is therefore an important parameter that should be considered to produce porous multilaminates. The amount of pore former is strictly linked to the final porosity and mechanical properties of the sintered sample.

In the next part of chapter, the effect of the amount of pore former on the mechanical properties will be presented and discussed. In order to assess its real influence on the properties of the green tape, three other tapes were produce changing the amount of the rice starch in the system (Table 2.5). The rice starch content was increased lowering the amount of the organics (binder + plasticizer) but keeping constant the binder/plasticizer ratio as well as the ceramic loading and the amount of dispersant.

Table 2.5 Formulation of the dried green tapes with different amounts of rice starch as pore former.

Tape	% V_{powder}	% $V_{dispersant}$	% V_{binder}	% $V_{plasticizer}$	% $V_{rice\ starch}$
BCZY_35	25,27	1,36	28,49	31,26	13,62
BCZY_40	25,27	1,36	26,95	29,57	16,84
BCZY_45	25,27	1,36	25,12	27,56	20,68
BCZY_50	25,27	1,36	22,93	25,16	25,27

Note that the BCZY_40 is the tape BCZY_25RS re-named. The change of name was made to highlight the amount of rice starch in the new composition and therefore help in the following discussion.

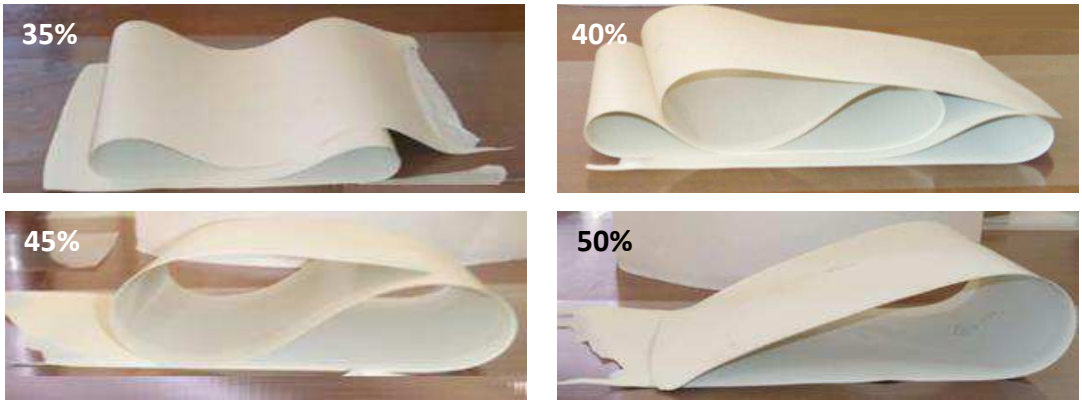

Figure 2.11 Pictures of the tapes with different amount of pore former. The correspondent Formulations are reported in Table 2.3.

Figure 2.11 reports the pictures of the tapes with the formulations reported in Table 2.3: it is visually evident the increase in the tape stiffness due to an increase amount of rice starch. All the tapes were defect-free except BCZY_50, which presented a

long central crack linked to the low binder content of this sample, that allowed nonetheless the following analyses.

Dog-bone samples were obtained from the different tapes and stress-strain curves were collected using the film-tension clamp. The results showed that the amount of rice starch formulation affected the elastic modulus, the elongation and stress to break (Figure 2.12 and Table 2.6).

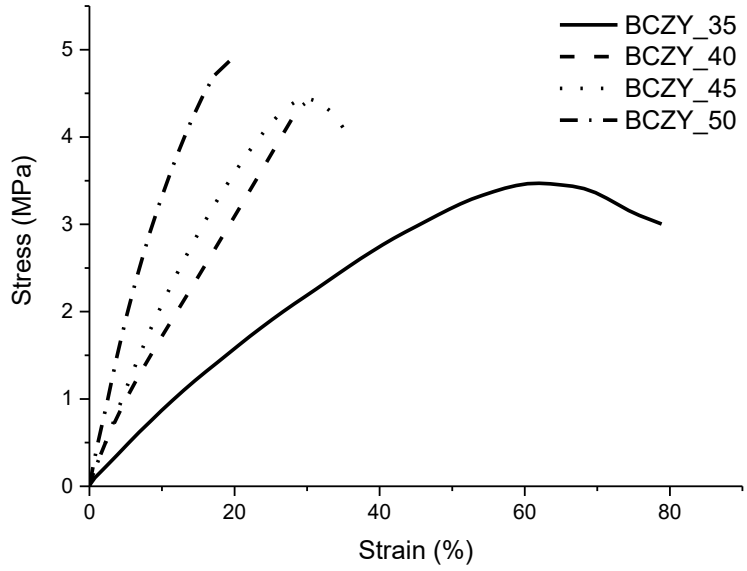

Figure 2.12 Stress-strain curves of the BCZY tapes with different rice starch contents.

Table 2.6 Elongation to break and maximum stress as a function of the RS content.

Tape	σ_{max} (MPa)	Elastic modulus (MPa)	Elongation to break (%)
BCZY_35	3,5 ± 0,1	8,9 ± 0,8	76,7 ± 5,7
BCZY_40	4,2 ± 0,1	20,5 ± 1,8	58,6 ± 5,9
BCZY_45	4,3 ± 0,1	21,7 ± 0,6	33,8 ± 1,5
BCZY_50	5 ± 0,1	40,4 ± 4,2	21,2 ± 1,5

Being the solid content the same, the increase of the organic pore former increased the elastic modulus of the tape. This is in agreement with results displayed in Figure 2.5, and may be due to the same two synergic effects: i) the blocking effect of the rice starch on the mobility of the B98 polymeric chains and ii) the lower content of the binder, which results, as explained above, in a more rigid net. This is confirmed by the results showed in Figure 2.13, were elastic moduli decreased increasing the binder content.

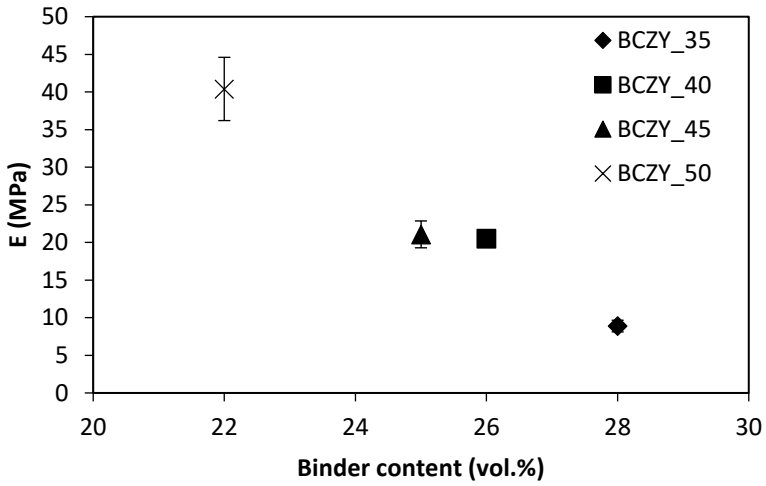

Figure 2.13 Elastic modulus(E) values as a function of the binder content. Standard deviations are also reported.

Figure 2.14 shows the σ_{max}/E values as a function of the binder content for the tapes with different amount of pore former.

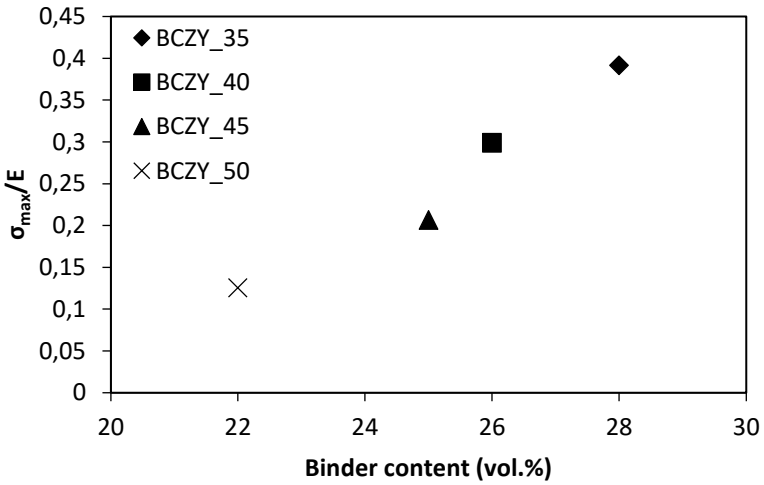

Figure 2.14 (σ_{max}/E) values as a function of the binder content. The standard deviation indicators are smaller than the symbols.

Results show the same trend previously seen for the ceramic load study (Figure 7): increasing the binder content, the σ_{max}/E increased. As already explained, high ratio values mean high fracture toughness. In fact, the tape BCZY_50 was cracked, and it led to the lower σ_{max}/E value detected.

Also in this case, the effect of the temperature was studied applying a sinusoidal stress on rectangular samples of the different compositions. Figure 2.15 shows the temperature-dependence of the storage moduli.

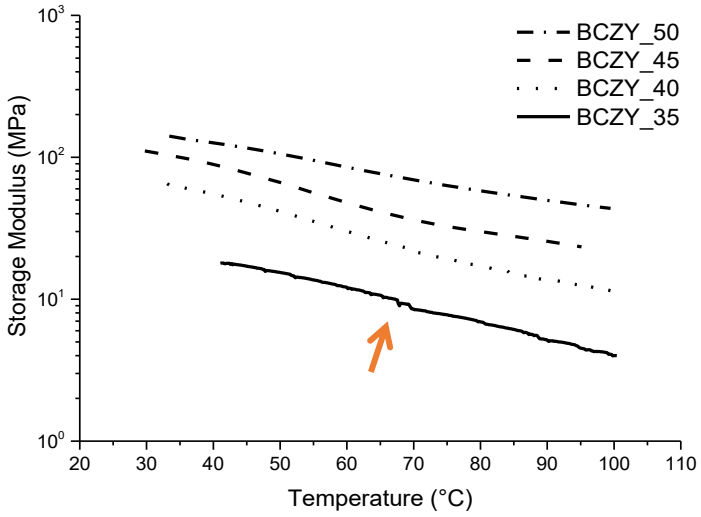

Figure 2.15 Storage moduli (E') of the different tapes as a function of temperature. The red arrow indicates the micro-fracture of the BCZY_35 tape during the test.

The trend obtained with the dynamic application load agrees with the results previously discussed for the tensile tests. The discontinuity of the E' curve at roughly 68°C for BCZY_35 is due to micro-cracking of the sample during test. In addition, the higher the rice starch content, the more E' varies with the temperature. For example, BCZY_50 had a E' value of 131 MPa at 40°C which decreased to 43 MPa at 100°C; while the E' of the BCZY_40 decreased from 57 MPa to 11 MPa in the same temperature range (note that the x-scale of Figure 2.15 is logarithmic).
As explained at the beginning of this paragraph, the optimization of the lamination parameters is extremely important in order to obtain a multilayer perfectly laminated without mass loss. In principle, the viscosity of the tape could give information about the mobility of the macromolecular chains, responsible for the tapes lamination. Therefore, viscosity measurements at different temperatures are useful to compare the behavior of tapes with different formulations. Figure 2.16 and Table 2.7 report viscosity values obtained by creep tests.

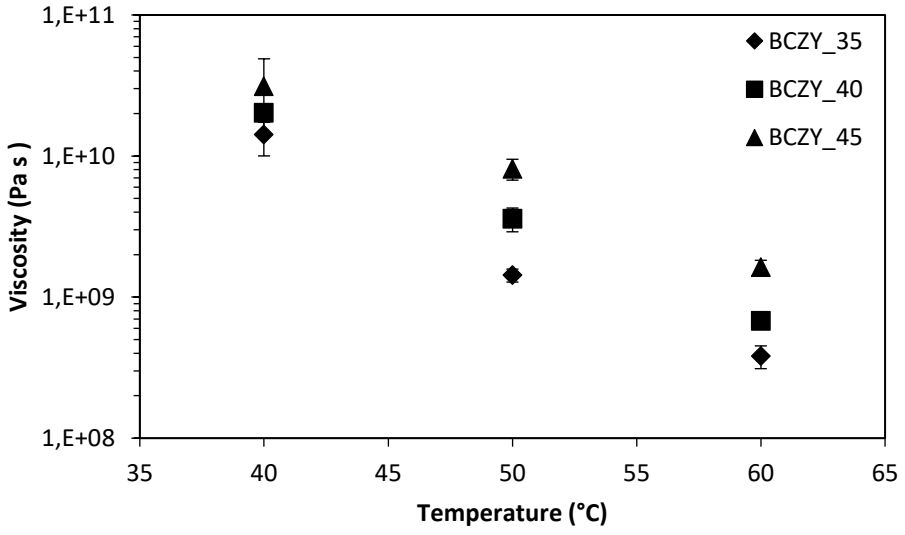

Figure 2.16 Temperature dependence of the viscosity values of the four tapes BCZY_35, BCZY_40 and BCZY_45. Standard deviations are reported.

Table 2.7 Viscosities values obtained from creep tests at different temperatures.

	η [Pa· s] · 10^9		
Temperature	**40°C**	**50°C**	**60°C**
BCZY_35	14,2 ± 4,1	1,4 ± 0,2	0,4 ± 0,1
BCZY_40	20,2 ± 2,9	2,6 ± 0,7	0,7 ± 0,1
BCZY_45	31,3 ± 17,6	8,1 ± 1,4	1,6 ± 0,2

Viscosity values had the same trend of the storage modulus (Figure 2.15): the higher the starch content the higher the viscosity. Data reported in Table 2.5 show that increasing the temperature, the viscosity values of the three systems differ more and more. This result highlights the importance of the lamination process optimization. To evaluate the temperature dependence of each tape, data plotted in Figure 2.16 were fitted using a linear relationship and slope values are reported in Table 2.8.

Table 2.8 Linear fitting results of data plotted in Figure 2.16.

	Slope	**R^2**
BCZY_35	-0,0785	0,9532
BCZY_40	-0,0737	0,9998
BCZY_45	-0,0641	0,9949

In particular, the higher the rice starch content, the more the viscosity value varies with the temperature. In fact, slope values of linear equations are lower for tapes with higher starch content, indicating a less temperature-dependence for tapes with high starch content in the investigate range.

This result confirms that the pore former content considerably affects the thermomechanical behaviour of the material, with serious implications on the lamination process.

Mimic of the Lamination Process

The optimization of the lamination parameters is a key parameter for the production of a multilayer. The previous results allowed to obtain a useful correlation between composition and viscosity as a function of temperature. To directly correlate these results with the actual lamination process, a new experimental set-up was designed: two rectangular samples cut off from the tapes were stacked and inserted between the plates of the compression clamp of the DMA. This new arrangement was used to directly measure the bilayer deformation and viscosity under a given pressure and temperature, showing the optimal lamination conditions.

Figure 2.17 correlates the strain and the viscosity of the two stacked layers of the BCZY_35 tape with the temperature. Optical microscope images are also reported to assess the lamination condition after each test. As shown by the change in behavior of the curves, the lamination starts at 55°C with a maximum strain during the test of 3%. At 60°C the pressure applied induced a definite mass flow with consequent sample's thickness reduction. Between 55 and 60°C there is an important increase of the creep compliance, which indicates that less force is needed to deform the material, i.e. the lamination is effective.

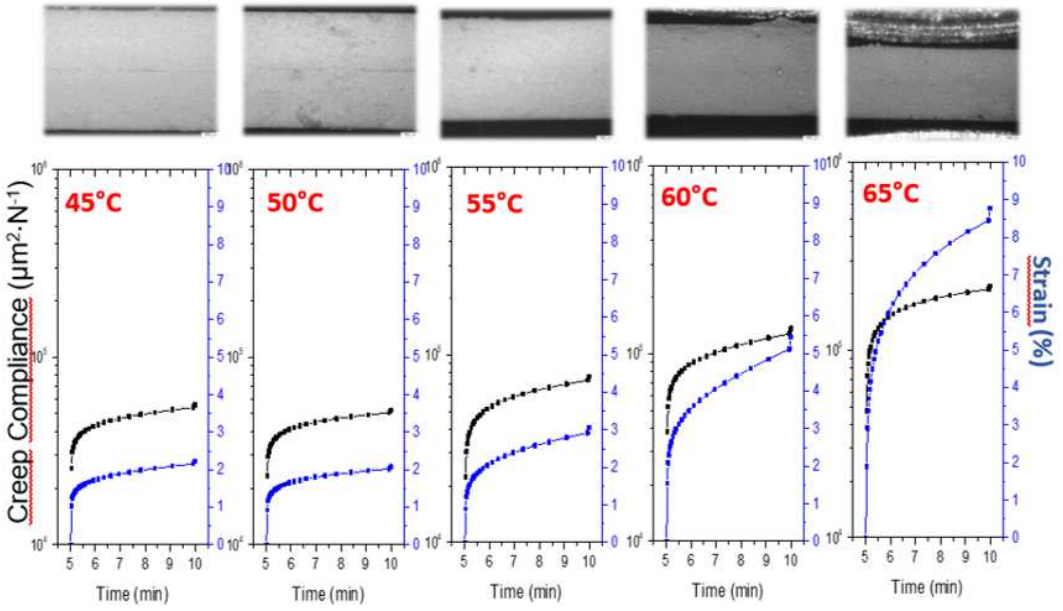

Figure 2.17 Creep compliance and stain values at different temperatures of the tape BCZY_35. Optical microscope images of the sample after each test are reported above.

The lamination temperature increased for BCZY_40 (60°C, Figure 2.18) BCZY_45 (70°C, Figure 2.19), and BCZY_50 (75°C, Figure 2.20). This is perfectly explainable on the basis of the assumptions drawn previously related to the amount of organics inside the different systems.

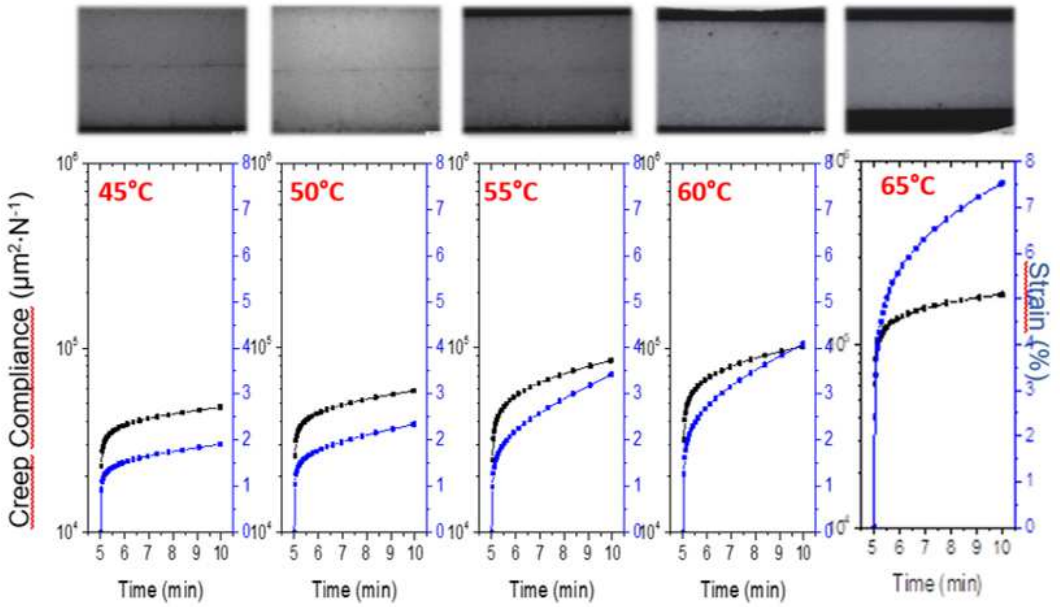

Figure 2.18 Creep compliance and stain values at different temperatures of the tape BCZY_40. Optical microscope images of the sample after each test are reported above.

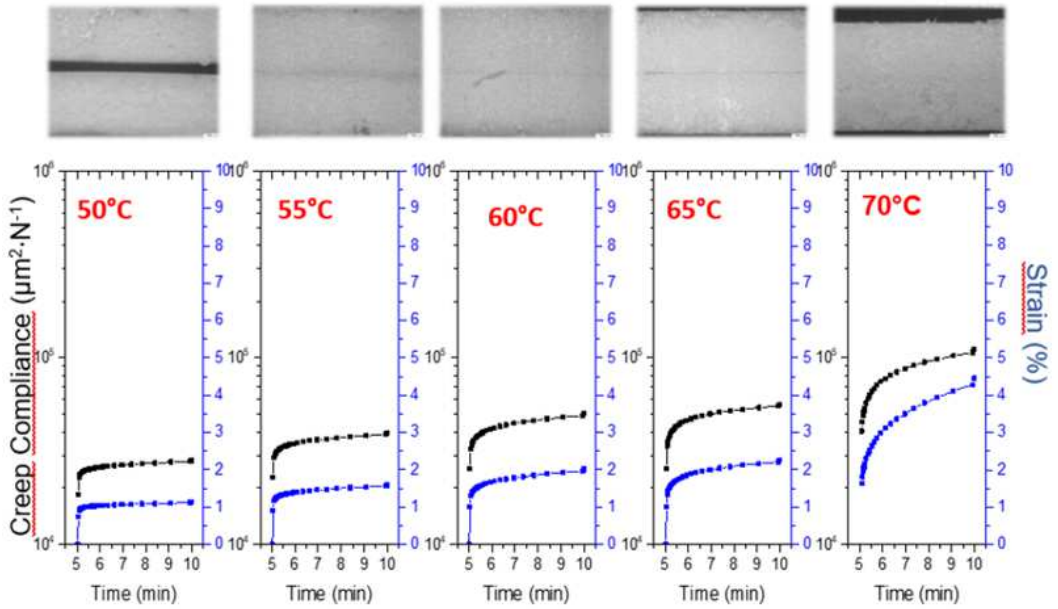

Figure 2.19 Creep compliance and stain values at different temperatures of the tape BCZY_45. Optical microscope images of the sample after each test are reported above.

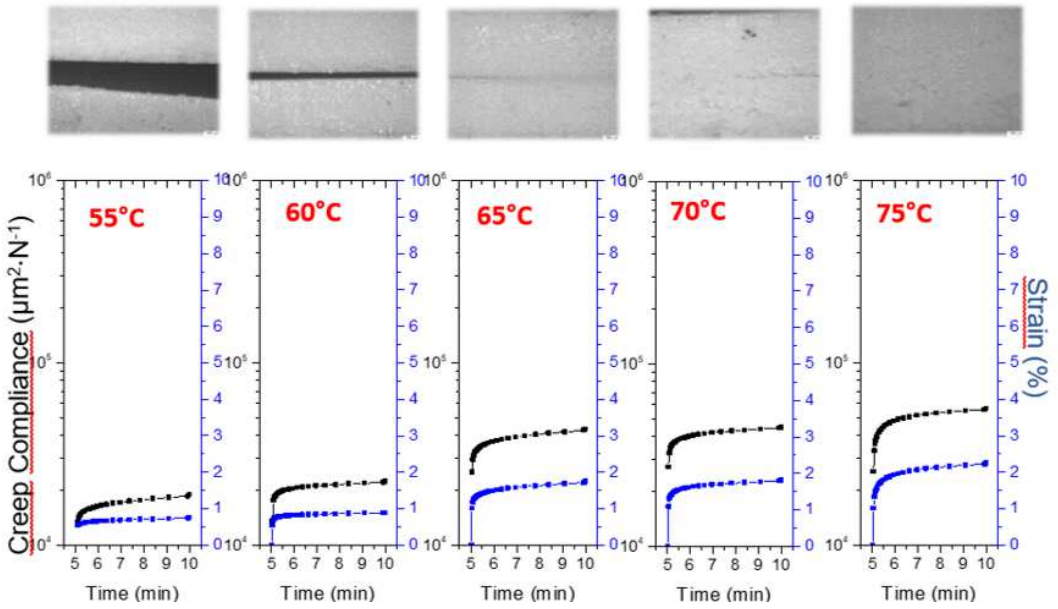

Figure 2.20 Creep compliance and stain values at different temperatures of the tape BCZY_50. Optical microscope images of the sample after each test are reported above.

As expected the trend of viscosity followed the one of the shrinkage (Figure 2.21): canches in viscosity implied changes in the material's shrinkage and thus the lamination of the bilayers. The shrinkage values are obtained by the strain values assessed at the end of the creep test at each temperature (Figures 2.17-2.20):

$$\text{Shrinkage (\%)} = \frac{L_f - L_0}{L_0} * 100 \qquad (5.1)$$

Where, L_f and L_0 are the sample thickness before and after creep test, respectively.

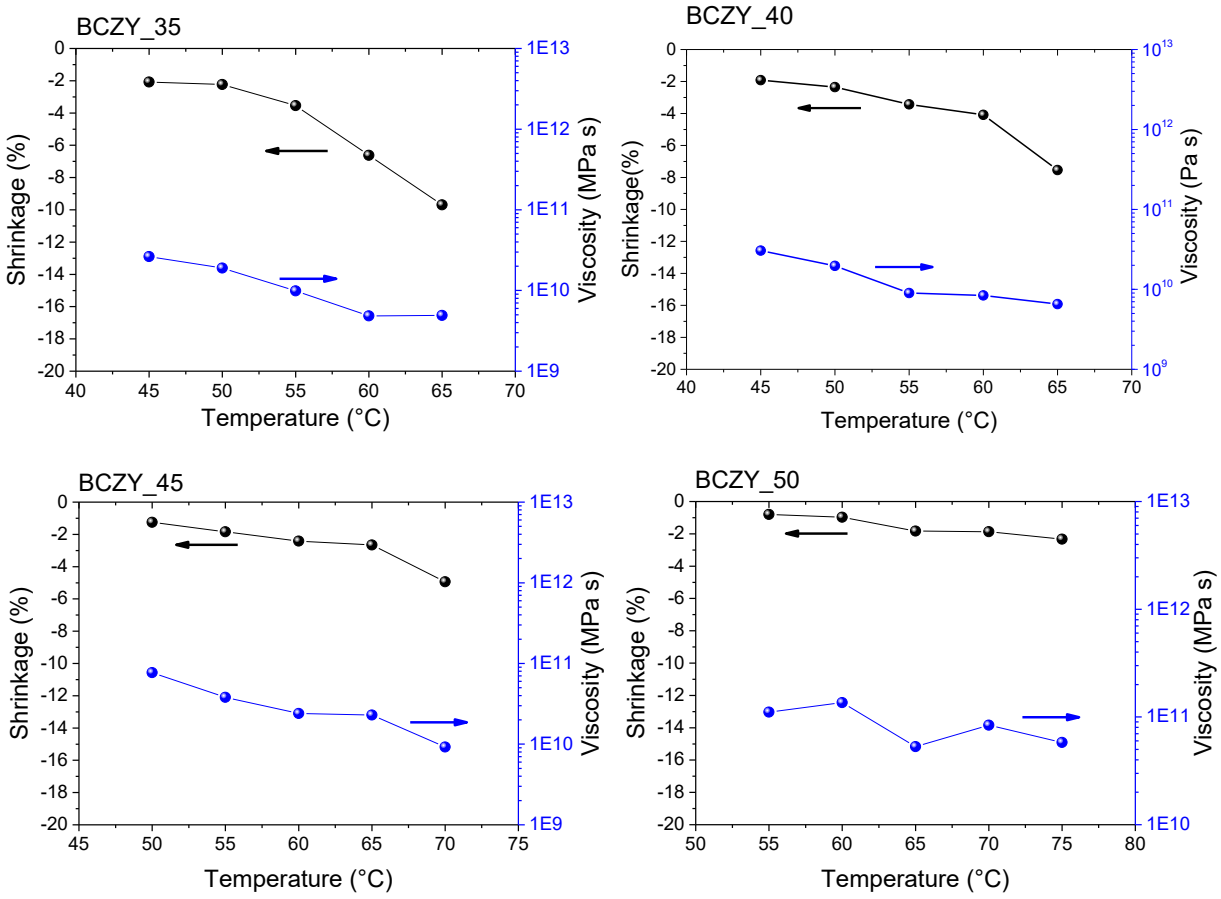

Figure 2.21 Strain and shrinkage values at different temperatures for all the tapes' formulation studied.

Figure 2.22 and Table 2.9 reports the viscosity and $T_{lamination}$ for each system. As shown, the lamination process is hindered by the presence of rice starch: the pore

former in fact increases the viscosity of the tape making the lamination proces more difficult.

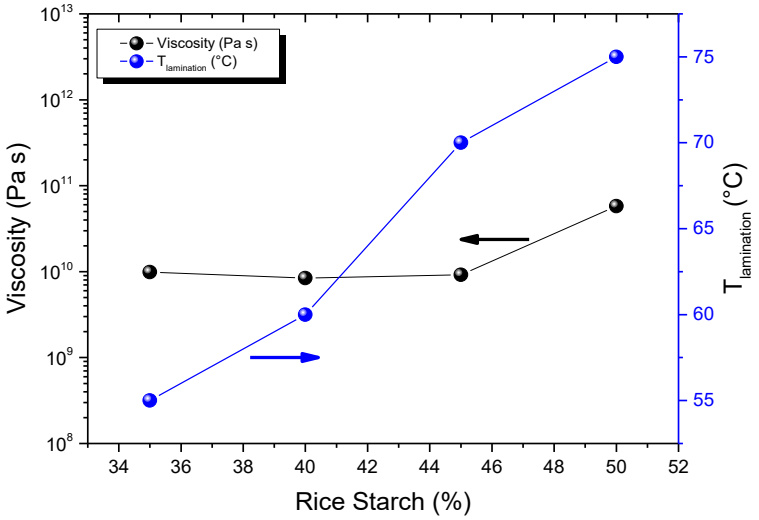

Figure 2.22 Viscosity and lamination temperature trend as a function of the rice starch content.

Table 2.9 Viscosity and lamination temperature for the different tapes.

RS (%)	η (Pa· s)	$T_{lamination}$ (°C)
35	$9{,}9 \cdot 10^9$	55
40	$8{,}4 \cdot 10^9$	60
45	$9{,}2 \cdot 10^9$	70
50	$58{,}0 \cdot 10^9$	75

It is interesting to note that the tapes showed similar values of lamination viscosity (10^{10} Pa s). The distinct difference showed by BCZY_50 is ascribed by the very high level of pore former in the system that lead that for the sake of comparison was not balanced. The formulation of this tape was clearly unsuitable for the process as shown by the cracked sample obtained. Even if more research has to be done to confirm this results, the possibility of identification a unique parameter identifying the best conditions for lamination will represent an important breackthrough for the multilayers field.

In conclusion, the tape characterisation through the DMA allowed to find helpful results which correlate the formulation with the mechanical properties and then with the lamination process. The rice starch has a ceramic particle-like blocking effect on the chain mobility at low temperature. However, this effect disappears at higher temperature as a consequence of the polymeric nature of the pore former. Temperature programmed static and dynamic experiments assessed the temperature-dependence of the rice starch blocking effect.

In consideration of the good mechanical properties and mild lamination conditions studied with this part of activity, BCZY_40 was chose as a suitable support layer for the asymmetric membrane. Circular samples of 24 mm in diameter were therefore punched from the BCZY-GDC and the BCZY_40 tapes. Then one membrane layer and two support layers were stacked and laminated together as described in the Chapter 4.
The lamination conditions used were those found with the creep tests, obtaining perfectly laminated multilayers:

- Pressure = 4 bar
- Temperature = 60°C
- Time = 5 min

The perfectly laminated samples obtained confirmed the predictive power of the DMA in selecting the suitable support formulation and the lamination conditions for the production of multilayers. However, it is worth to mention that the thermomechanical compatibility between the selected BCZY_40 layer and the thin BCZY-GDC one has to be still evaluated. In fact, in order to obtain flat and crack free asymmetric membranes, the support and dense layer must show compatible thermomechanical behavior. If this is condition will not be achieved, the formulation of the support layer will need be changed and further optimized. The next paragraphs will present and discuss the thermal treatment used to obtain the final asymmetric membrane.

5.4 Influence of the sintering temperature and atmosphere on the densification and phase composition of the asymmetric membranes

Green multilayers obtained as described in the previous paragraph must be thermally treated to obtain the final membrane microstructure. The treatment has to be carefully design to burnout the high quantity of organics without damaging the sample.

TG-GDC was used to evaluate the gas evolvement during the burnout as a function of temperature (Figure 3.1).

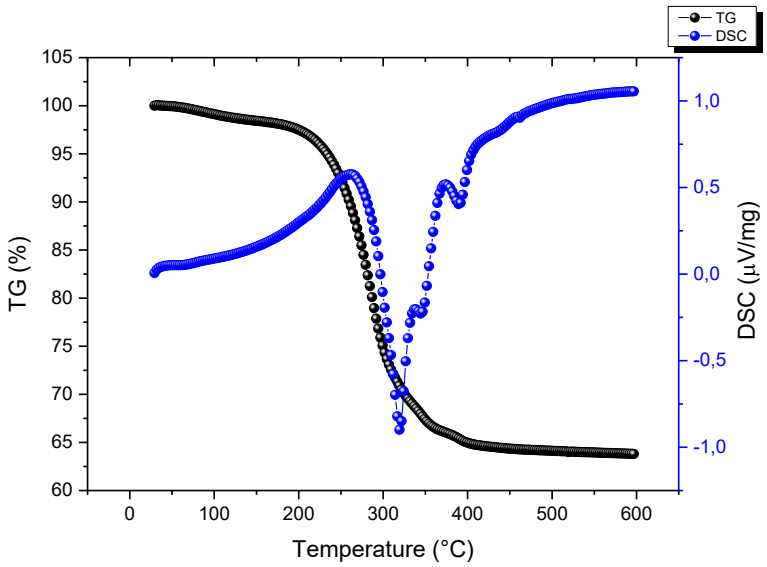

Figure 3.1 TG and DCS curves of the BCZY tape with starch rice as pore former.

The results revealed that the process starts at 150°C and ends at 500°C. As a consequence, two-step debinding temperature program was used:

(i) 50°C/h → 150°C

(ii) 4°C/h → 600°C

The particularly low heating rate 4°C/h reduced the chances of sample deformation or crack formation.

The set-up used for the debinding and sintering processes was the one described in the Chapter 4.

Samples were then sintered at 1400°C and 1450°C (heating rate 100°C/h) with for hours of dwelling time.

Figure 3.2 clearly shows that a proper dense composite BCZY-GDC layer cannot be obtained sintering in these conditions or even rising the temperature to 1450°C. This behavior is different to the one registered for the symmetrical membranes described in the previous paragraph.

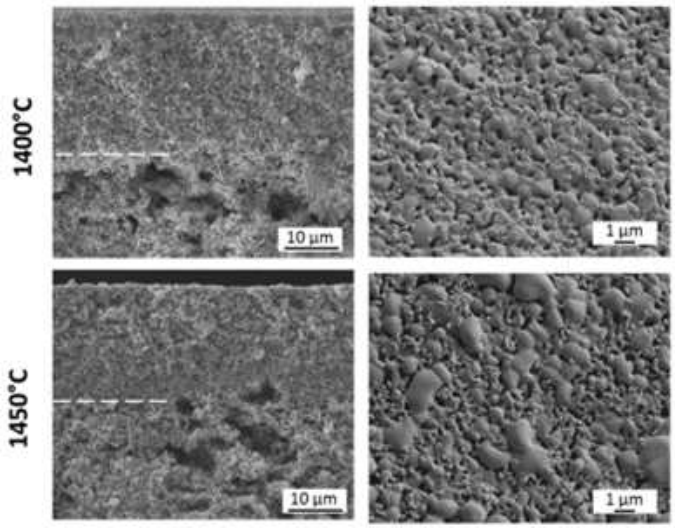

Figure 3.2 SEM micrographs of the cross sections and of the dense surfaces of the BCZY-GDC bilayers sintered at 1400°C and 1450°C.

The low-density degree achieved by the composite layer is due to the enhanced BaO evaporation that occurs at high temperature for these samples[31].

To further evaluate this superficial effect, multilayers (n°=10) of the thin and dense layer obtained through tape casting were laminated and sintered under the same previous conditions. High densities values were obtained for the 180 µm thick tape cast BCZY+GDC multilayers, reaching similar Archimedes' densities of the pellets: 97 ± 1%.

However, also in this case, a Ba loss effect was visible. The polished fracture reported in Figure 3.3 (b) revealed a porous-graded structure in a region of around twenty micrometers from the upper surface, with a corresponding decreasing in Ba concentration.

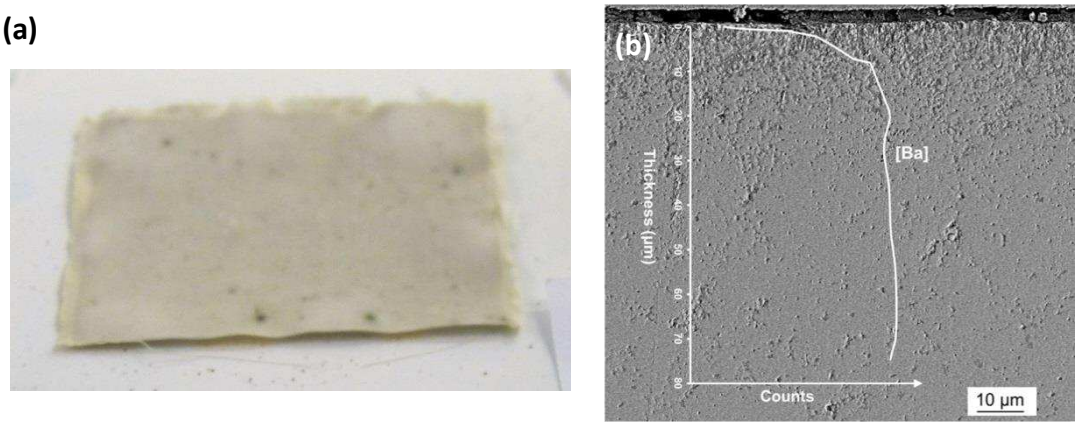

Figure 3.3 (a) image of the multilayer after sintering at 1400°C for 4 h and (b) SEM micrographs of the polished cross sections and
Ba-EDS profile of the multilayer after sintering at 1400°C for 4 h.

For the thick self-supporting symmetrical membranes produced by die pressing and tape casting, the "superficial" porosity was not affecting the total density and consequently their performances, remaining the bulk material completely dense. On the other hand, for the production of supported thin membrane, this aspect represents a crucial issue for obtaining barium cerate based films with the suitable characteristics. To overcome this problem, a very common technological strategy is the use of a sacrificial powder (pack) to control the sintering atmosphere. The sintering set-up was then modified in order to encapsulate the membrane in a protected atmosphere (Figure 3.4).

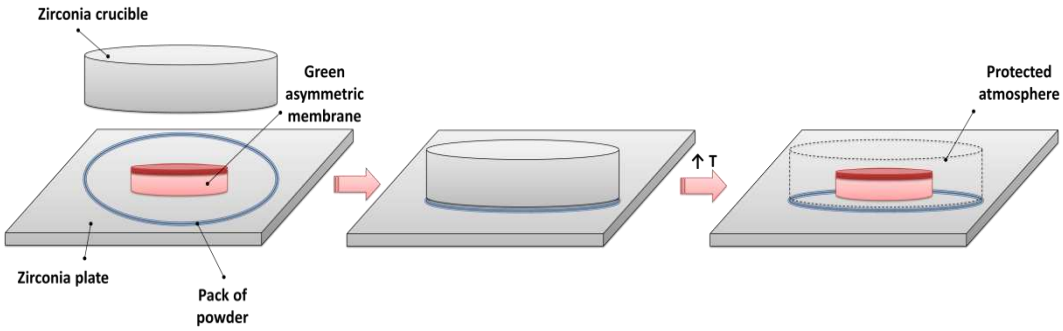

Figure 3.4 Graphical description of the modified set-up used: a pack of BCZY powder was used to seal the sintering atmosphere to prevent Ba loss from the membrane.

The modified sintering set-up is thought to saturate the sintering atmosphere, creating an equilibrium with the barium loss from the material and therefore preventing any compositional change. With this assembly, the membranes after sintering were crack-free and planar (Figure 3.5).

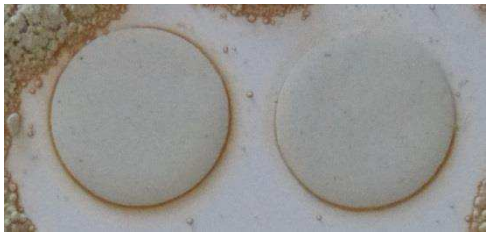

Figure 3.5 Picture of the asymmetric membranes sintered with the "pack" set-up at 1450°C for four hours.

Yet, the use of the pack only slightly improved the densification of the membrane layer. In fact, a high amount of residual porosity was still present especially in the middle of the layer (Figure 3.6).

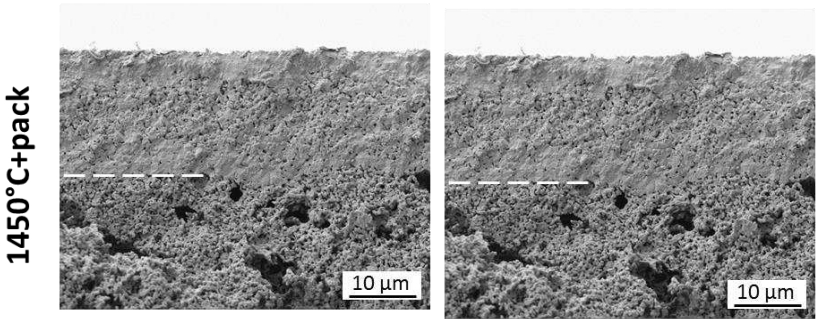

Figure 3.6 SEM micrographs of the cross sections and of the dense surfaces of the BCZY-GDC bilayer sintered at 1450°C with the "pack".

To densify the membrane, the choice of covering the top BCZY-GDC surfaces of the asymmetrical bilayers with pack, was also evaluated and it will be described in the next paragraph. This sintering configuration is thought to promote a dissolution-evaporation-reprecipitation mechanism, already observed for perovskite systems formed by volatile elements[23].

Modified sintering atmosphere

The work previously described showed that BaO loss from the BCZY lattice occurred during the sintering step with a detrimental effect on the densification of the 20 μm thick BCZY-GDC membrane layer. This phenomenon is attributed to the favorable formation energy of Ba and O vacancy pairs[32] that consequently modify the BCZY stoichiometry and properties[33,34]. Since BaO loss starts from the surface, only the superficial portion of the material is involved in compositional and microstructural changes. Therefore, a light mechanical abrasion of the surface is sufficient, and commonly considered, to obtain a 1-2 mm thick disc with the desired composition and stoichiometry[35]. However, this expedient cannot be applied for asymmetric architectures, for the low thickness of the dense membrane layer.

The activity reported in this chapter allowed to obtain ceramic-ceramic asymmetric membranes consisting of a dense 20 μm thick active BCZY-GDC layer and a porous 600 μm thick BCZY support by tape casting and lamination. The sintering atmosphere during the thermal treatment of the tape cast membrane was modified using different Ba-sources. Three different systems were used as sources of barium: $BaCeO_3$ powder (BC, d_{50} = 0.9 μm and SSA = 3.65 m^2/g, supplied by Praxair), $BaCe_{0.65}Zr_{0.20}Y_{0.15}O_{3-\delta}$ powder (BCZY) and a 50/50 vol% mixture of $BaCe_{0.65}Zr_{0.20}Y_{0.15}O_{3-\delta}$ and $Ce_{0.80}Gd_{0.20}O_{2-\delta}$ (BCZY-GDC; GDC with SSA = 6.8 m^2/g, supplied by Fuel Cell Materials). Round disks (ø = 30 mm) of the Ba-sources were obtained uniaxially pressing at 750 MPa.
Figure 3.7 describes the peculiar set-up used in this activity to control the sintering atmosphere: the Ba-containing discs were placed onto circular green asymmetric membranes of 26 mm in diameter and encapsulated with a zirconia crucible to seal the atmosphere. In this way, the active BCZY-GDC layer was put directly in contact with the Ba-source.

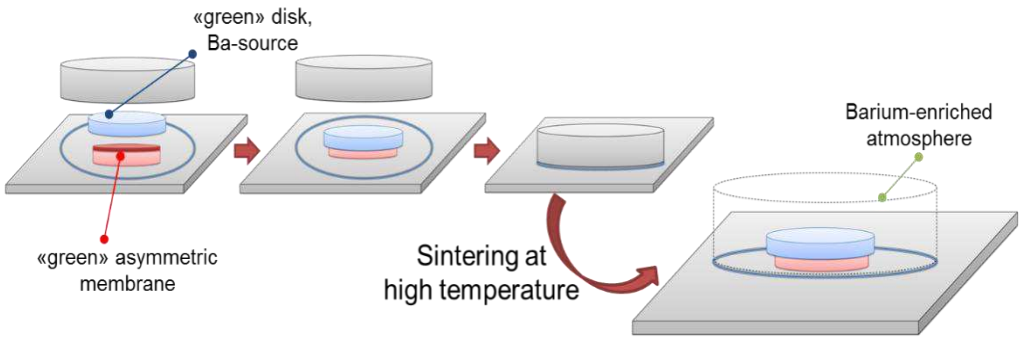

Figure 3.7 Graphical description of the modified set-up used: the green disk of Ba-source was placed onto the green multilayer, in contact with the BCZY-GDC thin layer.

First, an accurate evaluation of the effect of different barium sources on the density and phase purity of the thin BCZY-GDC membrane layer was performed. The sintering temperature and the Ba-enriching atmosphere were selected as the two main parameters. This activity assessed the importance of the right amount of Ba in the sintering atmosphere to produce dense separation membranes with the correct stoichiometry in the asymmetric configuration.

5.4.1 Ba-sources characterization

To assess the thermal stability of the different Ba-sources, the as-received powders were characterised through thermogravimetric analysis. The thermal stability of the selected systems is, in fact, a crucial parameter that must be considered in order to modify and control the sintering atmosphere at high temperatures. The TG curves of the three powders are reported in Figure 3.8.

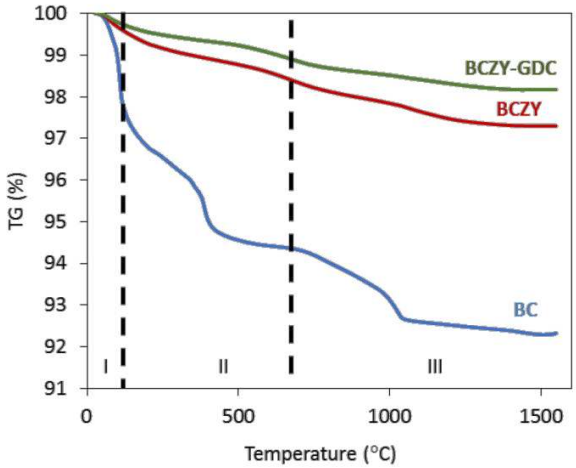

Figure 3.8 TGA of the BC, BCZY and BCZY-GDC powders used as Ba-sources.

The mass loss in the 25-200°C range is due to the evaporation of the water adsorbed on the surface of the powders, while the 200-700°C range is related to the dehydration of the perovskite lattice, mainly due to the water incorporation promoted by the oxygen vacancies. As reported by Kruth et al.[36] in fact, the amount of water contained in ambient condition is enough to fully hydrate Ba containing perovskites. Since the water incorporation into oxygen vacancies is fully reversible, a weight loss then occurs heating up the sample as described by the Equation:

$$2OH_{\ddot{O}} \leftrightarrow H_2O \uparrow + V_{\ddot{O}} + O_O^x \quad (3.1)$$

In the 700-1550°C range two distinct events may occur: the $BaCO_3$ decomposition and the BaO evaporation (Equations (3.2) and (3.3)):

$$BaCO_3 \leftrightarrow BaO\uparrow + CO_2 \quad (3.2)$$

$$BaCeO_3 \leftrightarrow xBaO\uparrow + Ba_{(1-x)}CeO_{(3-\delta)} \quad (3.3)$$

The presence of the barium carbonate is due to the low chemical stability of the barium cerate materials that under atmospheric condition, undergo to easy carbonation:

$$BaCeO_3 + xCO_2 \leftrightarrow xBaCO_3 + Ba_{(1-x)}CeO_{(3-x)} \quad (3.4)$$

As described by Equation (3.4) the carbonation of the material leads to oxygen vacancies which cause added water uptake, in accordance with Equation (3.1).
According to equations (3.2) and (3.3), the mass loss in the range 700-1550°C is strictly related to the tendency of the Ba-source to release barium into the sintering atmosphere.
TG analyses show that the un-doped BC displays the lowest chemical stability, followed by BCZY and BCZY-GDC[15,33]. The overall BC weight loss is 7.7 wt. %, of which 5.6 wt. % is due to H_2O evaporation/dehydration and 2.1% to decarbonation and Ba loss events.
The presence of $BaCO_3$ as associated phase in the BC system and its decomposition at elevated temperatures, was also verified by the XRD analyses (Figure 3.9): the main peak attributed to the orthorhombic $BaCO_3$ phase at about 24° (2θ) disappeared after thermal treatment at 1550°C.

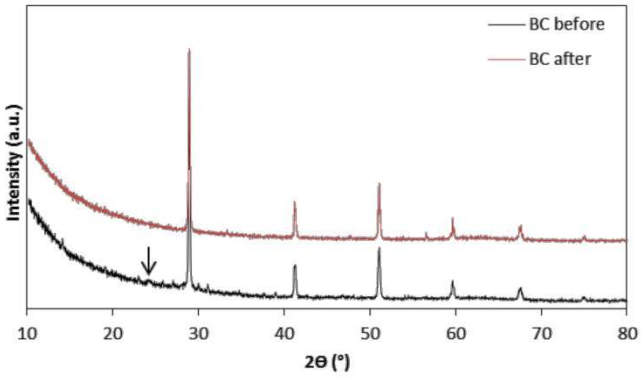

Figure 3.9 XRD analyses of the BC powder before and after the TGA. The arrow indicates the main peak of the $BaCO_3$ orthorhombic phase.

XRD analysis also revealed a slight shift of the diffraction pattern towards higher 2θ values after the TG analysis: this result is consistent with other works[36,17], that report a contraction of the crystalline lattice as a consequence of the barium loss from the BC lattice. It is worth to note that for the sacrificial systems, the $BaCO_3$

decomposition and the lattice contraction due to barium loss, are both sign of an enrichment in barium of the sintering atmosphere.

As expected, BCZY undergoes a lower weight loss: 2.7% in total and only 1.07 % related to decarbonation and BaO loss. The incorporation of Zr^{4+} in the perovskite lattice it is well-known to increase the perovskite structural stability against carbonation and water uptake[36,37]. As previously reported for the BC sample, XRD analysis in Figure 3.10 confirmed the presence of the barium carbonate also in the starting powder of BCZY.

Figure 3.10 highlights that the peaks of the main perovskite phase after TGA undergoes a clear sharpening associated with an intensity increasing after the thermal treatment. The XRD spectrum of perovskite phase in the BCZY before the TG analysis presents broad peaks that seem to be splitted as indication of two perovskite phases with different chemistry. This can be explained by the carbonisation reaction of barium-based materials with the atmospheric CO_2, that according to Equation 3.4, leads to the coexistence of two perovskite phases containing different Ba amount, as already observed in literature[36,38]. The powder after thermal treatment however (i.e. after TGA) is monophasic with an enhanced crystallinity.

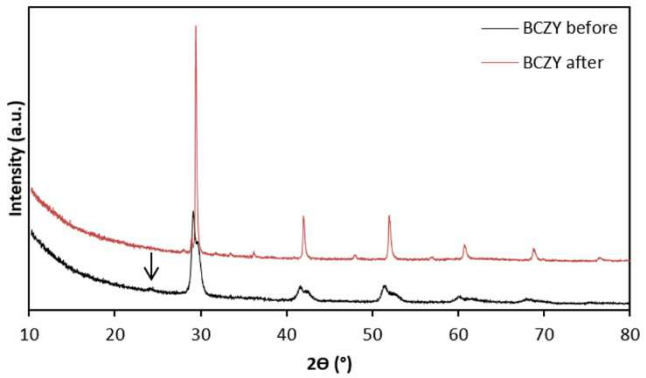

Figure 3.10 XRD analyses of the BCZY powder before and after the TGA. The arrow indicates the main peak of the $BaCO_3$ orthorhombic phase.

Finally, the thermogravimetric curve of the BCZY-GDC mixture (Figure 3.8) showed lower weight loss than the single BCZY phase for the presence of GDC

that reduces the relative amount of BCZY in the system. Even in this case, traces of $BaCO_3$ were detected by XRD (Figure 3.11). Analogously to what reported for BCZY, the untreated BCZY-GDC system showed broad and splitted diffraction peaks for the BCZY phase that, after the thermal treatment, disappeared as a sign of a monophasic system. After the TGA, peaks of BCZY and GDC are clearly detectable, and no-secondary phases appeared.

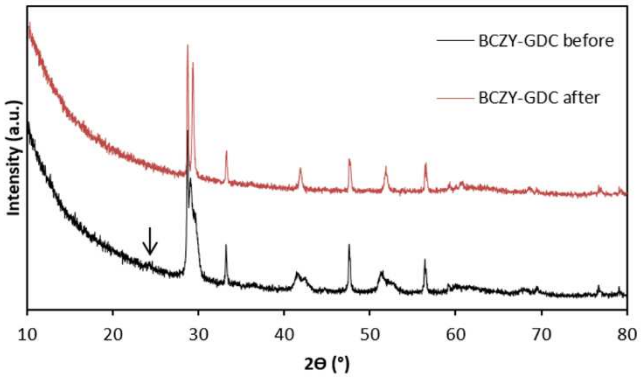

Figure 3.11 XRD analyses of the BCZY-GDC powder before and after the TGA. The arrow indicates the main peak of the $BaCO_3$ orthorhombic phase.

To evaluate the Ba evaporation from the different sources of barium during sintering, semi-quantitative EDS analyses were carried out on the powders of the three systems before and after being thermally treated at 1550°C for 4 hours (to mimic the sintering conditions). Table 3.1 reports the Ba/Ce atomic ratio values found with EDS before and after the thermal treatment.

Table 3.1 Ba/Ce atomic ratio values of the Ba-sources powders before and after being thermally treated at 1550°C for 4 hours determined by EDS semi-quantitative analysis.

	BC **Atomic Ba/Ce**	**BCZY** **Atomic Ba/(Ce+Zr+Y)**	**BCZY-GDC** **Atomic Ba/(Ce+Zr+Y+Gd)**
before	1,20 ± 0,02	1,11 ± 0,01	0,33 ± 0,01
after	1,04 ± 0,01	1,08 ± 0,02	0,33 ± 0,01

Semi-quantitative EDS analyses revealed that the Ba/Ce atomic ratio of the BC system decreased from 1,20 ± 0,02 to 1,04 ± 0,01 due to a 5 molar % of Ba loss at

the high sintering temperature. As predicted by the TGA, the BCZY was a more stable Ba-source than BC, in fact the Ba loss assessed by EDS was only 1.5 molar %. In the case of BCZY-GDC, no Ba loss was detected. This may be due to the lower amount of the BCZY phase in the overall system: the Ba loss results in this way below the detection limit of this technique.

The analyses confirmed the general trend in terms of thermo-chemical stability of the different compositions: BCZY-GDC < BCZY < BC (from the most to the less stable Ba-source). As it will be discussed in the next paragraph, this different stability affects the sintering atmosphere and therefore the microstructures and phase purity of the asymmetric membrane.

5.4.2 *Effect of the Ba-sources on the asymmetric BCZY-GDC/BCZY microstructure*

Depending on the sintering atmosphere, the asymmetric membranes, after being sintered at 1450°C, showed different color (Figure 3.12) and microstructures (Figure 3.6).

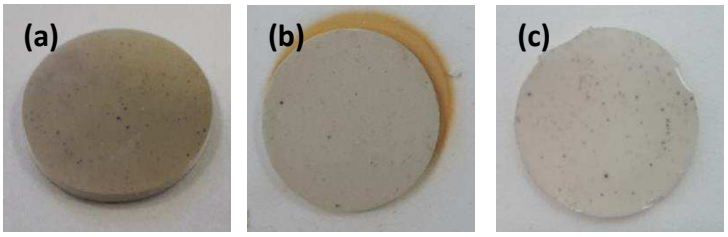

Figure 3.12 Picture of the membranes after sintering at 1450°C for 4 h with (a) BC, (b) BCZY and (c) BCZY-GDC Ba-sources.

The microstructural investigation showed that the modification of the sintering atmospheres highly affected the densification level. Only BC system led to a fully densified membrane layer at 1450°C. SEM micrographs at higher magnification of the fracture section (Figure 3.13) shows the presence of an intergranular glassy-phase, probably due to the formation of a liquid Ba-enriched phase, which promoted the grain mobility enhancing, as a consequence, the densification[39,40]. For sake of

comparison, Figure 3.14 reports also the fresh fractures at higher magnification of the membranes sintered with BCZY: as shown, the glassy phase is seen only in the samples sintered with BC.

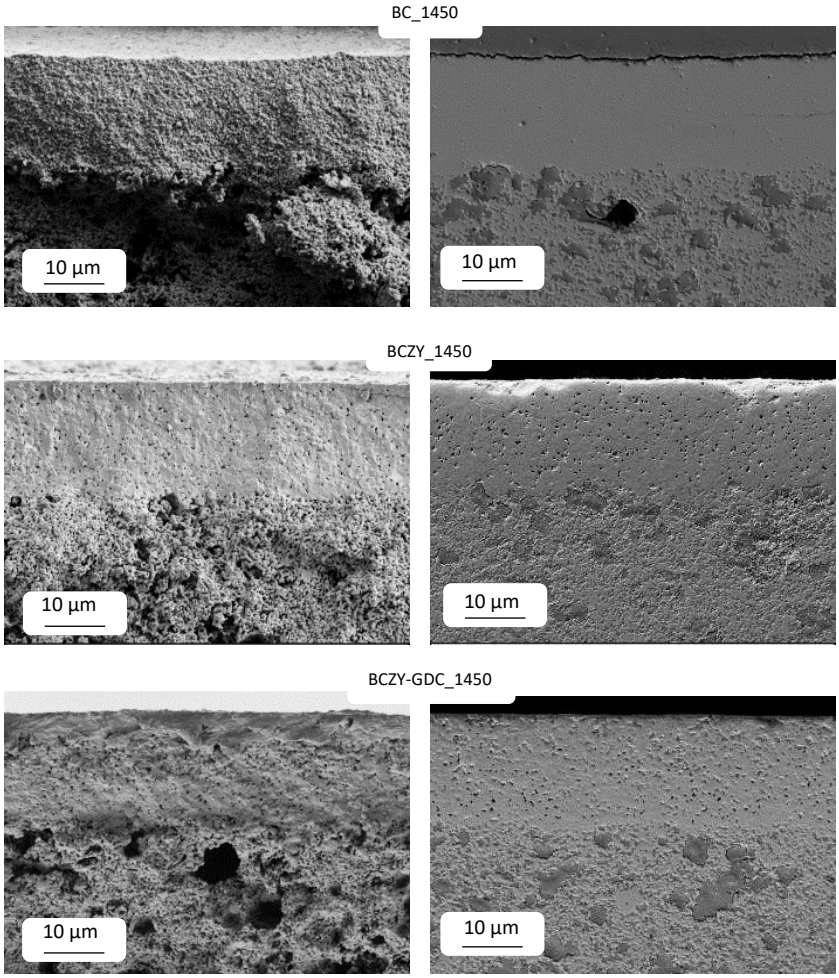

Figure 3.13 SEM micrographs of the fresh (on the left) and of the polished (on the right) cross sections of the asymmetric membranes sintered at 1450 and 1550°C using BC, BCZY and the mixture BCZY-GDC as Ba-sources.

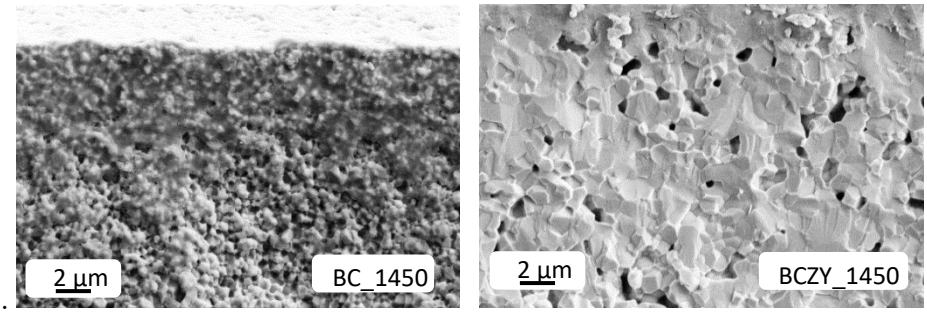

Figure 3.14 SEM micrographs at high magnification of the fresh fractures of the dense layer of the membranes sintered at 1450°C with BC and BCZY.

Also the membranes sintered at 1550°C showed different color (Figure 3.15) and microstructures (Figure 3.16), depending on the sintering atmosphere, even if the density of the different layers was considerably increased.

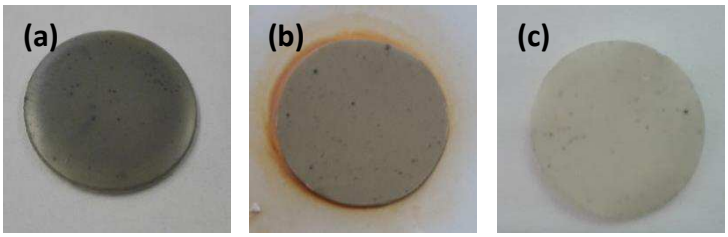

Figure 3.15 Picture of the membranes after sintering at 1550°C for 4 h with (a) BC, (b) BCZY and (c) BCZY-GDC Ba-sources.

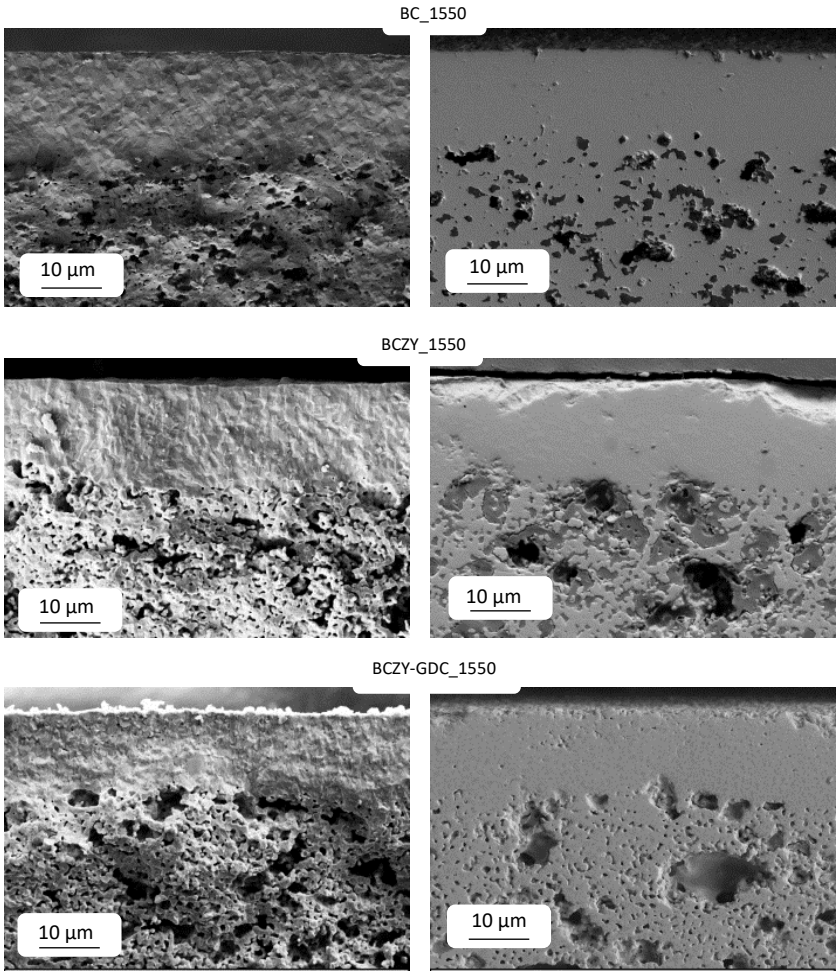

Figure 3.16 SEM micrographs of the fresh (on the left) and of the polished (on the right) cross sections of the asymmetric membranes sintered at 1450 and 1550°C using BC, BCZY and the mixture BCZY-GDC as Ba-sources.

The use of BC at 1550°C, led to a substantial grain coarsening, and the fracture morphology switched from intergranular to transgranular, clear indication that the glassy-phase in the intergranular region weakened the grain boundaries.
On the other hand, the more thermally stable BCZY and BCZY-GDC systems led to a fully densified membrane layer only at 1550°C (Figure 3.5).

Table 3.2 summarizes the residual porosity calculated by the image analysis of the membrane layers sintered at the two temperatures under different atmospheres.

Table 3.2 Porosity of the membrane layers calculated by image analysis of the SEM polished section's micrographs

	Residual porosity BC [vol.%]	**Residual porosity BCZY [vol.%]**	**Residual porosity BCZY-GDC [vol.%]**
1450°C	undetectable	4.7 ± 0.2	10.4 ± 0.2
1550°C	undetectable	0.7 ± 0.3	0.9 ± 0.4

All the samples sintered at 1550°C showed a residual porosity < 1%, while at 1450°C the membrane sintered using BCZY displayed a residual porosity around 5% and the one with BCZY-GDC had a residual porosity of about 10%, demonstrating that the BCZY-GDC system inadequately enriched the sintering atmosphere in barium at this temperature.

The influence of the different Ba-sources on the membrane grain size was evaluated analyzing the SEM micrographs of the dense membrane surfaces (Figure 3.17 and 3.18).

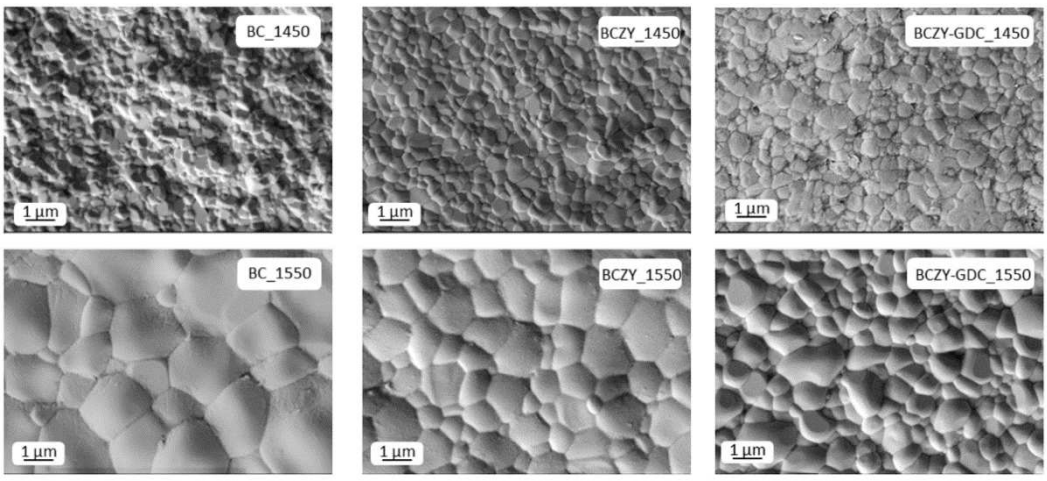

Figure 3.17 SEM analysis of the dense layer surfaces sintered at 1450 and 1550°C with the different Ba-sources.

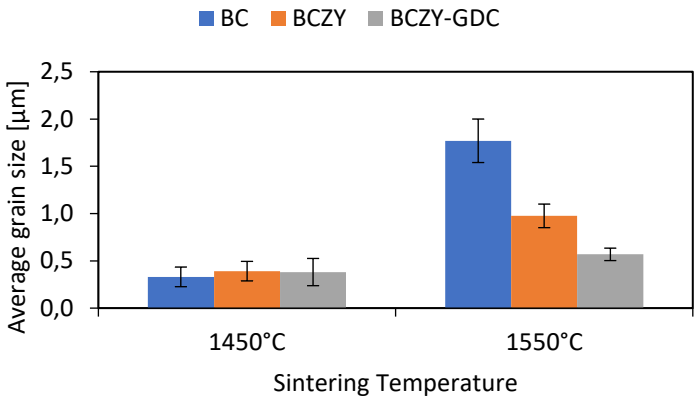

Figure 3.18 Average grain size of the membrane dense layers considered in this study.

The BC system led to the lowest grain size at 1450°C for the presence of the glassy phase previously mentioned which promoted the grain mobility but hindered the grain growth. These results are consistent with those of Babilo et al.[41], that reported that enriching in barium the sintering atmosphere of sintered yttrium-doped barium zirconate pellets, led to fully densified materials with a slightly smaller grain size. However, the average grain size increased from 0.3 ± 0.1µm to 1.8 ± 0.2µm at 1550°C due to the higher amount of barium released in the atmosphere. The BCZY system on the other hand, led to a slightly higher grain size at 1450°C, with the average value of 0.4 ± 0.1µm, that increased up to 0.9 ± 0.1µm at 1550°C. Finally, he most stable BCZY-GDC system followed the same trend of BCZY, even if the registered average grain sizes were smaller at the two temperatures investigated (0.4 ± 0.1µm at 1450°C and 0.6 ± 0.1µm at 1550°C), probably as a consequence of a globally lower amount of Ba containing compound.

Also the influence of the sintering conditions on the porosity and shrinkage of the supporting layer was accurately investigated. Figure 3.19 (a) and (b) report the variation of porosity and shrinkage of the support under the different two sintering conditions.

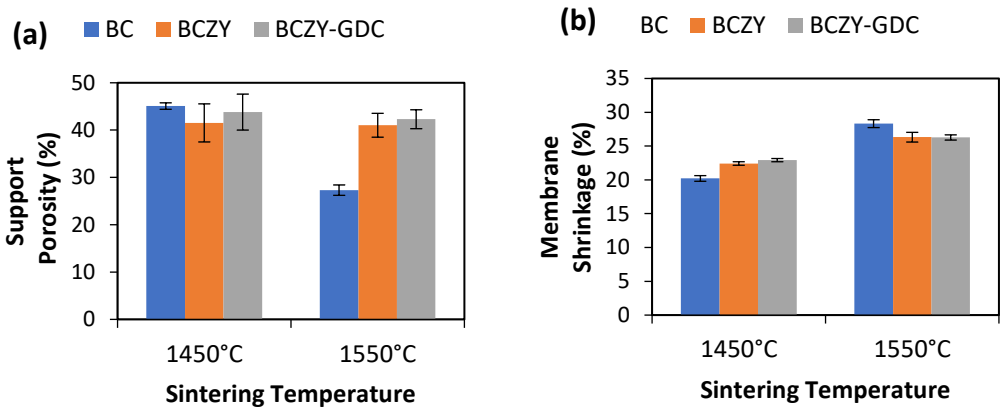

Figure 3.19 Porosity (a) and shrinkage (b) values of the membrane support.

It is evident that the sintering atmosphere not only affected the microstructure of the dense layer, but also influenced the porosity of the BCZY substrate and the shrinkage of the bilayer.

The membrane sintered with BC at 1450°C showed, in fact, the lowest shrinkage, maintaining a support porosity as high as 45%. However, the shrinkage strongly increased with the temperature, reaching at 1550°C the highest value among all the membranes studied. This behavior is due to the high quantity of barium released by BC. The formation of the glassy-phase at 1450°C promotes the grain mobility of the membrane layer without affecting the support porosity. Increasing the sintering temperature up to 1550°C, the high amount of barium released lead to the densification of the support with a consequent higher shrinkage of the bilayer. On the other hand, BCZY and BCZY-GDC systems slightly affected the support porosity even with the temperature increase, in accordance with their higher thermal stability and therefore barium release.

Samples sintered with BC at 1450°C and with BCZY and BCZY-GDC at 1550°C showed a sufficiently dense membrane layer, with a porosity of the support higher than 40%.

5.4.3 Effect of the sintering atmosphere on the membrane phase composition

The evaporation of Ba could, in principle, affect the stoichiometry of the dense layer and therefore its properties. In order to check that, XRD and semi-quantitative EDS analyses were carried out on the dense surfaces of the membranes sintered in different Ba-enriched atmospheres. The EDS profiles of Ba and Gd elements were also recorded on the polished fractures to evaluate the distribution of BCZY and GDC along the membrane layers.

Figure 3.20 a) and b) show the backscattered SEM micrographs of the polished section and Ba/Gd-EDS profiles of the BC_1450 and BC_1550 membranes. The analyses revealed that although the BCZY and GDC phases are not discernible from the backscattered image, the Gd and Ba elements are evenly distributed along the whole thickness of the membrane.

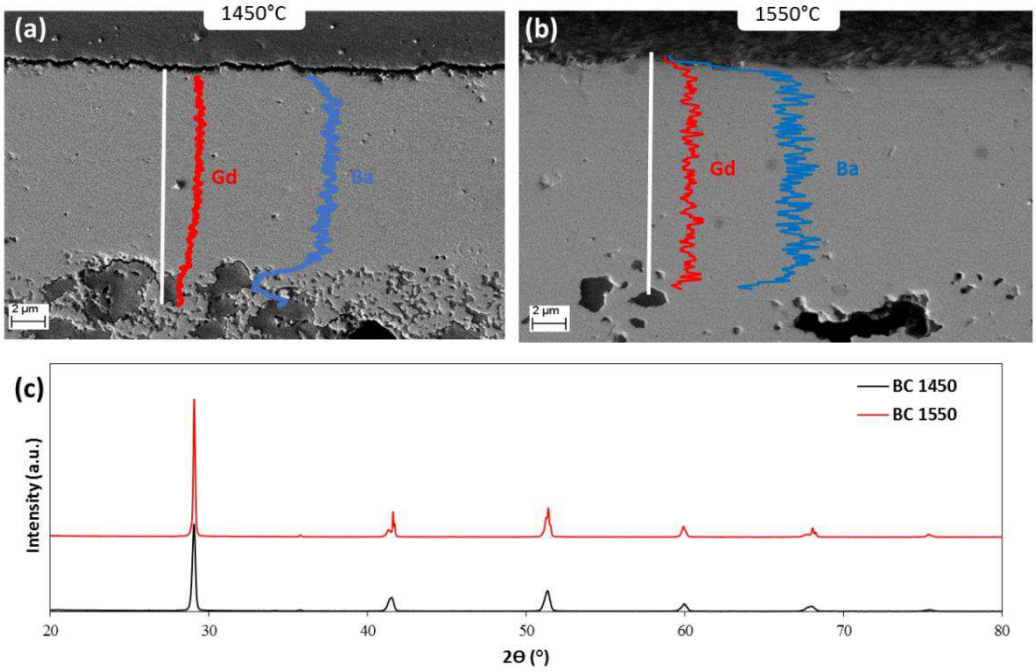

Figure 3.20 Back scattered SEM micrographs and Ba and Gd elements EDS profiles of the polished membrane section of the samples a) BC_1450 and b) BC_1550; c) XRD analyses of theBC_1450 and BC_1550 dense layer surface.

Thus, the sintering atmosphere modified with BC not only promoted the densification of the membrane layer even at low temperature, but it also produced

an undesired single mix-phase as a consequence of a solid-state reaction between the two starting systems. Such reaction can be explained by the barium migration through the membrane layer and its dissolution into the BCZY and GDC lattices. This phenomenon led to an increase of the defect concentration which boosted the grain mobility and cation migration from one lattice to the other, promoting the formation of the new undesired phase. A similar solid-state reaction between $Ce_{0.8}Gd_{0.2}O_{1.9}$ and $BaCO_3$was exploited by Serra et al. to obtain a $BaCe_{0.8}Gd_{0.2}O_{3-\delta}$ protonic electrolyte[42]. As reported in Figure 3.20 c), the XRD patterns of the membranes sintered with BC_1450 and 1550 revealed the presence of a single perovskite orthorhombic phase (s.g., *Pmcn*) confirming the formation of a single phase.

Unlike with BC, samples sintered using BCZY retained at least some of the dual phase composition (Figure 3.21).

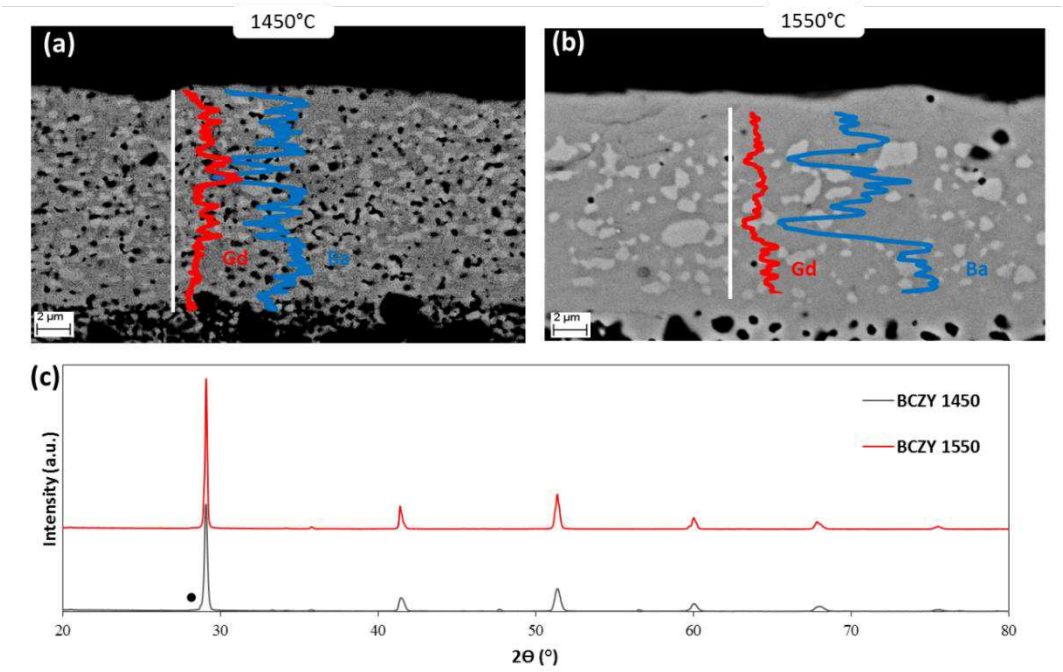

Figure 3.21 Back scattered SEM micrographs and Ba and Gd elements EDS profiles of the polished membrane section of samples a) BCZY_1450 and b) BCZY_1550; c) XRD analyses of the BCZY_1450 and 1550 dense layer surfaces.
The dot indicates the main peak of the GDC phase.

In the sample treated at 1550°C, the XRD analysis revealed the presence of the single perovskitic phase (s.g., *Pmcn*) in the superficial part, while the two phases

were still detected in the inner part of the dense layer through EDS (Figure 3.21 (b)). This result confirms that the Ba coming from the BCZY promotes the solid-state reaction only in the very top of the dense surface physically in contact with BCZY. In the 1450°C samples, on the other hand, (Figure 3.21 (c)) there is clearly some GDC even if the phase content is only 3.4%.

Figure 3.22 shows that BCZY-GDC allowed the preservation of the dual phase composition throughout the whole membrane layer at both temperatures. The XRD analyses performed on the top of the dense layer confirmed in fact the presence both of the perovskite (BCZY) and fluorite-type (GDC) phases.

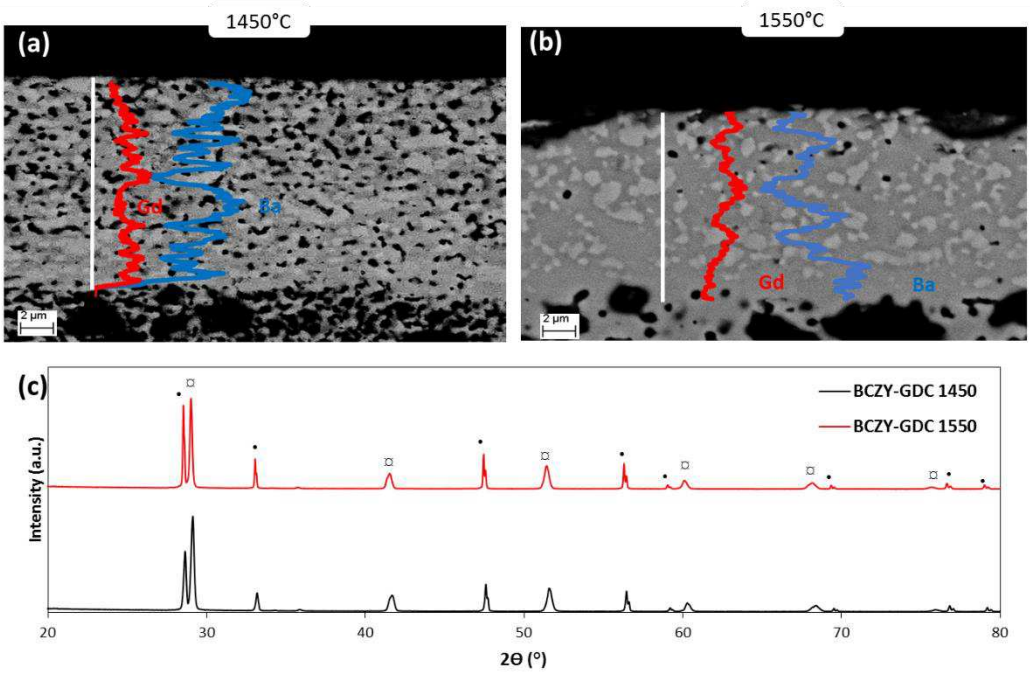

Figure 3.22 Back scattered SEM micrographs and Ba and Gd elements EDS profiles of the polished membrane section of samples a) BCZY-GDC_1450 and b) BCZY-GDC_1550; c) XRD analyses of the BCZY-GDC_1450 and 1550 dense layer surfaces.

Phase composition and lattice parameters of the main perovskite phases of the dense layer surfaces of all samples are listed in Table 3.3 and reported in Figure 3.23.

Table 3.3 Phase composition, and lattice parameters of the main perovskite phase from XRD analyses on the dense surfaces of the sample considered in this study. Standard deviation is indicated within parentheses.

Sample name	Phase/s	Space group	a [Å]	b [Å]	c [Å]	V [Å^3]
BC_1450	BCZY-like	*Pmcn*	8.7260(11)	6.1840(8)	6.2143(8)	335.33(13)
BC_1550	BCZY-like	*Pmcn*	8.7238(19)	6.1960(13)	6.2122(13)	335.78(21)
BCZY_1450	BCZY-like	*Pmcn*	8.7077(6)	6.1790(5)	6.1980(4)	333.48(6)
BCZY_1550	BCZY-like	*Pmcn*	8.7183(6)	6.1841(4)	6.2057(5)	334.58(7)
BCZY-GDC_1450	BCZY	*Pmcn*	8.6679(3)	6.1461(3)	6.1632(3)	328.34(2)
	GDC	*Fm-3m*	5.4107(1)	-	-	158.40(1)
BCZY-GDC_1550	BCZY	*Pmcn*	8.6812(5)	6.1534(4)	6.1717(4)	329.69(4)
	GDC	*Fm-3m*	5.4151(2)	-	-	158.79(2)

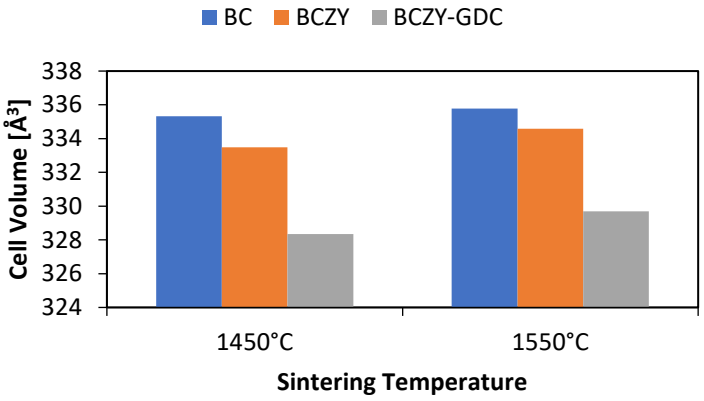

Figure 3.23 Cell volumes determined from XRD analyses reported in Table by EDS semi-quantitative analysis of the asymmetric membranes considered in this study.

Since Ba^{2+} is the biggest cation among the elements constituting the BCZY-GDC material, the Ba dissolution into the lattice lead to cell expansion. The BC_1450 and 1550 membranes showed the highest cell volumes (335.8 Å^3 at 1550°C and 335.3 Å^3 at 1450°C). The single phase produced by the solid-state reaction of the BCZY_1550 membrane displayed a lower unit-cell volume (334.6 Å^3), showing that the dense layer of the new undesired phase detected by SEM analysis had a lower amount of Ba. This is the consequence of the higher stability of BCZY in respect to BC. Only BCZY-GDC samples showed unit-cell volume values comparable to the ones reported in literature[14,43]. In this case, a unit-cell volume increasing was detected from low to high sintering temperature, i.e., the perovskite

unit-cell undergoes an expansion from 328.3 $Å^3$ to 329.7 $Å^3$, respectively, meaning that a higher sintering temperature promoted both Ba evaporation from the Ba-source and the Ba dissolution into the membrane lattice.

The different Ba content in the dense membrane surface was confirmed by semi-quantitative EDS spectra. Figure 3.24 reports the Ba/Zr atomic ratio values of the EDS results. A green BCZY-GDC pellet was also analyzed for comparison and the Ba/Zr value obtained (Ba/Zr = 4) was taken as reference.

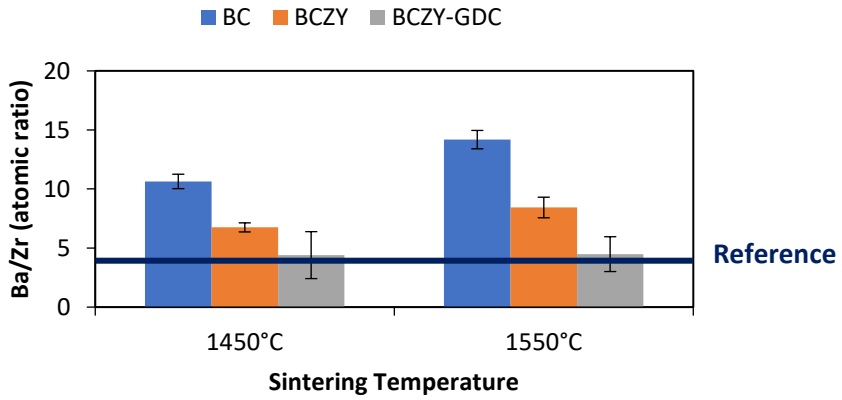

Figure 3.24 Ba/Zr atomic ratio values determined by EDS semi-quantitative analysis of the asymmetric membranes considered in this study.

The Ba amount in BC_1450 is more than double than the one of the reference, and it triplicates at 1550°C. Similarly, the dense membrane sintered with BCZY, showed a Ba/Zr value of 6 at 1450°C and a value closed to 8 at 1550°C. Only the less reactive BCZY-GDC allowed to achieve a Ba/Zr ratio value close to the reference one at both sintering temperatures.

The previous results prove how the sintering atmosphere can be crucial to obtain thin and dense membrane layer with the phase composition needed. The highest reactive Ba-source BC, other than promote the densification of the membrane layer, led to the formation of a single-phase material due to Ba dissolution into the BCZY and GDC lattices. Even the membrane sintered using BCZY as Ba source was completely densified at higher temperature (1550°C) but the formation of the undesired single phase occurred in the first 3-4 μm. The Ba dissolution into the perovskite and fluorite lattices due to the solid-state reaction was also confirmed by

the unit-cell parameters of the phases considered. Only using the BCZY-GDC as Ba source, the desired phase composition was achieved and a membrane of suitable microstructure (20 µm-thick dense layer and 42 vol.% porous support) was obtained.

Unfortunately, while the membranes sintered with BC at both temperatures were defect-free, samples sintered with BCZY and BCZY-GDC at 1550°C showed a cracked dense layer (Figure 3.25) not spotted at lower temperature.

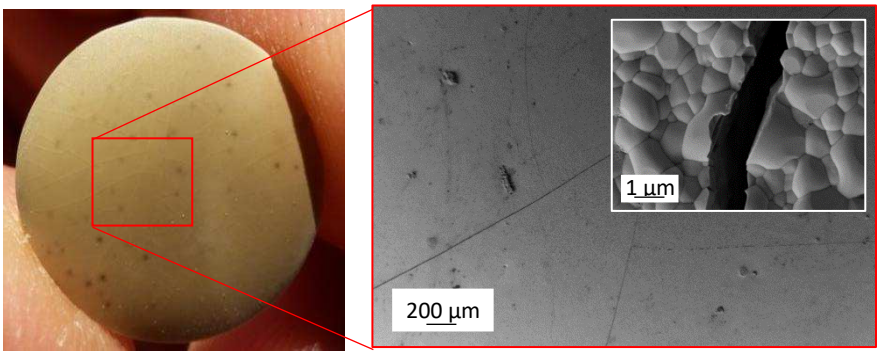

Figure 3.25 Picture of the BCZY_1550 sample and SEM micrographs of the dense surface. In the insert a micrograph at higher magnification is reported as well.

This could be due to the tendency of the multilayer to camber as a consequence of the different shrinkage between the dense and the porous layer. It is well established that the different densification rates of the layers of asymmetric architectures can develop stresses than can lead to defects (cracks or distortions). A common procedure to overcome bending effects is to apply a suitable pressure on the sample to constrain it in a flat geometry and relax afterwards the eventual stresses. Sometimes, the weight of the sample itself is sufficient to prevent cambered structures. In the case of the membranes here reported, at high temperature, the porosity of the support layer decreases with a consequent shrinkage of the layer, as testified by the analyses reported in Figure 3.19. Since the membrane is oriented with the dense membrane side up during sintering, the force developed by the sample's weight was already in the useful direction for the planarity (Figure 3.7).

In addition, as previously showed in Figure 3.7, a Ba-containing 8 grams pellet was placed onto each membrane. Therefore, the eight-grams pellet might apply an excessive pressure on the membrane, leading to cracks formation.
The sintering set-up was then modified replacing the BCZY-GDC pellet with 2 grams of powder of the same composition (Figure 3.26).

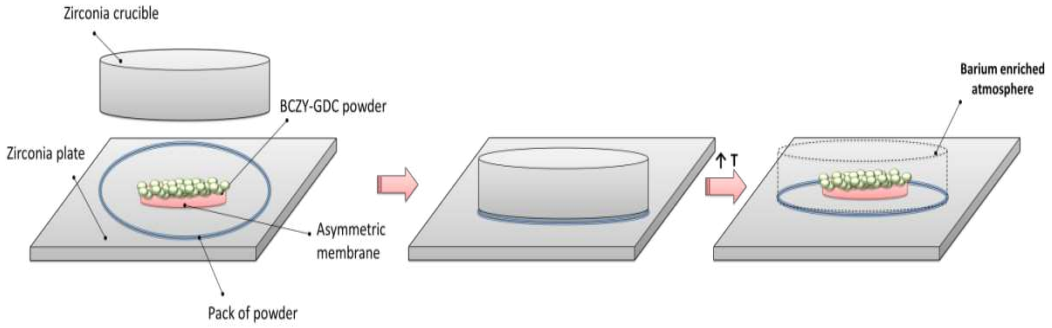

Figure 3.26 Graphical description of the modified set-up used: the BCZY-GDC layer was covered with BCZY-GDC powder.

The modified set-up led to a cambered membrane (Figure 3.27) with the same cracked dense layer of the membrane sintered with the pellet.

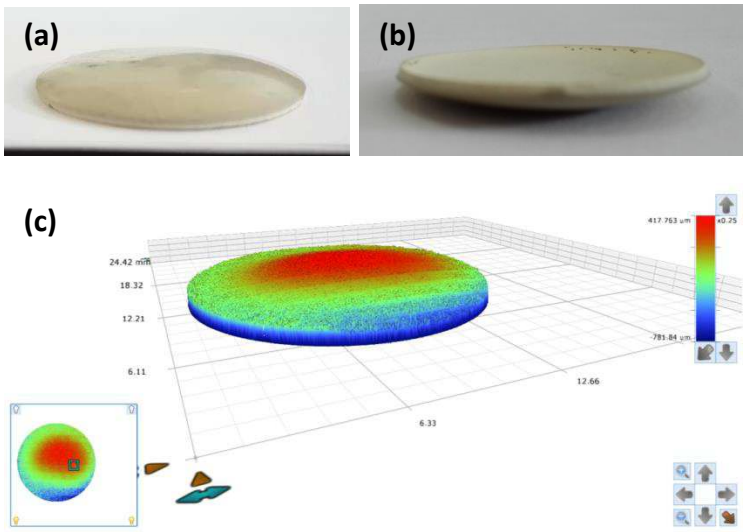

Figure 3.27 Pictures of the membrane sintered being covered with BCZY powder with the dense layer upside (a) and downside (b) and profilometer image (c) of the membrane acquired with the dense layer upside.

The profilometer analysis revealed that the distance between the lowest and highest points of the membrane was roughly 1 mm. The curvature towards the porous layer confirms the theory previously explained of the different densification rates. This result is consistent with mathematical models, such us modeling approach reported by Cai et al.[44] or Molla et al.[45] validated by experimental data[46]. The presence of cracks in the cambered membrane indicates that the origin of the defects lays on thermomechanical mismatch between the thin BCZY-GDC layer and the porous BCZY one. Therefore, despite the similar TECs reported previously for the BCZY-GDC and GDC materials, excessive stresses were formed at high temperature. The fact that samples sintered with BC were crack-free also when sintered at 1550°C may be due to the high influence of the Ba-source on both phase composition and microstructure evolution. In fact, the solid-state reaction that led to the formation of a new material, matching the thermomechanical properties of the thin and dense membrane with those of the BCZY porous support. To overcome these issues, the same composition (BCZY-GDC) was selected for both the dense and porous layers of the asymmetric membrane. In this way, the differences between the two layers can be restricted to the different microstructure (porous-dense).
In the next paragraph the activity related to the tape casting of a BCZY-GDC support layer to obtain defect-free asymmetric membranes will be reported.

5.5 BCZY-GDC supported membranes

The activity reported in this chapter aimed at the optimization of the ceramic process to obtain crack-free BCZY-GDC asymmetric membranes suitable for hydrogen separation. Such membranes must show the best compromise between the porosity of the support and the density of the membrane layer. To do so, two parameters were evaluated:

- the effect of the porous support shrinkage of the densification of the membrane layer, known as “co-firing effect”. Deibert et al.[47] showed that the densification of a $La_{5.4}WO_{12-\delta}$ membrane layer is improved when it is coupled with a porous support thanks to the simultaneously shrinking of the porous layer during sintering. Similarly, Zhan et al.[48] evaluated the effect of

the support composition on the shrinkage of gas tightness of asymmetric $SrCe_{0.95}Y_{0.05}O_{3-\delta}$ membranes. Therefore, in the present work, the correlation between the formulation of the support layer and the shrinkage of the membrane was deeply investigated in order to improve the densification of the membrane layer;

- the amount of ZnO used as sintering aid in the membrane layer. In the previous activities, BCZY-GDC pellets were successfully densified at 1450°C adding a 0.8 wt. % of ZnO. Here, the effect of different amounts of ZnO was evaluated on the densification of the tape casted membrane layer. In fact, because of the higher green density of the pressed pellets in respect to the tape, the optimum amount of ZnO may differ.

In the final part, the sintering atmosphere role in the densification and phase composition of the membrane layer is also reported.

5.5.1 Co-firing effect

The optimized BCZY formulation reported in Chapter 5 was used as starting point for the realization of the BCZY-GDC tape. The only modification was to substitute half volume of BCZY with GDC, in order to obtain in the support, the same mixture of the membrane (50-50 vol. %). The process for the slurry preparation and the casting is explained in Chapter 4. In Table 4.1 is reported the formulation used for this first tape, labelled as Tape 1.

Table 4.1 Formulation of Tape 1 with the BCZY-GDC (50:50 vol. %) ceramic fraction.

Ingredients	Vol. (%)
BCZY	12.6
GDC	12.6
Dispersant	1.6
Pore Former	16.3
Binder	26.9
Plasticizer	29.5

Unfortunately, organic phase separation was clearly observed during the drying step (Figure 4.1).

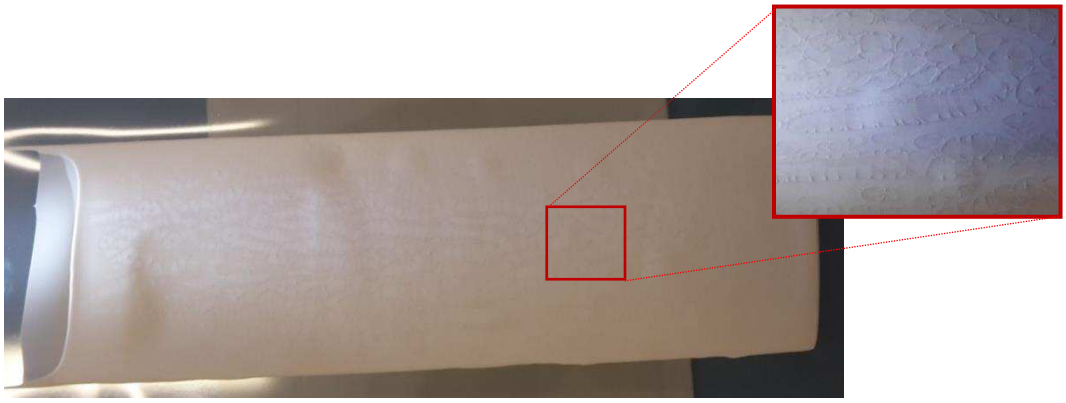

Figure 4.1 Picture of the dried Tape 1. In the inset a magnification of the picture to show better the phase separation is reported.

This effect is ascribable to an excess of the organics fraction, particularly to an excess of plasticizer which, in presence of a different inorganic matrix than BCZY, may exceed its solubility limit in the PVB polymeric network. Further studies are however necessary to deeply understand the effect.

Since the presence of the organic phase separation seemed to be exclusively superficial, an attempt was made to produce asymmetric membranes using Tape 1 as support layer. Thus, samples were obtained through lamination, debinding and sintering steps as previously described: the asymmetric membrane was placed over a zirconia plate, and a BCZY green disc was placed over it. Then, a zirconia crucible was used to cover the samples and BCZY powder to seal the atmosphere. After sintering (1550°C for four hours) the membranes were cracked. Figure 4.2 shows how the porous layer interacted with the zirconia plate and how the bilayers deformed and cracked during the thermal treatments.

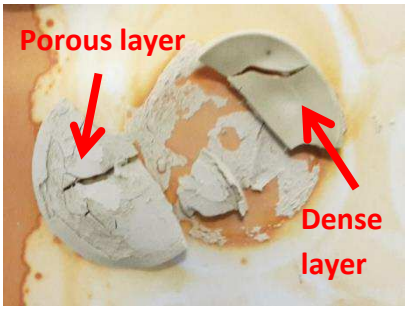

Figure 4.2 Picture of the membrane sintered at 1550°C for four hours.

In order to better evaluate the origin of the defects, green membranes were debinded on a drilled alumina plate to favour the organics burnout. The temperature program was kept the same. After debinding, the samples showed different kind of defects (Figure 4.3).

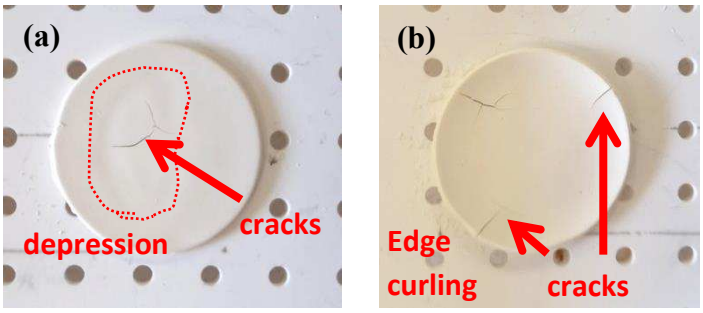

Figure 4.3 Picture of membranes after the debinding treatment.

The inhomogeneous green Tape 1 led to depressions in the membrane body after organics' burnout. Cracks appeared in correspondence to the depressions when the stress was too high (Figure 4.3 (a)). Some membranes displayed the edge curling effect and cracks as well (Figure 4.3 (b)).
Results indicated that the defects were not only superficial, but they affected all the body of the tape. Therefore, a modification of the tape formulation was mandatory to obtain crack-free samples after thermal treatments.

Two tapes were then obtained modifying the slurry formulation. To check if the defects formation is ascribable to an excess of binder and plasticizer ingredients, Tape 2 was obtained decreasing the content of both organics of Tape 1 (binder and plasticizer) by 30 vol. %.

On the other hand, as the phase that exoluted in Tape 1 was likely to be the plasticizer, Tape 3 was obtained decreasing the binder content by 30 vol. % (as Tape 2) and the plasticizer by 40 vol. %. After drying both tapes were defect-free with a good elasticity and plasticity (Figure 4.4), confirming that the defects of Tape 1 were due to excessive organic content. Tape 3 was more rigid because of the lower amount of plasticizer.

Figure 4.4 Picture of dried Tape 2 and Tape 3.

Both tapes were then laminated with the BCZY-GDC thin layer as previously done with the BCZY support in Paragraph 5.2. To avoid the interaction between the green membrane and the zirconia plate, the membrane was placed onto a sintered BCZY-GDC pellet. To prevent the Ba loss, each membrane was covered with BCZY powder and encapsulated in a ZrO_2 crucible using BCZY powder to seal the atmosphere, as reported in Figure 4.5.

Figure 4.5 Picture of samples before the thermal treatments of debinding and sintering.

Membranes were then debinded and then sintered (1550°C for four hours). Figure 4.6 shows that the membrane layers were crack-free, but not sufficiently densified.

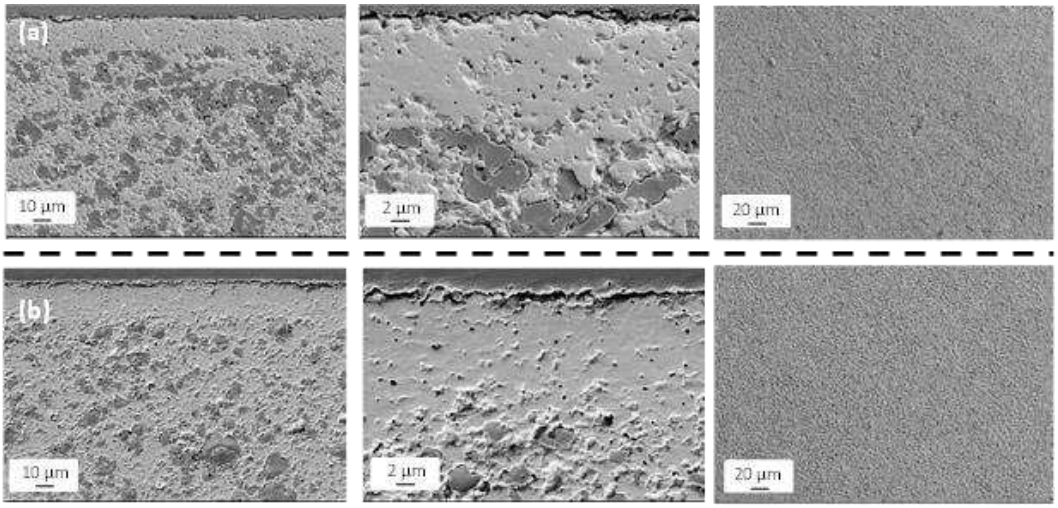

Figure 4.6 SEM micrographs of the polished fractures and of the membrane surfaces of the samples sintered at 1550°C with the Tape 2 (a) and Tape 3 (b) as porous supports.

It is worth to remind that the BCZY-supported samples showed a complete dense membrane layer when sintered at the same conditions (Paragraph 5.3, Figure 3.16). This may be explained by the higher shrinkage of the BCZY-supported membrane (26.3 %) in comparison to the BCZY-GDC-supported one (24.6%).

In addition, the image analysis of the SEM micrographs of the polished fractures revealed that the porosity of the Tape 3 support was slightly higher than the one of Tape 2 for its minor organics content.

Having discovered the role of the sample shrinkage on the densification of the membrane layer, the support tape formulation was iteratively modified in order to obtain the desired microstructure. Therefore, the iterative experimental process can be described as follows:

1. modification of the previous green tape formulation,
2. casting of the support layer, punching and lamination,
3. debinding and sintering of the green membrane;
4. microstructural evaluation through SEM analyses of the polished fractures;
5. then, back to point 1 depending on the result obtained in point 4.

This work aimed at correlating the composition of the tape with its shrinkage during thermal treatments which affected either the final support porosity and the membrane density.

Figure 4.7 reports the formulations and the modifications made for each BCZY-GDC tape to study the co-firing effect on the densification of the membrane layer. All tapes obtained were crack-free after drying, and therefore used as support layers for the asymmetric membranes: samples were laminated and then thermally treated as described above.

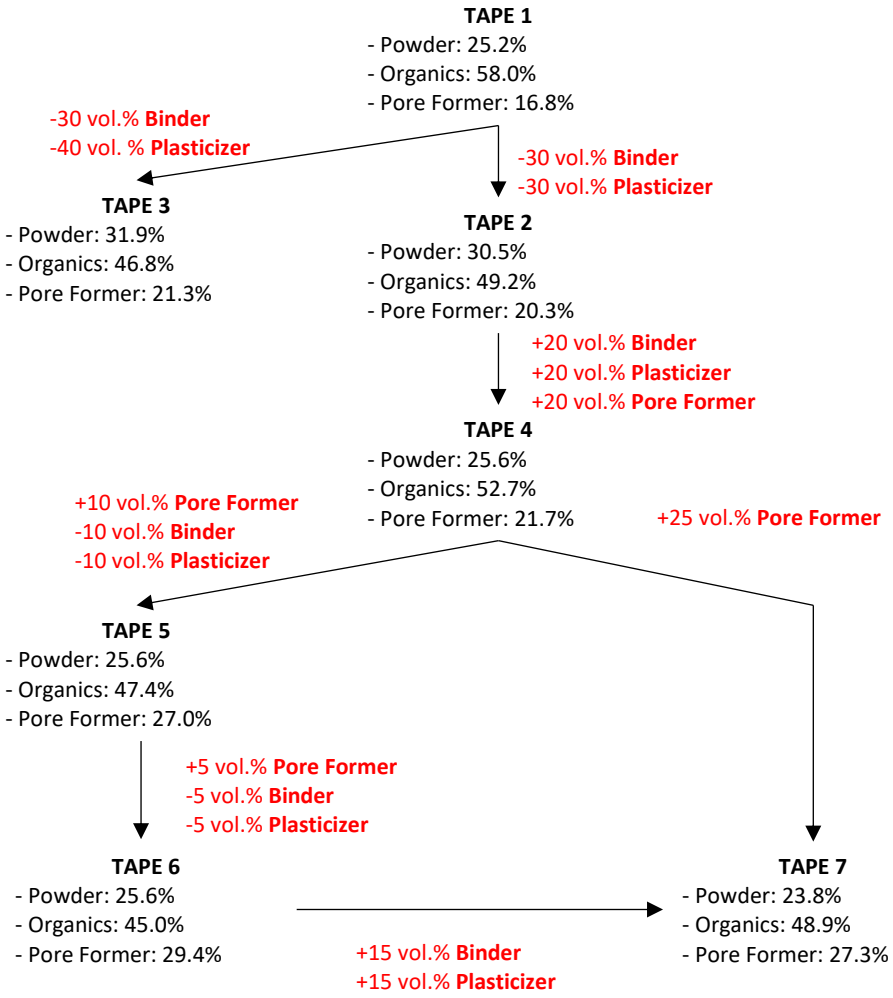

Figure 4.7 Flowsheet of the formulations studied. Volumes (vol. %) of the powder, organics (binder + plasticizer) and pore former fractions are reported for each tape. Modifications on the tape formulation are reported in red near each arrow, they refer to the volume modification (increase or decrease) of the tape components.

As expected the shrinkage of the membranes depends on the synergic effects of the three components of the slurry.

- Tape 2 and 3 displayed the lower shrinkage for the low organics content and high solid fraction. The lower amount of pore former hindered the porosity of the support layer, while the membrane layer had a low density value as a consequence of the low shrinkage percentage, as explained before.

- The high organics content of the Tape 4 promoted the shrinkage, and consequently the densification of the membrane layer. On the other hand, the low fraction of pore former hindered the support porosity.

- Tape 5 and 6 showed a good shrinkage percentage which led to a good densified membrane layer. Comparing the two formulations, the higher the organics content, the higher the shrinkage; while the higher the pore former fraction, the higher the support porosity. This means that the small porosity led by the binder and plasticizer burn-out after the debinding, is removed during sintering increasing the shrinkage of the membrane.

- Tape 7 displayed the highest support porosity and the highest densification of the membrane layer thanks to its optimised formulation and balance between organics/pore former contents.

Table 4.2 summarises the compositions of the tapes and the characteristics of each membrane after sintering: shrinkage, porosity of the support layer and density of the membrane layer.

Table 4.2 Volume composition of the green tapes (vol. %) and properties (shrinkage, support porosity, membrane density) of the membranes sintered at 1550°C for four hours, using BCZY as Ba-source.

Tape	Powder (vol. %)	Organics (vol. %)	Pore Former (vol. %)	Shrinkage (%)	Support Porosity (%)	Membrane Density (%)
1	25.2	58.0	16.8	-	-	-
2	30.5	49.2	20.3	24.7 ± 0.1	29.4 ± 2.3	87.1 ± 0.8
3	31.9	46.8	21.3	24.6 ± 0.2	29.5 ± 2.5	87.0 ± 0.7
4	25.6	52.7	21.7	27.5 ± 0.2	25.4 ± 2.9	98.3 ± 0.6
5	25.6	47.4	27.0	26.7 ± 0.4	35.3 ± 3.8	99.0 ± 0.5
6	25.6	45.0	29.4	26.3 ± 0.2	34.9 ± 3.6	98.9 ± 0.3
7	23.8	48.9	27.3	27.1 ± 0.1	36.2 ± 3.2	99.2 ± 0.3

Figure 4.8 reports ternary diagrams of the tapes as a function of the shrinkage (a), the porosity of the support layer (b), and the density of the membrane layer (c).

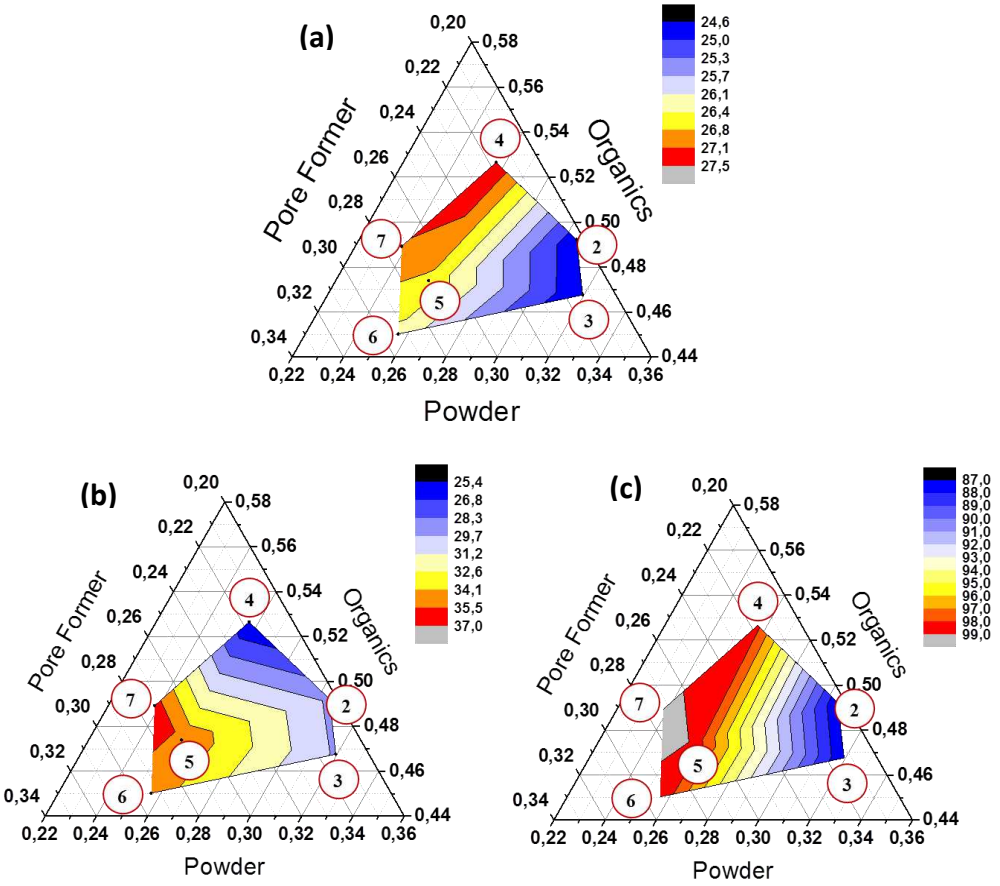

Figure 4.8 Ternary diagrams of the shrinkage (a), support porosity (b) and membrane density (c) of the samples depending on the green support layer formulation. In the red circles are reported the number of the tape used as support.

Figure 4.9 reports the SEM micrographs obtained detecting the secondary and back scattered electrons of the polished cross sections of the membranes with Tape 2, 4 and 7 as support layers.

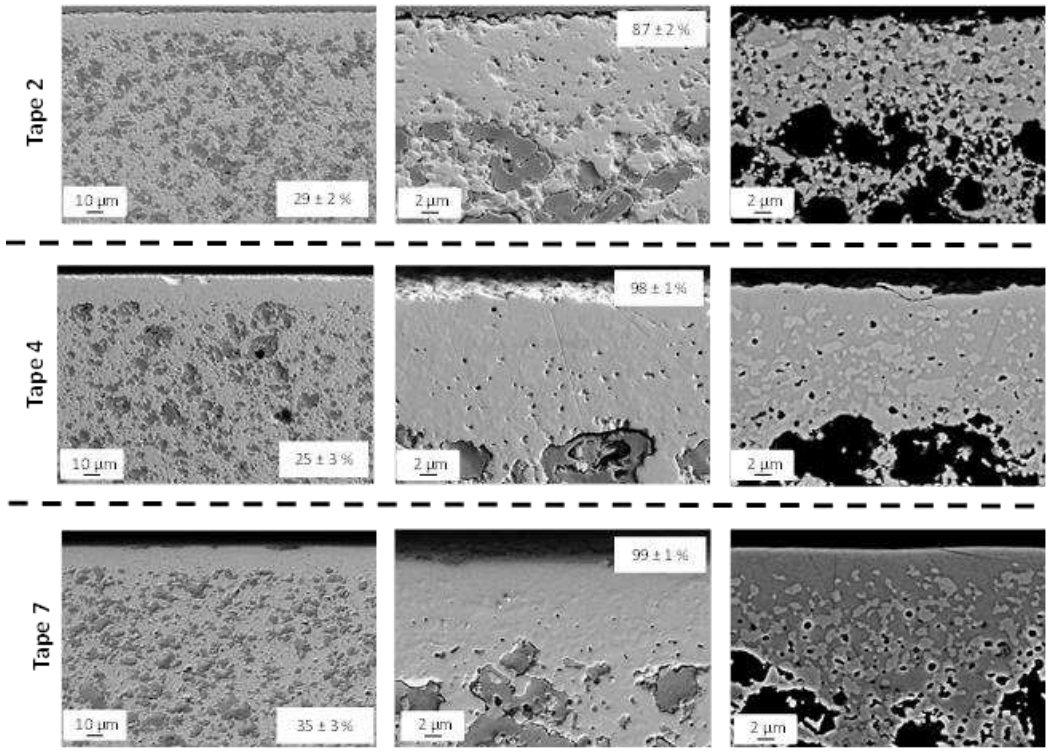

Figure 4.9 SEM micrographs of the polished fractures of the membranes sintered at 1550°C for four hours with BCZY powder using Tape 2, Tape 4 and Tape 7 as porous supports.

The densification of the membrane layer was improved from Tape 2 to Tape 4, as a consequence of the higher shrinkage of the latest. The back-scattered analysis performed on the polished membrane layer revealed the presence of the mix- single phase at the top of the membrane previously seen for the BCZY-supported samples. Its presence can be correlated with the shrinkage value of the membrane. In fact, the mix-phase was detected for membranes with high shrinkage values (Tape 4 and Tape 7), while was not visible for the Tape 3, which displayed a lower shrinkage percentage, and consequently, a lower densification of the membrane layer. Therefore, results suggest that the formation of the mix-phase is promoted by the physical contact between the BCZY and GDC particles. This is in accordance with the solid-state reaction hypothesis explained in the previous paragraph for the BCZY-supported membranes.

5.5.2 Sintering aid amount effect

The sintering aid content was increased to enhance the membrane layer densification aiming at lowering the sintering temperature as at 1550°C an undesired mix-phase is formed. In fact, lowering the sintering temperature may avoid the diffusion processes that take place during the solid-state reaction.

To study the influence of the amount of the sintering aid (ZnO) in the tape formulation, two other tapes were produced with 1 wt.% and 2wt.% of ZnO respect to the BCZY-GDC powders. Tapes after drying were defect-free and they looked the same of the thin BCZY-GDC tape shown in the previous Paragraph 5.3.

The thin layers were then laminated with the support layers in order to obtain green asymmetric membranes, which underwent the process previously described (Figure 4.5). Figure 4.10 depicts the SEM micrographs of the polished cross section of the membranes after sintering (1550°C for four hours) with Tape 2, 4, and 7 as porous supports and with different ZnO content in the membrane layer.

Results showed that the 1 wt.% of ZnO enhanced the densification of the membrane layer. This effect was particularly appreciable for the Tape 2, which had the minor shrinkage percentage, indicating that the slight increase of the ZnO counterbalanced the limited shrinkage of the supporting layer. As the membrane shrinkage increased, the effect of the sintering aid content was less pronounced.

ZnO content higher than 1wt% did not significantly improved the densification of the membrane layer.

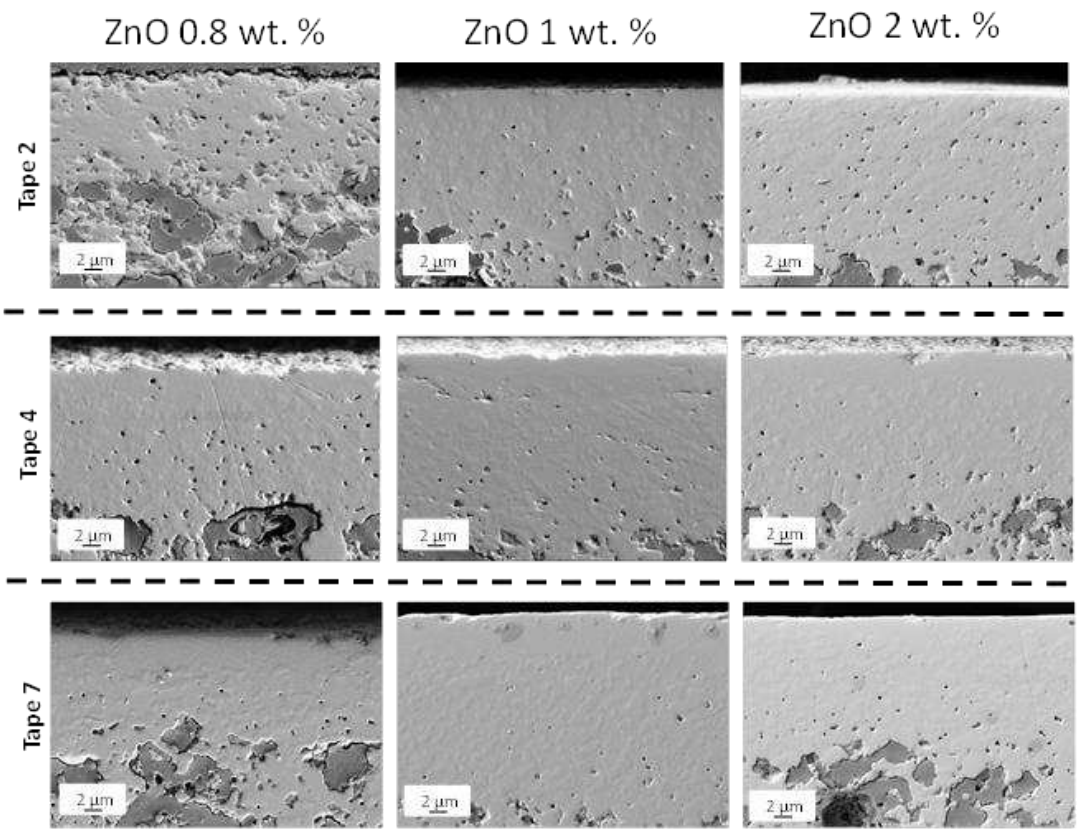

Figure 4.10 SEM micrographs of the polished fractures of the membranes sintered at 1550°C for four hours with BCZY powder with different amount of sintering aid and using Tape 2, Tape 4 and Tape 7 as porous supports.

Moreover, the introduction of 2 wt.% of ZnO other than be useless it could also be detrimental for the proton conductivity of the BCZY phase. In literature is reported[26,28,35,49] that the excess of Zn^{2+} in the perovskite lattice hinders the proton conductivity due to a proton-trapping effect. In fact, Zn^{2+} has the suitable radius ($r_{cationic}$ =0.74 Å) to replace the Zr^{4+} ($r_{cationic}$ = 0.72 Å) with a consequent formation of an effective -2 charge in the BO_6 octahedron which may be the responsible of the H^+ trapping:

$$ZnO \rightarrow Zn''_{Zr} + O_O + V''_{Ba} + 2\,V_{\ddot{O}} \qquad (4.1)$$

In conclusion, the asymmetric membrane formed by Tape 7 as support layer and BCZY-GDC with 1 wt.% as membrane was found to represent the best combination for obtaining hydrogen separation membranes.

Nonetheless the membrane phase purity was not obtained with the BCZY as Ba source. As already explained, to avoid Ba loss membranes were covered with BCZY powder and sintered at 1500°C for four hours. The asymmetric membrane was characterized through SEM and XRD analyses. The SEM analyses of the back scattered electron of the polished fracture were used to determine the presence and distribution of the BCZY and GDC phases in the membrane layer, while the XRD analyses the different phase composition.

Figure 4.11 reports the SEM micrographs of the fresh fractures and of the polished cross sections of the membrane sintered using BCZY as Ba-source during the sintering process.

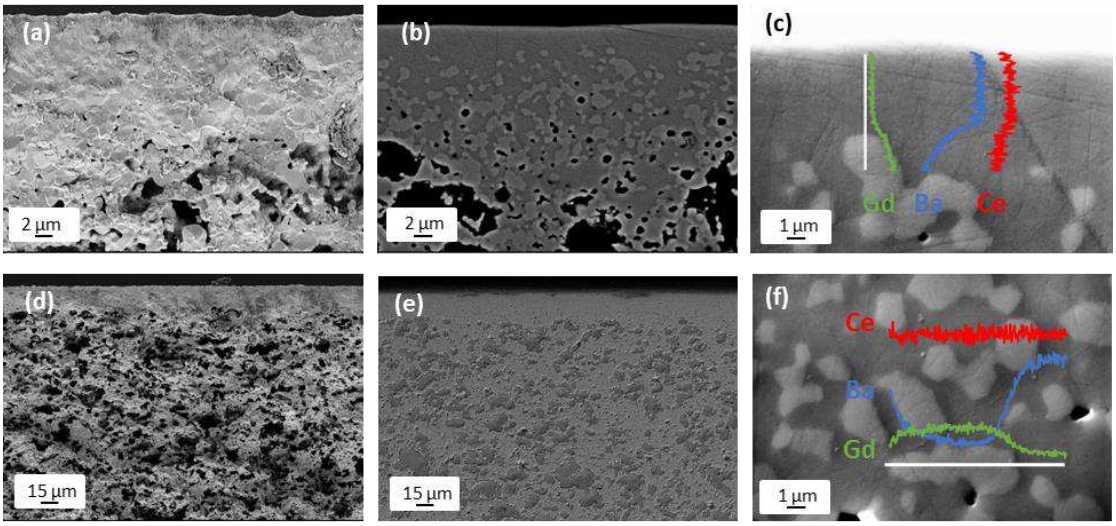

Figure 4.11 SEM micrographs at different magnification of (a) and (d) the fresh cross section, (b) and (e) of the polished cross sections of the BCZY-GDC asymmetric membrane sintered with BCZY powder as Ba-source. EDS scan lines of (c) the top part and (f) of the central part of the cer-cer dense layer.

The support layer displayed a good porosity, while the membrane layer was dense. Figure 4.11 (b) shows the backscattered SEM micrograph of the dense membrane layer. The light grey areas are the GDC phase, while the dark areas the BCZY. The topography of the polished cross sections (c) and (f) were due to the different hardness of the material: since the GDC is harder than BCZY, it is less prone to polishing and therefore remains more pronounced in the micrograph. This effect was already reported for similar systems by Ricote et al.[18] and Ivanova et al.[50]

Figure 4.11 (b) and (c) show a 1.7 ± 0.2 µm-thick dark grey layer on the top of the dense membrane, while the two BCZY and GDC distinct phases are still detected in the inner part of the membrane layer. The Ba- and Gd-EDS scanlines in Figure 5.1 (f) revealed that no interdiffusion between the two phases occurred in the central part of the material.

To better characterise the phase and the chemical composition of the dense surface, SEM with EDS element scan lines (Figure 4.12 (a)) and XRD analyses (Figure 4.12 (b)) were performed on the dense surface.

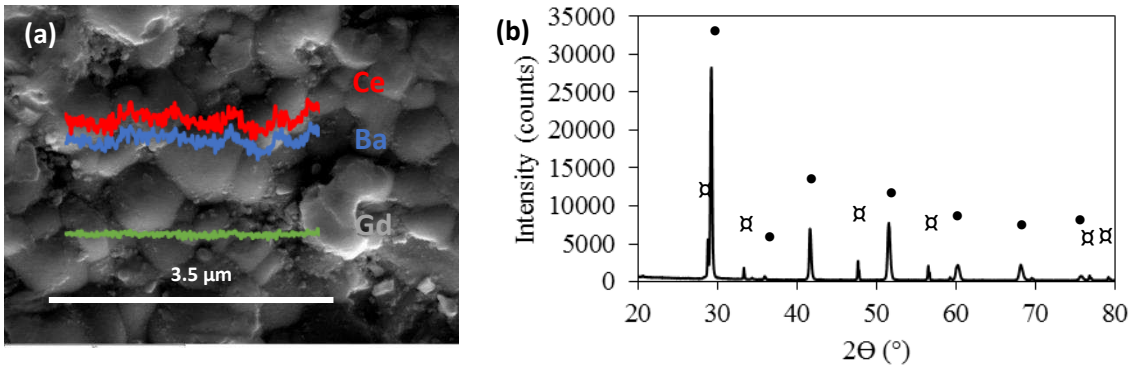

Figure 4.12 SEM micrograph and Ba, Ce and Gd elements EDS linescan distribution on the dense surface and XRD analysis of the dense layer surfaces of the membrane sintered with BCZY as Ba-source. BCZY and GDC phases are denoted with the symbol (•) and (¤) respectively.

EDS line scans revealed the even distribution of the Ba, Ce and Gd elements on the dense surface, confirming the presence of a mix-single phase previously seen with the polished fracture in Figure 4.11 (c).

Hereafter, the membrane sintered under these conditions is labelled as "single phase" membrane.

The Rietveld refinements of XRD analyses reported in Table 4.3, revealed that the dense surface was mainly composed by the perovskite BCZY phase (orthorhombic, s.g. Pmcn) (89.5%), with a lower content of the fluorite GDC one (cubic, s.g. Fm3m) (10.5%).

As indicated before, the formation of the new phase is ascribed to the Ba-source used during the sintering step. In fact, part of the high amount of Ba released by the BCZY source dissolved into the BCZY and GDC lattices promoting the formation

of a single mix-phase on the top of the membrane layer. This solid-state reaction was also seen in the BCZY-supported asymmetric membranes.
In the next paragraphs the attempts made to obtain a bi-phasic membrane layer are described and discussed.

5.5.3 BCZY-GDC phase purity

Mechanical abrasion

Since the solid-state reaction takes place in the superficial portion of the membrane, a polishing step is commonly introduced in bulk materials to eliminate the mix phase obtaining a thinner membrane layer with the dual phase composition. Therefore, the presence of the undesired single-phase layer was checked performing XRD experiments on the dense surface of the membrane after being polished with a SiC abrasive paper.
Figure 4.13 shows the SEM images of the polished cross section of the as sintered membrane and after being polished two times. The as sintered membrane had a layer of 2,5 μm of single phase nearby the surface. XRD analysis (Figure 4.13) revealed that the pattern of that material is the same of the one obtained with the BCZY-supported membranes. After the removal of 5 μm of materials by polishing peaks ascribable to the fluorite GDC phase appeared. The most intense peak of the fluorite phase was not detected, probably because it was under the BCZY most intense peak at 28.9°. After removal of 13 μm of material, the GDC peaks become more intense, and the most intense peak at 28.5° more evident. This data assessed a compositional gradient starting from the surface to the lower part of the dense membrane layer.
However, two drawbacks emerged following this procedure:

- The ratio between the two phases of the cer-cer are not 50:50; the XRD pattern obtained after the removal of 13 μm of material is very different from the one previously obtained for the BCZY-supported membrane using BCZY-GDC as barium source. In particular in the latter case, the fluorite

peaks were more intense, and the two more intense peaks were well distinguishable.

- Preliminary room-temperature He-leak tests showed that the polishing procedure was detrimental for the gas tightness of the membrane, making impractical the polished membranes for the selective H_2 separation for these architectures.

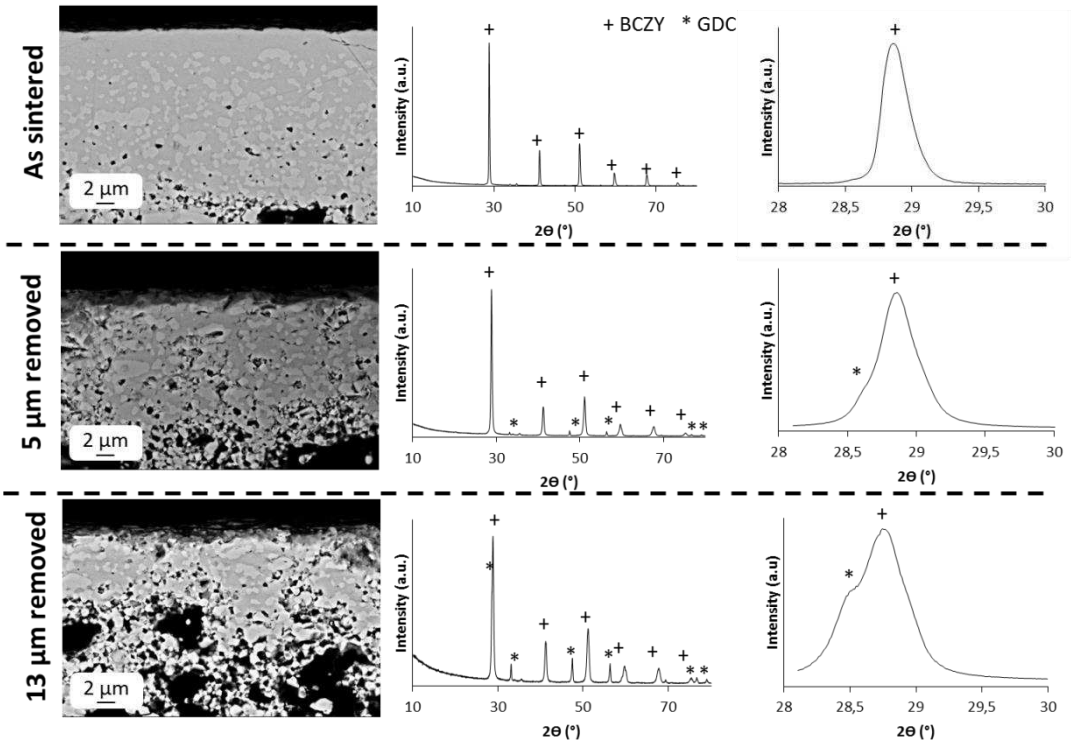

Figure 4.13 SEM micrographs of the polished fractures of the membranes as sintered and after different steps of the abrasion process. XRD analyses performed on the dense surface after each polishing step is also reported on the side of the corresponding SEM micrograph.

Membranes sintered with BCZY-GDC powder as Ba-source

To avoid the solid-state reaction which led to the undesired single mix phase on the top of the dense membrane layer, the BCZY-GDC mix was used instead of the BCZY one as Ba-source. The process used was the same previously described and reported in Figure 4.5.

Like the case of the BCZY-supported membranes, the less reactive BCZY-GDC Ba-source allowed the dual phase retention within the whole membrane thickness.

Figure 4.14 reports the SEM micrographs of the fresh fractures and of the polished cross sections of the membrane sintered using the BCZY-GDC mixture as Ba-source during the sintering process.

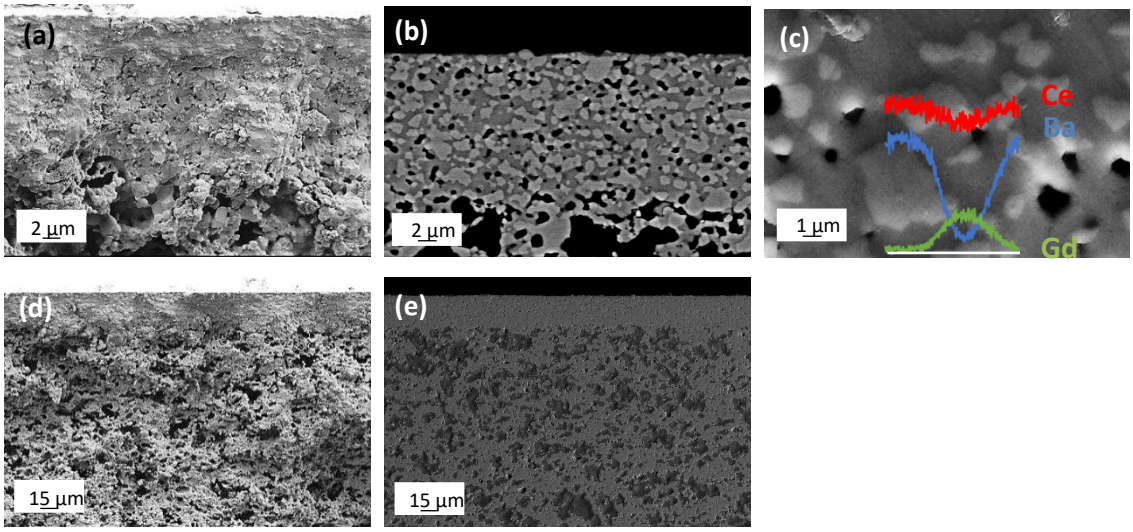

Figure 4.14 SEM micrographs at different magnification of (a) and (d) the fresh cross section, (b) and (e) of the polished cross sections of the BCZY-GDC asymmetric membrane sintered with BCZY-GDC powders as Ba-source. EDS scan lines of (c) of the central part of the cer-cer dense layer.

The SEM micrographs revealed that the membrane sintered with BCZY-GDC as Ba-source had a less dense membrane layer than the one sintered with BCZY. This effect might be due to the lower amount of Ba released in the sintering atmosphere by the BCZY-GDC source. On the other hand, the membrane showed a complete phase retention through the whole membrane thickness. In fact, the back scattered electrons revealed an even distribution of the two phases. The EDS analysis reported in Figure 4.15 (a) and the XRD analysis reported in Figure 4.15 (b) confirmed the presence of the two BCZY and GDC phases on the dense layer. Hereafter, the membrane sintered under these conditions is labelled as “dual phase” membrane.

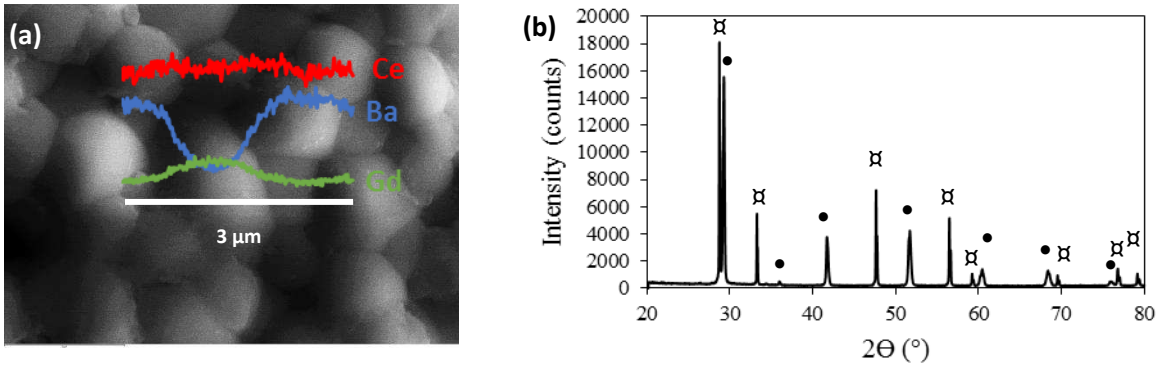

Figure 4.15 (a) SEM micrograph and Ba, Ce and Gd elements EDS linescan distribution on the dense surface and (b) XRD analysis of the dense layer surfaces of the membrane sintered with BCZY-GDC as Ba-source. BCZY and GDC phases are denoted with the symbol (•) and (¤), respectively.

The EDS scan lines for the Ce, Ba and Gd elements confirmed the presence of both BCZY and GDC grains on the dense surface, while the XRD pattern confirmed the presence of both the perovskite and fluorite structures.

Table 4.3 reports the Rietveld refinements of the diffractometric patterns of the "single phase" and "dual phase" membranes of Figure 4.12 (b) and 4.15 (b), respectively.

Table 4.3 Phase composition and lattice parameters of the BCZY and GDC phases from XRD analyses on the dense surface of the membranes considered in this study. Standard deviation within parentheses.

Membrane	Phases	System	Space group	a (Å)	b (Å)	c (Å)	V (Å^3)
"single phase"	BCZY, perovskite	Othorhombic	Pmcn	8,7429(8)	6,1829(5)	6,1514(5)	332,53(7)
	GDC, fluorite	Cubic	Fm-3m	5,4231(4)			159,50(3)
"dual phase"	BCZY, perovskite	Othorhombic	Pmcn	8,6853(4)	6,1719(3)	6,1448(3)	329,39(2)
	GDC, fluorite	Cubic	Fm-3m	5,4218(1)			159,38(1)

The data highlight that the perovskite unit-cell volume for the sample sintered with BCZY was (332.5 Å^3), slightly higher than that obtained for the membrane sintered with BCZY-GDC (i.e., V = 329.4 Å^3). This confirms the hypothesis of the Ba

dissolution in the BCZY and GDC lattices explained before. In fact, the Ba dissolution into the lattice lead to cell expansion, being Ba^{2+} is the biggest cation among the elements constituting the BCZY-GDC material.

Profilometer analysis (Figure 4.15 (b)) revealed that the sintered membrane (diameter ≈ 20 mm) was sufficiently flat to be used as planar asymmetric membrane for H_2 separation.

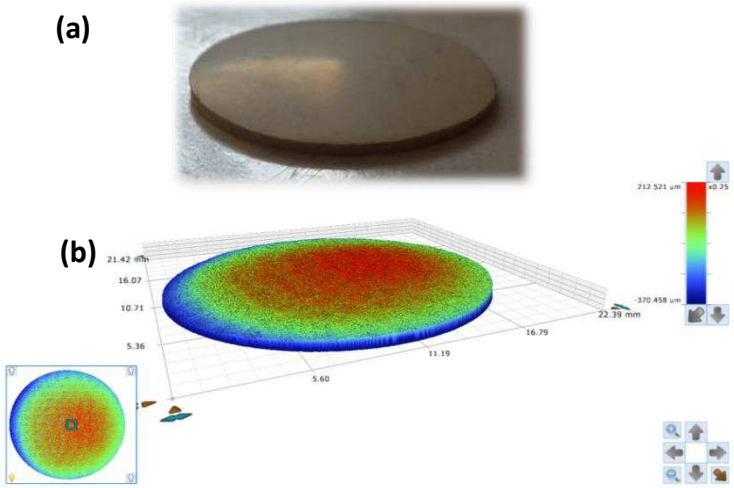

Figure 4.15 (a) Picture and (b) profilometer image of the asymmetric membrane sintered at 1550°C with BCZY-GDC as Ba-source.

In addition, even though the densification degree was not complete, room-temperature He-leak tests assessed the gas tightness of the asymmetric membrane.

In conclusion, this study proves that the formulation of the green support layer highly affects the sample shrinkage and, as a consequence, the densification of the membrane layer. The increase of the ZnO content from 0.8 wt % to 1 wt % enhanced the densification of the active layer while 2 wt. % of ZnO did not imply any further improvement. The formulation optimization and the sintering atmosphere modification allowed to obtain a sufficiently dense 20 µm-thick cer-cer membrane layer supported by a porous (36 %) 750 µm-thick BCZY-GDC layer. The asymmetric membrane was planar and crack-free, therefore suitable for H_2 separation application.

In the next paragraph, the H_2 separation measurements of the asymmetric BCZY-GDC membranes are reported. Either the "single phase" membrane (with the mix-phase on the top of the dense membrane layer) and the "dual-phase" one (with both BCZY and GDC on the dense surface) have been tested to verify the effect of the phase retention on the permeation properties.

5.6 Hydrogen permeation measurements

In the previous paragraph, asymmetric BCZY-GDC membranes showing the required characteristics for hydrogen separation application were obtained. Particular focus was given to the effects of the sintering temperature and atmosphere on the microstructure and phase retention. In this paragraph are reported the functional characterizations performed during the internship in the group of prof. J. M. Serra at the Politécnico de Valéncia.

Different samples were characterised:

- membranes with the mix-phase on the top of the dense layer ("single phase") and membranes with both $BaCe_{0.65}Zr_{0.20}Y_{0.15}O_{3-\delta}$ and $Ce_{0.8}Gd_{0.20}O_{2-\delta}$ phases on the top on the membrane layer ("dual phase") (Figure 5.1).

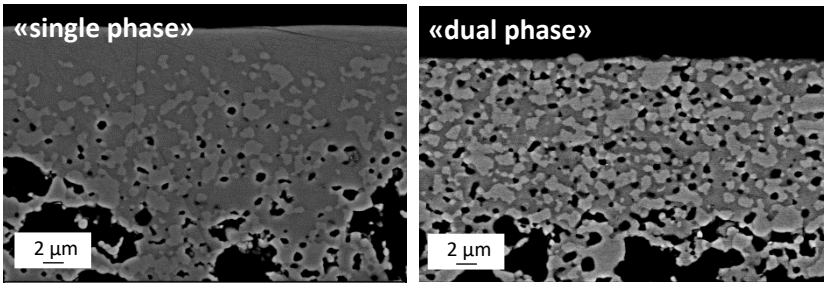

Figure 5.1 SEM micrographs of the membranes tested, the "single phase" one on the left and the "dual phase" one on the right.

The two membranes had the same support and thin layer compositions, the only difference was the sintering atmosphere that modified the surface composition as discussed in the previous paragraph. The"single phase" membrane was sintered with BCZY as Ba-source, while the "dual phase" with the BCZY-GDC mixture;

- membranes with both support and membrane layers catalytically activated with Pt.

The permeation properties of the membranes were thoroughly studied by analysing the influence of the environment humidification degree on the hydrogen permeation:

- C1, only the feed side humified;
- C2, both sides humified,
- C3, only the sweep side humified.

5.6.1 Influence of the phase composition

The effect of the phase composition on the hydrogen permeation was studied measuring the hydrogen flux of the membrane sintered with BCZY and BCZY-GDC as Ba-sources. Both surfaces were activated in order to avoid as much as possible the limitations of H_2 surface exchange and to evaluate the effect of the asymmetric membrane architecture on the H_2 permeation. The dense layer of the membranes was coated with a 20 μm thick Pt layer, while the support layer was catalytically activated with the deposition of Pt nanoparticles obtained calcining the salt precursor at 900°C for two hours, as described in Chapter 4 (Figure 5.2).

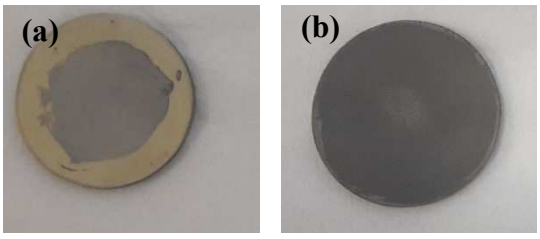

Figure 5.2 Pictures of (a) the dense Pt-activated layer and (b) of the support layer after calcination.

Figure 5.3 shows (a) the SEM micrograph and (b) EDS analysis carried out on the support layer to evaluate the Pt distribution after calcination of the Pt precursor salt.

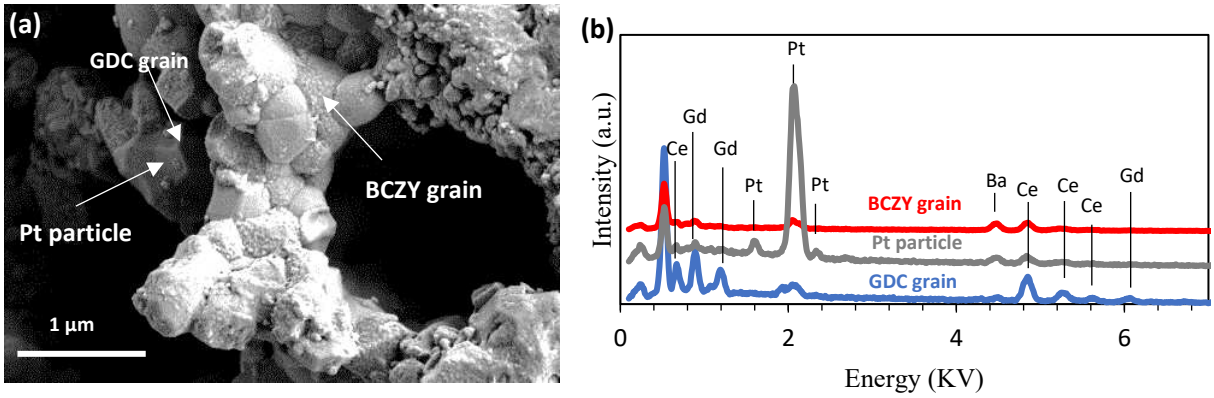

Figure 5.3 (a) SEM micrograph of the fracture of the Pt-impregnated porous support and (b) EDS spectra of the GDC and BCZY grains and of the Pt particle.

The microstructural analyses revealed Pt particles with bimodal size: finer (22.4 ± 0.6 nm) on the BCZY phase and larger (180.7 ± 10.4 nm) placed onto the GDC phase or at the top of the already Pt activated BCZY phase. EDS spectra confirmed the chemical nature of the particles detected through SEM analyses.

Figure 5.4 depicts the H_2 permeation results for the two Pt activated asymmetric composite membranes tested.

As expected, H_2 fluxes increased with temperature for all the membranes. The "single phase" membrane showed an H_2 flux as high as 0.07 mL min^{-1} cm^{-2} at 750°C. According to the Wagner equation, if the permeation flux is limited by the bulk diffusion, the H_2 flux increases linearly with the reciprocal of the membrane thickness. Contrarily to what postulated by the abovementioned equation, the hydrogen flux value was even lower than the one obtained with a 650 µm-thick BCZY-GDC membrane under the same conditions by Rebollo et al. (≈ 0.25 mL min^{-1} cm^{-2})[1]. The lower flux may be caused by the inefficient porous support activation. In fact, as shown in Figure 5.3 only the BCZY phase was fully activated with the Pt precursor impregnation, while the Pt thin layer screen printed on the membrane part assures a complete surface activation.

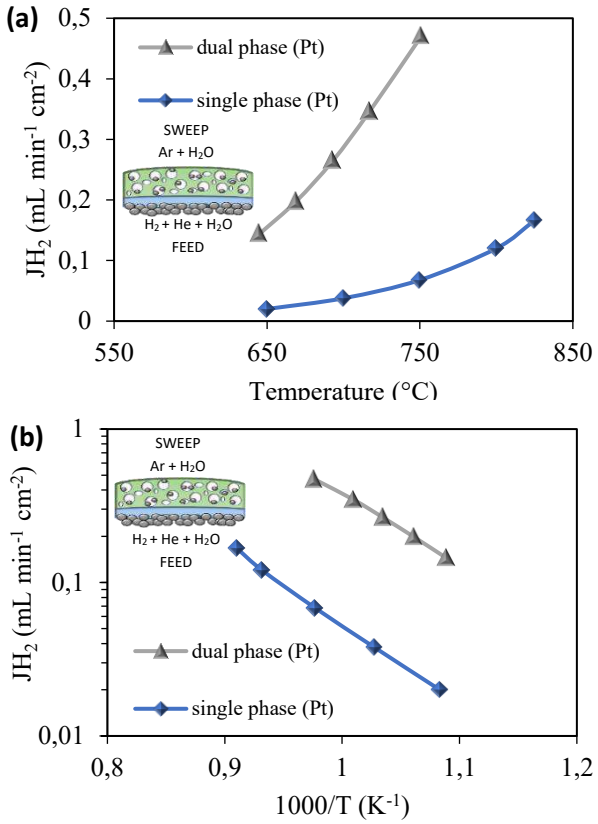

Figure 5.4 H_2 flux (mL min^{-1} cm^{-2}) (a) as a function of temperature and (b) as a function of reciprocal temperature for the dual phase membrane with (dual phase, Pt) and for the membrane with the single mix-phase on the top of the dense layer (single phase). Measurements were done with both membrane sides humified (C2 conditions) feeding the 50% of H_2 in He.

The lower flux might also due to the poor ambipolar conductivity of the single mix-phase layer on the top of the membrane, that hinders the proton/electron migration. As discussed in the previous paragraph, the EDS and XRD analyses assessed the presence of a Ba-Ce-Gd-Y-Zr-based orthorhombic perovskite at the top of the dense membrane. Even if the electrochemical characterization of the undesired layer was not possible, it can be assumed for it the same poor ambipolar conductivity of the doped barium cerate materials. In fact, the H_2 flux value of the membrane is close to those reported for asymmetric mixed proton electron conductor membranes (MPECs), where the low electron conductivity limits the hydrogen permeation. For example, Wei et al.[51] reported an H_2 flux of 0.05 mL min^{-1} cm^{-2} at 750°C feeding 50% of H_2 in He for the asymmetric $BaCe_{0.85}Tb_{0.05}Zr_{0.10}O_{3-\delta}$ membrane (50 µm-thick dense layer), while Sun et al.[52] reported an H_2 flux of 0.03 mL cm^{-2} min^{-1} with

40% of H_2 in N_2 at 800°C for a 21 μm-thick dense $Ce_{0.8}Sm_{0.2}O_{2-\delta}$ membrane supported on a NiO - $Ce_{0.8}Sm_{0.2}O_{2-\delta}$ porous layer.

The dual phase composition allowed a significant improvement of the H_2 flux, reaching values as high as 0.47 mL min^{-1} cm^{-2} at 750°C, indicating that the mix-layer formed by solid-state reaction during sintering is detrimental for the ambipolar conductivity properties of the membrane. The value measured is roughly the double of the 650 μm-thick membrane of the same composition under the same conditions. The flux registered is higher than that reported by Zhu et al.[53] testing an asymmetric Ni-$BaCe_{0.7}Zr_{0.1}Y_{0.2}O_{3-\delta}$ cer-met membrane (0.15 mL min^{-1} cm^{-2} at 750°C feeding 50% of H_2 in N_2 for a 30μm-thick membrane). Since the ambipolar conductivity of the cer-met membrane is higher than the cer-cer one, the low flux reported by Zhu could be explained with the low porosity value of the cer-met support layer (20%). Such result underlines the key role of the membrane microstructure on its hydrogen separation performances. Table 5.1 summarizes the performances of similar membranes (cer-cer and mixed proton electron conducting (MPEC) asymmetric membranes) found in literature. The symmetric 650 μm-thick BCZY-GDC membrane is added for the sake of comparison.

The asymmetric dual phase BCZY-GDC membrane reported in this work presents the best performances recorded up to now for the H_2 separation application among the ceramic membranes and comparable with the most efficient cer-met ones (but with considerable higher stability in operation).

H_2 flux under C2 conditions can be produced by two different processes. i) the transport of protons through the membrane from the high H_2 partial pressure side to the low partial pressure side; and ii) through the water splitting reaction (WSR) in the sweep side thanks to the oxide-ion conduction of the fluorite phase. The WSR contribution was already studied for cer-cer composite membranes where a ceria-based material was used as electron conducting phase[1,50].

Table 5.1 Summary of performances of different asymmetric membranes.

Membrane Material	Support Material	Thickness dense membrane (μm)	Gas atmosphere Feed - Sweep	T (°C)	J_{H2} (mL min^{-1} cm^{-2})	Ref.
$SrCeO_3$-based hydrogen separation membranes						
$SrCe_{0,95}Y_{0,05}O_{3-\delta}$	NiO - $SrCe_{0,95}Y_{0,05}O_{3-\delta}$	50	dry 80% H_2 in He - Ar	950	0.1	[48]
$SrCe_{0,95}Tm_{0,05}O_{3-\delta}$	$SrCe_{0,95}Tm_{0,05}O_{3-\delta}$	150	dry 10% H_2 in He - 20% O_2 in N_2	900	0.16	[54]
$SrCe_{0,7}Zr_{0,2}Eu_{0,1}O_{3-\delta}$	NiO - $SrCe_{0,7}Zr_{0,2}Eu_{0,1}O_{3-\delta}$	33	dry 100% H_2 - He	900	0.23	[55]
			wet (3% H_2O) H_2 - He	900	0.21	
$BaCeO_3$-based hydrogen separation membranes						
$BaCe_{0,85}Tb_{0,05}Zr_{0,1}O_{3-\delta}$		20 / 50	dry 50% H_2 in He - Ar	900	0.22 / 0.08	[51]
$BaCe_{0,65}Zr_{0,20}Y_{0,15}O_{3-\delta}$ - $Ce_{0,80}Gd_{0,20}O_{2-\delta}$	***$BaCe_{0,65}Zr_{0,20}Y_{0,15}O_{3-\delta}$ - $Ce_{0,80}Gd_{0,20}O_{2-\delta}$***	***20 / 20****	***wet 50% H_2 in He - wet Ar***	***750***	***0.47 / 0.07****	***This thesis***
$BaCe_{0,65}Zr_{0,20}Y_{0,15}O_{3-\delta}$ - $Ce_{0,80}Gd_{0,20}O_{2-\delta}$		650	wet 50% H_2 in He - wet Ar	755	0.27	[1]
Ni-$BaCe_{0,7}Zr_{0,1}Y_{0,2}O_{3-d}$	Ni-$BaCe_{0,7}Zr_{0,1}Y_{0,2}O_{3-d}$	30	wet 50% H_2 in N_2 - Ar	750	0.15	[53]
Ni-$BaCe_{0,7}Zr_{0,1}Y_{0,1}Yb_{0,1}O_{3-d}$	Ni-$BaCe_{0,7}Zr_{0,1}Y_{0,1}Yb_{0,1}O_{3-d}$	44	wet 50% H_2 in He - N_2	750	0.46	[56]
Other ceramic systems						
$La_{26,78}W_{5,22}O_{55,83}$	$La_{26,78}W_{5,22}O_{55,83}$	25	wet 10% H_2 in Ar - Ar	1000	0.14	[57]
$Ce_{0,8}Sm_{0,2}O_{2-\delta}$	NiO - $Ce_{0,8}Sm_{0,2}O_{2-\delta}$	35	dry 40% H_2 in N_2 - Ar	900	0.007	[52]

* ”single phase” membrane

From the H_2 flux reported in Figure 5.4 (b), activation energies were calculated (Table 5.2).

Table 5.2 Activation energies obtained from the H_2 permeation measurements with both sides humified (C2 conditions) and feeding the 50% of H_2 in He. For sake of comparison, the Ea of the 650 µm-thick membrane is also reported.

Sample	**Temperature Range**	**E_a (eV)**
BCZY-GDC (600 µm-thick, Pt)	T < 650°C	0,82
	T > 650°C	1,04
Asymmetric BCZY-GDC "dual phase" (Pt)	T < 700°C	0,79
	T > 700°C	0,97
Asymmetric BCZY-GDC "single phase" (Pt)	T < 700°C	0,99
	T > 700°C	1,1

Activation energies above 700°C are related to the prevailing oxide ion transport through the fluorite phase, while at lower temperatures the activation energies are lower for the higher contribution of the proton transport. Dual phase membrane displayed an E_a for the proton transport similar the one of the 650 µm-thick membrane. However, the E_a for higher temperatures is lower. This might be due to a lower contribution of the WSR because of the inefficient support activation. On the other hand, the asymmetric single-phase membrane displayed E_a higher than the other two membranes through the whole investigated temperature range.

5.6.2 Influence of the Pt catalytic activation

The influence of the Pt catalytic activation on H_2 permeation was studied measuring the H_2 flux of the bare and the Pt activate dual phase membrane. Figure 5.3 shows the H_2 permeation results.

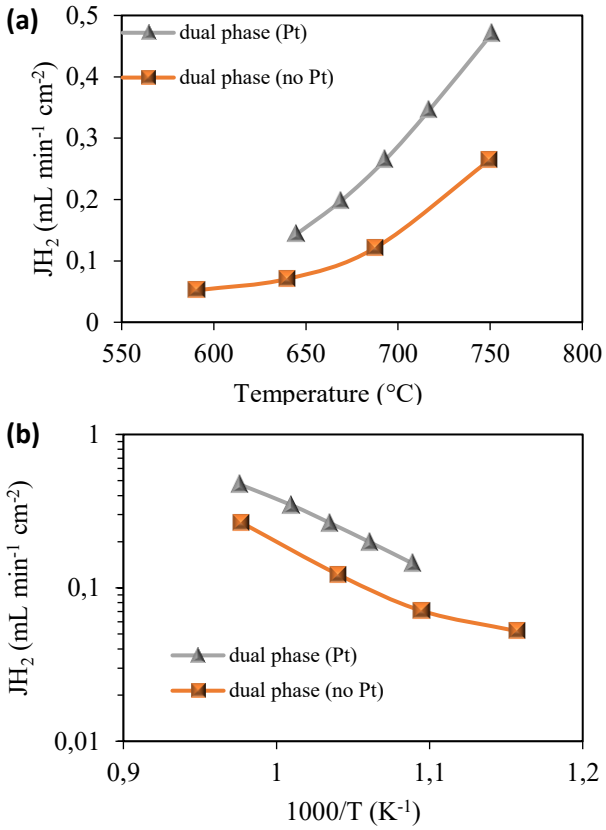

Figure 5.5 H_2 flux (mL min^{-1} cm^{-2}) (a) as a function of temperature and (b) as a function of reciprocal temperature for the bare (dual phase, no Pt) and the Pt activated (dual phase, Pt) membranes. Measurements were done with both membrane sides humified (C2 conditions).

The bare dual phase membrane showed an H_2 flux as high as 0.26 mL min^{-1} cm^{-2} feeding 50 % H_2 in He under C2 conditions at 750°C. This value is roughly the same of the Pt activated 650 µm-thick membrane, but it is one order higher than the un-activated 600 µm-thick one. In fact, under the same conditions, the symmetric membrane displayed a flux of 0.025 mL min^{-1} cm^{-2}. This comparison highlights the intrinsic high performances of the asymmetric membrane in comparison with the symmetric one. However, the H_2 flux improved by a reduction of thickness just by a factor of 10.4, which is lower than the expected factor of 30. This indicates that for the 20 µm-tick BCZY-GDC membrane the H_2 permeation is limited by surface exchange reaction rather than bulk diffusion. The difference is higher at lower temperature, where surface processes are slower. In fact, H_2 flux increased at 650°C by 104%, while at 750°C only by 77%. This is also confirmed by the higher E_a

values of the bare membrane than those of the Pt activated one in the whole investigated temperature range: E_a calculated from Figure 5.4 (b) under 700°C was 0.86 eV, while above 700°C was 1.1 eV.

To analyse the H_2 partial pressure effect on the bare and Pt activated membranes, gas mixtures of H_2/He with different ratio were fed to the dense membrane layer (20/80; 50/50; 80/20) and the corresponding H_2 flux are reported in Figure 5.6 (a) and (b) for the bare and Pt activated membranes, respectively.

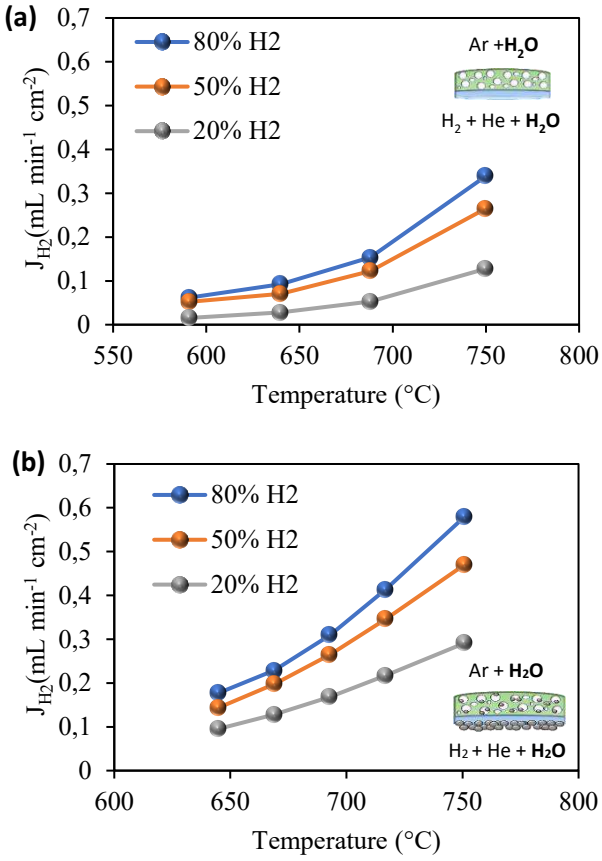

Figure 5.6 H_2 flux (mL min^{-1} cm^{-2}) as a function of temperature and H_2 partial pressure for (a) the bare (dual phase, no Pt) and (b) Pt activated (dual phase, Pt) membranes. Measurements were done with both membrane sides humified (C2 conditions).

The H_2 flux increases with increasing temperature and H_2 partial pressure, as postulated by the Wagner equation. As previously assessed by E_a measurements, also in this case that the difference between fluxes is more pronounced at lower temperatures.

5.6.3 Influence of the environmental humidification degree

Once assessed that the undesired layer on the top of the membrane highly affects the H_2 permeation, the effect of humidification was investigated for the bare and Pt activated "dual phase" membrane.

In this kind of membranes H_2 can be produced through two mechanisms: via WSR thanks to the oxide ion conduction of the fluorite phase, or by H_2 permeation through the membrane thanks to the ambipolar conductivity. To evaluate the transport mechanism that mainly contributes to the H_2 production, three different hydration configurations were used.

Figure 5.7 shows the H_2 permeation rates for the different humidification configurations as a function of temperature for (a) bare and (b) Pt activated membranes. Figure 5.7 (c) and (d) on the other hand, shows the H_2 permeation rates form the different humidification configuration as a function of time for the bare and the Pt activated membrane, respectively.

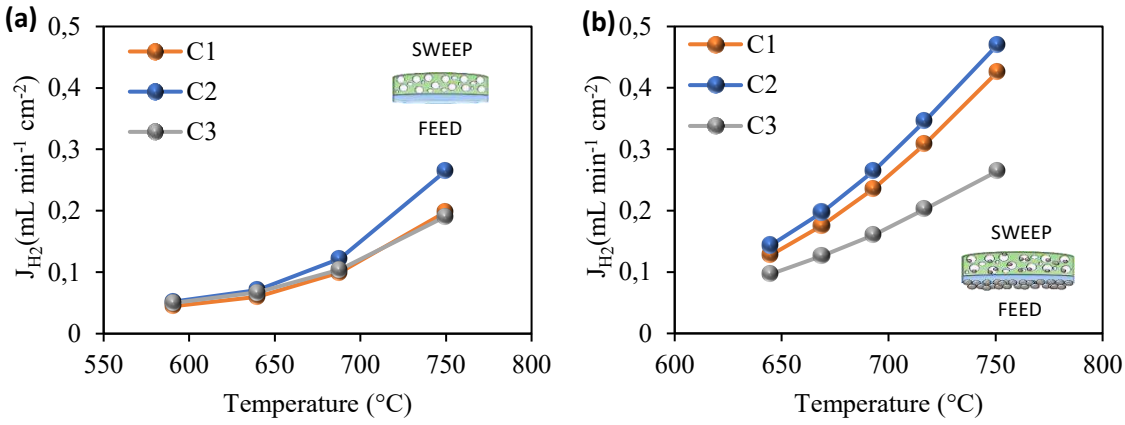

Figure 5.7 H_2 flux (mL min^{-1} cm^{-2}) as a function of temperature and humidification conditions (C1, only the sweep side humified; C2, both sides humified, C3, only the feed side humified) for (a) the bare ("dual phase", no Pt) and (b) Pt activated ("dual phase", Pt) membranes. Measurements were done feeding the dense layer with 50% of H_2 in He at 750°C.

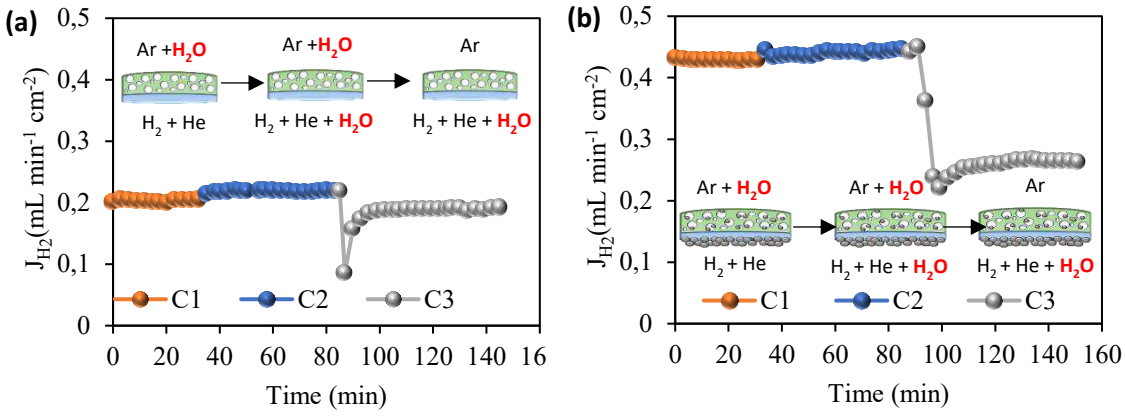

Figure 5.8 H_2 flux (mL min^{-1} cm^{-2}) as a function of time and humidification conditions for (a) the bare ("dual phase", no Pt) and (b) Pt activated ("dual phase", Pt) membranes. Measurements were done feeding the dense layer with 50% of H_2 in He at 750°C.

The catalytic activation with Pt increased the membrane's performances under all the hydration conditions studied. Changing from C1 to C2, the hydrogen flux slightly increased for both membranes. This effect is in contrast with the behaviour of the 650 µm-thick Pt activated BCZY-GDC membrane. In fact, under C1 condition (with the only sweep side humified) the WSR should be boosted up due to the higher O_2 partial pressure of gradient across the membrane. However, as showed in Figure 5.7 (a), when the only sweep side is hydrated, the maximum J_{H2} achieved by the bare membrane was 0.20 mL min^{-1} cm^{-2} feeding 50% of H_2 in He at 750°C, while when both sides were humified, J_{H2} increased to 0.26 mL min^{-1} cm^{-2}. A possible explanation of the unexpected behaviour may lay in the combination of different factors. Firstly, the hydration of both membranes layer led to a higher proton defect concentration in the perovskite lattice with consequent enhancement of proton conductivity. It is well known that the hydration of barium cerate materials promotes the formation of proton defect into the lattice with a consequent increased H_2 flux[18,32,58]. The second factor might be represented by the poor support activation. In fact, as depicted in Figure 5.3, the fluorite phase was not activated with Pt nanoparticles, therefore the contribution of the WSR was low. The lower H_2 flux means that the H_2 produced was not sufficient to overcome the lower H_2 permeation due to the uncomplete hydration of the membrane. In addition, the flux might be hindered by mass transfer resistance given by the porous support layer. This is confirmed by the fact that the Pt activated support showed the same

behaviour of the bare one. Therefore, the combination of these phenomena lowered the H_2 flux.

Drying the sweep stream, the J_{H2} values lowered again, because of the absence of the WRS contribution. Interestingly, the J_{H2} values of the bare membrane (0.19 mL min^{-1} cm^{-2}) was slightly lower that the Pt activated one (0.26 mL min^{-1} cm^{-2}) at 750°C. However, as reported in Table 5.3, the higher improvement achieved with the Pt activation was under C1 condition. This means that even if the GDC phase was not so well activated, the contribution of the WSR was boosted up by the Pt activation.

Table 5.3 Comparison between the J_{H2} obtained with the Pt activated membrane and the bare ones.

	Bare	**Pt activated**	**Increment**
	(mL min^{-1} cm^{-2})	(mL min^{-1} cm^{-2})	(%)
C1	0,1983	0,4264	**53,5**
C2	0,2652	0,4706	43,6
C3	0,1911	0,2646	27,8

To evaluate a possible effect of mass transfer resistance of the porous support, the sweep and feed composition were shift, to feed with hydrogen to the porous layer of the membrane.

Figure 5.9 shows the J_{H2} values when hydration conditions were changed from C2 to C1 feeding the 50% of H_2 in He at 750°C.

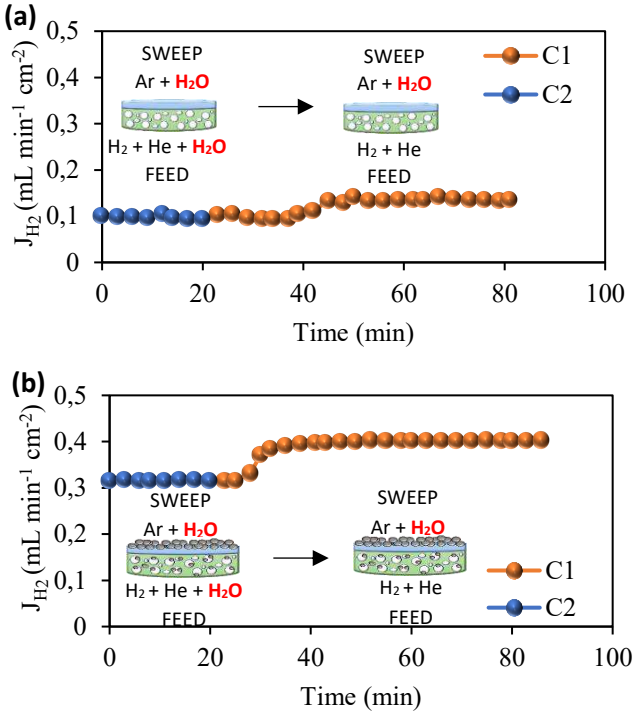

Figure 5.9 H_2 flux (mL min^{-1} cm^{-2}) as a function of time and humidification conditions (C1, only the sweep side humified; C2, both sides humified) for (a) the bare (dual phase, no Pt) and (b) Pt activated (dual phase, Pt) membranes. Measurements were done feeding the porous support layer with 50% of H_2 in He at 750°C.

As reported, feeding the porous support with dry H_2 in He sweeping the dense layer with humified Ar, lead to an increase of the H_2 flux. This means that in this asymmetric membrane architecture, the porous support offers mass transfer resistance. In fact, when the smooth and dense membrane layer was humified, the WSR contribution became appreciable thanks to the absence of mass transfer resistance.

5.6.4 Post-mortem characterization

After the permeation measurements, the membranes were investigated through SEM and XRD analyses. Figure 5.10 shows the SEM micrographs of the polished and fresh cross section of the single-phase membrane. EDS scan lines on the dense membrane revealed that no apparent alteration occurred during permeation tests. The presence of the cracks parallel to the dense surface is typically due to the stresses induced by the polishing process.

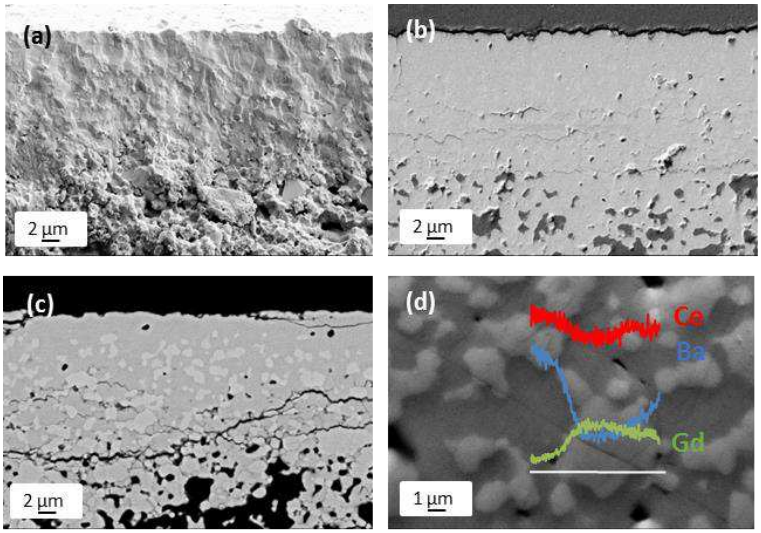

Figure 5.10 SEM micrographs of the polished and fresh fracture of the membrane after permeation measurements.

SEM micrographs of the fresh fracture depicted in Figure 5.11 showed that the Pt nanoparticles retained their morphology and distribution through the BCZY-GDC porous support, i.e. they are sited mainly on the BCZY phase.

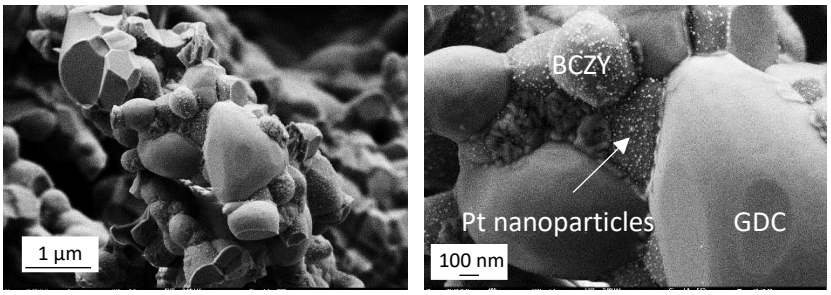

Figure 5.11 SEM micrographs of the fresh fracture of the Pt activated support of the "dual phase" membrane after permeation measurements.

Figure 5.12 shows the SEM micrographs of the polished and fresh cross section of the "single phase membrane" and the EDS scan lines (d).

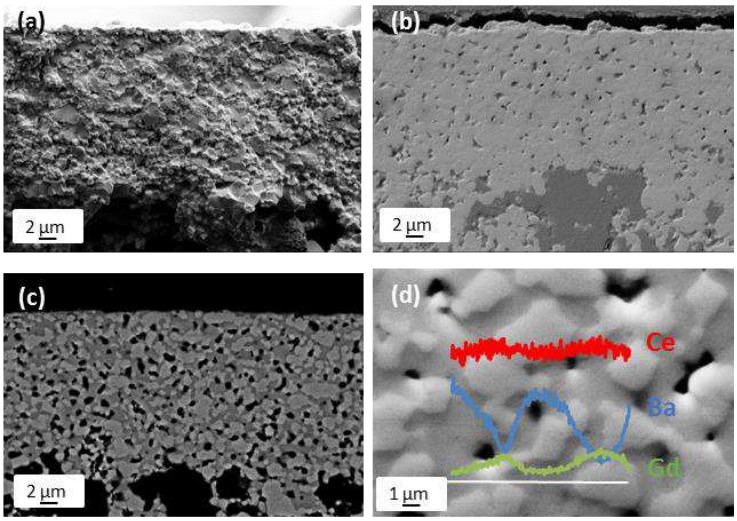

Figure 5.12 SEM micrographs of the polished and fresh fracture of the membrane after permeation measurements.

No interdiffusion occurred during permeation tests. In addition, the shape and the morphology of the BCZY and GDC grains remained unchanged.

The XRD analyses carried out on the dense membranes confirmed that the phase composition of the dense layer was not modified. No secondary phases were detected (Figure 5.13).

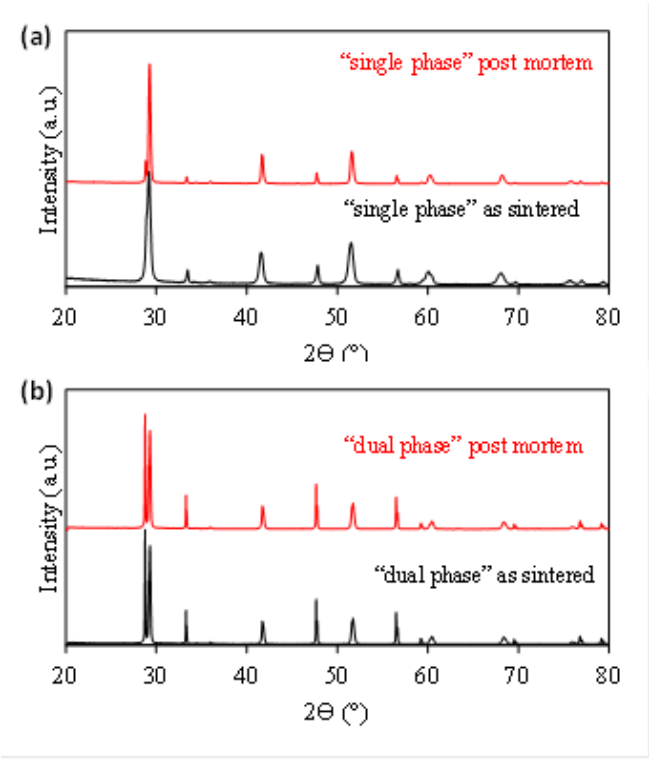

Figure 5.13 (a) XRD pattern of the "single phase" membrane and (b) of the "dual phase" membrane as sintered and after permeation measurements.

In conclusion, the H_2 permeation measurements revealed that a high phase purity is mandatory to obtain high hydrogen fluxes: the presence of a single mix-phase as thin as 2 μm highly affected the membrane's permeation performances.
The asymmetric architecture displays enhanced J_{H2} respect to the 650 μm-thick pellet. However, the porous support led to mass transfer resistance phenomena. In addition, the low thickness of the active layer made more and more important the surface kinetics, which could be improved by the Pt catalytic activation on both the porous and dense surfaces. The activated cer-cer asymmetric membrane showed the highest hydrogen flux reported to date for an all-ceramic membrane, with performances comparable to some cer-met systems. Post mortem characterization assessed microstructure and the phase purity retention after testing, confirming the stability of the system.

This activity showed how the ceramic process optimization can be useful to obtain engineered architectures with suitable microstructure and phase composition responsible of enhanced performances.

References

[1] E. Rebollo, C. Mortalò, S. Escolástico, S. Boldrini, S. Barison, J. M. Serra, M. Fabrizio, *Exceptional hydrogen permeation of all-ceramic composite robust membranes based on $BaCe_{0.65}Zr_{0.20}Y_{0.15}O_{3-d}$ and Y-or Gd-doped ceria*, Energy Environ. Sci. Energy Environ. Sci. 8 (2015) 3675–3686.

[2] K. Leonard, Y.-S. Lee, Y. Okuyama, K. Miyazaki, H. Matsumoto, *Influence of dopant levels on the hydration properties of SZCY and BZCY proton conducting ceramics for hydrogen production*, Int. J. Hydrogen Energy 42 (2017) 3926-3937.

[3] J. F. Basbus, M. D. Arce, F. D. Prado, A. Caneiro, L. V. Mogni, *A high temperature study on thermodynamic, thermal expansion and electrical properties of $BaCe_{0.4}Zr_{0.4}Y_{0.2}O_{3-\delta}$ proton conductor*, J. Power Sources 329 (2016) 262–267.

[4] W. Zając, J. Molenda, *Properties of doped ceria solid electrolytes in reducing atmospheres*, Solid State Ionics 192 (2011) 163–167.

[5] A. Sin, Yu. Dubitsky, A. Zaopo, A.S. Aricò, L. Gullo, D. La Rosa, S. Siracusano, V. Antonucci, C. Olivia, O. Ballabio, *Preparation and sintering of $Ce_{1-x}Gd_xO_{2-x/2}$ nanopowders and their electrochemical and EPR characterization*, Solid State Ionics 175 (2004) 361–366.

[6] A. Morán-Ruiz, K. Vidal, A. Larrañaga, J.M. Porras-Vázquez, P.R. Slater, M.I. Arriortua, *Laser machining of $LaNi_{0.6}M_{0.4}O_{3-\delta}$ (M: Co, Fe) dip-coated on a Fe–22Cr mesh material to obtain a new contact coating for SOFC: Interaction between Crofer22APU interconnect and $La_{0.6}Sr_{0.4}FeO_3$ cathode*, Int. J. Hydrogen Energy 40 (2015) 8407–8418.

[7] F. Wang, D. Yan, W. Zhang, B. Chi, J. Pu, L. Jian, *LaCo0.6Ni0.4O3-δ as cathode contact material for intermediate temperature solid oxide fuel cells*, Int. J. Hydrogen Energy 38 (2013) 646-651.

[8] P. Hjalmarsson, M. Sogaard, A. Hagen, M. Mogesen, *Structural properties and electrochemical performance of strontium- and nickel-substituted lanthanum cobaltite*, Solid State Ionics 179 (2008) 636–646.

[9] M. Hrovat, *Characterisation of $LaNi_{1-x}Co_xO_3$ as a possible SOFC cathode material*, Solid State Ionics 83 (1996) 99–105.

[10] O. Marina, *Thermal, electrical, and electrocatalytical properties of lanthanum-doped strontium titanate*, Solid State Ionics 149 (2002) 21–28.

[11] S. Hashimoto, F.W. Poulsen, M. Mogensen, *Conductivity of $SrTiO_3$ based oxides in the reducing atmosphere at high temperature*, J. Alloys Compd. 439 (2007) 232–236.

[12] S. Hashimoto, L. Kindermann, F.W. Poulsen, M. Mogensen, *A study on the structural and electrical properties of lanthanum-doped strontium titanate prepared in air*, J. Alloys Compd. 397 (2005) 245–249.

[13] S. Elangovan, B. Nair, T. Small, *Ceramic mixed protonic/electronic conducting membranes for hydrogen separation* WO 2005/086704 A2.

[14] D. K. Lim, C.J. Park, M.B. Choi, C.N. Park, S.J. Song, *Partial conductivities of mixed conducting $BaCe_{0.65}Zr_{0.2}Y_{0.15}O_{3-\delta}$*, Int. J. Hydrogen Energy 35 (2010) 10624-10629.

[15] E. Fabbri, A. D'Epifanio, E. Di Bartolomeo, S. Licoccia, E. Traversa, *Tailoring the chemical stability of $Ba(Ce_{0.8-x}Zr_x)Y_{0.2}O_{3-\delta}$ protonic conductors for Intermediate Temperature Solid Oxide Fuel Cells (IT-SOFCs),* Solid State Ionics 179 (2008) 558-564.

[16] A. Gondolini, E. Mercadelli, A. Sanson, S. Albonetti, L. Doubova, S. Boldrini, *Effects of the microwave heating on the properties of gadolinium-doped cerium oxide prepared by polyol method*, J. Eur. Ceram. Soc. 33 (2013) 67–77.

[17] C. Jin, Z. Huizhu, D. Lei, L. Yuehua, L. Wang, *Effect of Ba nonstoichiometry on the phase composition, microstructure, chemical stability and electrical conductivity of $Ba_xCe_{0.7}Zr_{0.1}Y_{0.1}Yb_{0.1}O_{3-\delta}$ ($0.9 \leq x \leq 1.1$) proton conductors*, Ceram. Int. 41 (2015) 7796–7802.

[18] S. Ricote, N. Bonanos, A. Manerbino, W.G. Coors, *Conductivity study of dense $BaCe_xZr_{(09-x)}Y_{0.1}O_{(3-\delta)}$ prepared by solid state reactive sintering at 1500°C*, Int. J. Hydrogen Energy 37 (2012) 7954-7961.

[19] D. Medvedev, J. Lyagaeva, G. Vdovin, S. Beresnev, A. Demin, P. Tsiakaras, *A tape calendering method as an effective way for the preparation of proton ceramic fuel cells with enhanced performance*, Electrochim. Acta 210 (2016) 681–688.

[20] S. Lubke and H.-D. Wiemhofer *Electronic Conductivity of Gadolinia Doped Ceria* Ber. Bunsenges. Phys. Chem. 102 (1998) 642-649.

[21] K. Eguchi, T. Setoguchi, T. Inoue, H. Arai, *Electrical properties of ceria-based oxides and their application to solid oxide fuel cells,* Solid State Ionics 52 (1992) 165-172.

[22] Y. Li, R. Guo, C. Wang, Y. Liu, Z. Shao, J. An, C. Liu, *Stable and easily sintered $BaCe_{0.5}Zr_{0.3}Y_{0.2}O_{3-\delta}$ electrolytes using ZnO and Na_2CO_3 additives for protonic oxide fuel cells*, Electrochim. Acta 95 (2013) 95– 101.

[23] A. Slodczyk, M.D. Sharp, S. Upasen, P. Colomban, J.A. Kilner, *Combined bulk and surface analysis of the $BaCe_{0.5}Zr_{0.3}Y_{0.16}Zn_{0.04}O_{3-\delta}$ (BCZYZ) ceramic proton-conducting electrolyte*, Solid State Ionics 262 (2014) 870–874.

[24] L.A. Villas-Boas, F. M. L. Figueiredo, D. P. F. de Souza, F. M. B. Marques, *Zn as sintering aid for ceria-based electrolytes*, Solid State Ionics 262 (2014) 522-525.

[25] S. Tao, J. T. S. Irvine, *A stable, easily sintered proton-conducting oxide electrolyte for moderate-temperature fuel cells and electrolyzers*, Adv. Mater. 18 (2006) 1581-1584.

[26] P. Babilo, S. M. Haile, *Enhanced sintering of yttrium-doped barium zirconate by addition of ZnO*, J. Am. Ceram. Soc. 88 (2005) 2362-2368.

[27] Z. Peng, R. Guo, Z. Yin, J. Li, *Influences of ZnO on the properties of $SrZr_{0.9}Y_{0.1}O_{2.95}$ protonic conductor*, J. Am. Ceram. Soc. 91 (2008) 1534-1538.

[28] H. Wang, R. Peng, X. Wu, J. Hu, C. Xia, *Sintering behavior and conductivity study of yttrium-doped $BaCeO_3$–$BaZrO_3$ solid solutions using ZnO additives*, J. Am. Ceram. Soc. 92 (2009) 2623-26239.

[29] C. Zhang, H. Zhao, N. Xu, X. Li , N. Chen, *Influence of ZnO addition on the properties of high temperature proton conductor $Ba_{1.03}Ce_{0.5}Zr_{0.4}Y_{0.1}O_{3-d}$ synthesized via citrate-nitrate method*, Int. J. Hydrogen Energy 36 (2009) 2739-2746.

[30] D. Montaleone, *Studio ed ottimizzazione di processi per la produzione di membrane ceramiche per la separazione di idrogeno*, Master Degree Thesis, University of Bologna, 2014.

[31] S. M. Haile, G. Staneff, K.H. Ryu, *Non-stoichiometry, grain boundary transport and chemical stability of proton conducting perovskites*, J. Mat. Sci. 36 (2001) 1149-1160.

[32] S. Barison, M. Battagliarin, T. Cavallin, L. Doubova, M. Fabrizio, C. Mortalò, S. Boldrini, L. Malavasi, R. Gerbasi, *High conductivity and chemical stability of $BaCe_{1-x-y}Zr_xY_yO_{3-d}$ proton conductors prepared by a sol–gel method*, J. Mater. Chem., 18 (2008) 5120-5128.

[33] D. Shima, S. M. Haile, *The influence of cation no-stoichiometry on the properties of undoped and gadolinia-doped barium cerate*, Solid State Ionics, 97 (1997) 443-455.

[34] S. Barison, M. Battagliarin, T. Cavallin, L. Doubova, M. Fabrizio, C. Mortalò, S. Boldrini, R. Gerbasi, *Barium non-stoichiometry role on the properties of $Ba_{1+x}Ce_{0.65}Zr_{0.20}Y_{0.15}O_{3-\delta}$ proton conductors for IT-SOFCs*, Fuel Cells 5 (2008) 360-368.

[35] C. Peng, J. Melnik, J. Luo, A. R. Sanger, K. T. Chuang, *$BaZr_{0.8}Y_{0.2}O_{3-\delta}$ electrolyte with and without ZnO sintering aid: preparation and characterization*, Solid State Ionics, 181 (2010) 1372-1377.

[36] A. Kruth, J. T. S. Irvine, *Water incorporation studies on doped barium cerate perovskites, Solid State Ionics*, 162 (2003) 83-91.

[37] K. H. Ryu, S. M. Haile, *Chemical stability and proton conductivity of doped $BaCeO_3 – BaZrO_3$ solid solutions*, Solid State Ionics 125 (1999) 355-367.

[38] D. Montaleone, E. Mercadelli, A. Gondolini, P. Pinasco, A. Sanson, *On the compatibility of dual phase Ba $Ce_{0.65}Zr_{0.2}Y_{0.15}O_3$-based membrane for hydrogen separation application*, Ceram. Int. 43 (2017) 10151-10157.

[39] K. Xie, R. Yan, Y. Jiang, X. Liu, G. Meng, *A simple and easy one-step fabrication of thin $BaZr_{0.1}Ce_{0.7}Y_{0.2}O_{3-\delta}$ electrolyte membrane for solid oxide fuel cells*, J. Membr. Sci., 325 (2008) 6-10.

[40] D. L. Corker, R. W. Whatmore, E. Ringgaars, W. W. Wolny*, Liquid-phase sintering of PZT ceramics*, J. Eur. Ceram. Soc. 20 (2000) 2039-2045.

[41] P. Babilo, T. Uda, S. H. Haile, *Processing of yttrium-doped barium zirconate for high proton conductivity*, J. Mater. Res., 22 (2007) 1322-1330.

[42] J. M. Serra, O. Büchler, W. A. Meulenberg, H P. Buchkremer, *Thin $BaCe_{0.8}Gd_{0.2}O_{3-\delta}$ protonic electrolytes on porous $Ce_{0.8}Gd_{0.2}O_{1.9}$-Ni substrates*, J. Electrochem. Soc., 154 (2007) B334-B340.

[43] L. Malavasi, C. Tealdi, C. Ritter, V. Pomjakushin, F. Gozzo, Y. Diaz-Fernandez, *Combined neutron and synchrotron X-ray diffraction investigation of the $BaCe_{0.85-x}Zr_xY_{0.15}O_{3-\delta}$ ($0.1 \leq x \leq 0.4$) proton conductors*, Chem. Mater. 25 (2011) 1323-1330.

[44] P. Cai, D. Green, G. Messing, *Constrained densification of alumina/zirconia hybrid laminates. 2. Viscoelastic stress computation*, J. Am. Ceram. Soc. 80 (1997) 1940–1948.

[45] T. T. Molla, H. L. Frandsen, R. Bjørk, D. W. Ni, E. Olevsky, N. Pryds, *Modeling kinteics of distortion in porous bi-layered structures*, 33 (2013) 1297-1305.

[46] P. Cai, D. Green, G. Messing, *Constrained densification of alumina/zirconia hybrid laminates. 1. Experimental observations of processing defects*, J. Am. Ceram. Soc. 80 (1997) 1929–1939.

[47] W. Deibert, M. E. Ivanova, W. A. Meulenberg, R. Vaßen, O. Guillon, *Preparation and sintering behavior of $La_{5.4}WO_{12-\delta}$ asymmetric membranes with optimized microstructure for hydrogen separation*, J. Membr. Sci. 492 (2015) 439-451.

[48] S. Zhan, X. Zhu, B. Ji, W. Wang, X. Zhang, J. Wang, W. Yang, L. Lin, *Preparation and hydrogen permeation of $SrCe_{0.95}Y_{0.05}O_{3-\delta}$ asymmetrical membranes*, J. Membr. Sci. 340 (2009) 241–248.

[49] S. Ricote , N. Bonanos , A. Manerbino, W.G. Coors, *Conductivity study of dense $BaCe_xZr_{(0.9-x)}Y_{0.1}O_{(3-d)}$ prepared by solid state reactive sintering at 1500°C*, Int. J. Hydrogen Energy 37 (2012) 7954-7961.

[50] M. E. Ivanova, S. Escolástico, M. Balaguer, J. Palisaitis, Y. J. Sohn, W. A. Meulenberg, O. Guillon, J. Mayer, J. M. Serra, *Hydrogen separation through tailored dual phase membranes with nominal composition $BaCe_{0.8}Eu_{0.2}O_{3-\delta}$:$Ce_{0.8}Y_{0.2}O_{2-\delta}$ at intermediate temperatures*, Scientific Reports 6 (2016) 34773.

[51] Y. Wei, J. Xue, H. Wang, J. Caro, *Hydrogen permeability and stability of $BaCe_{0.85}Tb_{0.05}Zr_{0.1}O_{3-\delta}$ asymmetric membranes*, J. Membr. Sci. 488 (2015) 173-181.

[52] W. Sun, Z. Shi, W. Liua, *Considerable hydrogen permeation behavior through a dense $Ce_{0.8}Sm_{0.2}O_{2-\delta}$ (SDC) Asymmetric thick film*, Journal of The Electrochemical Society, 160 (2013)F585-F590.

[53] Z. Zhu, W. Sun, L. Yan, W. Liu, W. Liu, *Synthesis and hydrogen permeation of Ni-Ba($Zr_{0.1}Ce_{0.7}Y_{0.2}$)O_{3-d} metal ceramic asymmetric membranes*, Int. J. Hydrog. Energy 36 (2011) 6337-6342.

[54] S. Cheng, V.K. Gupta, J.Y.S. Lin, *Synthesis and hydrogen permeation properties of asymmetric proton-conducting ceramic membranes*, Solid State Ionics 176 (2005) 2653–2662.

[55] J. Li, H. Yoon, E. D. Wachsman, *Hydrogen permeation through thin supported $SrCe_{0.7}Zr_{0.2}Eu_{0.1}O_{3-d}$ membranes; dependence of flux on defect equilibria and operating conditions*, J. Membr. Sci. 381 (2011) 126-131.

[56] M. Liu, W. Sun, X. Li, S. Feng, D. Ding, D. Chen , M. Liu,H. C. Park, *High-performance Ni-$BaZr_{0.1}Ce_{0.7}Y_{0.1}Yb_{0.1}O_{3-d}$ (BZCYYb) membranes for hydrogen separation,* Int. J. Hydrog. Energy 38 (2013) 14743-14749.

[57] V. Gil, J. Gurauskis, M. A. Einarsrud, *Asymmetric supported dense lanthanum tungstate membranes*, J. Eur. Ceram. Soc. 34 (2014) 3783-3790.

[58] S. Nikodemski, J. Tong, C. Duan, R. O'Hayre, *Ionic transport modification in proton conducting $BaCe_{0.6}Zr_{0.3}Y_{0.1}O_{3-\delta}$ with transition metal oxide dopants*, Solid State Ionics 294 (2016) 37-42.

Chapter 6
Conclusions and Future perspectives

6. Conclusions and future perspectives

High temperature hydrogen separation with all-ceramic asymmetric membrane is a suitable technology for the intensification of important industrial processes, such as H_2 separation/purification and H_2-related reactions. However, many technological challenges had to be addressed to obtain highly performing membranes with asymmetric architecture. This activity faced all the challenges related to the manufacturing of a thin and dense membrane supported by a porous and tough layer. In addition, the enhanced properties were evaluated through H_2 permeation measurements under different conditions.

The first part of the thesis was devoted to the individuation of the ceramic-ceramic composite comprising a proton conducting and an electron conducting phases forming a dual phase inter-percolating network with enhanced H_2 permeation properties. Y-doped $BaCe_xZr_{1-x}O_{3-\delta}$ (BCZY) was selected as the proton conducting phase as it represents the optimal balance between proton conductivity, sinterability and chemical stability against CO_2. The first step was the selection of a possible electron conductor to be coupled with BCZY. The screening activity indicated ceria-based - CeO_2 and $Ce_{0.8}Gd_{0.2}O_{1.9}$ (GDC) - as the most promising systems thanks their chemical and thermomechanical compatibility with BCZY. The addition of ZnO (0.8 wt.% respect to the BCZY and GDC mixture) enhanced the sinterability of the cer-cer system decreasing the sintering T_{onset} by 250°C: pellets sintered at 1400°C for four hours showed 96.8 ± 0.6 % of the theoretical density.

Afterwards, the attention was devoted to the production of a dense membrane of this composite supported by a porous layer of the same material. This asymmetric architecture was obtained through tape casting and lamination of both support and membrane layer. Tapes containing BCZY powder ad rice starch as pore former were then used for the manufacturing of the porous support. Dynamic Mechanical Analysis (DMA) allowed to find helpful results which correlate the formulation with the mechanical properties of the green tapes and then with the lamination process. The rice starch used as pore former dramatically modified the tape's

properties over the investigated temperature range. At low temperature it displayed a blocking effect on the binder chain mobility; but increasing the temperature this effect disappeared, indicating that a successful lamination process occurs in a narrow temperature range. Moreover, this activity showed the possibility to mimic the lamination process, allowing the identification of the best conditions for lamination. The correlation between the temperature and the viscosity of the multilayers during the lamination represents an important breackthrough for the multilayers processing.

The sintering atmosphere was found to play a key role on obtaining a thin and dense membrane layer with the required phase composition. In fact, sacrificial Ba-containing powders were necessary to counterbalance the Ba loss from the BCZY phase which occurs at the high temperatures required for the membrane densification. An excessive Ba content however, promoted the formation of a single-phase material due to Ba dissolution into the BCZY and GDC lattices. Only using the BCZY-GDC as Ba-source, the desired phase composition was achieved and the suitable microstructure (20 μm-thick dense layer and 42 vol.% porous support) was obtained. Unfortunately, as the densification of the membrane layers occurred, some cracks appeared in the dense layer, probably due to a thermomechanical mismatch between the porous support and the dense layer.

The thermomechanical compatibility was obtained only using BCZY-GDC for both layers. Different parameters were then evaluated to optimize the casting and sintering processes with this new support: the amount of sintering aid in the membrane layer, the shrinkage of the support layer during thermal treatments, and the effect of different Ba-sources during sintering. The increase of the ZnO content from 0.8 wt % to 1 wt % enhanced the densification of the active layer, while the introduction of 2 wt. % of ZnO did not imply any further improvement. Similarly, to the BCZY-supported membranes, when BCZY was used as Ba-source, a solid-state reaction took place in the first few microns of the membrane layer while only BCZY-GDC allowed the phase retention. The formulation optimization and the sintering atmosphere modification allowed the production of a sufficiently dense

20 μm-thick cer-cer membrane layer supported by a porous (36 vol. %) 750 μm-thick layer. The obtained asymmetric membranes were planar and crack-free, therefore suitable for H_2 separation applications.

H_2 permeation tests were done at the Instituto de Tecnología Química of Valencia under different conditions. Measurements revealed the asymmetric architecture displays remarkable H_2 permeation: 0.26 mL min^{-1} cm^{-2} at 750°C with both membrane sides humidified feeding 50 vol.% H_2 in He. The surface kinetics played a more important role with thin active layer than with thick pellets commonly used for this application, and was improved by Pt catalytic activation of both porous and dense surfaces. The activated cer-cer asymmetric membrane showed the highest hydrogen flux reported in literature for an all-ceramic membrane, with performances comparable to some cer-met systems: 0.47 mL min^{-1} cm^{-2} at 750°C with both membrane sides humidified feeding 50 vol.% of H_2 in He. The experiments showed also that to obtain high hydrogen fluxes, the system should be completely bi-phasic: the presence of just 2 μm-thick single mix-phase on its surface highly affected the performances. In addition, some efforts are still needed to reduce the mass transfer resistance phenomena on the support. Post mortem characterization assessed microstructure and the phase purity retention after testing, confirming the stability of the system.

In conclusion, this activity showed how the ceramic process optimization can be useful in obtaining engineered architectures with suitable microstructure and phase composition responsible of enhanced performances. The obtained asymmetric BCZY-GDC membrane showed the highest permeation flux known to date for this technology.

Despite the remarkable performances reported, the work done indicates some possible improvements that can be made to obtain even higher performant membranes. First, mass transport limitation could be addressed focusing on further support engineering through phase inversion casting or new shaping technologies, such as robocasting. In addition, the mechanical properties of the sintered

membranes have to be considered, as their life-time durability. Then, the scale-up of the membrane to larger area samples and their arrangement into stacks has to be validated.

Acknowlegments

First, I would like to thank Dr.ssa Anna Tampieri for having let me work at ISTEC-CNR, and Prof. Enrico Dalcanale for the coordination of my PhD course.
I thank Dr.ssa Alessandra Sanson for having taught me far more than academic notions. Thanks to my research group, made of friends as well as colleagues. Elisa, for being my support during these years. Angela for being so patient with me, even in hard times. I would like to thank the "other two" of my research group: Alex (my "PhD-mate"), and Nicola (the "screen-printing-guy"), thanks for the laughs and the good times. I am grateful to Paola, for her support inside and outside the lab "Formatura". I am going to miss that place. Thanks to the whole ISTEC-CNR staff: everyone has taught me something, it has been a pleasure working with you. Thanks to all the colleagues at ISTEC, for the lunch times spent together, coffee breaks or simple chitchat. Special thanks to Elisabetta for all the wonderful moments spent together (I still owe you some coffee cups…). Thanks to Dr. Matteo Ardit for the precious XRD refinements and the support. I thank Prof. J. M. Serra for having hosted me in his laboratories, and I thank his research group for having made me feel home: Sara, for her fundamental help with the permeation measurements, Juan E., Juan B. (ùs mégna?), Alvaro, las dos Marias, Raquel, Nuria, and Fidel for all the wonderful moments spent together during my internship in Valencia.
Thanks to my friends that are always there for me: you are so many, and so important to me. We know each other since ages, and I am sure it is just the beginning.
Finally, I would like to thank my parents, my role model, Francesco and Elena. Thank you for your continuous support, for loving us right as we are. Thanks also to my seven brothers and sisters: nothing would be the same without you.
But the biggest thank you goes to my wife Annamaria, "'cause we are lovers, and that is a fact – yes, we are lovers, and that is that".